Design of Functional Structures and Measurement Techniques for Electromagnetic Waves

Johan Lundgren

Doctoral Dissertation
Electromagnetic Theory

Lund University
Lund, Sweden
2021

Doctoral dissertation which, by due permission of the Faculty of Engineering, Lund University, will be publicly defended on June 18, 2021, at 1 p.m. in lecture hall E:B, John Ericssons väg 4, Lund, for the degree of Doctor of Philosophy in Engineering in Electromagnetic Theory.

A long time ago in a galaxy far, far away....

Abstract

Electromagnetic fields exist all around us. Through evolution, nature has developed tools to interact and use these fields, where our eyes are a spectacular example. Humans have a long history of developing structures and objects of their own to alter and interact with these fields. Today they are important cornerstones in society, with radiating devices such as cell phones, Wi-Fi routers, or car radar and functional structures such as tinted windows, 3D glasses, and microwave oven doors. There is a high demand for these objects in various application areas. This dissertation deals with the design of functional structures along with measurement techniques of the electromagnetic field.

The dissertation is centered on two parts, a general introduction and research overview (Part I) and six scientific papers, published in peer-reviewed international journals (Part II). The general introduction and research overview puts the results from the scientific papers in perspective and presents a path between them. It starts with fundamental theoretical concepts in electromagnetic theory and continues into discussing functional structures, measurement techniques, near-field measurements, and simulations of scattering media. The two primary categories of the included papers are functional structures, Papers I, II, III, V, VI, and electromagnetic measurements Paper III, IV, V, VI.

Paper I investigates a functional structure in transmission through periodic sub-wavelength apertures. Fundamental limitations are presented and a functional structure is designed and optimized to reach a bandwidth close to the attainable limit. The design is manufactured and measured to verify the validity of a sum rule.

In Papers II and III, functional structures exhibiting circular polarization selectivity are explored. A circular polarization selective structure is designed for satellite communication applications with dual band performance. The design is manufactured and measured through an experimental technique and post-processing scheme, specifically aimed at accurate characterization.

Papers IV–VI are concerned with mm-wave imaging systems and measurement techniques of radiating devices. Techniques for reflection-based non-destructive testing measurements are developed along with techniques for measurements of the radiative near field of devices using functional structures. The measurement technique in Paper V consists of measuring the radiative near field, computing equivalent currents, and reconstructing the electromagnetic field at points of interest. This is carried out through a system calibration using a small aperture as a functional structure. In Paper VI, the functional structure is a metasurface that converts incident radiation to heat imaged with an infrared camera. The metasurface is designed for the low power levels of consumer hand-held devices.

Finally, the dissertation discusses a simulation approach of full-wave solutions for highly scattering random media. The simulation tool aims to describe focusing of light into, and through, random media using wavefront shaping with functional structures to enable measurements of regions deep within tissue.

Populärvetenskaplig Sammanfattning

Elektromagnetisk strålning är en grundpelare för livet på jorden. Denna trådlösa överföring av energi utnyttjas av fotosyntesen hos växter och på senare tid till människans uppkopplade samhälle. Likt ringar på vattnet, eller svängningarna på en gitarrsträng, utbreder sig elektromagnetisk strålning som vågor i rummet. Egenskapen hos ljud som gör att två toner upplevs olika, våglängden, återfinns också hos strålning; såsom att ljus med olika våglängder upplevs som olika färger. En röd boll är röd för att den i huvudsak reflekterar den våglängd som svarar mot rött och absorberar de övriga.

Ljus har även en annan viktig egenskap, som styr hur det interagerar med omvärlden. När fiskar rör sig framåt svänger de sin stjärtfena från höger till vänster och delfiner svänger istället upp och ner. På liknande sätt kan ljusvågor svänga i olika riktningar när de utbreder sig. Denna egenskap kallas för polarisation. En vanlig indelning är så kallad linjärpolarisation. Då kan strålningen svänga vertikalt, så som delfinen, eller horisontellt, så som fisken. Det finns även en mer abstrakt svängning som kallas cirkulärpolarisation, i vilken svängningarna sker som korkskruvar som är antingen höger- eller vänstervridna.

Precis som att färg demonstrerar egenskapen att skilja på våglängder av ljus, så kan polarisationen också användas. En vanlig användning är polariserade glasögon, där horisontellt polariserat ljus inte passerar glasögonytan, eller passiva 3D glasögon då ena ögat tar emot högervriden polarisation och det andra ögat vänstervriden polarisation. Vi kan betrakta dessa som funktionella strukturer vars beteende beror på vågornas egenskaper. Dessa beskrivna egenskaper innefattar även våglängder vi inte kan se. Osynligt ljus kan påverka oss; såsom att vi blir solbrända av ljus med en kortare våglängd.

Elektromagnetiska vågor och dess egenskaper har, genom århundradena, fascinerat människan och fortsätter än idag att ge upphov till vetenskapliga upptäckter och innovationer. Vanliga användningsområden för strålning, relevant för denna avhandling, är bland annat medicinsk diagnosticering och kommunikation. Laserljus kan till exempel undersöka blödningar och cancer. Men, synligt ljus tränger inte långt in i kroppen utan kommer bara någon millimeter. Detta är för att vävnad är kraftigt spridande och absorberande. Genom att styra ljuset man skickar in så kan man motverka denna spridning och tränga flera centimeter in i kroppen. I denna avhandling behandlas konstruktionen av en simuleringsmodell för att kunna fokusera och styra ljus långt in i kroppen.

I dagens samhälle är vi omgivna av olika trådlösa elektroniska produkter som förser oss med omvärldsuppkoppling. Detta sker genom strålning som har mycket längre våglängd än synligt ljus. Med den senaste generationen av trådlösa system så har det blivit ökat fokus på våglängder mellan $0,1-1\,\mathrm{cm}$. Den tekniska utvecklingen samt användningen ökar kraftigt och ställer stora krav på hastighet och tillgänglighet. Dessa våglängder och krav möjliggör utveckling av nya tekniker för att lösa dessa komplicerade problem.

Ett av huvudområdena i denna avhandling är funktionella strukturer som

kan särskilja på vågor baserat på bland annat våglängd och polarisation. Dessa ytor utvecklas genom kunskap i den bakomliggande fysiken, fundamentala begränsningar samt genom datorsimuleringar med optimering. Likt att en spegel gör så att ett rum upplevs större så kan funktionella ytor göra vårt elektromagnetiska "rum" större. Detta kan exempelvis bidra till att ge ökad kapacitet i kommunikationslänken mellan en satellit och jorden, vilket i sin tur kan resultera i snabbare kommunikationshastigheter. En cirkulärpolarisationsselektiv struktur designades och konstruerades i denna avhandling med avsikt att förbättra denna del av kommunikationskedjan.

Ett annat huvudområde i avhandlingen berör mätning av funktionella strukturer och strålande objekt, såsom mobiltelefoner. Då strålningen är osynlig är det viktigt att kunna mäta för att verifiera att objekten fungerar som förväntat och att strålningsnivån inte överstiger bestämda nivåer. Vid dessa mätningar används ofta elektromagnetiska prober, "ögon" för andra våglängder. Detta är inte helt okomplicerat att göra då dessa objekt, till skillnad från våra ögon, påverkar det infallande fält det mäter på. Ju närmre mätningen sker, desto starkare blir kopplingen. Klassiskt beräknas kopplingen bort genom att ha en välspecificerad prob, men osäkerhet i positionering kvarstår. Avhandlingen undersöker hur en funktionell yta kan assistera mätningar och kalibrera hela mätsystemet. Somliga problem är svåra att kringgå då de är fundamentala för elektromagnetiska fält. En mätmetod som presenteras i avhandlingen använder istället den värme som bildas när strålning absorberas. En bild av värmeutvecklingen ger en indirekt bild av det elektromagnetiska fältet. Genom att kombinera multifysikaliska fenomen och optimera olika subprocesser designas och konstrueras en funktionell yta som kan hantera denna avbildning för energinivåer motsvarande telefoners utstrålning.

Preface

This thesis summarizes the research I have carried out over the past four years at the Department of Electrical and Information Technology, Lund University, Sweden. The thesis starts with a research overview followed by the scientific papers as listed below.

List of Included Papers

I. A. Ludvig-Osipov, J. Lundgren, C. Ehrenborg, Y. Ivanenko, A. Ericsson, M. Gustafsson, B.L.G Jonsson, and D. Sjöberg "Fundamental Bounds on Transmission Through Periodically Perforated Metal Screens with Experimental Validation." *IEEE Transactions on Antennas and Propagation*, Vol. 68, No. 2, pp. 773–782, 2020.

   Contributions of the author: I designed and optimized the extraordinary transmission sheet and the measurement setup, performed the measurements, wrote post-processing algorithms for the experimental data, and wrote parts of the paper.

II. J. Lundgren, A. Ericsson and D. Sjöberg, "Design, Optimization and Verification of a Dual Band Circular Polarization Selective Structure." *IEEE Transactions on Antennas and Propagation*, Vol. 66, no. 11, pp. 6023-6032, 2018.

   Contributions of the author: The author of this thesis is the main contributor to this paper. I designed and optimized the structure in a numerical software, fabricated a prototype, carried out experimental characterizations of the structure, and wrote the majority of the paper.

III. A. Ericsson, J. Lundgren and D. Sjöberg, "Experimental Characterization of Circular Polarization Selective Structures using Linearly Single-Polarized Antennas." *IEEE Transactions on Antennas and Propagation*, Vol. 65, No. 8, pp. 4239–4249. 2017.

   Contributions of the author: I co-designed and fabricated the measurement setup, performed the measurements, wrote post-processing algorithms for the experimental data, and wrote parts of the paper.

IV. J. Helander, J. Lundgren, D. Sjöberg, C. Larsson, T. Martin and M. Gustafsson, "Reflection-Based Source Inversion for Sparse Imaging of Low-Loss Composite Panels." *IEEE Transactions on Antennas and Propagation*, Vol. 68, no. 6, pp. 4860–4870, 2020.

   Contributions of the author: I co-designed the experimental setup, carried out the measurements and wrote parts of the paper. The data processing and algorithms in this work were implemented by Jakob Helander.

V. J. Lundgren, J. Helander, M. Gustafsson, D. Sjöberg, B. Xu and D. Colombi, "A Near-Field Measurement and Calibration Technique: Radio-Frequency Electromagnetic Field Exposure Assessment of Millimeter-Wave 5G Devices." *IEEE Antennas and Propagation Magazine*, early access, 2020.

Contributions of the author: The author of this thesis is the main contributor to this paper. I designed and optimized the structure in a numerical software, carried out measurements with post processing of data, and wrote the majority of the paper.

VI. J. Lundgren, M. Gustafsson, D. Sjöberg, and M. Nilsson, "IR and Metasurface based mm-Wave Camera." *Applied Physics Letters*, Vol. 118, pp. 184104, 2021.

Contributions of the author: The author of this thesis is the main contributor to this paper. I designed and optimized the structure in a numerical software, carried out measurements with post processing of data, and wrote the majority of the paper.

Other Scientific Work by the Author

The author of this dissertation is also the author or co-author of the following publications and scientific work which are related to but not considered part of the dissertation:

VII. J. Lundgren, M. Gustafsson, D. Sjöberg, "New Approaches to EMF Measurements of mmWave Devices." *15th European Conference on Antennas and Propagation (EuCAP),* Düsseldorf, Germany, 2021.

VIII. J. Lundgren, J. Helander, M. Gustafsson, "Measurement Characterization of Aperture Correction Technique for EMF." *14th European Conference on Antennas and Propagation (EuCAP),* Copenhagen, Denmark, 2020.

IX. J. Lundgren, J. Helander, M. Gustafsson, "Near-Field Reconstruction Using Aperture Probe Correction Technique for mm-Wave Devices." *13th European Conference on Antennas and Propagation (EuCAP),* Krakow, Poland, 2019.

X. J. Helander, J. Lundgren, D. Sjöberg, "Reflection-Based Inverse Scattering Image Reconstruction for Non-Destructive Testing." *Antenna Measurement Techniques Association (AMTA),* Williamsburg, Virginia, USA, 2018.[1]

---

[1] Honored with best student paper award at AMTA 2018.

XI. J. Lundgren, J. Helander, M. Gustafsson, D. Sjöberg, B. Xu and D. Colombi, "Near Field Reconstruction for Electromagnetic Exposure of 5G Communication Devices." *Antenna Measurement Techniques Association (AMTA),* Williamsburg, Virginia, USA, 2018.[2]

XII. J. Lundgren, A. Ericsson and D. Sjöberg, "Optimization and Experimental Verification of Dual Band Circular Polarization Selective Structures." *Swedish Microwave Days, AntennEMB*, Lund, Sweden, 2018.

XIII. A. Ericsson, J. Lundgren and D. Sjöberg, "Design and Characterization of Circular Polarization Selective Structures." *Swedish Microwave Days, AntennEMB*, Lund, Sweden, 2018.

XIV. A. Ericsson, J. Lundgren and D. Sjöberg, "A Portable Measurement Setup for Characterizing Circular Polarization Selective Structures." *11th European Conference on Antennas and Propagation (EuCAP)*, Paris, France, 2017.

XV. J. Lundgren, A. Ericsson and D. Sjöberg, "An Optimization Strategy for Dual Band Circular Polarization Selective Structures." *International Conference on Electromagnetics in Advanced Applications (ICEAA),* Verona, Italy, 2017.

XVI. D. Sjöberg and J. Lundgren, "Characterization of the Performance of a Dual Band Circular Polarization Selective Structure Illuminated by Short Pulses." *International Conference on Electromagnetics in Advanced Applications (ICEAA),* Verona, Italy, 2017.

---

[2]Honored with third place, best student paper award at AMTA 2018.

Acknowledgments

Lund, May 2021

Johan Lundgren

Acronyms and Abbreviations

2D   two-dimensional

3D   three-dimensional

5G   fifth generation mobile networks

AR   axial ratio

CEM   computational electromagnetics

CP   circular polarization

CPSS   circular polarization selective structure

CS   compressive sensing

CST MWS   Computer Simulation Technology Microwave Studio

DUT   device under test

EM   electromagnetic

EMF   electromagnetic field

EoT   extraordinary transmission

FDTD   finite difference time domain

FEKO   Feldberechnung für Körper mit beliebiger Oberfläche

FEM   finite element method

FSS   frequency selective structure

HP   horizontal polarization

IL   insertion loss

IR   infrared

LHCP   left hand circular polarization

LHCPSS   left hand circular polarization selective structure

LP   linear polarization

LPSS   linear polarization selective structure

MATLAB®   matrix laboratory

mm-wave	millimeter wave
MoM	method of moments
NDT	non-destructive testing
PDE	partial differential equation
PEC	perfect electric conductor
RCS	radar cross section
RF	radio frequency
RHCP	right hand circular polarization
RHCPSS	right hand circular polarization selective structure
RL	return loss
RX	receiver
SAR	specific absorption rate
SATCOM	satellite communications
SNR	signal to noise ratio
SVD	singular value decomposition
TE	transverse electric
TM	transverse magnetic
TX	transmitter
UOT	ultrasound-modulated optical tomography
VNA	vector network analyzer
VP	vertical polarization
XPD	cross polarization discrimination

Notation

The following is a summary of the most important aspects of the mathematical notation is used throughout the thesis:

- Scalars are written by regular font, italic, a

- Vectors are written using bold font, italic, $\boldsymbol{A}$

- Matrices are written using bold font, roman, $\mathbf{A}$

- Mathematical constants, well-known functions and operators are written in roman font, π, i, j, e, ∂, $\int f(x)\,\mathrm{d}x$

- Subscripts or superscripts representing a word is written in roman font, $\boldsymbol{E}_\mathrm{i}$ (incident)

- Elements in vectors/matrices are scalar with index indicated by subscripts in italic, A_m

- Time domain vectors are written by calligraphic font, $\boldsymbol{\mathcal{E}}(\boldsymbol{r}, t)$

- Frequency domain vectors use normal font, $\boldsymbol{E}(\boldsymbol{r}, \omega)$

Contents

Part I: Introduction and Research Overview

Johan Lundgren

1   Background and Motivation

The arguably most important incident known to man marks the starting point of this journey and everything. Ever since the Big Bang when four fundamental forces emerged from a soup of energy, electromagnetic radiation has been an essential part of the universe as we know it [8]. Stars provide planets with energy mediated through electromagnetic radiation and have been very important to the evolution of life on our planet [207]. Evolution has provided us with sensors, our eyes, which can detect the peak of the solar spectrum [213]. Naturally, this information has not always been known. However, we as humans have always been intrigued by the world and used the benefits of radiation, sometimes unknowingly. For instance, fires gives us heat and vision, a cornerstone of our civilization [84]. The sun, the moon, and starlight have interested mankind and have had a significant cultural and scientific impact throughout the ages [183]. An early example is the ancient Egyptians and Mesopotamians, which in their quest for knowledge, developed lenses to manipulate light [65].

The techniques and their uses developed throughout the civilizations and have led to grand discoveries with new scientific areas to explore and significant cultural pieces [55, 240]. Objects with color can be described as regions manipulating light, reflecting certain frequencies of light, and absorbing others. In this view beautiful objects such as the highly complex, both in construction and the underlying physics, stained glass windows in religious buildings are a collection of surfaces manipulating electromagnetic radiation, a kind of functional structure [227].

In today's standard, we may think that not much was known regarding electromagnetic radiation, at least not until the 1800s. It was at this time James Clerk Maxwell combined important experimental results and described the connection between physical quantities through what we today know as Maxwell's equations [162–164]. The equations describe how electromagnetic radiation behaves and how it is created. During this period, there was a rapid advancement of technologies. Invisible light was discovered [95, 113], electromagnetic radiation which our eyes cannot capture. With an increased understanding of the underlying physics, electromagnetic radiation was something we could use in our favor. Technologies such as X-rays [204], wireless communication systems [96, 134], telephones [20], and photophones [21] were created. Electromagnetic radiation began to be used within medical applications and communication. Since this time there has been an explosion of new concepts and ideas for electromagnetic radiation.

Apart from the early stained glass windows as an example of a functional structure, there are a plethora of structures that serve a scientific purpose [173, 194]. Some of them are based within optics and include beam splitters, polarization filters, quarter-wave plates, *etc.* [32, 208]. Naturally, they have been expanded and improved upon since the invention of the laser in the 1950s [23]. The interest in controlling light, fueled by a war-torn world, gave progress within radio, radar, and later frequency selective surfaces to protect the radiating an-

Figure 1: Illustration of some use cases for everyday devices, yellow, transmitting or interactive with electromagnetic radiation.

tennas, radomes [40, 104, 132], to name a few. In the post-war and the Cold War era, space was a large political frontier that provided many advances within communication and functional structures [106, 173]. Space is a harsh environment that puts an extreme requirement on the devices serving, both in electromagnetic performance, structural integrity, and physical allocation [108]. Controlling the radiation with functional structures can help alleviate some of these problems. Much work on functional structures has been carried out during the second half of the 20th century. However, new technologies have emerged, along with an increase in computational capacity and optimization techniques, creating several new possibilities.

A lot has happened since the Big Bang and in the context of this work, humans have gone from unaware of electromagnetic radiation to using it and later manipulating it. Today we live in a world where many find it hard to imagine life without certain electromagnetic devices and technologies. The world is global, and we are surrounded by radiating devices providing internet daily.

Operating close to our everyday life, we have several functional structures, such as microwave oven doors, 3D glasses, polarization filters for cameras *etc.* Further away from us, communication satellites are using functional structures to provide efficient uplink and downlink data streams through directing signals and increasing the data capacity [7]. The world is also in the midst of introduc-

Figure 2: Scattering of a beam (left) incident on a highly scattering non-absorbing media (right).

ing the next generation communication system, 5G and beyond [215, 231]. This system provides the architecture enabling higher data streams, multiple devices and connectivity, in turn supporting innovation [27, 199, 250]. In the future, we can expect several new items to use the internet and we will see the sheer number of devices increase significantly [150]. With these emerging technologies and the expanding Internet of Things (IoT), radiation and functional structures will be all around us even more than today [86]. In Fig. 1 we see some example uses of communication devices and functional structures, satellites in space, communication base stations both large and smaller 5G base stations in street light or similar urban objects, phones, tablets, smart home devices, cars with car radar and hospital equipment. It is important to verify the performance of devices to make sure that they comply with existing regulations on electromagnetic radiation. With the inclusion of higher frequencies in the 5G bands, to enable higher data rates, there are new challenges in the measurements with other metrics of interest and higher phase errors for positioning offsets.

Radiation is not just something we measure, but something we can use to measure with. A well-known example of a medical application using electromagnetic radiation is X-ray, a staple technique at any medical facility [99]. Another technique, relevant to this work, is to use laser light to retrieve information from deep within the body through tagging of photons using ultrasound modulation [87]. This may sound simple, but tissue is absorbing and highly scattering. An example of the scattering of an incident beam on a scattering medium is seen in Fig. 2. Here the power flow of a beam, 15 wavelengths wide and incident from the left, is seen on a linear scale. The region right of the black bar is a highly scattering environment and the incident beam is rapidly scattered as it enters this region. The output power density at the right side of the figure is much smaller compared to the incident power density to the left.

This highly scattering environment of human tissue can also be illustrated

with a simple experiment, shine a bright light through the skin between your fingers, light quickly scatterers and the entire region shines with a reddish glow. With great control of the input light and having a receiver collecting the output light, it is possible to describe how the incident wave should be shaped in order to penetrate deep within tissue, several centimeter, and avoid this detrimental random scattering.

There are many interesting areas described above that will be explored in this thesis. One of the central themes is functional structures. Some familiar names for functional structures are Frequency Selective Structure (FSS), metasurfaces, and polarization selective structures. An FSS creates a stop band or pass band over a frequency range such as metalized windows or radomes [172, 173, 190, 191]. Metasurfaces may, for instance, alter beam patterns and grating lobe performance using impedance variations, or control angular dispersion in the optical regime [5, 166, 217, 262]. Polarization selective structures, for both linear and circular polarization, have varying performance based on the incident polarization, transmitting, reflecting, or perhaps converting between polarizations [169, 181]. These are a few of the subgroups and applications under the larger umbrella name of functional structures. This thesis deals with some of them, along with measurement techniques to measure functional structures, which is another major theme of the thesis. We investigate measurements characterizing functional structures, techniques to measure electromagnetic fields of radiating devices using functional structures, and a simulation model of functional structures for wavefront shaping in deep tissue focusing.

1.1   Structure

The structure of the first part of the thesis is as follows. First, in Sec. 2 the fundamental theory needed in this work is presented, building from Maxwell's equations. After this, in Sec. 3, functional structures are briefly introduced, followed by computational modeling considerations in Sec. 4 where the design process of these structures is included. A use case for functional structures in space applications using circular polarization selective structures is presented in Sec. 5. In that section, previous design types and relevant metrics are introduced. Then in Sec. 6 measurement techniques and post-processing steps for both functional structures and near field of devices are introduced. In the following sections, functional structures are used to improve the near-field measurement setup of devices. Sec. 7 contains two functional structures. One is constructed for electromagnetic measurements to address some measurement difficulties calibrating the system using a small aperture. The second functional structure is a metasurface transforming electromagnetic radiation to infrared radiation detected using an infrared camera. Finally, before conclusions, Sec. 9, and future work, Sec. 10, we discuss using electromagnetic radiation and wavefront shaping to measurement in tissue-like material. We cover a method to do numerical simulations in full-wave for large problems in order to focus deep into tissue, Sec. 8.

2   Theory

In order to build up to the results in this thesis, we start with introducing relevant equations and concepts of electromagnetics. Four fundamental equations are governing all classical phenomena in electromagnetics [114]. Thus they serve as a great starting point. We begin with important equations, concepts and their relation to the fundamental equations.

2.1   Maxwell's Equations and Electromagnetic Waves

Mathematical notation was very different in the 1800s when Maxwell presented the now-famous equations [162–164]. At the time of publication, they consisted of twenty equations and were later reduced to four equations using vector notation [105]. The set of equations are today known as Maxwell's equations. Three of the four included equations have a name of their own and in the time domain the four equations read [114],

$$\text{Faraday-Maxwell equation:} \quad \boldsymbol{\nabla} \times \boldsymbol{\mathcal{E}}(\boldsymbol{r},t) = -\frac{\partial \boldsymbol{\mathcal{B}}(\boldsymbol{r},t)}{\partial t}, \tag{2.1}$$

$$\text{Ampère-Maxwell law:} \quad \boldsymbol{\nabla} \times \boldsymbol{\mathcal{H}}(\boldsymbol{r},t) = \boldsymbol{\mathcal{J}}(\boldsymbol{r},t) + \frac{\partial \boldsymbol{\mathcal{D}}(\boldsymbol{r},t)}{\partial t}, \tag{2.2}$$

$$\text{Gauss's law:} \quad \boldsymbol{\nabla} \cdot \boldsymbol{\mathcal{D}}(\boldsymbol{r},t) = \rho(\boldsymbol{r},t), \tag{2.3}$$

$$\boldsymbol{\nabla} \cdot \boldsymbol{\mathcal{B}}(\boldsymbol{r},t) = 0, \tag{2.4}$$

where $\boldsymbol{\mathcal{E}}, \boldsymbol{\mathcal{B}}, \boldsymbol{\mathcal{H}}, \boldsymbol{\mathcal{D}}, \boldsymbol{\mathcal{J}}$ are real valued vector fields and ρ is a real valued scalar field. The fields are a function of the time, t, and position, $\boldsymbol{r}$. The names and units of the quantities are,

$\boldsymbol{\mathcal{E}}(\boldsymbol{r},t)$ Electric field intensity, [V/m],

$\boldsymbol{\mathcal{B}}(\boldsymbol{r},t)$ Magnetic flux density, [Vs/m^2],

$\boldsymbol{\mathcal{H}}(\boldsymbol{r},t)$ Magnetic field intensity, [A/m],

$\boldsymbol{\mathcal{D}}(\boldsymbol{r},t)$ Electric flux density, [As/m^2],

$\boldsymbol{\mathcal{J}}(\boldsymbol{r},t)$ Current density, [A/m^2],

$\rho(\boldsymbol{r},t)$ Charge density, [As/m^3].

There are two quantities directly related to electric fields: the electric field intensity, $\boldsymbol{\mathcal{E}}$, and electric flux density, $\boldsymbol{\mathcal{D}}$. Similarly, there are two quantities related to magnetic fields: the magnetic field density, $\boldsymbol{\mathcal{H}}$, and magnetic flux intensity, $\boldsymbol{\mathcal{B}}$. The remaining two quantities describe the sources of the fields, charge density, ρ, and current density, $\boldsymbol{\mathcal{J}}$. The four unknown vector fields, $\boldsymbol{\mathcal{E}}, \boldsymbol{\mathcal{D}}, \boldsymbol{\mathcal{B}}, \boldsymbol{\mathcal{H}}$, cannot be solved by these four equations alone as (2.3)–(2.4) can be derived by (2.1)–(2.2) with the addition of a continuity equation, the conservation of charge and

suitable conditions. In differential form, this continuity equation reads,

$$\boldsymbol{\nabla} \cdot \boldsymbol{\mathcal{J}}(\boldsymbol{r}, t) = -\frac{\partial \rho(\boldsymbol{r}, t)}{\partial t}. \tag{2.5}$$

Harshly, there are two equations with four unknowns. A fully determined system is obtained by introducing two additional relations [133]. The terms relating to flux density and field intensity can be connected through constitutive relations,

$$\begin{pmatrix} \boldsymbol{\mathcal{D}} \\ \boldsymbol{\mathcal{B}} \end{pmatrix} = \mathbf{F} \begin{pmatrix} \boldsymbol{\mathcal{E}} \\ \boldsymbol{\mathcal{H}} \end{pmatrix}, \tag{2.6}$$

where $\mathbf{F}$ is the operator describing the mapping between them. Mathematically this operator can be anything, but there are certain requirements to fulfill if the model should be physical (causal *etc.*) [260]. With the addition of (2.6) Maxwell's equations (2.1)–(2.4) can be solved. It is with the mapping in (2.6) that material enters the description. In the time domain, for general material, this description can be mathematically cumbersome. Instead, if we consider time translation invariant linear material, which is most of the cases in everyday life, (2.6) can be written as a temporal convolution over the fields and the material properties [133],

$$\boldsymbol{\mathcal{D}}(t) = \varepsilon_0 \boldsymbol{\mathcal{E}}(t') + \varepsilon_0 \int_{-\infty}^{t} \boldsymbol{\chi}_{\mathrm{ee}}(t - t') \cdot \boldsymbol{\mathcal{E}}(t') \, \mathrm{d}t' + \frac{1}{c_0} \int_{-\infty}^{t} \boldsymbol{\chi}_{\mathrm{em}}(t - t') \cdot \boldsymbol{H}(t') \, \mathrm{d}t', \quad (2.7)$$

$$\boldsymbol{\mathcal{B}}(t) = \frac{1}{c_0} \int_{-\infty}^{t} \boldsymbol{\chi}_{\mathrm{me}}(t - t') \cdot \boldsymbol{\mathcal{E}}(t) \, \mathrm{d}t' + \mu_0 \boldsymbol{\mathcal{H}}(t) + \mu_0 \int_{-\infty}^{t} \boldsymbol{\chi}_{\mathrm{mm}}(t - t') \cdot \boldsymbol{H}(t') \, \mathrm{d}t', \quad (2.8)$$

here $\varepsilon_0 \approx 8.854 \cdot 10^{-12}\,\mathrm{As/(Vm)}$ is the permittivity of free space and $\mu_0 \approx 1.256 \cdot 10^{-6}\,\mathrm{Vs/(Am)}$ is the permeability of free space. The material is described by the induced polarization and magnetization given by the dyadic convolution kernels, $\boldsymbol{\chi}_{\mathrm{ee}}, \boldsymbol{\chi}_{\mathrm{mm}}, \boldsymbol{\chi}_{\mathrm{em}}, \boldsymbol{\chi}_{\mathrm{me}}$. To simplify the treatment we assume that there is no coupling between the electric and magnetic quantities in this material description, thus $\boldsymbol{\chi}_{\mathrm{em}}, \boldsymbol{\chi}_{\mathrm{me}}$ vanish. The remaining 3×3-dyadics describe an anisotropic medium where the properties depend on the position and direction. However, for simplicity, consider an isotropic material, where the material properties are the same in each direction [133]. Moreover, assume that the material's response is instantaneous and does not depend on any temporal evolution, it is non-dispersive. With these assumptions, the constitutive relation, (2.7)–(2.8), in time domain becomes,

$$\boldsymbol{\mathcal{D}} = \varepsilon_0 \varepsilon_{\mathrm{r}} \boldsymbol{\mathcal{E}}, \tag{2.9}$$

$$\boldsymbol{\mathcal{B}} = \mu_0 \mu_{\mathrm{r}} \boldsymbol{\mathcal{H}}, \tag{2.10}$$

where ε_{r} is the relative permittivity and μ_{r} is the relative permeability. If we assume a region of space without sources, but with electromagnetic fields and

linear isotropic non-dispersive material, then we may write Maxwell's equations as,

$$\boldsymbol{\nabla} \times \boldsymbol{\mathcal{E}}(\boldsymbol{r},t) = -\mu_0\mu_\mathrm{r}\frac{\partial \boldsymbol{\mathcal{H}}(\boldsymbol{r},t)}{\partial t}, \tag{2.11}$$

$$\boldsymbol{\nabla} \times \boldsymbol{\mathcal{H}}(\boldsymbol{r},t) = \varepsilon_0\varepsilon_\mathrm{r}\frac{\partial \boldsymbol{\mathcal{E}}(\boldsymbol{r},t)}{\partial t}, \tag{2.12}$$

$$\boldsymbol{\nabla} \cdot \boldsymbol{\mathcal{D}}(\boldsymbol{r},t) = 0, \tag{2.13}$$

$$\boldsymbol{\nabla} \cdot \boldsymbol{\mathcal{B}}(\boldsymbol{r},t) = 0. \tag{2.14}$$

With the vector identity $\boldsymbol{\nabla} \times (\boldsymbol{\nabla} \times \boldsymbol{F}) = \boldsymbol{\nabla}(\boldsymbol{\nabla} \cdot \boldsymbol{F}) - \nabla^2\boldsymbol{F}$ and by taking the curl of (2.11) and (2.12) Maxwell's equations (2.1)–(2.4) can be reformulated as,

$$\frac{\partial^2\boldsymbol{\mathcal{E}}}{\partial t^2} = \frac{1}{\mu_0\mu_\mathrm{r}\varepsilon_0\varepsilon_\mathrm{r}}\nabla^2\boldsymbol{\mathcal{E}}, \tag{2.15}$$

$$\frac{\partial^2\boldsymbol{\mathcal{H}}}{\partial t^2} = \frac{1}{\mu_0\mu_\mathrm{r}\varepsilon_0\varepsilon_\mathrm{r}}\nabla^2\boldsymbol{\mathcal{H}}, \tag{2.16}$$

provided that the medium is homogeneous. These two equations are wave equations, where the propagation speed of the wave in the medium is $1/\sqrt{\mu_0\mu_\mathrm{r}\varepsilon_0\varepsilon_\mathrm{r}}$. For an electromagnetic wave, this is the speed of the wave in the medium, c, and $c_0 = 1/\sqrt{\mu_0\varepsilon_0} = 299\,792\,458\,\mathrm{m/s}$ is the speed of light in free space, vacuum. The speed depends on the material parameters and is the reason light bends at the boundary of an object such as a prism, or at the surface of water. In optics, this property is called the refractive index and may be written as $n = c_0/c = \sqrt{\mu_\mathrm{r}\varepsilon_\mathrm{r}}$.

With the wave equations (2.15)–(2.16), it is clear that electromagnetic fields also behave as waves. These waves carry energy, which can be expressed with the instantaneous Poynting vector [133],

$$\boldsymbol{\mathcal{S}}(\boldsymbol{r},t) = \boldsymbol{\mathcal{E}}(\boldsymbol{r},t) \times \boldsymbol{\mathcal{H}}(\boldsymbol{r},t), \tag{2.17}$$

and the time-average Poynting vector,

$$\langle\boldsymbol{\mathcal{S}}(t)\rangle = \frac{1}{T}\int\limits_0^T \boldsymbol{\mathcal{S}}(t)\,\mathrm{d}t, \tag{2.18}$$

where T is the time for one period of the wave. Thus far we have introduced the equations in the time domain, an alternative representation is the frequency domain, which often simplifies computations and notation (for time translational invariance) [123,179,260]. There are many cases in which both the sources generating the waves, and in extension the wave itself, display time-harmonic behavior. Using the time convention $\mathrm{e}^{\mathrm{j}\omega t}$ ($\omega = 2\pi f$), the relation between the time-domain fields and frequency-domain fields is given by,

$$\boldsymbol{\mathcal{A}}(\boldsymbol{r},t) = \mathrm{Re}\left\{\boldsymbol{A}(\boldsymbol{r},\omega)\mathrm{e}^{\mathrm{j}\omega t}\right\}. \tag{2.19}$$

The time-average Poynting vector can then be expressed as,

$$\langle \boldsymbol{\mathcal{S}}(t) \rangle = \frac{1}{2} \operatorname{Re}\{\boldsymbol{E}(\omega) \times \boldsymbol{H}^*(\omega)\} = \operatorname{Re}\{\boldsymbol{S}(\omega)\}, \tag{2.20}$$

where $.^*$ denotes the complex conjugate. Converting the remaining equations to the frequency domain through the Fourier transform is straightforward [133,238], $\partial/\partial t \to \mathrm{j}\omega$ and convolutions become multiplications. As before, we consider linear media, which in this case can be anisotropic and dispersive as the convolutions presented in the material model (2.7)–(2.8) are simple multiplications in the frequency domain. Below are Maxwell's equations along with the constitutive relations and the wave equations in the frequency domain,

$$
\text{Maxwell's Equations:} \quad
\begin{cases}
\boldsymbol{\nabla} \times \boldsymbol{E} = -\mathrm{j}\omega \boldsymbol{B}, & (2.21) \\[4pt]
\boldsymbol{\nabla} \times \boldsymbol{H} = \mathrm{j}\omega \boldsymbol{D} + \boldsymbol{J}, & (2.22) \\[4pt]
\boldsymbol{\nabla} \cdot \boldsymbol{D} = \rho, & (2.23) \\[4pt]
\boldsymbol{\nabla} \cdot \boldsymbol{B} = 0, & (2.24)
\end{cases}
$$

$$
\text{Constitutive Relations:} \quad
\begin{cases}
\boldsymbol{D} = \varepsilon_0 \boldsymbol{\varepsilon}_{\mathrm{r}} \cdot \boldsymbol{E}, & (2.25) \\[4pt]
\boldsymbol{B} = \mu_0 \boldsymbol{\mu}_{\mathrm{r}} \cdot \boldsymbol{H}, & (2.26)
\end{cases}
$$

$$
\text{Wave Equations:} \quad
\begin{cases}
\nabla^2 \boldsymbol{E} + k^2 \boldsymbol{E} = \boldsymbol{0}, & (2.27) \\[4pt]
\nabla^2 \boldsymbol{H} + k^2 \boldsymbol{H} = \boldsymbol{0}, & (2.28)
\end{cases}
$$

where we introduce the wavenumber $k = w/c$. The fields have a dependence on $\boldsymbol{r}$ and ω which, moving forward, will be written only if needed to avoid confusion. The presented wave equations in the frequency domain, (2.27)–(2.28), are only valid if the material is homogeneous, similar to the time-domain equations (2.15)–(2.16). The propagating waves, solutions to the wave equation, have an electric and a magnetic field oscillating in a plane perpendicular to one another and the propagation direction, $\hat{\boldsymbol{k}}$. Many sets of solutions to the wave equation can be written up. Here we focus on two simple sets, plane waves and spherical waves. The plane wave solution is a wave described by,

$$\boldsymbol{E}(\boldsymbol{r}, \omega) = \boldsymbol{E}_0(\omega) \mathrm{e}^{-\mathrm{j}k\hat{\boldsymbol{k}} \cdot \boldsymbol{r}}, \tag{2.29}$$

$$\boldsymbol{H}(\boldsymbol{r}, \omega) = \frac{1}{\eta} \hat{\boldsymbol{k}} \times \boldsymbol{E}_0(\omega) \mathrm{e}^{-\mathrm{j}k\hat{\boldsymbol{k}} \cdot \boldsymbol{r}}, \tag{2.30}$$

where $\eta = \sqrt{\mu_0 \mu_{\mathrm{r}}/(\varepsilon_0 \varepsilon_{\mathrm{r}})}$ is the wave impedance. A plane wave is a wave that has equal amplitude and phase at each position in a plane perpendicular to the propagation direction. Consider the sun as a single source of light. The earth is situated very far away from this source, and the curvature of the wavefront relative to the size of the earth is large[1]. The wavefronts can be said to be ap-

---

[1]The argument is to illustrate waves and is valid for the intensity of light and not necessarily the phase, as the sun is considered an incoherent source of light.
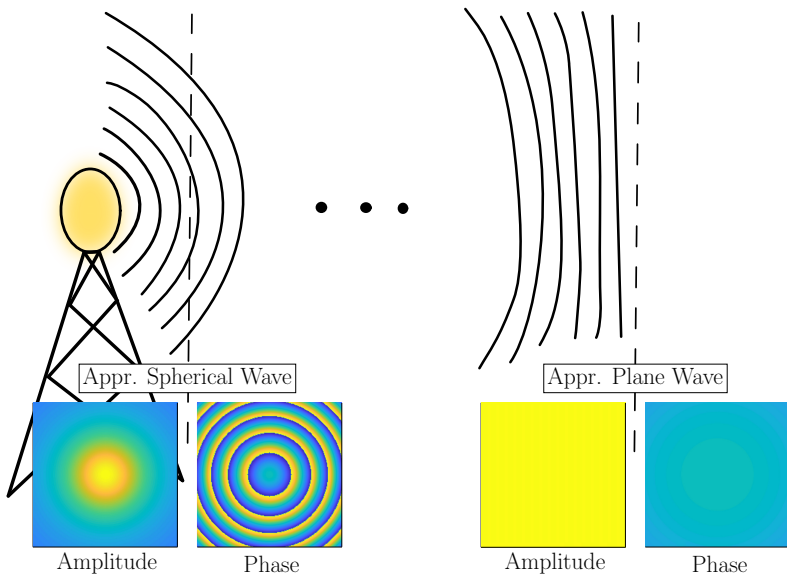
Figure 3: Wavefronts of an electromagnetic wave generated from a source (yellow) to the left. The wavefronts are shown on two finite planes, close and far, exhibiting behavior close to spherical waves and plane waves, respectively.

proximately plane over the surface of the earth. A similar approximation is often made in basic optics courses when a source far away generates parallel rays. However, there are situations when the curvature of the wavefront matters. Another important set of solutions is suitable for this setting, the spherical vector waves using vector spherical harmonics [133]. Far from the sources, these solutions are,

$$\boldsymbol{E}(\boldsymbol{r},\omega) \approx \boldsymbol{F}(\hat{\boldsymbol{r}},\omega)\frac{\mathrm{e}^{-\mathrm{j}kr}}{r}, \tag{2.31}$$

$$\boldsymbol{H}(\boldsymbol{r},\omega) \approx \frac{1}{\eta}\hat{\boldsymbol{r}} \times \boldsymbol{F}(\hat{\boldsymbol{r}},\omega)\frac{\mathrm{e}^{-\mathrm{j}kr}}{r}, \tag{2.32}$$

where $\boldsymbol{r} = r\hat{\boldsymbol{r}}$ and $\hat{\boldsymbol{r}}$ is the radial unit vector in spherical coordinates and $\boldsymbol{F}$ is a complex-valued vector such that $\boldsymbol{F} \cdot \hat{\boldsymbol{r}} = 0$ [133]. Depending on the use case, close to sources of electromagnetic radiation, spherical waves can be a good approximation whereas further away a plane-wave solution may be more useful approximation. An illustration of the wavefronts of a propagating wave is seen in Fig. 3, where the field in the marked region either looks like a plane wave or a spherical wave, depending on the distance from the source and the size of the evaluation plane.

We have so far described the electromagnetic field as time harmonically oscillating waves but not completely addressed their vector nature. To simplify the introduction of the following concept a plane wave propagating through free space
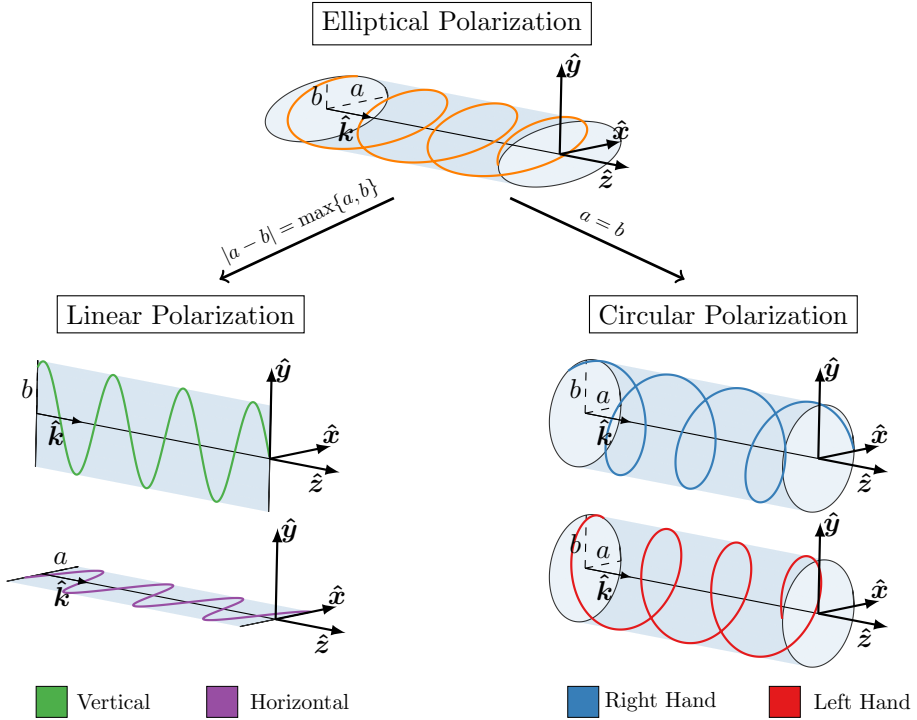
Figure 4: Polarization of a wave propagating in the $\hat{z}$-direction. Elliptical polarization is shown in the top and two important special cases, linear and circular polarization, to the left and right, respectively.

is considered. The oscillation of the electric field is in a direction perpendicular to the propagation direction. However, that does not imply that the direction of the electric field vector in that plane is constant. In fact, it is in general not true and the direction changes in an oscillatory manner. The oscillation of the wave in this plane is a property called polarization. The general polarization, or oscillation state, is that the electric field vector traces an ellipse in the plane perpendicular to the propagation direction. This is illustrated in the top illustration of Fig. 4. As the wave propagates along $\hat{k} = \hat{z}$ the tip of the electric field vector is on the colored line, rotating along an ellipse with major and minor axes a and b, respectively. A wave with this property is said to be elliptically polarized [133].

Two important polarization states are linear polarization (LP) and circular polarization (CP), which both form a basis. The polarization ellipse reduces to a line when the minor axis in the ellipse is zero (either a or b is zero in Fig. 4). The oscillations then occur along a line, in a linear polarization state. An example of linear polarization is $E_0\hat{x}$ and $E_0\hat{y}$ which span a basis ($E_0\hat{x} \cdot E_0\hat{y} = 0$) and are often referred to as Vertical Polarization (VP) and Horizontal Polarization (HP).

Circular polarization is obtained when the major and minor axes of the polarization ellipse are equal ($a = b$ in Fig. 4), described by $\boldsymbol{E}_0 = \sqrt{2}/2E_0\,(\hat{\boldsymbol{x}} \pm \mathrm{j}\hat{\boldsymbol{y}})$. The circle can be traced either in positive or negative direction, Right Hand Circular Polarization (RHCP) is described by $\boldsymbol{E}_\mathrm{R} = \sqrt{2}/2E_0\,(\hat{\boldsymbol{x}} - \mathrm{j}\hat{\boldsymbol{y}})$ and Left Hand Circular Polarization (LHCP) by $\boldsymbol{E}_\mathrm{L} = \sqrt{2}/2E_0\,(\hat{\boldsymbol{x}} + \mathrm{j}\hat{\boldsymbol{y}})$ and they span a basis in the plane ($\boldsymbol{E}_\mathrm{R} \cdot \boldsymbol{E}_\mathrm{L} = 0$). Both of these sets of polarization states are illustrated in Fig. 4. Polarization is a very useful and important property as electromagnetic waves interact differently with objects depending on polarization. Uses are for instance quarter-wave plate, dual-gridded reflectors, polarizers, passive 3D glasses, *etc.* [32, 198, 208].

2.2 Fields from Radiating Devices

Electromagnetic waves, presented in Sec. 2.1, have to be generated by some kind of source, namely a current or charge density. The source terms were omitted in the derivation of the time-domain wave equations (2.15)–(2.16) and frequency-domain wave equations (2.27)–(2.28). Sources are needed to generate propagating waves and we shall now investigate how these fields behave in the regions near and far from the sources. Time harmonic dependence on the fields and the sources, current density and charge density, is assumed and (2.21)–(2.24) serve as a starting point. To solve these equations with an interest to keep the result clean, we introduce an electric scalar potential V [V], and a magnetic vector potential $\boldsymbol{A}$ [Vs/m]. From (2.24) the vector potential is introduced as,

$$\boldsymbol{B} = \boldsymbol{\nabla} \times \boldsymbol{A}, \tag{2.33}$$

and, through (2.21), the electric scalar potential is introduced as,

$$\boldsymbol{E} = -\boldsymbol{\nabla}V - \mathrm{j}\omega\boldsymbol{A}. \tag{2.34}$$

Using these two new quantities and linear isotropic media, Maxwell's equations (2.21)–(2.24) reduce to,

$$\nabla^2 V + \mathrm{j}\omega\boldsymbol{\nabla} \cdot \boldsymbol{A} = -\frac{\rho}{\varepsilon_0\varepsilon_\mathrm{r}}, \tag{2.35}$$

$$\nabla^2 \boldsymbol{A} + k^2 \boldsymbol{A} - \boldsymbol{\nabla}\left(\boldsymbol{\nabla} \cdot \boldsymbol{A} + \frac{k}{\omega}V\right) = -\mu_0\mu_\mathrm{r}\boldsymbol{J}. \tag{2.36}$$

The description of Maxwell's equations using the two potentials is identical to the previous representation using the fields and flux densities. However, as the constitutive relations were introduced to describe the coupling of the field quantities, the potentials are also coupled. Unlike the fields, there is a mathematical arbitrariness in the creation of these potentials due to the differentiation involved [114]. We are free to choose a gauge and will consider the Lorenz gauge in this thesis [114],

$$\boldsymbol{\nabla} \cdot \boldsymbol{A} = -\mathrm{j}\frac{k}{c}V. \tag{2.37}$$

This relation allows for uncoupling of (2.35)–(2.36) to,

$$\nabla^2 V + k^2 V = -\frac{\rho}{\varepsilon_0 \varepsilon_{\mathrm{r}}}, \tag{2.38}$$

$$\nabla^2 \boldsymbol{A} + k^2 \boldsymbol{A} = -\mu_0 \mu_{\mathrm{r}} \boldsymbol{J}. \tag{2.39}$$

These two equations are wave equations, similar to (2.27)–(2.28), but with source terms. Utilizing the Green's function of the problem, the solution can be written as [114],

$$\boldsymbol{A}(\boldsymbol{r}) = \frac{\mu_0 \mu_{\mathrm{r}}}{4\pi} \int \boldsymbol{J}(\boldsymbol{r}') \frac{\mathrm{e}^{-\mathrm{j}k|\boldsymbol{r}-\boldsymbol{r}'|}}{|\boldsymbol{r}-\boldsymbol{r}'|} \, \mathrm{d}v', \tag{2.40}$$

where $\boldsymbol{r}$ is the evaluation position and $\boldsymbol{r}'$ are the positions of the source current. This equation along with (2.33)–(2.34) and (2.37) connects the currents on a device to the fields in a homogeneous background material. Consider the current distribution to be confined to a region, *e.g.* an antenna. Then the surrounding region of this device can roughly be divided into three regions where the behavior of the electromagnetic field can be very different. Closest to the antenna is the reactive near field or quasistatic zone. In this region, the distance to the antenna is much smaller than the operating wavelength, around $\lambda/(2\pi)$. This close to the sources, the exponential in (2.40) can be replaced by unity. For a simple antenna, a dipole, the fields in this region have a spatial dependence described by,

$$\boldsymbol{H} \approx \frac{\mathrm{j}\omega}{4\pi} \hat{\boldsymbol{r}} \times \boldsymbol{p} \frac{1}{r^2}, \tag{2.41}$$

$$\boldsymbol{E} \approx \frac{1}{4\pi\varepsilon_0 \varepsilon_{\mathrm{r}}} 3\hat{\boldsymbol{r}}(\hat{\boldsymbol{r}} \cdot \boldsymbol{p}) \frac{1}{r^3}, \tag{2.42}$$

where $\boldsymbol{p}$ is the electric dipole moment. The expressions are similar in their spatial dependence to the static counterparts of a dipole, apart from an oscillating temporal behavior. This is the reason for one of the names for this region, the quasistatic zone [114]. Moreover, this close to the antenna $kr \ll 1$, the magnetic field scales a factor kr smaller than the electric field, and the total field is dominated by the electric field.

Further back, but still close to the antenna (λ), is the inductive region. The capacitive and inductive effects in these regions are typical for the reactive, also called non-radiative, near field. This region is complicated as the relation between the electric and magnetic fields can change rapidly and the fields can have components in the radial direction. The electric and magnetic fields are effectively uncoupled. Accurately measuring power density in this region is thus very complicated. Hence, both the magnetic and electric fields must be measured in both amplitude and phase at every point.

Far away from the source, $\lambda \ll r$ and $|\boldsymbol{r}'| \ll r$, the exponential in (2.40) can be approximated as, $|\boldsymbol{r}-\boldsymbol{r}'| \approx r - \hat{\boldsymbol{r}} \cdot \boldsymbol{r}'$, which simplify the calculations. For a
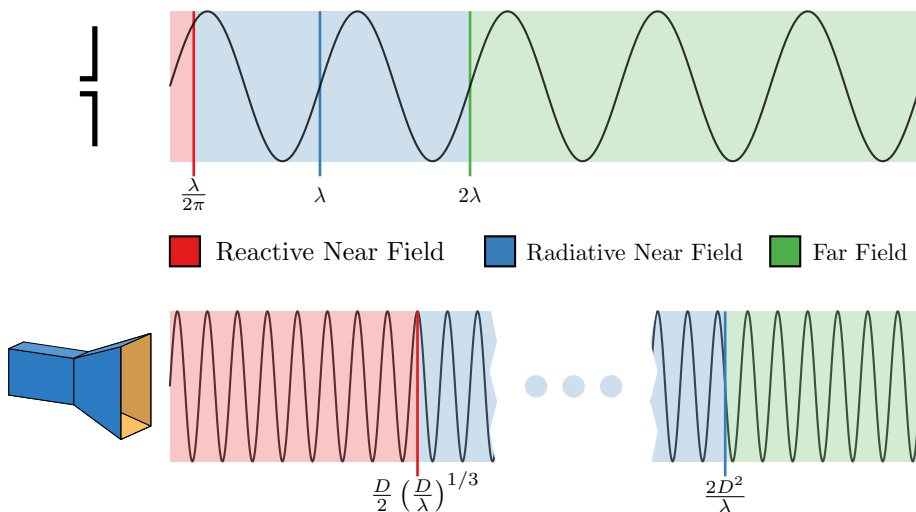
Figure 5: Regions of the electromagnetic fields for electrically small (top) and electrically large (bottom) radiating devices. The discontinuity in the bottom graph represents $\approx 100\,\lambda$ for a standard gain horn antenna.

dipole antenna the fields in this region approach,

$$\boldsymbol{H} \approx \frac{ck^2}{4\pi}(\hat{\boldsymbol{r}} \times \boldsymbol{p})\frac{\mathrm{e}^{-\mathrm{j}kr}}{r}, \tag{2.43}$$

$$\boldsymbol{E} \approx \eta\frac{ck^2}{4\pi}(\hat{\boldsymbol{r}} \times \boldsymbol{p}) \times \hat{\boldsymbol{r}}\frac{\mathrm{e}^{-\mathrm{j}kr}}{r}, \tag{2.44}$$

In this region, the power falls off as $1/r^2$ and the fields oscillate transverse to the propagation direction, compare with (2.31)–(2.32). This is the radiation zone, far field/zone, or Fraunhofer region [16].

These two presented regions, very close to the sources and very far away, are the edge cases and there is a region in between, a transition region where the effects of both regions matter. This region is often called the radiative near field, or Fresnel region [16, 238]. Where one region ends and another begins depends on the antenna and frequency. A general rule for the different regions for small and large antennas can be seen in Fig. 5. Here we consider the larger antenna, size $D \gg \lambda$ (bottom row), and small antenna (top row) to be operating at a wavelength of $\lambda = 2\pi c/\omega$. The boundaries between the regions for the antennas differ, especially the Fresnel boundary. For arbitrarily shaped planar apertures this limit is given as $D/2(D/\lambda)^{1/3}$ [214]. In other literature, this boundary is sometimes given as $0.5\sqrt{D^3/\lambda}$ or $0.62\sqrt{D^3/\lambda}$ [188]. The difference depends on the derivations using Fresnel approximations and a line source [91, 228] or scalar diffraction theory for rectangular-shaped apertures [188]. In the standard gain horn antenna illustrated in Fig. 5, these boundaries are around $8\,\lambda$ and $130\,\lambda$

away from the device, which is significantly further out compared to the small dipole antenna imaged in the top row of Fig. 5. The measurement method differs depending on the region measured and the quantities sought. There exist techniques to transform results from one region to another, for instance, near-to-far-field [53]. In this thesis, we are mostly concerned with measuring devices in the radiative near-field region.

2.3   Scattering

Generated electromagnetic waves seldom propagate through time and space unhindered but often encounter different objects which impact propagation through scattering and absorption [133]. The brief description of electromagnetic waves presented in this thesis will end with scattering theory in the frequency domain. The principle of superposition of electromagnetic waves can be used favorably in scattering problems. The total electric field $\boldsymbol{E}(\boldsymbol{r})$, and magnetic field $\boldsymbol{H}(\boldsymbol{r})$, can be decomposed into incident fields and scattered fields,

$$\boldsymbol{E}(\boldsymbol{r}) = \boldsymbol{E}_\mathrm{i}(\boldsymbol{r}) + \boldsymbol{E}_\mathrm{s}(\boldsymbol{r}), \qquad \boldsymbol{H}(\boldsymbol{r}) = \boldsymbol{H}_\mathrm{i}(\boldsymbol{r}) + \boldsymbol{H}_\mathrm{s}(\boldsymbol{r}), \tag{2.45}$$

where the subscript indicates whether the field is incident (i) or scattered (s). Calculating the scattered field with given incident fields is known as a scattering problem [133]. An inverse problem is the contrary, for a given incident field and resulting scattered field, compute material properties, the shape of objects, or sources generating the scattered field [51, 90, 133].

From Sec. 2.2 we remember that the near field of objects is nontrivial thus we consider the far field of the scatterers. In this region, there are only transverse components of the fields and the far-field amplitude can be introduced as seen in (2.31),

$$\boldsymbol{F}(\hat{\boldsymbol{r}}) = \lim_{r \to \infty} r\mathrm{e}^{\mathrm{j}kr} \boldsymbol{E}_\mathrm{s}(\boldsymbol{r}), \qquad \boldsymbol{E}_\mathrm{s}(\boldsymbol{r}) \simeq \frac{\mathrm{e}^{-\mathrm{j}kr}}{r} \boldsymbol{F}(\hat{\boldsymbol{r}}). \tag{2.46}$$

With a locally plane wave incident at the scatterer, described as $\boldsymbol{E}(\boldsymbol{r}) = \boldsymbol{E}_0 \mathrm{e}^{-\mathrm{j}k\hat{\boldsymbol{k}}_\mathrm{i} \cdot \boldsymbol{r}}$, a mapping between the incident field, $\boldsymbol{E}_0$, and the far-field amplitude is given by,

$$\boldsymbol{F}(\hat{\boldsymbol{r}}) = \mathbf{S}(\hat{\boldsymbol{r}}, \hat{\boldsymbol{k}}_\mathrm{i}) \boldsymbol{E}_0, \tag{2.47}$$

where $\mathbf{S}(\hat{\boldsymbol{r}}, \hat{\boldsymbol{k}}_\mathrm{i})$ is the scattering dyadic containing the mapping between the incident wave and outgoing far-field amplitude where the $\hat{\boldsymbol{k}}_\mathrm{i}$-direction is the propagation direction of the incident wave. Another often used mapping in scattering problems is the transition matrix [168]. If we would expand the incident wave in a basis, for instance, spherical vector waves, then the transition matrix or T-matrix describes the scatterer specific relation between incident expansion coefficient a_n and expansion coefficients of the scattered field,

$$f_n = \sum_{n'} T_{nn'} a_{n'}. \tag{2.48}$$

A useful property when discussing scattering objects is the differential scattering cross section, which can be expressed as [133],

$$\frac{\mathrm{d}\sigma}{\mathrm{d}\Omega}(\hat{\boldsymbol{r}}, \hat{\boldsymbol{k}}_\mathrm{i}) = 4\pi \frac{|\boldsymbol{F}(\hat{\boldsymbol{r}})|^2}{|\boldsymbol{E}_0|^2} = 4\pi \left| \mathbf{S}(\hat{\boldsymbol{r}}, \hat{\boldsymbol{k}}_\mathrm{i}) \cdot \frac{\boldsymbol{E}_0}{|\boldsymbol{E}_0|} \right|^2, \tag{2.49}$$

describing the ratio of the scattered and incident power densities normalized with the area of the sphere and is a function of observation direction and incident plane wave. It is often referred to as the bistatic, or monostatic if $\hat{\boldsymbol{r}} = -\hat{\boldsymbol{k}}_\mathrm{i}$, Radar Cross Section (RCS). In many situations the interest lies in the total scattered and absorbed power of an object. This is described by the extinction cross section, also called total cross section,

$$\sigma_\mathrm{t} = \frac{P_\mathrm{a} + P_\mathrm{s}}{\langle \boldsymbol{\mathcal{S}}_\mathrm{i}(t) \rangle \cdot \hat{\boldsymbol{k}}_\mathrm{i}}, \tag{2.50}$$

where P_a and P_s is the absorbed and scattered power given an incident power density $\langle \boldsymbol{\mathcal{S}}_\mathrm{i}(t) \rangle \cdot \hat{\boldsymbol{k}}_\mathrm{i}$. Related to the differential scattering cross section,

$$\int_\Omega \frac{\mathrm{d}\sigma}{\mathrm{d}\Omega}(\hat{\boldsymbol{r}}, \hat{\boldsymbol{k}}_\mathrm{i}) \, \mathrm{d}\Omega = \frac{P_\mathrm{s}}{\langle \boldsymbol{\mathcal{S}}_\mathrm{i}(t) \rangle \cdot \hat{\boldsymbol{k}}_\mathrm{i}}, \tag{2.51}$$

where the integration is over the unit sphere. Another useful relation is the optical theorem [133],

$$\sigma_\mathrm{t} = -\frac{4\pi}{k} \mathrm{Im} \left\{ \frac{\boldsymbol{E}_\mathrm{i}^* \cdot \boldsymbol{F}(\hat{\boldsymbol{k}}_\mathrm{i})}{|\boldsymbol{E}_\mathrm{i}|^2} \right\}. \tag{2.52}$$

Scattering problems quickly become tedious to write up and require much bookkeeping. In Sec. 8, scattering in very large systems is discussed and further explored. However, the scattering of a small dipole object is simple to write analytically using the scattering dyadic and transition matrix. Using the Lorenz gauge (2.37) and equation (2.40) we may write the scattered field from such an object. However, a single dipole scatterer is seldom of interest. Adding more of these scatterers will create a larger system and requires that one deal with their influence on one another. One way this may be done and simulated is discussed further in Sec. 4 and Sec. 8. In Fig. 6 the magnitude of the total, scattered, and incident electric field of an incident dipole field on a tight row of scatterers is displayed. The pattern visible in the top-left figure results from undersampling the specific field. In the rightmost column, the scatterers can be seen as small bright dots. The row of scatterers reflects a majority of the incident field. It is an object blocking transmission for a certain frequency and polarization of light.
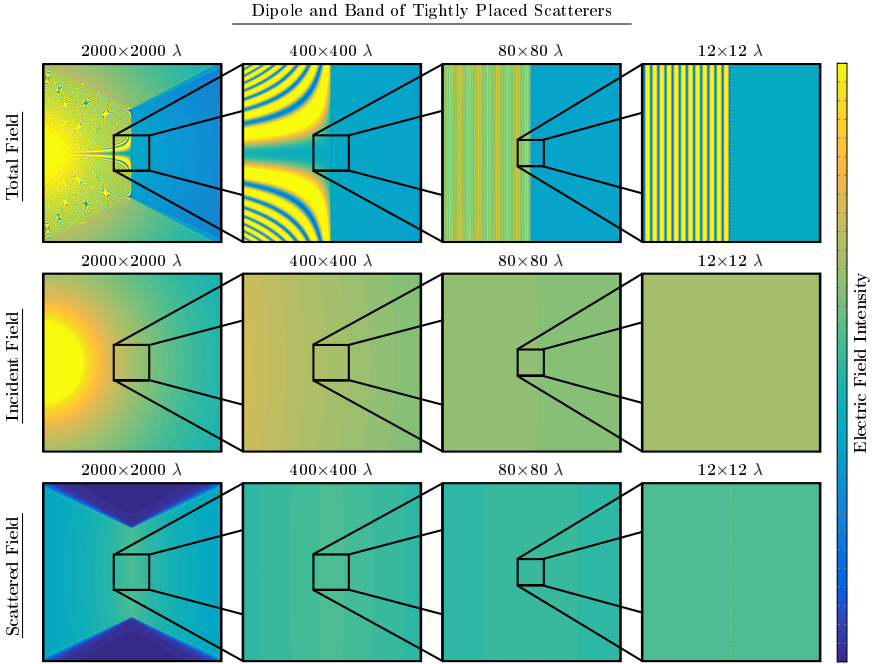
Figure 6: The total (top), incident (middle) and scattered (bottom) field intensity from an incident dipole field on a row of tightly placed scatterers with increasing magnifications from left to right.

The scattering dyadic, $\mathbf{S}(\hat{\boldsymbol{r}}, \hat{\boldsymbol{k}}_i)$, contains a lot of information and in scattering problems the full information of the field at all points in space is not requested. Returning to the row of scatterers in Fig. 6 as a functional structure, our interest often lies in polarization, transmission, and reflection properties. The relevant information can be obtained from a smaller representation of the scattering dyadic. This representation is the scattering matrix which comes from network theory [158]. It describes the relation between voltage waves on different ports. An example of ports in the case presented in Fig. 6 is the voltage over the illuminating dipole port and another to the right of the row of scatterers.

A measurement of a functional structure, such as the one in Fig. 6, can consist of two dual-polarized antennas, one on each side of the functional structure. A vector network analyzer (VNA) connected to the antennas measure voltage waves corresponding to reflection and transmission for the different polarizations. More formally, input and output signals are related through the scattering matrix for an N-port network as [192],

$$\begin{pmatrix} V_1^- \\ V_2^- \\ \vdots \\ V_N^- \end{pmatrix} = \begin{pmatrix} S_{11} & S_{12} & \cdots & S_{1N} \\ S_{21} & \ddots & & \vdots \\ \vdots & & \ddots & \vdots \\ S_{N1} & \cdots & \cdots & S_{NN} \end{pmatrix} \begin{pmatrix} V_1^+ \\ V_2^+ \\ \vdots \\ V_N^+ \end{pmatrix}, \quad (2.53)$$

where V_i^-, $i = 1, 2, ..., N$ is the amplitude of the scattered wave voltage at port i and V_j^+ is the amplitude of the incident wave voltage at port j. The scattering matrix elements are defined as,

$$S_{ij} = \left. \frac{V_i^-}{V_j^+} \right|_{V_k^+ = 0 \text{ for } k \neq j}, \quad (2.54)$$

where S_{ij} is the ratio between the scattered wave voltage V_i^- at port i and the incident wave voltage V_j^+ at port j when all other ports are terminated with matched loads [192]. The matrix is symmetric, provided the system is reciprocal. In our use cases, with one transmitting (labeled 1) and one receiving antenna (labeled 2) operating with two polarizations, the matrix is a 4×4 matrix with elements as,

$$\begin{pmatrix} S_{11}^{VV} & S_{11}^{VH} & S_{12}^{VV} & S_{12}^{VH} \\ S_{11}^{HV} & S_{11}^{HH} & S_{12}^{HV} & S_{12}^{HH} \\ S_{21}^{VV} & S_{21}^{VH} & S_{22}^{VV} & S_{22}^{VH} \\ S_{21}^{HV} & S_{21}^{HH} & S_{22}^{HV} & S_{22}^{HH} \end{pmatrix}. \quad (2.55)$$

The subscript indicates the port, or antenna in this scenario, and superscript the polarization state, V (vertical) and H (horizontal) for linear polarization and R (right hand) and L (left hand) for circular polarization. Due to reciprocity, and defining one antenna as the transmitting antenna, it is often sufficient to measure the elements highlighted by the red box to obtain the performance parameters of interest.

From Maxwell's equations, we have briefly introduced electromagnetic waves, polarization, sources, field regions, and scattering. These are some of the fundamental concepts needed to understand functional structures and measurement of the electromagnetic field. The continuing section of the thesis is a presentation of functional structures, their categories, and possibilities — setting the stage for the structures designed in this work.

3 Functional Structures

In our pursuit of knowledge and understanding, we have as a species come a long way from the early lenses to our modern functional structures [65, 173]. There

was enormous interest and research devoted to these functional structures during the second half of the 1900s. During this era, selectivity in frequency drove much of the research and a more complete historical overview can be found in [173]. Today we can control electromagnetic waves in many ways for equally varying goals; block a certain frequency, alter the polarization state of the wave, or perhaps change the radiation pattern. This thesis cannot hope to cover all application areas and designs but will provide an overview for later sections. Conceptually, the functional structures either stop or allow a certain electromagnetic configuration or, in other ways, alter the electromagnetic field. Roughly they can be divided into three categories which are not in all aspects mutually exclusive,

- Frequency Selective Structures

- Polarization Selective Structures

- Metasurfaces

The names are partly self-explanatory, a Frequency Selective Structures (FSS) exhibits a selectivity based on the frequency of the incoming wave, a polarization selective structure operates using polarization as its primary selection category. However, metasurfaces are different and often have other goals including other parameters such as shaping the radiation pattern or converting energy [5, 194]. There are several concepts and use cases for these different categories of functional structures and we shall now mention some in order to understand the use cases relevant to this thesis.

3.1   Frequency Selective Structures

A classical use case of an FSS is a radome. In its most simple form, it is a structure based on using a dielectric medium to shield radiating structures from wear and tear during operation, but more advanced versions exist [132, 190, 191]. The antenna situated within the structure transmits an electromagnetic wave which should not be reflected at the surface of the radome but be transmitted through it, as though the structure did not exist. For an electromagnetic wave impinging on a planar surface with normal incidence, some back-of-the-envelope calculations on the thickness and permittivity of the material can yield a decent design for which there is optimal transmission [180]. The structure can be improved by including more layers/slabs of varying permittivity and thicknesses.

In the most simple case, expressions of propagation matrices and field matching conditions at the boundary of the slabs can be used to cascade several slabs to compute total transmission and reflection coefficients [180]. However, the protecting structures are seldom simply planar but curved, and the impinging wave is most often not of normal incidence. The technique of cascading matrices works for oblique incidence, after some modification, and can be imported into different software suites for further analysis.

Dielectric functional structures such as the simple radomes have several uses, but it is not optimal in every regard. Improved differentiation between frequencies and polarizations, for polarization selective structures, can be done by conducting elements [173]. A conductive element can be viewed as an antenna in its own right. The antenna can respond extremely well to certain frequencies, resonant frequencies. An example is a simple dipole, as the one described in Sec. 2.3, Fig. 6. If the electric field oscillates, is polarized, in the same direction as the orientation of the dipole then it will interact with the incoming electromagnetic wave and reflect parts of it. If several of these dipole elements are placed close to one another, periodically, a band stop structure is created, albeit for a very narrow frequency range. The performance of a single layer of dipoles can be seen by the red lines of Fig. 7. This design is both selective in frequency and polarization. The separation between polarizations is useful for satellite communication [108]. A typical FSS consists of one or several layers of often periodic conductive/dielectric elements, components, or apertures.

In recent decades, computational power has increased many times over and has helped in producing designs for functional structures [233]. Newer design approaches of not only cascading surfaces and spacers but designing elements in a 3D setting, along the propagation direction, have been investigated. Frequency selective structures using these designs are referred to as 3D-FSS [13, 143, 201]. Compared to resonant 2D structures 3D-FSS have a significantly improved performance with respect to angle-of-incidence variations [200]. An important aspect to mention is that the materials used to construct these designs are often very specific. The material parameters cannot arbitrarily be chosen, and this puts certain limitations on real-world designs [108].

In the field of electromagnetics, there are many forms of interesting symmetry and symmetry-related properties. One such property, relevant in this work, is Babinet's principle [32]. It states that the transmitted electric field from a structure is equal to the scattered field from the complementary magnetic structure. Under the assumption that the included objects are thin and perfect electric conductors, then the compliment, also constructed out of perfect electric conductors, has opposite polarization characteristics. A high reflectance/transmittance in one polarization state gives low respective values for the opposite polarization. For a dipole array and complementary structure, this is seen in Fig. 7. The dipole array has a low transmission at dipole resonance and consequently high transmission in the opposite polarization for the complementary structure.

Conceptually it is interesting that a structure with a low amount of area coverage can reflect most of the incident energy. However, it is perhaps more remarkable that a metal screen with small holes can be transparent to the incident wave. Nevertheless, this is what Babinet's principle tells us. The concept can be called extra-ordinary transmission [62, 130, 160] and it is interesting to investigate the limits of these designs in terms of bandwidth. In Paper I a thin structure is created and can be seen in the left of Fig. 8. It is designed to maximize the bandwidth of the first transmission resonance in relation to the attainable capacity as described by a sum rule relating the bandwidth to the static polarizability [151].
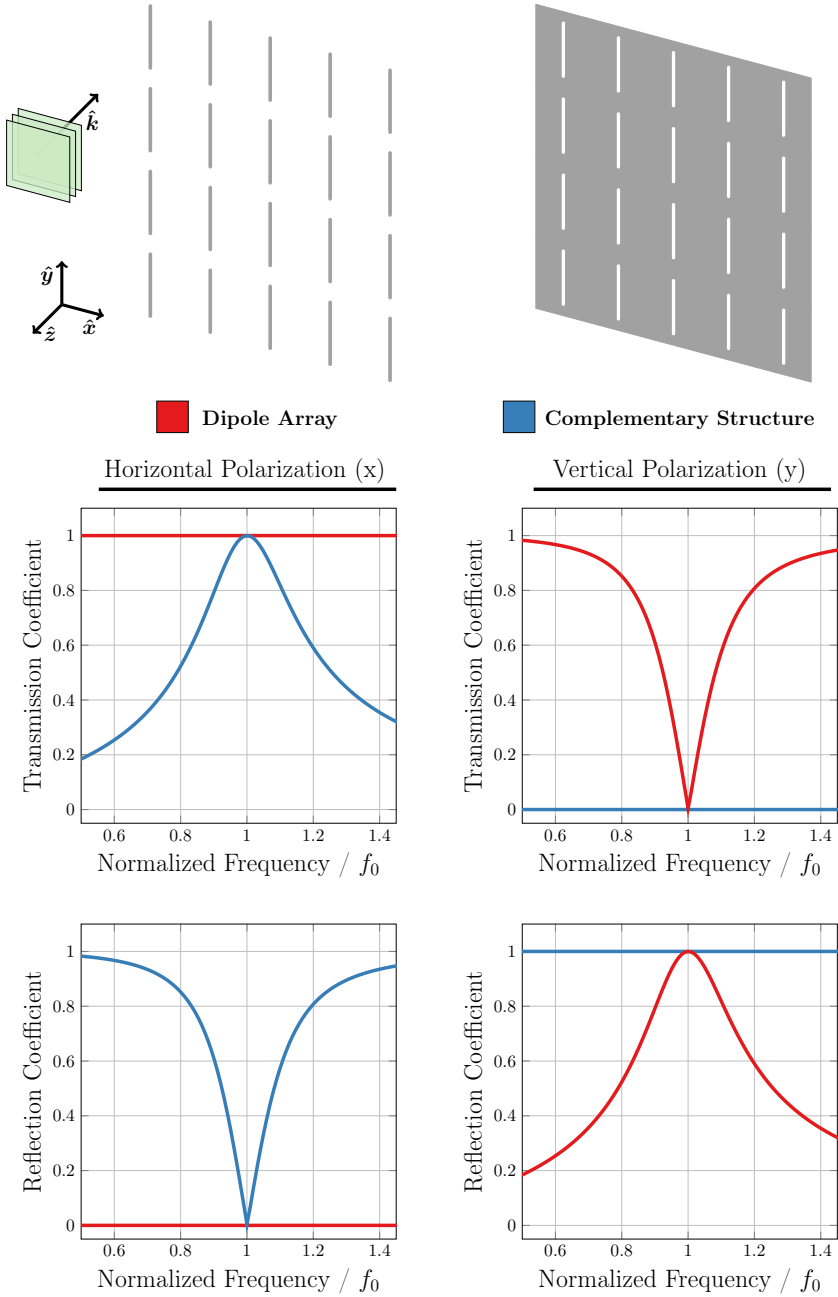
Figure 7: Amplitude of the reflection and transmission coefficients for two normal incidence, $\hat{\boldsymbol{k}}$, linear polarizations of a dipole array, top left, and its complementary structure, top right.
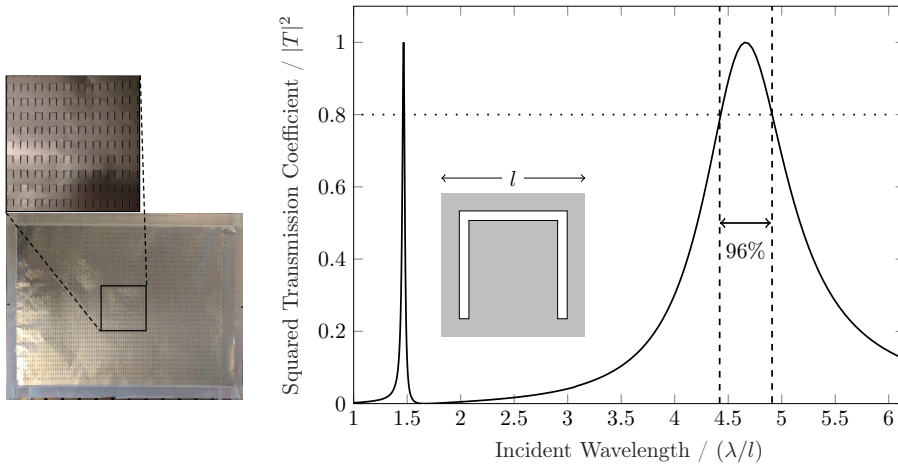
Figure 8: Manufactured functional structure in an aluminum foil of dimensions 238 mm×320 mm (left) and simulation of the squared absolute value of the transmission coefficient of the design, solid, with 96% of the attainable bandwidth captured in the first transmission peak [151].

The polarizability of the chosen design type is high compared to other investigated designs and the mechanical stability is suitable for in-house manufacturing. The design had 96 % of the total available sum rule predicted bandwidth in the first transmission peak. The simulations and measurements agree well, indicating the validity of the sum rule for real applications, even though it was derived for an ideal model.

This example of a functional structure used a periodic design, which is a very common approach in the cases of general transmission and reflection properties. With periodic designs, the performance will be similar over the entire structure. It is, moreover, favorable in certain numerical modeling applications. A description of a single element can be used to construct a larger structure in strategies similar to cascading of matrices described previously.

3.2   Polarization Selective Structures

The presented structures so far are evaluated mostly with respect to transmission and reflection properties based on frequency. Another large application area is polarization selectivity. The dipole array, Fig. 7, and the structure presented in Paper I exhibit polarization selectivity, though it is not the primary focus. Designs can be constructed with the explicit focus to block a certain polarization and transmit another. A very simple example is a strip grid. It operates similarly to the dipole array but blocks one linear polarization in a larger frequency interval. This kind of simple grid-based structure can be utilized in dual-gridded
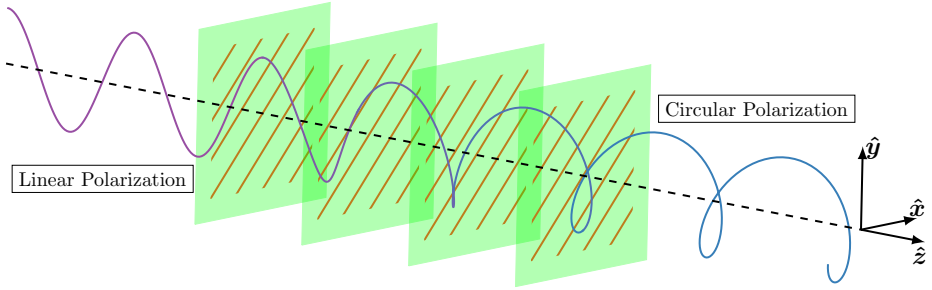
Figure 9: Incident linearly polarized wave, propagating along the z-direction, gets converted to circular polarization through four layers of anisotropic sheets.

reflector systems for satellite communication [19, 181, 203]. As presented in Sec. 2, circular polarization is another polarization representation. Polarization selective structures can convert from linear polarization to circular polarization, LP to CP, or convert between circular polarization states in reflection and transmission. In satellite communication, circular polarization is often the preferred polarization. This is discussed more in Sec. 4 and it may be achieved by linearly polarized antennas in a feed system interacting with a structure converting the linearly polarized signal to a circularly polarized signal. From Sec. 2, circular polarization can be constructed by two linear components with a phase shift between them. Thus, by decomposing an incident linear polarized wave in two orthogonal components and introducing a phase shift between these components, circular polarization can be obtained. A structure comprising several cascaded anisotropic layers can achieve this effect. This has been implemented in several works with different designs [66, 83, 127, 137, 142, 173] and an example illustration is seen in Fig. 9, where an incident linearly polarized wave gets converted to circular polarization after propagating through four layers of anisotropic sheets.

3.3   Metasurfaces

It was mentioned at the start of this section that functional designs can control other aspects of electromagnetic radiation. Controlling electromagnetic radiation has been of interest for a long time. In recent decades, much research has been devoted to altering materials and their properties to create fascinating behavior. From the material parameters, introduced in Sec. 2, special phenomena can occur for certain values and behavior of these parameters. Materials designed to use this are typically called metamaterials [44, 54, 64, 218]. Examples include near-zero refractive index [41], negative refraction [222] and chiral metamaterials (negative refractive index for one circular polarization) [235, 246, 261]. However, the bandwidth of these exotic materials is limited to a few percent as dictated by sum rules [88] and often suffer from large losses [64]. As these metamaterials exhibit exotic behavior, it is interesting to return to the functional structures and

introduce metasurfaces, which are thin structures whose behavior alters other properties of the electromagnetic field. Metasurfaces can be active/tuneable, may alter beam patterns and grating lobe performance, control angular dispersion in the optical regime in addition to underlying frequency and polarization selectivity [5, 92, 144, 166, 217, 262]. Not all of these structures require the exotic materials of metamaterials and can be constructed in the same way as FSSs, using periodic elements. These metasurfaces, unlike the exotic metamaterials, are not as restricted in bandwidth. The name encompasses a large category of structures and the definition of what is classified as a metasurface differs on the field of research. One distinction is that, given a periodicity, it should be less than a wavelength, and other distinctions are based on requiring both magnetic and electric responses in the structure [100, 195]. Some metasurfaces break the global periodicity and have local elements rotated around some point to manufacture rotational symmetric surfaces. Examples include Luneburg lens antenna, iso-flux antennas and circular polarization broadside antennas [33, 165, 166]. In this work, we describe the non-resonant circular polarization selective structure, Paper II, and mm-wave-to-infrared surface converter, Paper VI, as metasurfaces. Naming conventions aside, these structures have many uses and much research on varying types of structures has been made. The field is extensive with many applications and for further information see for instance [41, 44, 64, 218, 251].

The usefulness of many of the structures, FSS, metasurfaces, and polarization selective structures, might not be immediately clear until investigating the specific use case and problem formulation. The techniques and structures have become increasingly complex and before going further we shall briefly review techniques of modeling electromagnetic problems, both in general and specifically for periodic structures often used for these types of structures.

4 Modeling and Design

Maxwell's equations (2.21)–(2.24) and the constitutive relations (2.25)–(2.26) form a powerful description of electromagnetics, but they are not always easy to solve. The dipole radiator in Sec. 2 can be handled analytically, but realistic problems quickly become too complicated to solve in an analytical closed-form where large sums over special functions are commonplace. Solutions for many canonical problems exist, but in order to solve other problems, some modeling of the problem must be made [237]. The two commonly used approaches for these complex problems include approximations to simplify and solve the problem analytically and to discretize the problem and solve the equations numerically in full-wave solvers.

Before the introduction of Maxwell's equations, optics was studied extensively [55]. Light was drawn as rays that could reflect and be absorbed. This ray optics, or geometrical optics, can be utilized for large structures. A version of this approximation is used today in rendering to produce photo-realistic lighting in images and 3D-produced environments. The technique, in this setting,

is called ray tracing and is one of the most computationally intense rendering processes and one of the driving forces in the evolution of consumer graphical processing units (GPUs) [226]. Geometrical optics does not incorporate diffraction phenomenon [129]. Physical optics, on the other hand, is an intermediate technique between geometrical optics and full-wave solution [236].

In Sec. 3, it was briefly mentioned that scattering of layered planar structures, dielectric slabs for radomes, could be used to approximate the transmission and reflection properties of the design. Another approximation technique is circuit models and network theory. Each layer, with some transverse structure, is viewed as a transmission line with equivalent circuit parameters [158,192]. The validity of the technique depends on the structure in the transverse direction. The details should be small compared to the wavelength. However, the method is often used to evaluate FSS with resonant elements with lengths on the order of half a wavelength. The technique provides a fast evaluation of structures and, in FSS applications, may provide a good starting design for more detailed numerical solvers. These analytical and semianalytical solvers are fast but lack accuracy, especially for complicated structures. Here we turn to numerical solvers and computational electromagnetics (CEM). In full-wave solvers, Maxwell's equations are discretized into a finite number of points on which the fields or currents are evaluated through computationally efficient approximations [28, 57]. The discretization is known as meshing and differs depending on the computational technique.

4.1   Numerical Techniques

All the computational techniques mentioned within this subsection exist in standard software suites with more sophisticated implementation and acceleration techniques than the basics presented here. The choice of solver and software will depend on the specific problem. The basics of the techniques are presented below, with some specific details for periodic structures used heavily in this work.

One of the predominant methods in computational electromagnetics is the Method of Moments (MoM) [48,116]. The technique models the electromagnetic problem by replacing all structures and objects with currents, often described on surfaces and wire segments. A coupling between the segments to all other segments is written up and through the Green's function, the unknown field can be computed. The technique only discretizes the regions with current and not the entire space, which results in a favorable memory performance. The technique is very effective for simulating perfect electric conductors. Materials and dielectrics other than perfect electric conductors can be included.

A time-domain method that discretizes the entire region of interest is the Finite-Difference Time-Domain (FDTD) [116]. In this technique, space is divided into several smaller cubes. Maxwell's equations in the space are transformed to central difference problems on the mesh, consisting of the cubes. The technique is simple in implementation and the full frequency spectrum can be obtained using

Fourier transforms on the generated time sequences [28]. The meshing must be rather fine, 10-20 steps per wavelength, to reduce phase errors. Spheroidal geometry suffers from staircasing which also implies a fine mesh for an accurate solution. Simulating wave propagation with this technique requires a special absorbing boundary condition, also called radiating boundary condition or non-reflective boundary condition [229].

The technique mainly used in this work for simulations of functional structures is the Finite Element Method (FEM) [115, 116]. The method is based on approximating the solution to the partial differential equations, rather than the differential operators themselves, on a meshed structure. Similar to other non-integral methods, the entire geometry is meshed. Traditionally the mesh elements are triangular for surfaces and tetrahedrons for volumes. The method is well-suited for inhomogeneous media and regions with boundary conditions. The technique is good at handling multi-physics, provided the given mesh works well in both settings. FEM works well for bounded geometries but also plane waves incident on inhomogeneous media. Combined with periodic boundary conditions, expressed further in this section, it was the method of choice to develop functional structures in this work.

Light propagating and wavefront shaping through random media, a media filled with randomly placed scatterers, is of interest in many medical fields [31, 61, 87]. These problems are often very large in terms of wavelength and hard to deal with using conventional approaches. The memory requirement quickly makes the problem unfeasible to solve with any technique solving the problem in a traditional full-wave solver sense, in which the entire volume is discretized. However, integral solvers only discretize the scatterers and the size of the volume is in this setting not important. In order to get scattering on the level of random scattering in tissue requires a lot of scatterers. In these situations, memory will still be an issue for larger structures. This is problematic and is discussed further in Sec. 8.

Conventional approaches to simulate structures of random media use the statistical nature of scattering. Monte Carlo type simulations are used along with radiative transport theory, which describes the wave propagation through a medium characterized by a random distribution of scatterers and applies to both electromagnetic and acoustics waves. However, these techniques are not full-wave solvers and do not provide phase information. It is a diffusion model type in the sense that it describes the average intensity and power flow. These techniques are well suited for many applications but in emerging technologies, it is of interest to control light through a medium through wavefront shaping, see for instance [12, 25, 29, 36, 46, 121, 242–244, 254, 264, 264]. An example is to optimally transmit power through a medium. It is important to have both phase and amplitude information of the fields and to be able to test approaches of a single realization of the random media. Traditional Monte Carlo techniques do not provide this and it is useful to have a full-wave solver. FDTD and FEM techniques can handle smaller regions but are still orders of magnitude away from the end-use case of several centimeters of simulation region.

Many mathematical tricks can be done with integral solver techniques and they can often be tailored to the specific problem whereas FEM and FDTD, in general, are approaches where there is not as much room for a great improvement in the formulation, meaning that the meshing is the most important thing the user needs to investigate and has direct control over. Several advanced versions of the techniques exist and hybridizations, such as Multilevel Fast Multipole Method (MLFMM), adaptive cross approximation (ACA), transmission line matrix (TLM), finite integration technique (FIT), hybrid FEM-FDTD, to name a few [28, 49, 263].

The choice of solver and software depends on the use case of the project and the respective strength of the solver in each software. For the functional structure in Paper I and V, everything was constructed in metal and simulated as a perfect electric conductor in the MoM-based solver in Altair Feko [9]. It was also simulated in the manufactured material of aluminum and verified with the FEM model in CST MWS [220]. The functional structures in Paper II and VI comprised several materials and layers. As such, they were both done entirely in FEM. CST MWS was used for Paper II whereas COMSOL [52] was used to incorporate multi-physical phenomena crucial to the design of the structure in Paper VI. For simulations of scattering in random media in Sec. 8 we used point scatterers connected through a Foldy-Lax type model [76, 139, 140].

The strength of FEM has been lifted but we have not addressed how large structures can be simulated in this environment without memory issues. Here the periodicity of the structure is important. When illuminating the structure such that the illumination on all elements is equal, up to phase offsets, *i.e.* a plane wave, and if the structure is periodic so is the solution, with the same periodicity. This is known as Floquet's Theorem [74]. The theorem states that the solution to a partial differential equation with periodic coefficients is periodic with the same periodicity. The structure is periodic and thus the currents and electric field will be periodic such that,

$$\boldsymbol{a}(\boldsymbol{r}) = \boldsymbol{a}_{\mathrm{p}}\mathrm{e}^{-\mathrm{j}\boldsymbol{k}\cdot\boldsymbol{r}}, \tag{4.1}$$

where $\boldsymbol{a}$ is either the electric field or current density and $\boldsymbol{a}_{\mathrm{p}}$ is a periodic function in the unit cell. A rectangular unit cell aligned with the x and y direction can be implemented with periodic boundary conditions where $p_x\hat{\boldsymbol{x}}$ and $p_y\hat{\boldsymbol{y}}$ are translation vectors containing the periodicities [52, 220]. The periodic functions can be expanded in a Fourier series and for a periodicity in a 2D structure this expansion can be written as,

$$\boldsymbol{a}_{\mathrm{p}} = \sum_n \sum_m b_{n,m}\mathrm{e}^{-\mathrm{j}2\pi(nx/p_x+my/p_y)}, \tag{4.2}$$

where $b_{n,m}$ are the expansion coefficients. These equations can be inserted into the governing equations and form the basics of Floquet mode expansions. The simulation can be carried out over just one unit cell and the fields are expanded and matched with Floquet modes at the ports, where some propagation distance
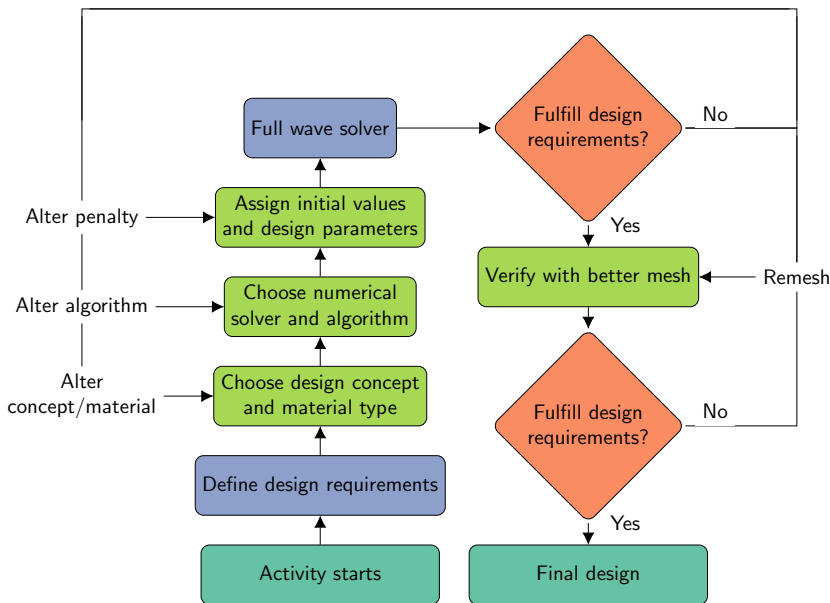
Figure 10: Flow chart for designing functional structures used in this thesis.

between the port and structure has been added. The unit cell does not have to be rectangular; for example, in Paper II a parallelogram was used. In a measurement setting, the structure is neither infinite nor illuminated by a plane wave. However, a finite structure where edge illumination is avoided provides results similar to the simulation of the infinite structure and plane wave incidence.

4.2   Design Process

As presented in Sec. 3 there are many possible functional structures and use cases. In order to construct a feasible design, simulations and numerical techniques play an integral part. The entire design process used for the functional structures in this work is summarized by the flowchart seen in Fig. 10.

The first step in the design process is to define a problem or use case scenario from which electromagnetic performance requirements can be formulated. Most of the designs use transmission and reflection measures, but polarization purity through axial ratio and isolation is also used [173, 241, 252]. Other goals can also be of interest in a metasurface settings, such as tunable/active designs, beam-bending performance and Spatial Light Modulators (SLM) [92, 144, 176, 217]. In Paper VI a metasurface absorbing electromagnetic fields is created, where the important metric is the creation of radiating infrared photons from absorbed electromagnetic energy.

Certain application areas have strict requirements on the materials to use,

not based on electromagnetic constraints. For instance, in space applications, these requirements can be structural, weight/dimension limitations, and thermal properties [108]. It is important to consider the availability of materials, as the range of values for a given electrical parameter can impact the design choice. Functional structures can in large control the effective properties of the structure, but the performance of larger substrates cannot be controlled further. Examples in this work include spacer thicknesses and overall material choice in Paper III, the mechanical stability of the laser milled design in Paper I, line-width of the copper lines, resistance values and thermal properties in Paper VI.

A concept design can be drafted with a selection of usable materials and through an investigation into previous work. It may be investigated in terms of analytical expressions prior to implementation in numerical solvers. It is key when creating the numerical model that the model should be able to work with optimization routines without breakdown. The geometrical parameters could be set in relation to other parameters, through scaling, to ease this process.

In the previous section, we established the use of FEM and periodic boundary conditions with Floquet mode for developing functional structures. A single element is repeated infinitely to create the full structure. An illustration of a unit cell is seen in Fig. 11 along with a repeated structure. In simulations of the infinite structure, grating lobes can show up, with possibly a detrimental impact on the results. The grating lobes occur for frequencies higher than $c/(2p)$, where p is the periodicity [173]. However, in our measurements performed on the finite structures, these effects are not visible. Further considerations for a multilayered design is that the spacing between layers should be larger than $\lambda/4$ to avoid higher-order mode coupling [173].

The construction of the unit cell will also impact the packing density of the elements and offset between different rows in the structure. In Fig. 11 an illustration of square and non-square unit cells is seen. With a tilted unit cell, the alignment of the element can be different compared to the square unit cell. These factors depend on the geometrical parameters of the element and are problem-specific. In Paper II, a design consisting of multiple layers of rotated meander-type wires is produced. Each layer comprises of long wires connecting several elements, with one unit cell describing the entire structure, described in Sec. 5. For this to be the case these wires and the tilt of the unit cell cannot be rotated arbitrarily but are restricted to have a rotation of 45° or 60° [153]. This is purely a mathematical consequence of the numerical implementation one should be aware of in certain specific scenarios.

Initial designs of functional structures, whether or not it is based on approximations, does seldom fulfill all design requirements. It is the first step in an iterative process where optimization techniques typically play a major role to get improved performance. For the optimizations to function, one has to choose a suitable algorithm and penalty function. The penalty function judges the performance of the structure, given some pre-defined constraints. An example is a polarization selective structure that should convert electromagnetic radiation in a frequency f_0 from one linear polarization to the other in transmission. With
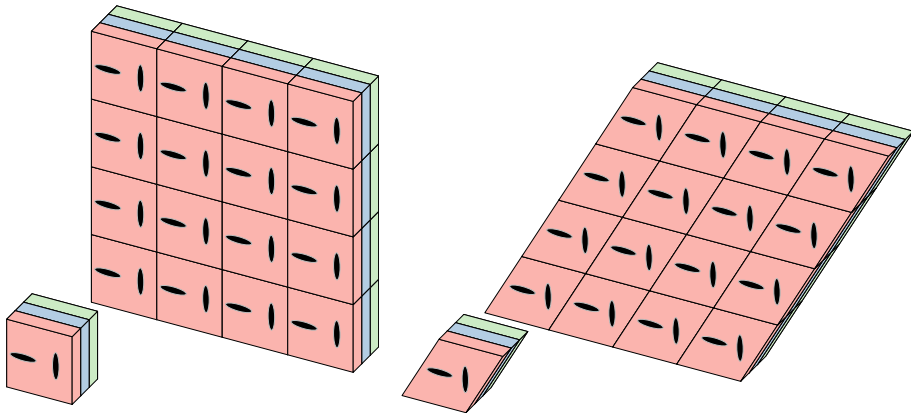
Figure 11: Cuboid unit cells and complete structure (left) and a parallelepiped unit cell and a complete structure.

the structure in a numerical solver and one port on each side, excited by linearly polarized plane waves, the scattering matrix, (2.53), is,

$$
\begin{pmatrix} V_1^{\text{X}-} \\ V_1^{\text{Y}-} \\ V_2^{\text{X}-} \\ V_2^{\text{Y}-} \end{pmatrix} = \begin{pmatrix} S_{11}^{\text{XX}} & S_{11}^{\text{XY}} & S_{12}^{\text{XX}} & S_{12}^{\text{XY}} \\ S_{11}^{\text{YX}} & S_{11}^{\text{YY}} & S_{12}^{\text{YX}} & S_{12}^{\text{YY}} \\ S_{21}^{\text{XX}} & S_{21}^{\text{XY}} & S_{22}^{\text{XX}} & S_{22}^{\text{XY}} \\ S_{21}^{\text{YX}} & S_{21}^{\text{YY}} & S_{22}^{\text{YX}} & S_{22}^{\text{YY}} \end{pmatrix} \begin{pmatrix} V_1^{\text{X}+} \\ V_1^{\text{Y}+} \\ V_2^{\text{X}+} \\ V_2^{\text{Y}+} \end{pmatrix}, \tag{4.3}
$$

where port 1 and 2 refer to the port number, and X / Y the polarization state, for instance, linear or circular polarization as seen in Fig. 4, with the notation introduced in (2.55). The superscript + indicates waves entering the port, and − indicates waves leaving the port. Different notation is used in the literature depending on if the ports on one side of the Device Under Test (DUT) are referred to as one single port containing two separate polarization states or if these ports are labeled with individual port numbers. With the described end goal we can write the optimal scattering matrix, with no comments on feasibility,

$$
\mathbf{S}_{\text{opt}} = \begin{pmatrix} 0 & 0 & 0 & 1 \\ 0 & 0 & 1 & 0 \\ 0 & 1 & 0 & 0 \\ 1 & 0 & 0 & 0 \end{pmatrix}, \tag{4.4}
$$

up to some phase factor. With this information, optimization goals are constructed. For instance, in this trivial example, the goal to maximize $|S_{12}^{\text{XY}}|+|S_{12}^{\text{YX}}|$ over a certain frequency interval or angle of incidence. In certain cases, as in Paper I, fundamental limitations existed which could be used as an alternative goal or threshold.

In general, the penalty function includes several parameters of interest $h_{i,j}$ where j represents the measure, for different frequency intervals Ω_i, denoted by

$$F = \sum_{i=1}^{M} \sum_{j=1}^{N} \frac{a_{i,j}}{\Delta \Omega_i} \int_{\Omega_i} |g_{i,j}|^{p_{i,j}} \, \mathrm{d}f,$$

where

$$g_{i,j} = h_{i,j}(f) - l_{i,j}$$
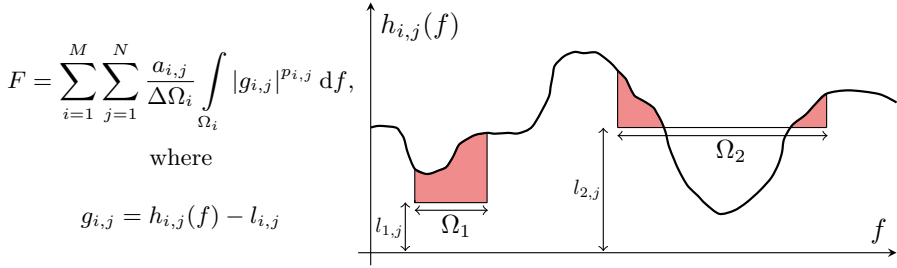
Figure 12: A general penalty function (left) along with a graphical representation of the penalty value for one performance function of interest, $h_{i,j}$, over two frequency bands and threshold values (right). The red area represents the penalty value in the case of $p_{i,j} = 1$.

the subscript i, and for certain thresholds values $l_{i,j}$. For a single measure of interest and frequency band, the penalty function becomes,

$$F = \int_{\Omega} |h(f) - l|^p \, \mathrm{d}f, \tag{4.5}$$

where the subscripts are suppressed and p is a chosen constant to alter the significance of large deviations from the threshold value. For several parameters of interest and frequency bands, a general form of a penalty function is seen in Fig. 12 alongside a graphical representation, where $a_{i,j}$ are the weights. The value of the integral, for $p = 1$ is displayed in red in the right-hand figure.

As a part of the optimization process, the weights $a_{i,j}$ and scaling $p_{i,j}$ could be reviewed several times as more information has become available through the design evaluations. An example is a multiband FSS where transmission of one band might be easier to achieve due to geometrical constraints than the other. The second band should then be penalized harder, *i.e.* a larger weight value for this specific evaluation parameter.

The optimization process in the design chain is often non-trivial as the problem is non-convex [24]. Several local minima exist and without prior knowledge of a suitable candidate design, the numerical solvers and algorithm may end up in poor-performing local minima. In most of the presented designs in this work, to solve the local minima problem, genetic algorithms were used as a first step in the optimization process. After this yielded a satisfactory design and the parameter space consequently could be reduced, we employed other techniques. Paper II consists of a high dimensional optimization problem and the final design was obtained using genetic algorithms followed by the Nelder-Mead method and trust region framework [220]. All optimization steps are not needed for all structures presented in this work but serve as a general guide. We used a combination of in-program optimization tools for each respective simulation program, along with external tools in MATLAB optimization toolbox [232].

Genetic algorithms typically require evaluations of a multitude of candidate designs. Therefore, it is important that each simulation is done in a timely manner. The accuracy of the simulation is traded for computational time, primarily by reducing the mesh or introducing symmetry into the design. Simulations of a candidate design for varying mesh settings can give a crude estimate of what the mesh settings should be to have a fair trade between accuracy and time. Observing currents on the structure can help identify regions of low and high mesh density. As a solution with coarser mesh might not be accurate, it is important for the last steps of the optimization process to use a fine mesh for verification purposes. A final design is obtained if the satisfactory results stand, perhaps through iterative re-meshing. Otherwise, the optimization process should be carried out anew. The entire process described in this section is summarized in Fig. 10. In the following section, a use case of functional structure and design produced by following this design process is displayed.

5   Functional Structure in Satellite Communication

Until this section various types of functional structures and design processes have been described, see Sec. 3 and Sec. 4. The presented use case of an extraordinary transmission surface, see Sec. 3 and Paper I, is not aimed at a particular practical application but investigates interesting fundamental limitations. Many functional structures serve a more practical purpose. In this section, a problem in satellite communication is presented and solved using a functional structure designed according to the steps in Sec. 4. In this scenario, it is not only important to manage frequency selectivity but also polarization selectivity for circular polarization. The functional structure is characterized as a Circular Polarization Selective Structure (CPSS). The section contains a description of the problem, categories of circular polarization selective structures, previous structures, and lastly our solution.

5.1   Dual Band Use Case

Communication satellites are key components in today's interconnected world. Most of them are in the geostationary orbit, at a height of $36\,000\,\mathrm{km}$, and thus have a fixed position in the sky [224]. They can provide uplink and downlink coverage over a large geographical area using multiple spot beams as illustrated in the left of Fig. 13. Each hexagon type in the illustration corresponds to a certain frequency and polarization combination. The number of combinations needed to color a general map with no overlap is four [10]. However, in this illustration, three is sufficient. With this spot beam configuration, most radiated power will reach a landmass and not illuminate regions lacking users, such as the
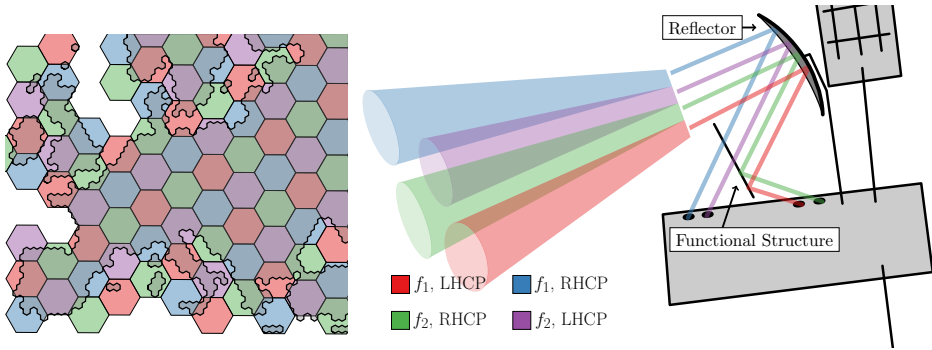
Figure 13: A satellite (right) with antennas operating using two polarizations and frequencies illuminates a reflector through the use of a functional structure, CPSS, as a diplexer. The beams create a frequency/polarization reuse scheme covering a Europe-shaped landmass without mutual overlap (left).

sea. We can achieve this coverage using four unique frequency and polarization combinations from two orthogonal polarizations and two frequency bands.

In wireless communication, there is an ever-increasing demand for higher data rates with each communication generation [108, 198]. An increase in throughput can be obtained by using reuse schemes in both polarization and frequency, as illustrated in the left of Fig. 13 [7, 19, 108, 198, 209]. This pushes the devices and satellites to operate with multiple bands and at higher frequencies. The two frequency bands we consider are the K and K_a bands at $17.7 - 20.2$ GHz and $27.5 - 30$ GHz, respectively.

The end multi-beam coverage can be realized with one reflector per frequency-polarization combination. But the reflectors are large and take up a lot of space; a costly resource for satellites. Instead, a polarization (and frequency) selective structure can be included. For linear polarization, one can use a dual grid-ded reflector (DGR) or a diplexer [19, 181, 203]. However, most times circular polarization is the preferred polarization as alignment problems and impact of atmospheric effects like the Faraday effect are avoided [111, 238]. From an engineering point of view, circular polarization can be trickier to design for. There is no equivalent simple structure with a similar performance level as the strip grid for linear polarization. In this work, we consider diplexer use cases for circular polarization as illustrated in the right of Fig. 13 where the beams share a common reflector surface.
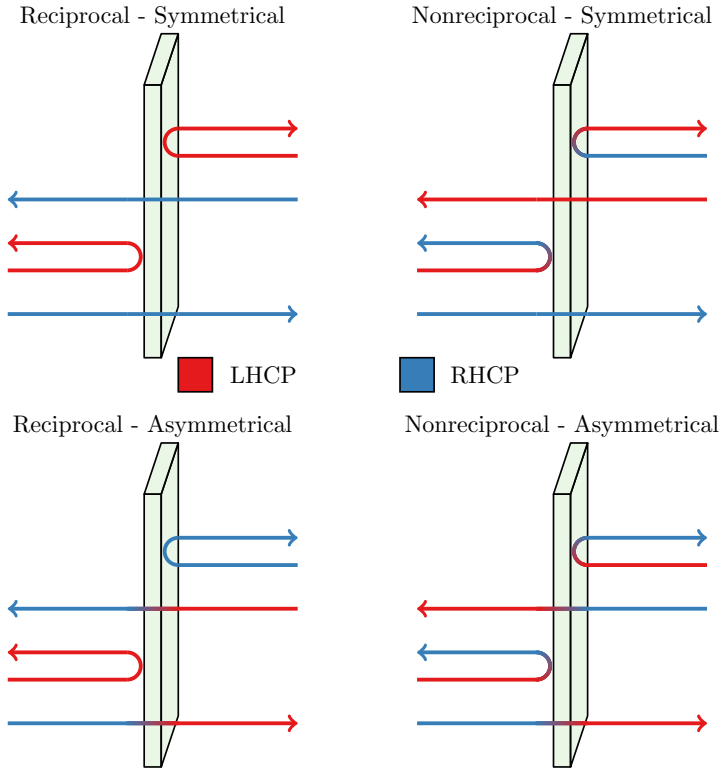
Figure 14: Four CPSS categories are illustrated for a left-hand CPSS case. The characterization is based on the polarization of the reflected and transmitted wave with regard to the incident wave.

5.2   Ideal Performance and Parameters of Interest

A dual-band CPSS provides a solution to create a system as seen in Fig. 13. However, the term CPSS incorporates several possible types, illustrated in Fig. 14 [206]. Reciprocal structures keep the polarization state through reflection and symmetrical structures through transmission. Breaking reciprocity requires exotic materials, such as magnetized ferrite crystals, which are not suitable for space applications [42]. The transmitted and the reflected polarization of an asymmetrical CPSS are the same, unless it is nonreciprocal, and thus will not help create the frequency-polarization reuse scheme seen in Fig. 13 alone. Thus, the interesting structure for this configuration is a reciprocal symmetrical CPSS. Evaluating

the CPSS can be done in terms of the scattering matrix, introduced in Sec. 2. In circular polarization for a dual-polarized two port system, the scattering matrix is,

$$\mathbf{S}^{\mathrm{CP}} = \begin{pmatrix} S_{11}^{\mathrm{RR}} & S_{11}^{\mathrm{RL}} & S_{12}^{\mathrm{RR}} & S_{12}^{\mathrm{RL}} \\ S_{11}^{\mathrm{LR}} & S_{11}^{\mathrm{LL}} & S_{12}^{\mathrm{LR}} & S_{12}^{\mathrm{LL}} \\ S_{21}^{\mathrm{RR}} & S_{21}^{\mathrm{RL}} & S_{22}^{\mathrm{RR}} & S_{22}^{\mathrm{RL}} \\ S_{21}^{\mathrm{LR}} & S_{21}^{\mathrm{LL}} & S_{22}^{\mathrm{LR}} & S_{22}^{\mathrm{LL}} \end{pmatrix}, \tag{5.1}$$

where the superscript indicates right (R) or left (L) handed circular polarization, see (4.3). The ideal dual-band CPSS will for example in the lower frequency band, f_1, reflect Right-Handed Circular Polarization (RHCP) and transmit Left-Handed Circular Polarization (LHCP) and the converse for the upper-frequency band, f_2. The ideal scattering matrices can be described in circular polarization by,

$$\mathbf{S}(f_1) = \begin{pmatrix} e^{-\mathrm{j}\phi_{\mathrm{r}}} & 0 & 0 & 0 \\ 0 & 0 & 0 & e^{-\mathrm{j}\phi_{\mathrm{t}}} \\ 0 & 0 & e^{-\mathrm{j}\phi_{\mathrm{r}}} & 0 \\ 0 & e^{-\mathrm{j}\phi_{\mathrm{t}}} & 0 & 0 \end{pmatrix}, \tag{5.2}$$

$$\mathbf{S}(f_2) = \begin{pmatrix} 0 & 0 & e^{-\mathrm{j}\phi_{\mathrm{t}}} & 0 \\ 0 & e^{-\mathrm{j}\phi_{\mathrm{r}}} & 0 & 0 \\ e^{-\mathrm{j}\phi_{\mathrm{t}}} & 0 & 0 & 0 \\ 0 & 0 & 0 & e^{-\mathrm{j}\phi_{\mathrm{r}}} \end{pmatrix}, \tag{5.3}$$

where ϕ_{r} and ϕ_{t} are phases of the reflection and transmission coefficient, respectively. From (5.1), we can define three main quantities for characterizing the performance of a given CPSS structure. In this work we use the performance in reflection (return loss), performance in transmission (insertion loss), and purity of the transmitted/reflected polarization (axial ratio). Another commonly used measure of polarization purity is cross-polarization discrimination (XPD). The quantities are defined, through (5.1) as,

Return Loss: $\qquad \mathrm{RL}_{\mathrm{dB}} = -20\log_{10}(|S_{mm}^{kk}|),$ \hfill (5.4)

Insertion Loss: $\qquad \mathrm{IL}_{\mathrm{dB}} = -20\log_{10}(|S_{mn}^{kk}|) \quad m \neq n,$ \hfill (5.5)

Axial Ratio: $\qquad \mathrm{AR}_{\mathrm{dB}} = 20\log_{10}\left(\left|\dfrac{|S_{mn}^{ll}| + |S_{mn}^{kl}|}{|S_{mn}^{ll}| - |S_{mn}^{kl}|}\right|\right) \quad k \neq l,$ \hfill (5.6)

Cross Polarization Discrimination : $\qquad \mathrm{XPD}_{\mathrm{dB}} = 20\log_{10}\left(\dfrac{|S_{mn}^{kk}|}{|S_{mn}^{kl}|}\right) \quad k \neq l,$ \hfill (5.7)

XPD and AR relation: $\begin{cases} \mathrm{XPD}_{\mathrm{dB}} = 20\log_{10}\left(\frac{\mathrm{AR}+1}{\mathrm{AR}-1}\right), \\ \mathrm{AR}_{\mathrm{dB}} = 20\log_{10}\left(\frac{10^{\mathrm{XPD}_{\mathrm{dB}}/20}+1}{10^{\mathrm{XPD}_{\mathrm{dB}}/20}-1}\right). \end{cases}$ \hfill (5.8)
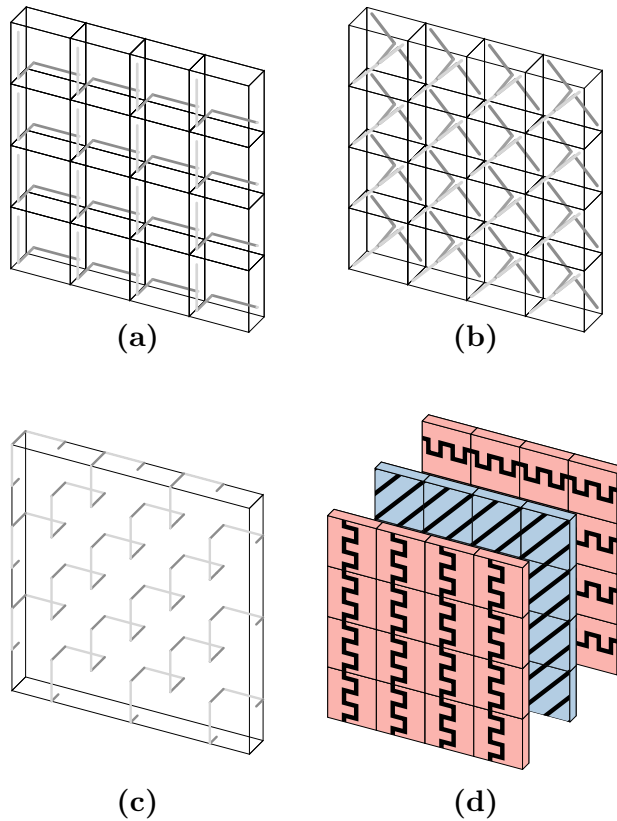
Figure 15: Geometry of varying CPSS designs: (a) Pierrot design [186], (b) Tilston [234], (c) Morin [169–171], and (d) a simplified illustration of a multi-layer cascaded design [120].

In antenna design, fractional bandwidth is often based on the return loss, and for a CPSS we use more metrics which are based on reflection, transmission and polarization purity. For a CPSS in space applications, such as satellite communication, typical governing values are return loss and insertion loss less than 0.5 dB and axial ratio less than 0.78 dB [7, 69]. In other scientific work, not necessarily space application oriented, relaxed requirements are used where return loss and insertion loss should be less than 1 dB and axial ratio less than 3 dB [2, 3, 118–120].

5.3   Possible Designs

We can divide possible CPSSs into two categories, resonant and non-resonant. CPSSs have been investigated since the 1960s when Pierrot presented the first
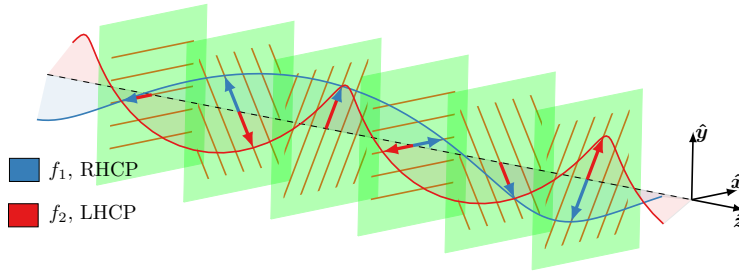
Figure 16: Conceptual illustration of a dual-band CPSS operation at a fixed instant in time. RHCP waves (blue) at frequency f_1 rotate 60° between each layer and the LHCP waves (red) rotate 120° in between each layer, in the opposite direction.

design [186]. The design and many which followed later by Tilston and Morin work on the same principle of resonant elements [78, 147, 148, 169–171, 209, 210]. These types of elements are shown in Fig. 15. The classical elements in (a)–(c) are based on a single-layer design. Several variations of these classical designs have been made throughout the years. However, the drawback of resonant elements is small bandwidth performance, typically less than 8 % with respect to the strict requirements, and less than 20 % with respect to the relaxed requirements and often much lower [70]. They are furthermore sensitive to the angle of incidence [69].

There have been improvements in the concept of CPSS in recent years [2, 118, 120]. Instead of resonant elements, several polarizers in linear polarization are cascaded [34, 35, 120]. The principle is illustrated in Fig. 15 (d). An incident circularly polarized wave is converted to linear polarization. One of the linear polarizations is transmitted by the central layer, the other gets reflected. The transmitted wave is converted back to the initial circular polarization. The bandwidth of this structure is higher than the traditional resonant designs [70].

The presented case of a dual-band CPSS, with two bands relatively close, K and K_a, with opposite performance, reflect one polarization in the first band and transmit in the other, is a challenge. Resonant elements are not suitable for this task. Due to their resonant nature it is difficult to excite the opposite polarization for a band close to the first. Moreover, they suffer from low bandwidth and poor angle-of-incidence performance. Thus we constructed a design based on cascading layers of meander lines. The design concept was initially used to construct a wideband CPSS but can also be used in a dual-band setting [70, 152, 153]. An illustration of the cascaded anisotropic layers is seen in Fig. 16.

The design was investigated through circuit theory and simulations with more information in [70, 152]. Conceptually, the principle of operation can be described as follows: An incident LHCP wave on the structure interacts with the first layer. The following layers are rotated and positioned such that a LHCP wave is aligned similarly to the first layer for the subsequent layers, illustrated by the blue line in
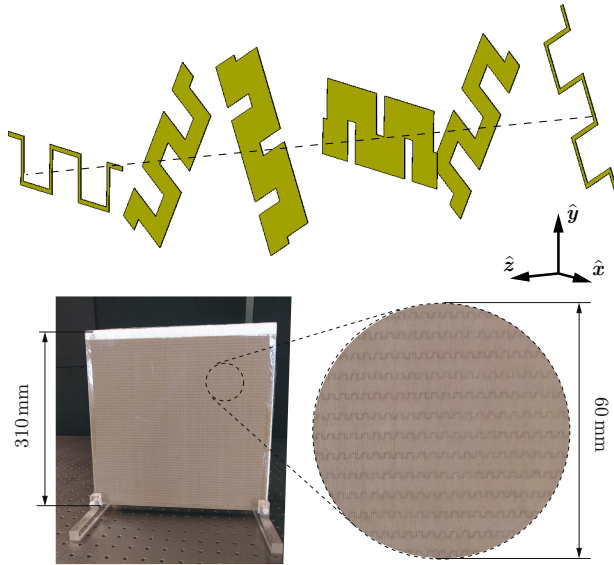
Figure 17: Illustration of the meander lines within one unit cell, as viewed in the simulation program CST MWS (top), and the manufactured six-layer design (bottom).

Fig. 16. A wave of opposite polarization can also align similarly if the wavelength of the wave is different. See the red line in Fig. 16. For the low frequency, LHCP is reflected and RHCP transmitted whereas LHCP is transmitted and RHCP reflected for the higher frequency. The frequency of interest and the separation between the bands depend on the rotation of the grids and their spacing. For the bands of interest here, an ideal rotation is theoretically 76° [152]. For a multi-layered structure in a periodic solver, this not possible, instead a rotation of 60° is used. The theoretical band separation for 60° rotation is larger, and performance has to be sacrificed in order to get the operational bands closer. The number of layers also influences the performance, and through circuit theory, a certain number of layers are preferred for a given rotation, to minimize the cross-polarization. Designs between 3 and 9 layers have been investigated using the strategy presented in Sec. 4.2. The meander lines in a unit cell for the resulting six-layer structure are seen in Fig. 17 along with the measured performance in Fig. 18. The measured data is indicated by the red (LHCP) and blue (RHCP) solid lines with markers. Simulations of the manufactured design is shown in black dashed lines. The solid black lines show the target goals in the two bands. The design is further presented in Paper II.

We have now presented a functional structure with a use case within satellite communication for the K and K_a bands. To verify the performance, it is important to manufacture the design and conduct measurements. This is true
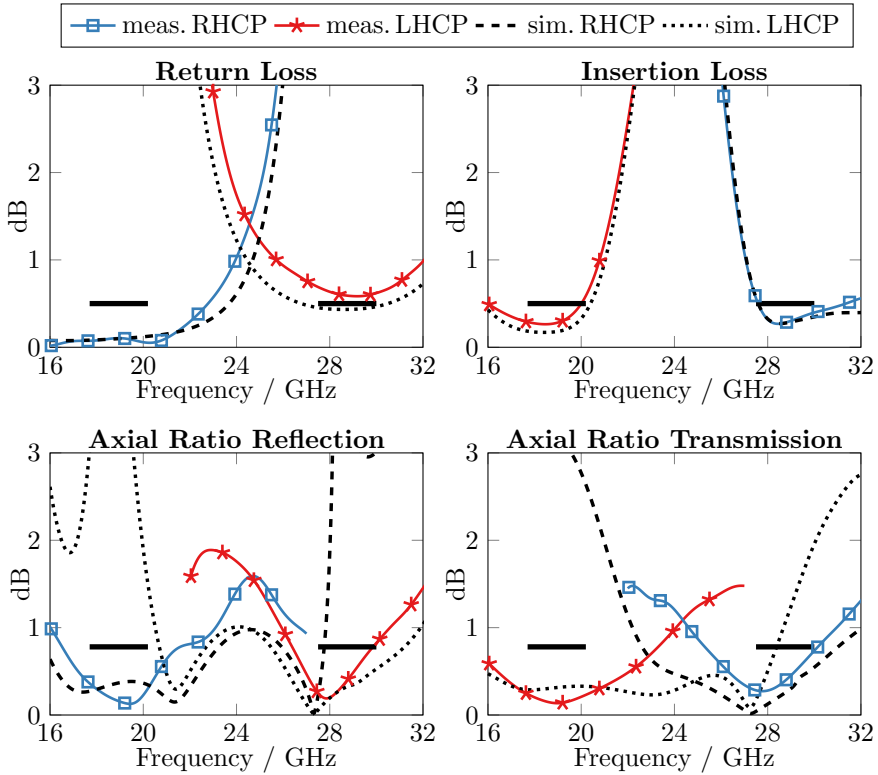
Figure 18: Experimental results of the dual-band CPSS, Fig. 17. The upper left plot shows the return loss in both frequency bands and the left plot the corresponding axial ratio. The upper right plot shows the insertion loss in both frequency bands and the lower right plot the corresponding axial ratio. Simulation results are given by the dashed black curves and the requirements by the solid black lines [152].

for most electromagnetic designs. Measurements are not without problems, and one must be careful and methodical. The topic of the following section is how measurements are carried out not only of functional structures but devices in the near field as well.

6   Measurement Techniques

Not only satellites but the entire mobile communication systems impact our society. Mobile data traffic is growing by around 50 % yearly [97]. Society has great expectations of what technology should achieve. As an individual in society, much of the technology around us has gone through massive upgrades during the last 10–15 years. It was not long ago smartphones were a scarcity and most videos streamed at sub HD quality with several buffering breaks. Now low latency 4K videos in our smartphones are soon to be expected. This is the front end of what 5G and the future may hold for us. However, the architecture is much more than better video quality. It will support massive network capacity, increased availability, and connectivity between not only humans but devices, objects, and machines [59, 107].

Similarly to the functional structure in Sec. 5, these future demands on traffic capacity can be handled by the next generation wireless access systems (5G) [67]. A solution, within 5G, to increase traffic capacity is among other things to use larger bandwidths and higher frequencies. Currently, the most used frequencies in mobile communication are under 6 GHz. With 5G and beyond, higher frequency bands will become more common. 5G has higher bands allocated around 28 and 60 GHz [67]. Electromagnetic waves in the 30–300 GHz range are also called mm-waves, due to their corresponding wavelength being on a millimeter scale, and have an important position in the near future as there will be a huge influx of radiating devices and passive structures. The performance of the structures and devices must be verified for characterization reasons, and in the case of radiating devices, to verify compliance with existing regulations of electromagnetic field (EMF). Up to this point, we have presented two functional structures and will now discuss how they can be verified through measurements. Then we will continue with measurements of radiating devices, specifically in the lower frequencies of the mm-wave regime.

6.1   Functional Structures

6.1.1   Setup

In the process of designing a functional structure, described in Sec. 4, the important performance metrics are often described by elements in the scattering matrix, see Sec. 5.2. The elements correspond to reflection and transmission values and are in principle measured in two ways. Both of these techniques are electromagnetic techniques in which, for instance, a Vector Network Analyzer

(a)

(b)

(c)
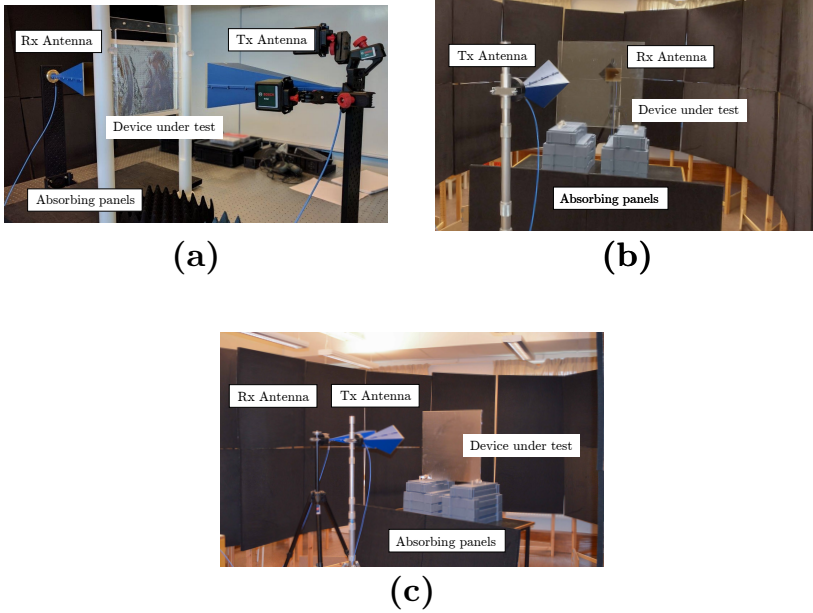
Figure 19: Experimental setups for measurements of functional structures. The images depict a measurement in transmission for a frequency selective structure (a) and a measurement setup for a circular polarization selective structure in transmission (b) and reflection (c).

(VNA) is used and voltage waves on different ports are recorded [192]. As we saw in Sec. 4 the individual simulated elements periodically repeated generate an infinite structure, but a manufactured structure is finite. The first measurement technique is to place the finite structure within a waveguide. The two ends of the waveguide serve as the ports and the walls of the metal cavity provide boundary conditions yielding an infinite structure, as expected by image theory. Positioning of the structure within the waveguide is crucial, as any offset is detrimental to periodicity. If there are issues in manufacturing and the sample has defects, then it will be amplified since the sample is repeated infinitely. Strengths are high signal integrity and small manufactured samples.

The second technique, used in Paper I, II, and III, is a measurement of a finite structure in free space. In this setup, the finite functional structure is placed between two antennas that illuminate the structure. The setup is seen in Fig. 19. In (a) a transmission measurement is displayed with the functional structure from Paper I inserted at the midpoint between the horn antenna apertures. Picture (b) and (c) show reflection and transmission measurement setups for a structure similar to the CPSS in Paper II. Positioners, not visible in these pictures, are favorably used to control the position and rotation of the antennas, in particular

for measurements of circular polarization.

In the simulations, an infinite structure with a plane wave incidence was used (FEM solver and periodic boundary condition as described in Sec. 4). The distance between the structure and the illuminating antennas should be sufficient to avoid any strong near-field interaction, as indicated by the regions in Fig. 5. It is also important to not be in the far field of the now finite structure. In the far-field region, we will see edge effects of the sample start dominating [101,184]. A difference between simulations and measurements is that an infinite structure has no far field, in this sense, but inherits the far field of the illuminating antenna. Calculations of the illuminating antennas' beamwidths are used to determine the distances to avoid edge illumination and the issues it brings. Moreover, it is possible to use dielectric lenses to focus the beam on the structure with a near plane wave behavior [211].

For functional structures and measurement of the scattering matrix, one can use either single-polarized or dual-polarized antennas. Dual-polarized antennas simplify measurements in the reflection scenario, as the receiving and transmitting antenna is one and the same. Thus, cross-polarized reflection can be measured with a single antenna. For single-polarized antennas, this will require two antennas and a slightly oblique angle of incidence as the antennas have a finite physical size, seen in Fig. 19 (c). Larger antennas typically illuminate the edges less but result in a larger angle of incidence in reflection measurements. Thus, reflection measurements with single-polarized antennas require additional thought when constructing the setup. The performance of dual-polarized antennas is in general worse than that of the single polarized counterparts and the choice of polarization is entirely up to the measurement in question. In this work, we only used single-polarized linearly-polarized antennas for all measurements, regardless of polarization of interest.

Alignment in a free-space setting is important and can be difficult. Even a slight misalignment can cause large effects, especially in polarization purity, axial ratio (5.6). Instead of having both antennas co-aligned to a common basis, one of the antennas is rotated 45 degrees with respect to the other as seen in Fig. 19 (b) and illustrated in Fig. 20. This gives an equal signal-to-noise ratio in both measurements of X and Y polarization, in the reference measurement. The sought-after scattering matrix is obtained by changing the basis, using matrix multiplications, back to a co-aligned system.

One strength of a free-space setup is that angles of incidence and positioning of the structure with the illuminating antennas can be done in a free manner. The freedom in positioning comes with the drawback of alignment, taken care of by sample holders and positioners. The structure is not as geometrically restricted as in a cavity measurement and the testing is nondestructive. However, any defects in the structure due to the finite shape, such as tensions creating curvatures *etc.* can cause large errors. Minor defects, on the other hand, are not as important as in the cavity measurement setup as they can be seen to be averaged out over the larger structure.

CPSSs can be measured using both circularly-polarized antennas and linearly-
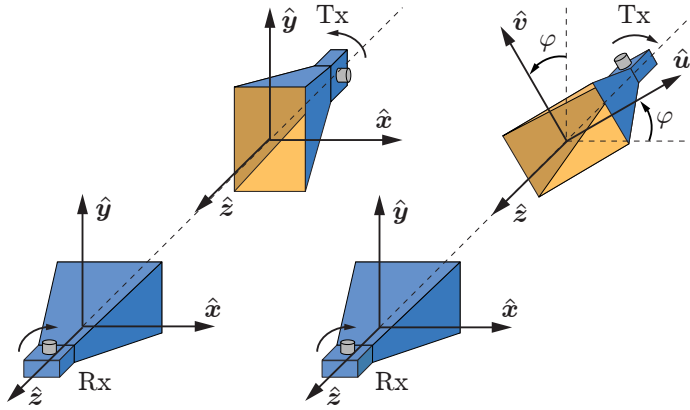
Figure 20: A principal sketch of antenna orientations in measurements of circular polarization transmission. To the left, the main directions of the transmitting and receiving antennas are aligned, and the relative rotation between the antennas is either 0° (co-polarization) or 90° (cross-polarization). To the right, the main directions of the transmitting and receiving antennas are not aligned, and if the antenna orientation angle $\varphi = 45°$, the relative rotation between the transmitting and receiving antenna is always 45° [68].

polarized antennas. Circularly-polarized antennas might seem like the natural choice, as linearly-polarized antennas require matrix transformations to be applied to the measurement result in order to generate the performance in circular polarization. However, the reason for the strength of linearly-polarized antennas is the aforementioned polarization purity. In applications using circular polarization, the axial ratio is important and should be less than 0.78 dB and in some relaxed requirements, that figure is 3 dB. A measurement setup should be able to measure lower than these required limits. When an antenna radiates one polarization, it also excites the orthogonal polarization to a minor extent. This is characterized by the antenna's XPD, which needs to be high to avoid unwanted polarization affecting the system. In [209] a CPSS was measured with circularly-polarized antennas in an anechoic chamber, but the XPD of the antennas was too low and partly made it impossible to measure the low levels of axial ratio needed.

The XPD limits the measurable values of the axial ratio through a relation demonstrated in Fig. 21. Measuring axial ratio lower than the strict limit of 0.78 dB requires an XPD higher than $30 - 40$ dB, which is easier to obtain in single-polarized linearly-polarized antennas. Circularly-polarized antennas need careful designs to reach these values [79] and are often not wideband [77, 141]. Circularly polarized antennas seldom have this high cross-polarization discrimination, within a reasonable budget, and the same goes for dual-polarized linearly polarized antennas. The only choice to reliably measure a low axial ratio in this setup is with single-polarized linearly-polarized antennas. This measurement
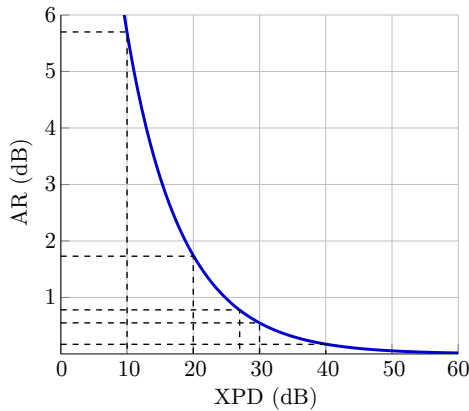
Figure 21: Simulation results of the relation between cross-polarization discrimination (XPD) and axial ratio (AR) in a measurement system are presented. The dashed lines indicate the relation at specific XPD values of interest [68].

strategy for CPSSs is described in Paper III.

6.1.2   Post-Processing

In electromagnetic measurements, the antennas illuminating the structures of interest, or the probe sampling the field from a radiating device must be connected to a device generating the signal and one device collecting the data. In this work, the primary device is a VNA where signals are generated, transmitted, and received. The data collected by the VNA comprise of several voltage waves corresponding to the elements in the scattering matrix.

In a free-space measurement, a transmitted electromagnetic wave interacts with the objects in the surrounding, generating several multipath responses and reflections. A measurement of a single frequency will not only contain a boresight component between the receiving and transmitting antenna but may include multiple reflections, edge illumination, and responses from other passive objects in the vicinity. The impact of the unwanted signal contributions can be reduced by placing electromagnetic absorbers around the setup [258].

Another way to remove these unwanted effects is in post-processing of the signal. A measurement of multiple frequencies can be transformed to the time domain through an inverse fast Fourier transform (FFT) [197]. The data viewed in the time domain, or transformed to approximate distances through the speed of light, will separate between the multipaths and surrounding reflections. A measured transmission signal in frequency and time domain is seen in Fig. 22. The signal has severe ripples in the frequency domain and we can observe several peaks in the time domain. The first large peak corresponds to the boresight transmission, and the smaller following peaks are reflections in the structure and multipath components. We only want the boresight data, and anything other
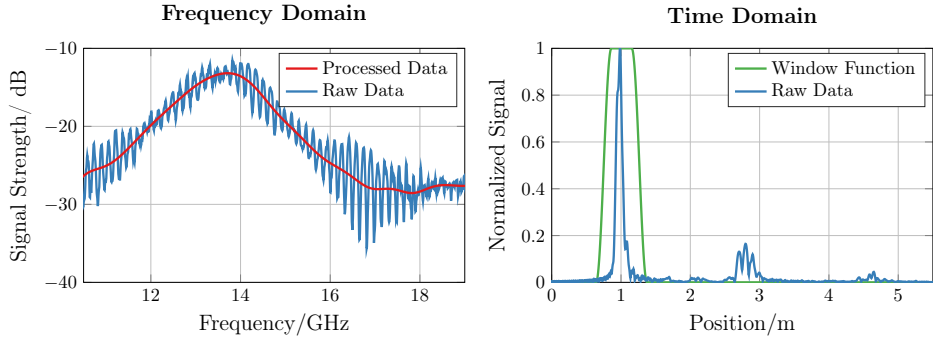
Figure 22: Experimental results from a transmission measurement of a frequency selective structure. The left graph shows the raw frequency-domain data (blue), along with the data after processing in the time domain (red). The right figure displays the time-domain data of the same data set, raw data (blue), and the window function centered over the transmission peak (green). Data from measurements in [151].

than the first peak is not of interest. The time-domain data can be filtered with a window function, *e.g.* a cosine-tapered Tukey window [45]. Filtering out the relevant data from the time domain and transforming back to the frequency domain through another Fourier transform gives us the data of interest. This is known as time gating [197]. The time-gated data, processed data, is seen in red in the left graph of Fig 22. It is important that the measurement settings enable us to carry out this process. In free space, the relation between spatial resolution and frequency bandwidth is,

$$\delta t = \frac{1}{\Delta f}. \tag{6.1}$$

The measurement bandwidth should be set such that multiple reflections within the structure can be resolved, or larger scatterers are spatially resolved. Another useful technique prior to time gating is to zero pad the frequency-domain data. Zero padding is the process of adding zeroes at the start and end of the measurement data. No additional information is added, but the interpolation between the true time-domain data points is increased, resulting in smoother time-domain data curves [221]. This process of time gating alongside zero padding is used in all electromagnetic measurements in Paper I, II, III, IV, and V.

The measured data will depend on the physical setup, placement of antennas, objects nearby, *etc.* A transmission measurement of a structure must be put in reference to a transmission without the structure present to obtain the performance of the structure itself. This is a typical normalization process where the scattering matrix data is obtained from,

$$S_{mn}^{kl,\text{Norm.}}(f) = S_{mn}^{kl,\text{Struct.}}(f) \oslash S^{\text{Ref.}}(f), \tag{6.2}$$
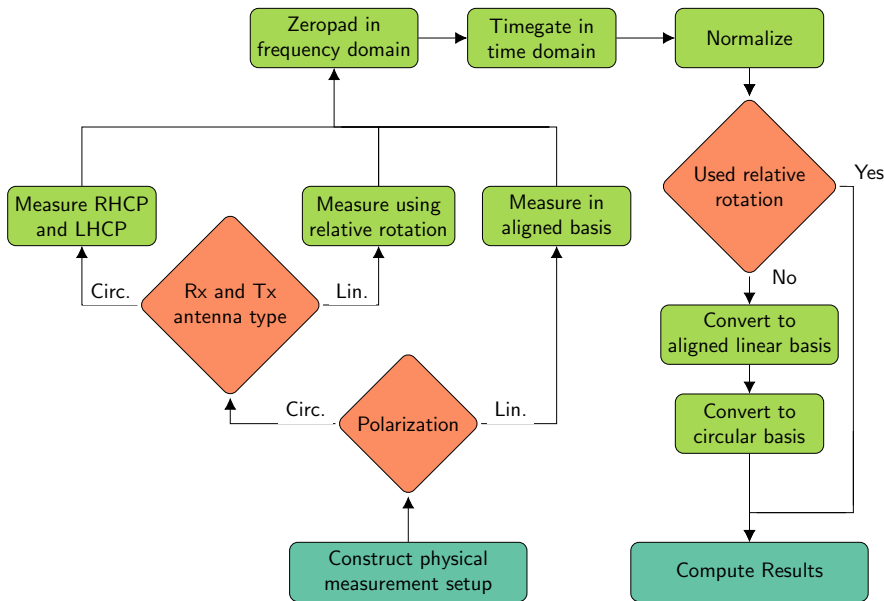
Figure 23: Flow chart of the measurement and post-process technique used for characterization of functional structures in this thesis.

where S are the complex values of the scattering matrix and the normalized values (Norm.) are obtained by the measured data (Struct.) divided by the reference values (Ref.), a process represented by the Hadamard division $\oslash$.

The reference values depends on the specific measurement. In transmission they can be obtained by removing the structure and measure on an empty setup. For reflection reference measurements, the structure should be replaced with a conducting structure, metal, of equal dimensions and shape. In Paper III aluminum is carefully attached to the structure, using water as adhesive, to create a reference surface in reflection.

The significant measurement decisions and post-processing steps discussed in this section is summarized in the flowchart seen in Fig. 23. These steps were used for all measurements of functional structures in this thesis.

6.2   Radiating Devices

It is not only important to measure the performance of functional structures but also the devices generating the radiation. These devices can be anything from ordinary mobile phones to base stations, fridges, or car radars. With IoT, the introduction of 5G, and future systems, the sheer number of devices and applications is increasing by the minute [216]. One aspect for wanting to measure the radiation these devices produce is from a characterization perspective. For in-
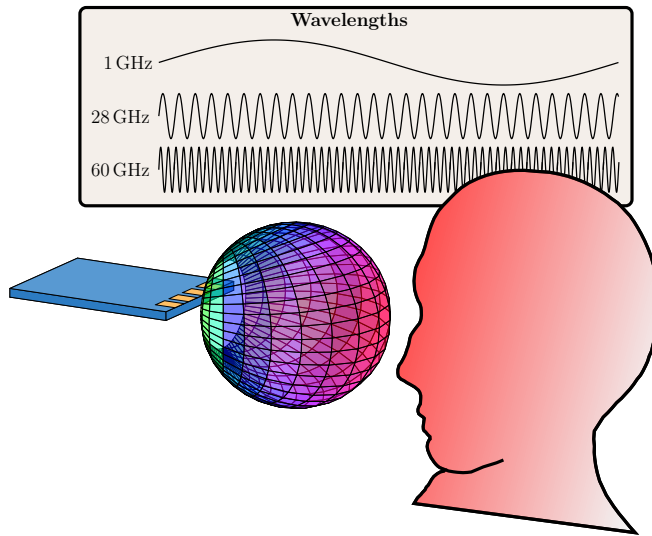
Figure 24: Illustration of a radiating device and a human head along with a scale representing different frequencies and wavelengths of the radiated field.

stance, to verify that multi-beam and MIMO antennas can generate appropriate beam patterns [6, 124]. However, it is also important from an electromagnetic field (EMF) compliance perspective [50, 253]. Electromagnetic radiation carries energy, parts of the energy get deposited in the medium, as losses, when propagating, generating heat [114]. This is the fundamental principle of what happens when radiation impinges on tissue. Guidelines and regulations exist stating limits on radiation for normal use cases, and these are frequency dependent [109].

In Fig. 24 a human head is shown to scale with three frequencies of electromagnetic radiation. A rule of thumb is that electromagnetic waves interact with objects based on their size compared to the wavelength. The wavelength of the lower frequency radiation, 1 GHz, representing GSM bands, is much longer than the length of the head and the wave will penetrate, depositing energy along the way. Heating will occur from within. For higher frequencies, 28 GHz and 60 GHz seen in Fig. 24, the wavelength is much shorter and it will not penetrate the head. Instead, the energy will be deposited near the surface of the skin, resulting in superficial heating.

This simple example demonstrates that different compliance metrics, depending on frequency, should be used. If energy is deposited in tissue, then the specific absorption rate is preferable, measured in W/kg. If the energy is deposited near the surface of the skin, then the incident power density, measured in W/m^2 is preferred.

The distinction when one metric should be used over the other differs slightly. The ICNIRP states that incident power density should be used over 6 GHz [109].

Table 1: Limits of power density described by ICNIRP [109] for frequencies in the 6-300 GHz range.

Spatial Averaging	General Public	Worker	Health Effects
$4\,\mathrm{cm}^2$	$20\,\mathrm{W/m}^2$	$100\,\mathrm{W/m}^2$	$200\,\mathrm{W/m}^2$
$1\,\mathrm{cm}^2$	$40\,\mathrm{W/m}^2$	$200\,\mathrm{W/m}^2$	$400\,\mathrm{W/m}^2$

With 5G, power density has become important in compliance measurements. The exposure guidelines they provide can be seen in Table 1. The power density restrictions in these cases are determined over a plane, with a spatial averaging. The specific limits differ based on the use case. Devices such as mobile phones operate very close to the human body. We thus want to measure very close to the devices in their antennas' radiative near field. There is already an interest in measurements of the near fields for these devices, and these compliance regulations enforce it further. The near fields of the devices should be imaged at close distances, either directly or indirectly through reconstruction techniques. We shall now describe techniques of measuring the near field from devices in this mm-wave regime.

6.2.1   Setup

In this framework and talking about measurements of the near field, it is the radiative near field which is implied, Sec. 2. The reactive near field of the devices is very close, $\lambda/(2\pi)$, and a few millimeter from the device one is in the radiative near field. In this region, either the electric field, magnetic field, or power density can be measured. The incident power density (2.20) can be computed as [16],

$$S_n(\boldsymbol{r}) = \frac{1}{2}\,\mathrm{Re}\{\boldsymbol{E}(\boldsymbol{r}) \times \boldsymbol{H}^*(\boldsymbol{r})\} \cdot \hat{\boldsymbol{n}}, \tag{6.3}$$

where the real part is denoted by $\mathrm{Re}\{\}$, $\boldsymbol{E}$ and $\boldsymbol{H}^*$ denote the electric field and the complex-conjugate of the magnetic field, respectively, and $\hat{\boldsymbol{n}}$ denotes the unit vector normal to the evaluation surface. Traditional measurement setups to image the field use electromagnetic components. The probes can, for instance, be open-ended waveguides measuring the electric field or loop probes for magnetic fields where the former is more common. An example setup is seen in Fig. 25.

A device under test is mounted and an open-ended waveguide probe positioned on a scanning apparatus placed some distance away. The probe can move and register a complex voltage wave signal at each point in the scanning plane. This information can then be used to reconstruct the field at other positions in space and is described further in Sec. 6.3. More sophisticated setups using multiple probes exist, but the principle is the same [72, 75]. Moreover, there exists a multitude of techniques such as phaseless measurement, in which the measured value is not complex, and a combination of measurements generates the relevant information [1, 185, 225].
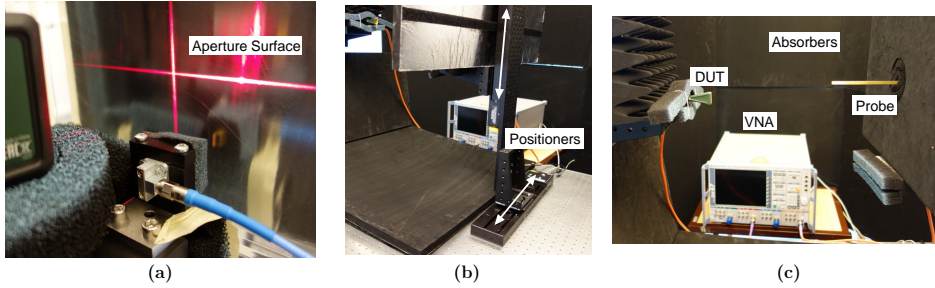
Figure 25: Images of the experimental setup used in the near-field scanning of devices in this work.

As in the case of measurements of functional structures, Sec. 6.1, the device under test and the probe can be connected to a VNA. Information of the electric field in a certain polarization state is obtained as the probe scans over the pre-defined scanning plane. The measurements can take place in anechoic chambers. In our work, the post-processing technique included time gating and zero padding as described in Sec. 6.1.2. For traditional techniques, the sampling of the field is chosen to be on a $\lambda/2$ increment or lower to avoid aliasing issues [159]. The effect of sampling depends on technique and result requirement. The time-consuming part of the measurement is the scan itself, a reduction of measurement points, a decrease in measurement time, comes at an aliasing cost. Depending on the measured device or structure and the sought-for quantity, one can significantly reduce the measurement time with compressive sensing (CS) [43], for instance, in spherical near-to-far-field transformation measurements [53]. Newer techniques with more advanced algorithms, such as the ones presented within this thesis, do not require a $\lambda/2$ sampling to function.

The complex voltage value registered from the port connected to the probe corresponds to some field value. However, the probe has a size and a radiation pattern of its own; it is non-ideal. The probe has a non-local interaction with the electromagnetic field at each spatial measurement point. This interaction depends on several factors, including its radiation characteristic and position relative to the device under test [138,256,258]. For the measured value to represent the radiating device under test one must account for the interaction between the field from the radiating device and the probe. Traditional probe correction takes the radiation pattern of the probe into account and is thus probe specific [182]. When measuring, each measurement probe must be well characterized for these techniques, yet there is still an uncertainty in the relation between the physical position of the probe and the corresponding electrical position of the measurement.

6.3   Information Retrieval

With a probe-corrected measurement, one obtains the field from the radiating device. However, these are often not the only spatial positions of interest. In applications such as in non-destructive testing (NDT) and the described near-field measurements of devices, the fields very close to a device are of interest, or the currents generating the scattered field itself. The type of problem in which the sources of the fields are computed given a measured field is called either an inverse scattering or inverse source problem [39, 90, 133]. The sources can then be used to compute the fields at other positions in space. These types of inverse source problems arise in several scientific fields, tomography, geology, near-field measurements, NDT [11, 125, 131]. In near-field measurements, the reconstructed near fields can be obtained by computing equivalent currents generating the measured field. This is explored in Paper V. In NDT a transmitting antenna illuminates a test subject with defects, which can be found by analyzing the currents on the test subject. A measurement of this in reflection is displayed in Paper IV. The inverse source problem can be described by linear operator whereas the inverse scattering is non-linear, though often formulated with linear operators through approximations and reformulations [58, 187, 239].

The equivalent sources, electric $\boldsymbol{J}$ and magnetic $\boldsymbol{M}$ current densities, generating the measured radiated electric field are connected through the electric field integral equation (EFIE) [28, 48, 116].

$$\boldsymbol{E}(\boldsymbol{r}) = \mathrm{j}k\eta_0 \int\limits_{S} \boldsymbol{J}(\boldsymbol{r}')G(\boldsymbol{r} - \boldsymbol{r}') + \frac{1}{k^2}\boldsymbol{\nabla}G(\boldsymbol{r} - \boldsymbol{r}')\boldsymbol{\nabla}' \cdot \boldsymbol{J}(\boldsymbol{r}')$$
$$+ \boldsymbol{M}(\boldsymbol{r}') \times \boldsymbol{\nabla}G(\boldsymbol{r} - \boldsymbol{r}')\,\mathrm{d}S', \quad (6.4)$$

where η_0 is the intrinsic impedance of free space, k is the wavenumber, G is the free-space Green's function, $\boldsymbol{r}'$ are the positions of the sources, S is the reconstruction surface and $\boldsymbol{r}$ is the position vector belonging to the measurement surface. $\boldsymbol{J}$ is needed if the problem is a half-space through the field equivalence principle and $\boldsymbol{J}$ and $\boldsymbol{M}$ are needed for arbitrary geometries on the surface of the DUT [238]. The magnetic currents will thus be omitted moving forward. One way to solve this problem using numerical solvers is with the method of moments where the surface and the currents are discretized and expanded on a set of basis functions. Using MoM the EFIE is represented on the following matrix form,

$$\boldsymbol{E} = \mathbf{N}\boldsymbol{J}, \quad (6.5)$$

where $\mathbf{N}$ is the moment matrix representing the relationship between the sources and fields. This representation is used in Paper IV and V. Ideally the sources can be found through minimization of,

$$|\boldsymbol{E} - \mathbf{N}\boldsymbol{J}|. \quad (6.6)$$
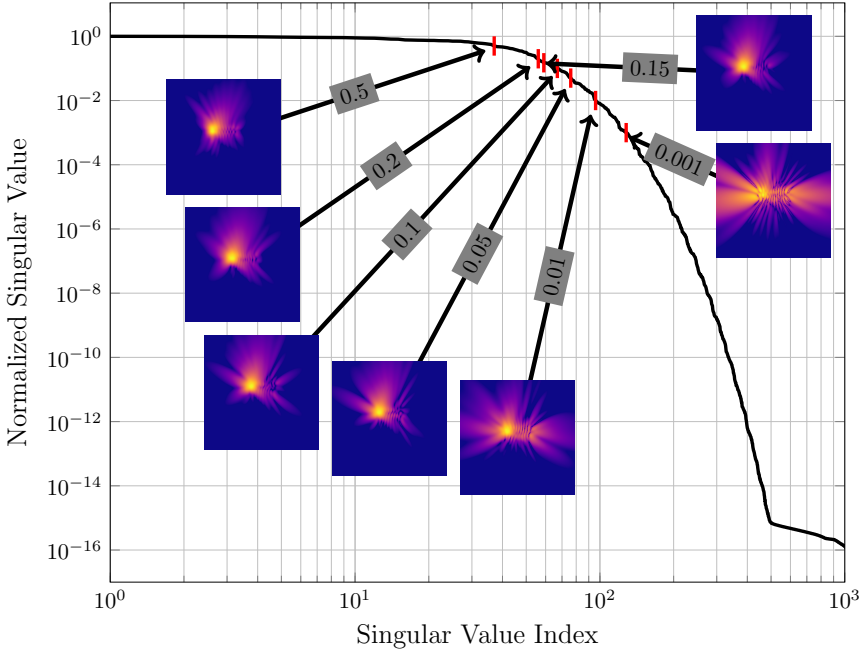
Figure 26: Normalized singular values of the moment matrix in a 28 GHz measurement case. Inset figures display power density reconstruction results for different choices of truncation, displayed in the gray boxes [155].

With the sources known, another moment matrix can be used to transform the equivalent sources to fields at another position in space.

However, the moment matrix can be ill-conditioned and non-invertible and techniques such as truncated singular value decomposition can regularize the problem [90, 94]. The singular values of the moment matrix, normalized to the maximal value, corresponding to a measurement of a 28 GHz mockup phone and reconstructed sources on the surface of the antenna is seen in Fig. 26. The inset figures display a reconstructed field image at a plane, different from the measurement and source plane, for varying values of truncation in the singular value decomposition (SVD). Typically, a truncation around the knee in the graph in Fig. 26 is a suitable choice [90]. This reconstruction of the electromagnetic field is presented in Paper V. Discretizing a surface and computing the equivalent sources in this manner is computationally heavy and is mostly done for smaller structures. When measuring large structures in the search for defects, an alternative method is used. The mapping between the electric fields and currents, (6.6) is valid for the scattered field. Assuming that the defects are few, the elements in $\boldsymbol{J}$ are mostly zero, a minimization technique with respect to some norm can be utilized instead [161]. This compressive sensing technique is well equipped to

find solutions in under-determined linear problems [43].

There are many measurement techniques for near-field measurements, and this section focused on VNA based measurements for inverse source and inverse scattering setups. There is a significant amount of post-processing and numerical handling of the input data in these techniques, and the development of these codes is time-consuming. The numerical implementation aside, the physical setup also has difficulties. For previous generation communication systems, and for the lower frequencies sub 6 GHz, one wavelength in free space is physically long. The errors in any positioning system must be put in relation to the electromagnetic wave. An uncertainty in 1 mm corresponds to $0.01\,\lambda$ at 3 GHz but $0.1\,\lambda$ at 30 GHz. This corresponds to a relative phase error of 4° and 36°, respectively. Not only is the wavelength shorter, but the distances to be measured are very close to the device, often only a few millimeters away. The reconstruction technique described above is sensitive to these spatial uncertainties. Knowing the position of the device under test, probe, and their relation is very important and challenging. Further, the measurement, much like for functional structures, uses a probe that is non-ideal and the closer one is when measuring one can expect more interaction between the probe and device.

7   Functional Structures in Near-Field Measurements

Measurements of the radiative near field for devices are important and not without problems, as described in the previous section. However, a theme of this thesis is the use of functional structures to solve electromagnetic problems. In this section, functional structures are combined with the measurement setups to assist in data retrieval. First, a functional structure aimed at addressing the probe calibration and positioning uncertainty is presented. Second, a metasurface, measuring using conversion between electromagnetic waves to thermal energy as an alternative measurement technique, is presented.

7.1   Aperture Calibration

One of the larger problems in near-field measurements, as mentioned in Sec. 6, is the positioning of the devices, both the radiating structure of interest and the probe. A well-defined physical position of each of the devices can be set with devices such as positioners and it requires higher precision with a robust setup to maintain a defined relative position. Even under the assumption that a perfect alignment and positioning is obtained, one cannot be sure of what the registered value of the probe corresponds to. The probe has a physical size and interacts with the electromagnetic field with some non-local interaction [138, 257, 258]. Does the registered complex voltage value correspond to the position of the aperture of the probe? Conceptually, we have a set of complex voltage values retrieved

at different unknown electrical positions but at known physical positions. The knowledge of an absolute positioning does not translate to an absolute positioning in the electromagnetic measurements without further information. The electrical and physical positions are offset. This is impactful when measuring close to the devices as any small shift is large relative to the wavelength and the assumed measurement distance, as described in Sec. 6.3.

Another problem might occur when the probe moves over the scanning surface, seen in Fig. 25. It is common for the cable connecting the probe to the VNA, or similar device, to have different bends at the different measurement positions. Turns and twists of the cable introduce phase shifts on the measured signal, which then will vary over the measurement plane. This is measurement setup specific and not dealt with using standard probe calibration techniques.

Similar to measurements of functional structures, it is good to have a reference measurement reducing the impact of the environment. In measurements of functional structures, Sec. 6, they consist of an empty setup in transmission or reference metal surface for reflection. Any specifics of the measurement setup will be included, cable bending, *etc.* We want to construct a reference object for near-field measurements that simultaneously calibrates the probe and the setup.

A reference measurement will in this context be a measurement providing a probe calibration. This is obtained by measuring the field distribution of a well-known source to understand how the receiving probe's radiation pattern impacts. Several techniques can be employed to use the measured data of the well-known device. For instance, the measured data can be compared with simulated data through matching coefficients of expansions using spherical waves or a point-wise investigation, where each measurement point is calibrated separately. The latter is simpler and a lower order correction and the first requires more post-processing. Any technique can be used and matters little for the design of the functional structure. The main idea is that the reference measurement for the specific measurement setup should be simple and robust.

To capture the details of the measurement setup, the reference measurement should be done in conjunction with the measurement of the device under test, similar to other reference measurements. The problem of accurate physical positioning remains, but the device under test's position and phase of the wave will be put in relation to the reference measurement's well-known object's position and phase. Conceptually, one obtains a map between the physical and electrical positions and removes a large uncertainty. The measurements will have a common frame of reference.

Ideally, the reference object should be a point source with a simple radiation pattern, as it serves as the origin of the new reference frame. The general strokes of the technique are that first the reference object is measured over a plane some well-defined distance away. The simple radiation pattern of the object is simulated, in our case with the method of moments and compared with the measured field, in both amplitude and phase.
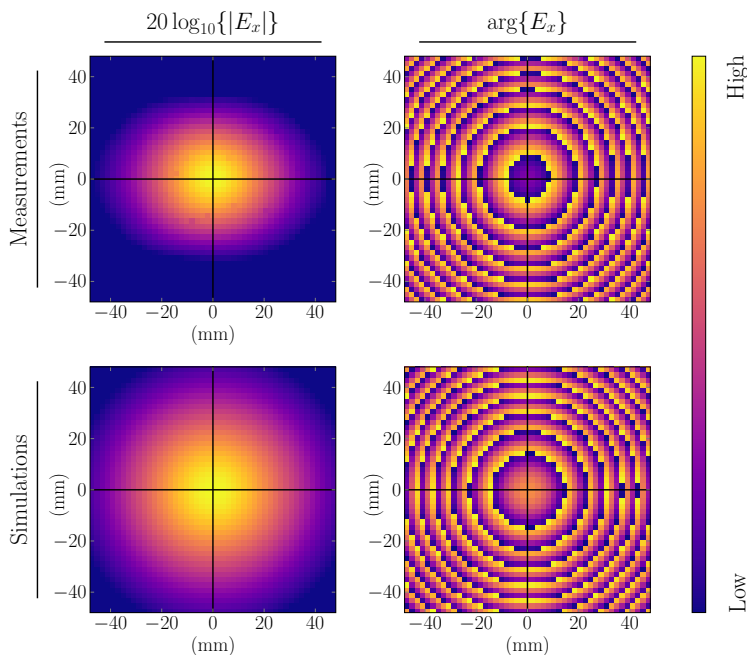
Figure 27: Measurement and simulation of the electric field from the aperture, in the aperture correction technique, in both amplitude and phase.

In Fig. 27 the simulations and measurements of the electric field of a reference object are displayed in amplitude and phase for a plane $\approx 6\,\text{cm}$ away at $28\,\text{GHz}$. As expected from a rectangular open-ended waveguide it does not have equal performance in the top-bottom direction as the left-right direction. This is corrected using the simulated values and altering the value of each measurement point with a computed prefactor, similar is done for the phase. This phase correction part of the calibration anchors the reference systems and creates a measurement-specific calibration.

A correction, or probe calibration, is obtained where the probe's impact is accounted for and a well-defined electrical position becomes known. The next step in the measurement procedure is to remove the reference object and position the device under test at the same position as the reference point and a new measurement is initialized. The measured field of the device is corrected using the probe correction information from the previous measurement. The equivalent currents on the device under test can be computed, see Sec. 6.3, and the field reconstructed at other surfaces of interest [48, 63, 133].

For the functional structure to fit the needs, it should have a simple radiation pattern and transmit enough power to avoid signal-to-noise issues in the receiver. A candidate can be obtained from the functional structure presented in Sec. 3
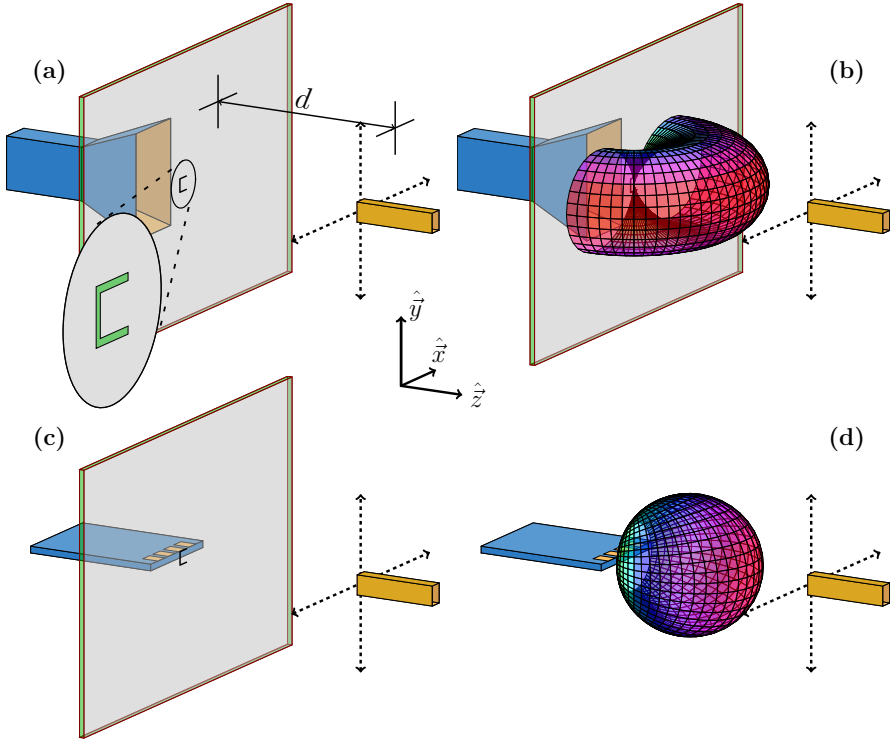
Figure 28: Schematic of the measurement procedure. (a): A receiving probe is situated in the center of a planar measurement surface, a distance d away from a small aperture in a finite metallic plane. A transmitting antenna is positioned on the other side of the metallic plane. A high-gain broadside antenna is preferable to ensure sufficient power flow through the aperture, although in theory, nothing prohibits the usage of the DUT itself. (b): The transmitting antenna excites the aperture which then radiates as a dipole. The reference measurement is conducted by sampling the fields in a discretized grid across the measurement surface using the receiving probe. (c): The transmitting antenna is removed, and the DUT is aligned with respect to the previous position of the aperture. (d): A second measurement is conducted on the DUT, and the field is sampled in the same grid as before [156].

Fig. 8, with Babinet's principle [32]. That structure dealt with extra-ordinary transmission, but a single element in that functional structure radiates with a dipole pattern resonant for some frequency, ensuring a high transmission given the cut-out area. Given a large enough metal sheet with a small aperture, any illuminating antenna can be placed behind as the radiation characteristics will be that of the aperture and not the illuminating antenna [114]. A schematic of the measurements using this aperture is seen in Fig. 28 and it follows the steps outlined above.

With this aperture structure, we simultaneously calibrate the impact of the probe and solve the issue of positioning. We may call this a measurement setup calibration. The technique is explored in Paper V for $28\,\mathrm{GHz}$ and $60\,\mathrm{GHz}$. The devices measured were: a mockup phone, 4×4 patch array antenna, and a standard gain horn antenna. A comparison between reconstructed field data from measurements and simulations for the mockup phone is seen in Fig. 29. In (a), the top side of the phone mockup is displayed, and in (b), the front. The measurements were done at $28\,\mathrm{GHz}$ and measured $6\,\lambda$ away from the device, sampled on $3/4\,\lambda$ uniform grid. The fields were reconstructed on planes 5, 10, and $20\,\mathrm{mm}$ away from the device using the technique described in Sec. 6. The technique captures the features of the fields with very accurate positioning.

7.2   Infrared Based Measurement Technique

The aperture calibration presented in the previous section and Paper V helps solve some difficulties of near-field measurements with electromagnetic methods. The measurements presented so far measure the voltage waves and can be seen as a direct measurement of the electromagnetic field. Many methods exist and are well developed, but the question of positioning and probe calibration is present to some extent. We wish to develop an alternative measuring technique addressing some shortcomings of direct electromagnetic methods and carry out the measurements in a new way. When we measure with probes, the non-local interaction [138, 257, 258] must be dealt with and the functional structure in the previous section assisted with this. However, instead of assisting through means of calibration, we can create a structure on which the measurement itself takes place [154]. Instead of looking solely at electromagnetics, the phenomena can be looked at from a larger perspective.

As introduced in Sec. 2.3, (2.50), electromagnetic energy gets absorbed and scattered when interacting with objects. The absorbed energy will be converted to heat through the movement of electrons [114]. This is well understood, and the regulations given by ICNIRP, Sec. 6 Table 1, consider health effects to occur if the temperature of the tissue is increased above a certain threshold [109]. The idea of using temperature to assess and view electromagnetic fields is thus well in line with the general understanding. However, temperature itself is seldom used but is the purpose of this subsection. The heat generated in absorption will generate infrared photons that radiate from the heated object and can be
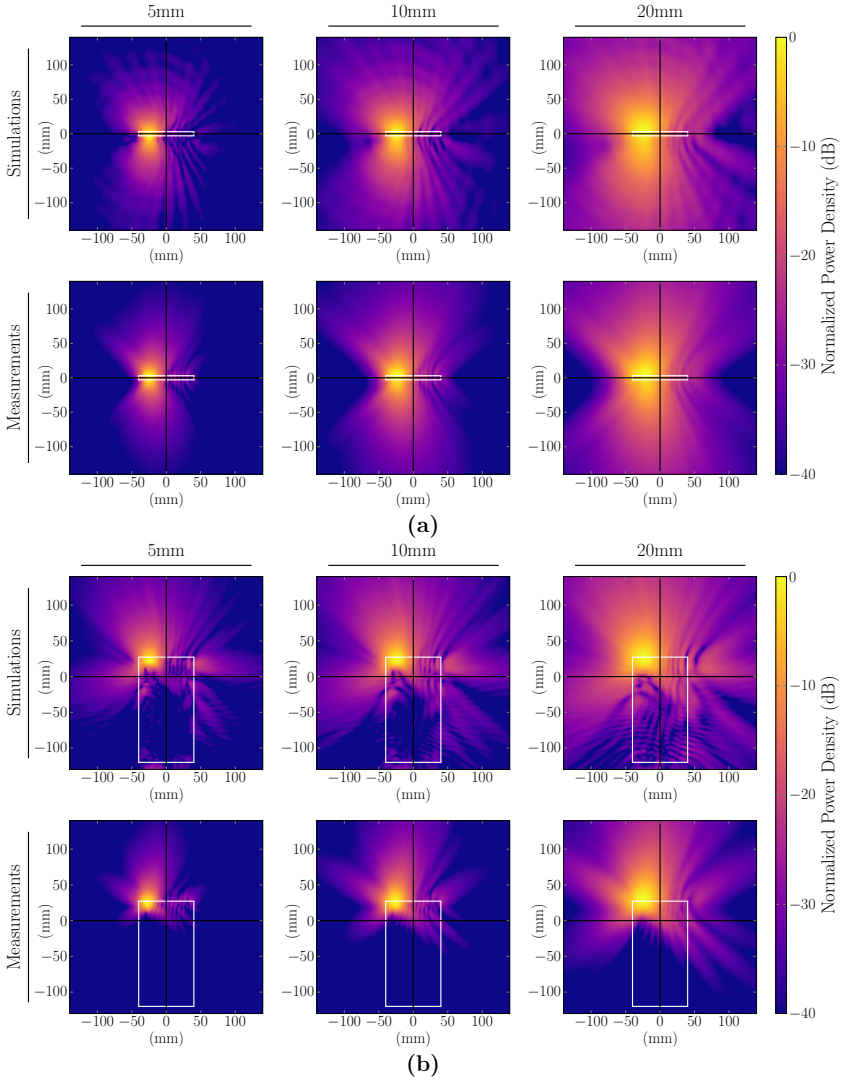
Figure 29: Normalized power density at 28 GHz in, from measurements, reconstructed planes distanced 5 mm, 10 mm, and 20 mm (left to right) for a Sony Mobile phone mockup. Two planes **(a)**, and **(b)**, corresponding to the front and top of the phone were measured. The white lines depict the outline of the DUT, and the black crosshair marks the mutual origin. The rows depict: full-wave simulations of the DUT in FEKO (top), and the results of the measurement data as input to the reconstruction technique (bottom). The dynamic range of all plots is 40 dB [156].

detected with an infrared camera [15, 38, 85, 135, 136, 174, 177]. Thus one can image the electromagnetic field through the temperature distribution of another object. This is an indirect measurement of the electromagnetic field.

With this concept, the signal strength corresponds to the number of infrared photons collected by the camera, which is related to the temperature of the object and in turn the absorbed energy. Arguably the most simple implementation of such a functional structure is an electromagnetic absorber, traditionally sheets of material designed to absorb radiation over large frequency intervals. Indeed, this has been demonstrated, in for instance [38], but for high-power density levels, several orders of magnitude higher than the power density levels of handheld communication devices and their guideline restrictions, Table 1 [109]. There are other works using homogeneous sheets, such as resistive sheets of polyimide film *etc.*, that have provided measurements for power density levels around $27 - 220 \, \mathrm{mW/cm^2}$ for frequencies around 2–95 GHz [85, 174, 175, 177, 193].

homogeneous sheets have favorable electrical properties to absorb incident electromagnetic waves. The drawback is that these favorable electrical properties often exhibit unfavorable thermal properties. The connection between thermal and electric conductivity in a metal can be described by the Wiedemann–Franz law [128],

$$\frac{\kappa}{\sigma} = LT, \tag{7.1}$$

where κ is the thermal conductivity, σ is the electrical conductivity, L is a constant (the Lorenz number), and T is the temperature of the object. This demonstrates that metal of good electrical conductivity also conduct heat well. This simple relation is not valid for semiconductors where the relationship is more complicated [122, 255].

The drawback of homogeneous sheets is that heat can be generated and spread over the entire surface of the absorbers which consequently cools off from interactions with the surrounding environment. Moreover, since heating occurs over the entire homogeneous sheet, a lot of mass is heated resulting in a lower temperature increase and fewer infrared photons to detect. High power densities are needed in order to detect a temperature change. Many everyday communication devices do not operate using these high power densities and we are instead interested in measuring power levels at, and below, the guidelines presented in Table 1, as this is the region where many devices in the near future will operate. The sheets needs improvement for our purpose.

To further understand the problem and to identify areas of improvement, we consider a thin two-dimensional sheet of thickness d. The equation governing the thermal part of the problem is the heat equation [102],

$$\frac{\partial u}{\partial t} = \frac{P(t)}{c_{\mathrm{p}}\rho} f(\boldsymbol{r}) + \frac{k}{c_{\mathrm{p}}\rho}\nabla^2 u + \frac{2h}{c_{\mathrm{p}}\rho d}(T_0 - u) + \frac{2\varepsilon\sigma}{c_{\mathrm{p}}\rho d}(T_0^4 - u^4), \tag{7.2}$$

where $u(\boldsymbol{r}, t)$ is the temperature in the sheet at position $\boldsymbol{r} = (x, y)$ and time t, $P(t)$ is the radiated power incident on the structure, c_{p} is the specific heat capacity at constant pressure, ρ is the density of the material, k is the thermal

conductivity, ε is the emissivity of the object, σ is Stefan-Boltzmann's constant, and T_0 is the background temperature[2] [102]. The different terms correspond to sources, convection and conduction. The term which should be maximized is the amount of generated infrared photons while keeping the other terms low. These radiative losses are represented by the last term in the equation (T^4). Improvements to the structures can be made by restricting the heating to a localized region of low mass. A reduction of total heated mass is preferable as the number of detectable photons depends on the temperature, which depends on the incident energy and total mass. In a work done at $605\,\mathrm{GHz}$, small dielectric cylinders repeated in a periodic fashion were used to measure a power density of $4.4\,\mathrm{mW/cm^2}$ [72]. The heat generation was in this instance localized to the cylinders. Furthermore, it is important that the structure has a low specific heat capacity and thermal conductivity. This is not the case with a homogeneous sheet, the electromagnetic and thermal properties must be divided and dealt with separately. A metasurface with periodically repeated elements, designed to absorb and re-radiate power through infrared photons, is an interesting idea.

Previous techniques have not measured at low power density levels, sub $1\,\mathrm{mW/cm^2}$, and thus we need to make sure that the elements' interaction with the electromagnetic field is increased [135]. A metasurface consisting of periodically repeated elements, for instance, small resonant antennas loaded with resistors is a possible solution. These elements are placed on a sheet with low thermal conduction and specific heat capacity to isolate the elements from each other thermally. Previous techniques covered one of these aspects, whereas this technique separates the problem electromagnetically and thermally. Heat is not distributed over a large surface but localized. Each element can be considered as a pixel in a traditional camera that interacts with a region on the order of λ surrounding the element, spaced the order of $\lambda/2$ [219]. This kind of metasurface was constructed and measured in Paper VI.

The properties of the metasurface can be viewed initially through the absorptance and reflectance of a resistive sheet. Modeled as a resistive sheet with resistance R, the reflectance and transmittance can be written as [238],

$$\mathcal{R} = \frac{1}{(2R/\eta_\mathrm{T} + 1)^2}, \tag{7.3}$$

$$\mathcal{A} = \frac{4R/\eta_\mathrm{T}}{(2R/\eta_\mathrm{T} + 1)^2}, \tag{7.4}$$

where η_T is the transverse wave impedance. These relations are illustrated in Fig. 30 for normal incidence where the transmittance $\mathcal{T}$ is obtained from power conservation, $\mathcal{R} + \mathcal{A} + \mathcal{T} = 1$. The dashed line show the relations presented in (7.3)–(7.4) and the solid line results from a simulated design in COMSOL. There is a trade-off to consider, maximal signal strength comes with $25\,\%$ reflectance. Depending on the measurement scenario, reflected waves can be im-

---

[2]The notation here follows that of heat transfer [102] which regrettably has some overlap to electromagnetic notation.
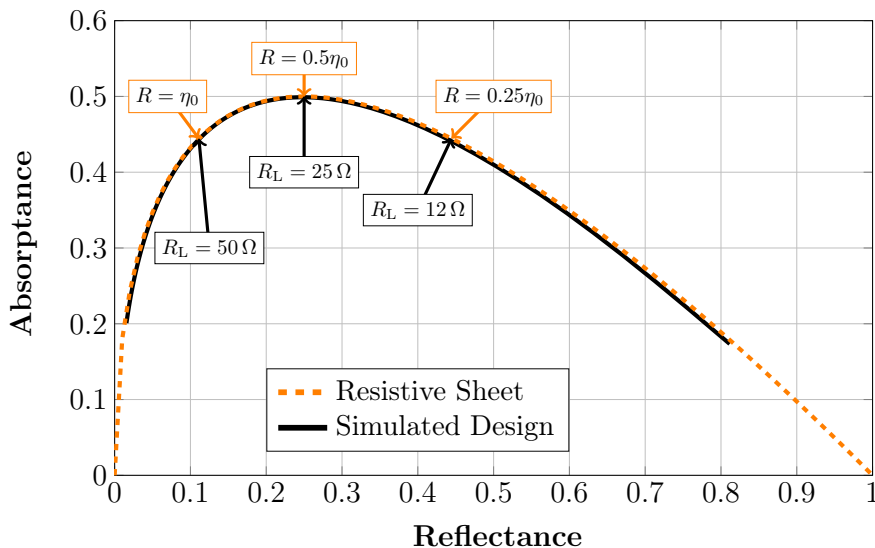
Figure 30: Relationship between reflectance and absorptance for a resistive sheet, dashed, and simulated design, solid. The solid curve was generated by changing the load resistance, R_L, of a tuned design [154].

portant as they will interact with the radiating device under test. The values on this curve can be obtained by altering the value of the load resistor [238].

Measuring with this metasurface is summarized with Fig. 31. A device of interest (a) is placed near the metasurface sensor (b) and in front of the infrared camera (c). The device of interest transmits a signal (d). The radiation impinges on the sensor which absorbs part of the energy and becomes warmer, seen by the infrared image (e). The camera detects the heating and generates an output signal (f) used to retrieve information of the electromagnetic field (g).

In contrast to direct electromagnetic measurements with a moving probe, we can now image a surface at a given position with responses in real-time with no numerical reconstruction of the fields. The measurement technique differs significantly from direct measurements and there are new challenges as we measure a dynamic system.

In previous work, there are two major measurement techniques to measure the heat distribution. The first technique is to let the device under test radiate continuously. The metasurface will heat up and reach thermal equilibrium [177]. A drawback is that this takes time and thermal conduction will be important as well as the environment, airflow, and camera type [14]. Detecting a small temperate increase corresponding to the low power density levels of a consumer device is difficult with large fluctuations in the background temperature.

The second technique is to use modulation, such as on/off modulation or sinusoidal modulation [14, 15, 135]. Modulating the signal periodically comes
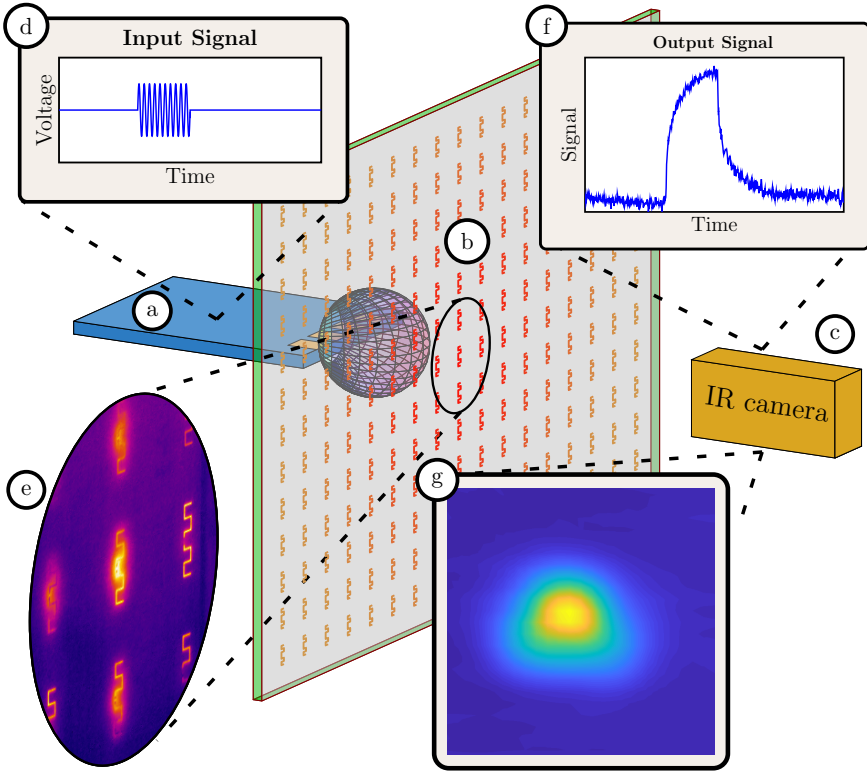
Figure 31: An illustration of a measurement using the metasurface sensor composed of an array of a radiating device (a), thermally isolated elements (b), IR camera (c), the input signal (d), IR image of the metasurface (e), temporal evolution (f), and the resulting image of the field (g) [154].

with benefits and drawbacks. On the one hand, and the primary reason for modulation, is that the impact of thermal conduction is diminished and depends on the modulation signal period length [14]. However, with short periods the temperature increase of the element is smaller, and signal strength is sacrificed. In Paper VI we constructed a metasurface and measured in a multitude of variations where we found that the use of on/off modulation improved the sensitivity.

The response from an element subject to an on/off modulated signal can be approximated from linearization of (7.2) to be an exponential,

$$T(t) \propto \begin{cases} 1 - \mathrm{e}^{-t/\tau_\mathrm{r}} & 0 < t \le t_0, \\ \mathrm{e}^{-(t-t_0)/\tau_\mathrm{f}}\left(1 - \mathrm{e}^{-t_0/\tau_\mathrm{r}}\right) & t > t_0. \end{cases} \tag{7.5}$$

Here, $\tau_\mathrm{r,f}$ are the characteristic rise and fall times of the system and the signal is on from $t = 0$ to $t = t_0$. A typical measurement consists of measuring several
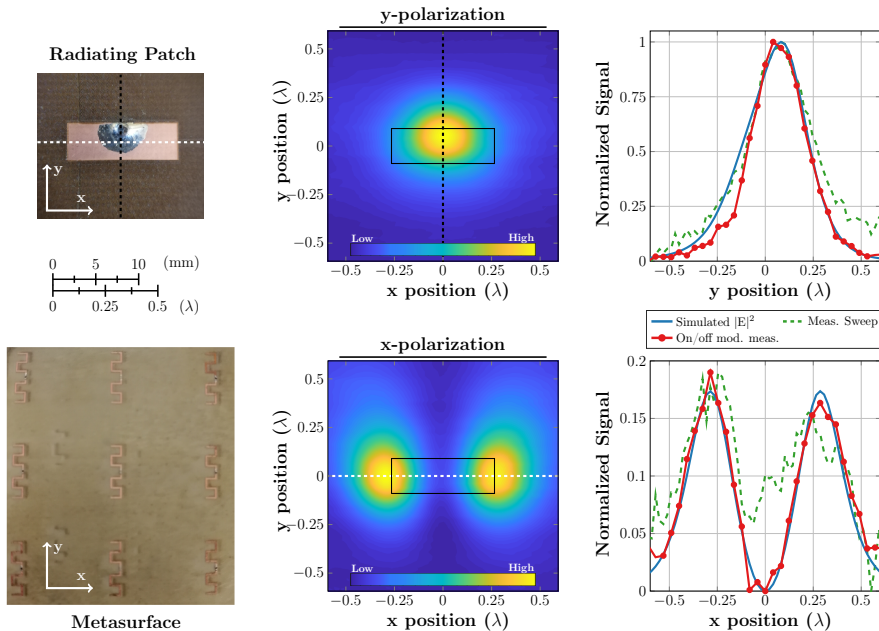
Figure 32: The metasurface and radiating patch to scale (left column). Temperature increase for a continuous scan in a plane 5 mm away from the radiating device in both x (cross) and y (co) polarization (center column). The output signal along the dashed lines for on/off modulation, continuous sweep, and simulation (right column) [154].

periods to average out system noise. The temperature increase corresponds to the incident power density on the element in the sheet. A value of power density is obtained from each element and an image of the field can be constructed representing the fields from the radiated device. In paper VI we use this technique to measure power density levels in the range of 10^{-2}–10^1 mW/cm^2, levels much lower than previous techniques and guidelines. The metasurface and measurement results are seen in Fig. 32 where a custom-made patch antenna was measured over a plane $\lambda/5$ away using both continuous measurement techniques and on/off modulation for varying incident power densities. In the lower left image we see the metasurface consisting of meanderlines loaded with a resistor in the center. The top-left image display the measured device, a planar patch antenna polarized in y-direction but with significant cross polarization (x-direction). The center image display the measured signal over the measurement plane and the right column display measurements along the dashed lines for input power of 0.6 mW corresponding to a power density measurement of 0.05–0.5 mW/cm^2. More details are found in Paper VI.

8   Controlling Light Propagation Through Random Media

In this thesis, electromagnetic waves are controlled by functional structures to reach very specific goals and responses. Moreover, the near field from radiating objects is measured. These devices are often constructed according to a pre-defined performance. However, not everything is as structured and controlled as this. Until this point, the waves have propagated through simple media with little interference; the inside and surface of functional structures aside. This section deals with, in one regard, the opposite situation, wave propagation in a medium filled with randomly placed objects such that incident light loses directionality after propagating some distance in this medium. Media where the material properties, ϵ_r and μ_r, are not known at each point, but rather the statistical properties of the medium, are called random media [110, 167]. Similar to electromagnetic scattering problems and NDT testing, there might be regions within the media that are of higher interest than the rest. A measurement of an embedded object now faces an additional problem. How can we get sufficient energy to the region, and how can we get it out? Focusing the electromagnetic field through a random medium, and into regions of interest, is of interest in several application areas, and here we focus on the medical environment.

One aspect used in medical applications is the oxygenation of tissue. Cells need oxygen to live and oxygenation can be a sign if the tissue is affected by ischemia [247]. Oxygenation can also help detect the presence of blood and thus investigate hemorrhages. Electromagnetic measurements enter the picture through the different electromagnetic responses of oxygenated and deoxygenated blood cells. The absorption of hemoglobin, which carries oxygen in our blood, differs depending on wavelength and if it has oxygen or not. This is shown in Fig. 33, where the absorption factor is displayed [112]. In the region, known as the near infrared window, wavelength $600 - 700\,\mathrm{nm}$, there is a large difference between oxygenated (red) and deoxygenated (blue). Tissue illuminated by an electromagnetic wave of a wavelength in this window could probe and detect differences in oxygenation.

Using light to probe tissue is, unlike an alternative approach, biopsy, a non-intrusive technique, and it is of interest to use this technique deep within tissue [81, 87, 178]. However, even an incident laser beam quickly loses its focus and scatters throughout the tissue. Illuminating further than millimeters is challenging. The focus of this section is to develop a numerical tool that can simulate wave propagation deep within tissue such that different approaches of focusing into the highly scattering environment can be investigated [26, 202, 248]. Before venturing into the numerical description, we shall describe an experimental setup. The details of the experimental measurement technique, albeit interesting, are outside the scope of the thesis and are presented solely to understand the simulation problem it develops into [22].
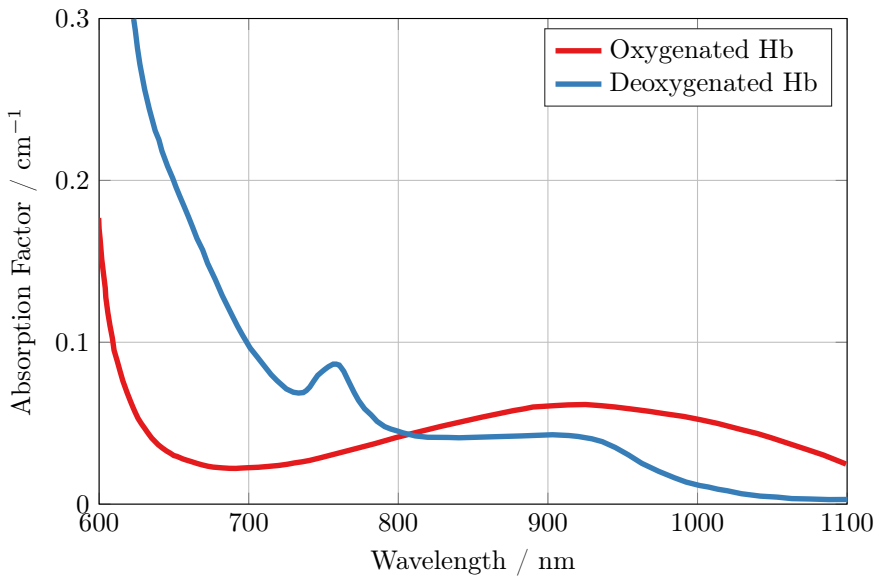
Figure 33: The absorption factor of oxygenated (red) and deoxygenated (blue) hemoglobin for wavelengths around the visible spectrum. Based on data from [112].

A simple approach to probe tissue is to attach a laser transmitter on one side of the tissue and a receiver on the opposite side, as displayed in the left of Fig. 34. The scenario is shown for a 2D slab where light propagates from the sources on the left side towards the receiver on the right. The receiver will collect photons, in this case with some frequency and intensity spread corresponding to the laser specifications. A small region of interest is marked by a circle and is positioned within the medium. In the left illustration, we see the magnitude of the Poynting vector, further called total power flow, for a beam incident on the scattering medium. The boundary between the scattering medium and free space is marked by the black line.

At the receiver, the collected photons could have taken any path through this medium and have not necessarily taken the path through the region of interest. Optical imaging at depths greater than a few millimeters is thus very difficult. However, over the last decades a technique to circumvent this issue is to mark, or tag, the photons passing through the region of interest using ultrasound. The technique is known as ultrasound-modulated optical tomography (UOT) and uses the acousto-optic effect to modulate the frequency of the light by the frequency of the ultrasound [37]. The ultrasound causes vibrations in the media, with the same frequency as the modulation frequency of the ultrasound, and a photon interacting with this vibrating media will gain or lose momentum corresponding to the ultrasound frequency. By creating an ultrasound beam with a focus on

the region of interest, displayed in the center of Fig. 34, some of the photons will be frequency modulated [98]. This is shown in the center column of Fig. 34 by the small bumps on the photon distribution. These modulated photons have become tagged and are likely from the ultrasound focus in the region of interest. The incident electromagnetic wave is of frequency on the order of 10^{14} Hz and the ultrasound modulation on the order of 10^6 Hz, which makes them hard to filter out. Furthermore, the situation is not made easier by the fact that the ratio between tagged photons to the total number of photons is around $10^{-3} - 10^{-4}$ [245]. Different techniques exist to extract only the tagged photons. Self-adaptive wavefront holography is one technique that has response times around 1 ms which is too slow for imaging in vivo [245], in which fluids and tissue are constantly in motion [145].

Another technique is to use extremely narrowband filters, rare-earth-doped crystals prepared through spectral hole burning [245]. In short, the rare-earth-doped crystals allow certain atomic transitions, corresponding to certain frequencies of light. A spectral hole is burned by a spectrally narrow laser saturating the line absorption. For a very narrow frequency band, there is a transparency window in the absorption spectrum. Through Kramer-Kronig relation we can see that this rapid change of behavior in absorption results in a narrow frequency region where the propagation speed of light is very slow, orders of magnitude slower than free space [149]. A name for these filters is thus slow-light filters and can be constructed with different doped crystals depending on which frequency the laser operates at [245].

The information obtained from a measurement is given by the tagged photons. An improvement of the measurement is easy to identify as the majority of the photons do not even reach the region of interest. By controlling the light and focusing the photons towards the region of interest less energy will be scattered through the tissue and the signal will increase, as illustrated in the right column of Fig. 34 where the optimal signal is displayed. We can visually see more power flow in the region of interest and the bumps on the photon distribution have become larger. This is the problem we focus on, controlling the incident light to focus into tissue, through tissue, and how to simulate it. This is a brief summary of the major parts of the technique used and we shall now discuss simulations and problems to solve in those settings. Other electromagnetic imaging techniques for medical applications exist but are not described, see [26, 87, 202, 248] for further information. The results and cases in this section are summarized examples of possible scenarios where the simulation model can be used. There are many more investigations and comparisons which has been done in this work with several other interesting scenarios to investigate in the future. This work is ongoing research in a larger collaborative work with other research groups. The simulation model developed in this section can be used to investigate different experimental approaches and techniques in this collaborative project.
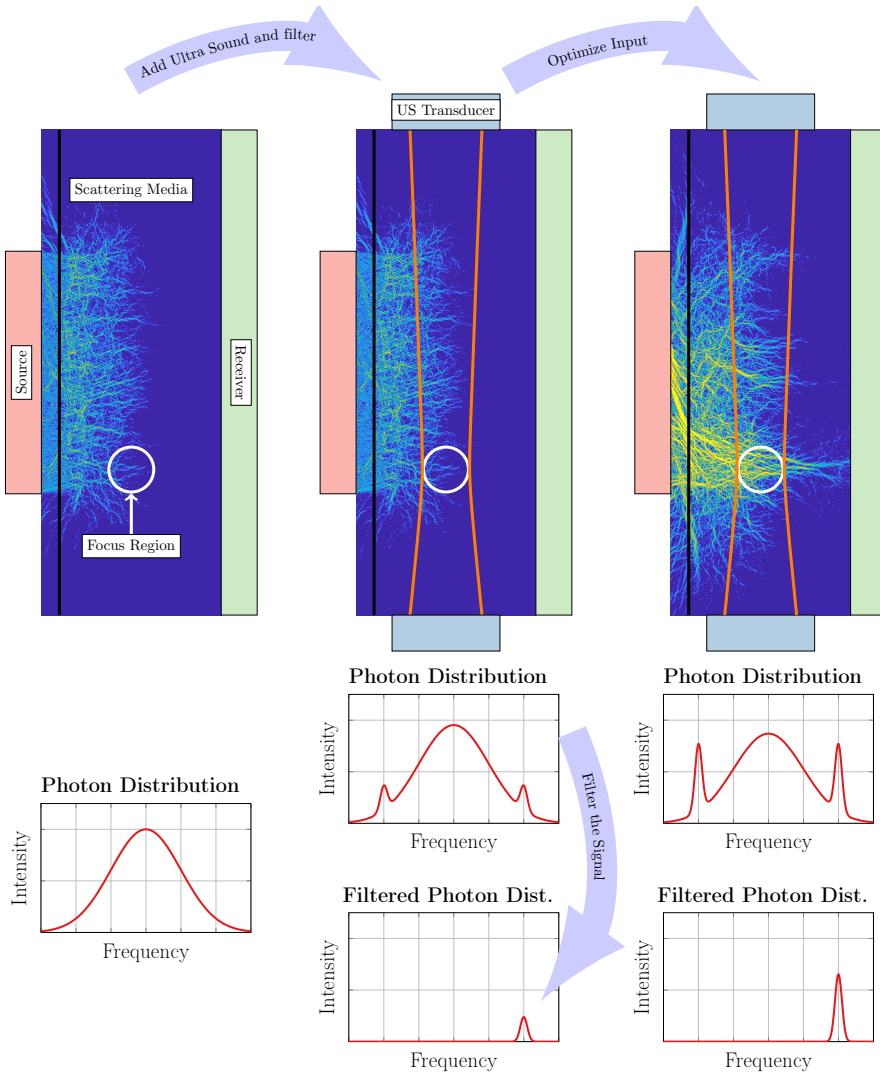
Figure 34: A beam incident on a scattering media with a receiver on the opposite side detecting photons from the incident photon distribution (left). Ultrasound is added to modulate the photons, with a focus point within the region interest (white circle). The modulated photons are extracted with a filter on the receiver side (center). The number of photons from the regions of interest is increased by optimizing the input signal (right).
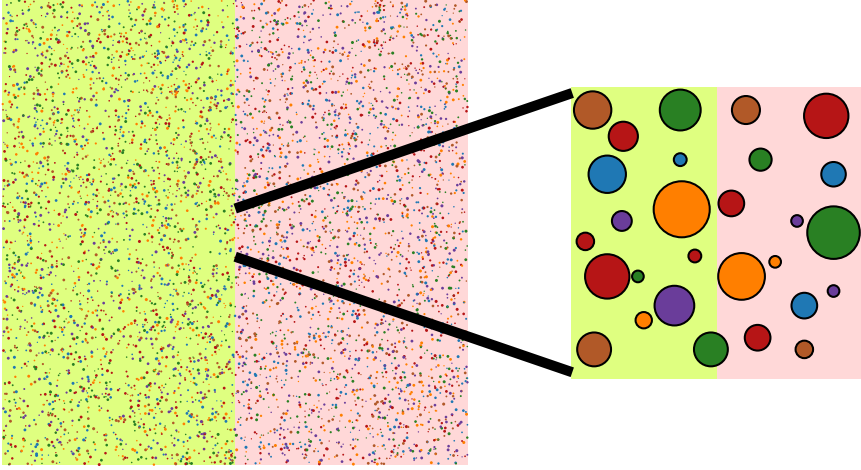
Figure 35: Illustration of a medium with two background properties (yellow and pink) filled with scatterers of various sizes and properties indicated by the colors.

8.1   Simulation Types

Focusing and controlling light through millimeters up to several centimeters, $\approx 5\,000 - 150\,000\,\lambda$, into tissue corresponds to a massive simulation region. Tissue is a complicated medium, oversimplified in the illustration in Fig. 35. The illustration shows several objects of varying sizes and properties, illustrated by the different colored circles, in different background media. This problem deals with multiple scattering on a mesoscopic scale and in these situations, the important quantities are typically the scattering and transport mean free path [205]. Even though the medium is complicated, it is in practice described with only a few parameters, mainly one for absorption and one for scattering [56]. In experimental setups, a mapping between the input and output sources is described by the transmission/scattering matrix [205]. Due to the randomness of the media placed between input and output, one can use the statistical models of random matrix theory [230] to investigate the properties of the transmission/scattering matrices, such as open and closed channels, eigenvalue distributions, Hankel distribution, semi-circular law, enhancement of focusing, *etc.*

Returning to modeling, the objects can be viewed as randomly placed and light propagating through can be modeled as a random walk process. A technique to model this is Monte Carlo type simulations based on radiative transport theory [73]. A number of photon packets are initialized and interact with scatterers through a random process. However, as mentioned in Sec. 4, this technique only provides intensity and hence no phase information. Focusing through the same realization in Monte Carlo is difficult.

With further assumptions on the governing equations, one can, from radiative

transport theory, obtain the diffusion model [110]. Diffusion of light hold under specific conditions and cannot describe focusing of light as the medium of scatterers is replaced with a homogeneous medium with diffusion properties. These techniques are commonly used to describe attenuation and absorption in media but are not suitable for the case in this work of focusing through and into media.

Instead, we turn to full-wave type solvers and specifically FDTD and method of moments (MoM), introduced in Sec. 4. The FDTD technique is limited to smaller samples as the entire volume is discretized and, typically on the order of $10 - 100 \, \lambda$ for a 2D scenario, and smaller for 3D. Other techniques include solving a scalar wave equation in 2D with variations in permittivity throughout the medium using recursive Green's method [17, 259] with similar computational domain sizes as FDTD.

Even though simulations are carried out in 2D, the presented techniques in full-wave solvers handle regions orders of magnitude smaller than the intended case. One way to handle larger regions is to simulate using solvers which do not discretize the space as this will help conserve memory. One approach is the previously presented MoM technique. Very large regions can be simulated and the complexity lies in the size of the scatterers, discretization, and the number of basis functions used. For a collection of scatterers and the incident field, combined with boundary equations and coupling between all scatterers, gives the currents on each of the scatterers, which results in a scattered field.

The tissue-like media is complicated as seen in Fig. 35, but we also remember that it is often only described in a measurement setting using two parameters. Instead of having multiple different sizes and objects, we can idealize it to a single background material and objects of similar size. This is not an identical configuration to reality but they possibly describe the same effective scattering scenario. The strength of the scatterers and their density will determine the scattering behavior in the region. The goal of the full-wave solver is large physical dimensions and with significant attenuation through scattering. It is thus important that many scatterers can be included and described as simply as possible for memory purposes. In a three-dimensional setting, they can be small cylinders of length l and radius a. The scattering cross section (2.52) for a metal cylinder described with one triangular basis function is seen in Fig. 36 and an equivalent simulation in FEKO in red. A finer meshed structure yields a different result but it can be viewed as a calibration issue as the scattering is the interesting phenomenon. Why should the objects be cylinders, can they not be small dielectric spheres? The scattering cross section of a small dielectric sphere of radius a in free space is,

$$\sigma_{\mathrm{s}} = \frac{8\pi k^4 a^6}{3} \left(\left| \frac{\mu_{\mathrm{r}} - 1}{\mu_{\mathrm{r}} + 2} \right|^2 + \left| \frac{\epsilon_{\mathrm{r}} - 1}{\epsilon_{\mathrm{r}} + 2} \right|^2 \right), \tag{8.1}$$

in the Rayleigh limit [133]. Large values of scattering are obtained as $\epsilon_{\mathrm{r}} \simeq -2$ which corresponds to plasmonic scatterers [157]. However, instead of trying to find the geometry of the scatterers, and the material parameters we describe the scatterers based on their scattering performance, scattering cross section. With
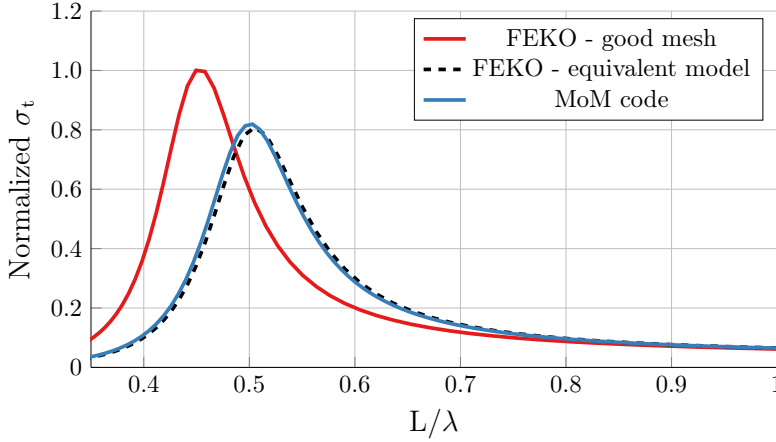
Figure 36: Two figures showing the scattering cross section for a metal cylinder in 3D. The blue line corresponds to a custom MoM code and the dashed line is the same object simulated in the commercial solver FEKO. The solid red line corresponds to a simulation of the cylinder with a finer mesh.

no information on attainability or feasibility we can describe the maximal scattering behavior of a point scatterer. This mindset is the basis of the computational toolbox of this section.

8.1.1   Implementation

In the scattering problem, there will be an incident field and multiple scatterers which react to this field and radiate a scattered field. As seen in Sec. 2.2, the equations for an environment of sources differ from the source-free case. The scalar and vector potential were introduced to describe the fields from radiating sources (2.40). It is also common to describe radiating sources using the electric fields, through the 'curl curl' equation, obtained from the rotation and combination of (2.21)–(2.22) [80, 133],

$$\boldsymbol{\nabla} \times (\boldsymbol{\nabla} \times \boldsymbol{E}) - k^2 \boldsymbol{E} = -\mathrm{j}\omega\mu\boldsymbol{J}. \tag{8.2}$$

The general solution is written in terms of the Green's function or the Green's dyadic, in a 3D homogeneous medium,

$$G(\boldsymbol{r}, \boldsymbol{r}') = \frac{\mathrm{e}^{-\mathrm{j}k|\boldsymbol{r}-\boldsymbol{r}'|}}{4\pi|\boldsymbol{r}-\boldsymbol{r}'|}, \tag{8.3}$$

$$\mathbf{G}(\boldsymbol{r}, \boldsymbol{r}') = \left(\mathbf{I}_3 + \frac{\boldsymbol{\nabla}\boldsymbol{\nabla}}{k^2}\right) \frac{\mathrm{e}^{-\mathrm{j}k|\boldsymbol{r}-\boldsymbol{r}'|}}{4\pi|\boldsymbol{r}-\boldsymbol{r}'|}, \tag{8.4}$$

where $\mathbf{I}_3$ is the identity dyadic. In the method of moments, the boundary condition on the scatterers relate the incoming and scattered fields yielding the

Figure 37: An incident wave impinges on a small scatterer generating a scattered field.

relation,

$$\hat{\boldsymbol{n}} \times \boldsymbol{E}_\mathrm{i}(\boldsymbol{r}) = \mathrm{j}k\eta_0 \hat{\boldsymbol{n}} \times \int\limits_{S} \boldsymbol{G}(\boldsymbol{r}, \boldsymbol{r}') \cdot \boldsymbol{J}(\boldsymbol{r}') \,\mathrm{d}s'. \tag{8.5}$$

The scattering of an object can be described by the scattering cross section, which for non-absorbing scatterers equals the extinction cross section and can be expressed through the optical theorem as (2.52),

$$\sigma = -\frac{4\pi}{k}\mathrm{Im}\left\{\frac{\boldsymbol{E}_\mathrm{i}^* \cdot \boldsymbol{F}(\hat{\boldsymbol{k}}_\mathrm{i})}{|\boldsymbol{E}_\mathrm{i}|^2}\right\}. \tag{8.6}$$

Instead of writing the integral formulation (8.5), we consider the scenario illustrated in Fig. 37. In most simulations presented in this work, we consider a 2D structure. The waves are either transverse electric (TE) or transverse magnetic (TM) and to simplify the notation we consider the waves to be scalar. In a 3D setting, scalar waves are also used. There is no limitation in the implementation and vector waves can be implemented. In this work, the waves are governed by the scalar wave equation in free space,

$$\nabla^2 E + k^2 E = 0. \tag{8.7}$$

An incident wave, from a source, or another scatterer, impinges on the scatterer of interest. The scatterer is small and the incident wave is locally plane. The relation between the incident and scattered field is given by,

$$E_\mathrm{s}(\boldsymbol{r}) = \tau E_\mathrm{i}(\boldsymbol{r}_s)G(\boldsymbol{r}, \boldsymbol{r}_s), \tag{8.8}$$

where $\boldsymbol{r}_s$ is the position of the scatterer and τ describes the transition. The scatterer radiates the field as described by the Green's function of the problem. The value of τ is related to the extinction cross section through the optical theorem [71, 133],

$$\sigma \propto -\mathrm{Re}\{\tau\}, \tag{8.9}$$

where the proportionality depends on the dimension and if one considers scalar or vector waves. Regardless, large negative real parts correspond to high scattering. However, the scatterers should be passive/absorbing and not be a source
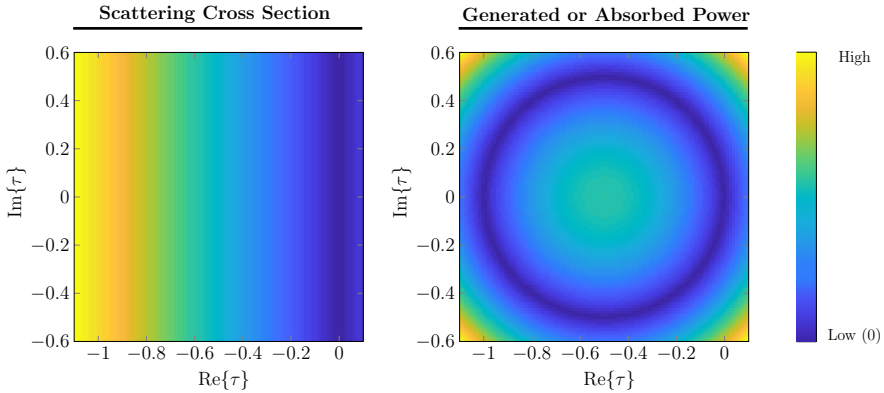
Figure 38: Scattering from a single point for different values of τ. Left shows the scattering cross section and right displays the power flow of the scattered field through a box surrounding the scatterer.

of energy. Conservation of energy occurs when [133],

$$\text{Re}\{\tau\} + \tau^*\tau = 0. \tag{8.10}$$

Returning to the scattering from the small dielectric sphere (8.1). In that scenario,

$$\tau = -\frac{2\text{j}}{3}k^3 a^3 \frac{\epsilon_\text{r} - 1}{\epsilon_\text{r} + 2} + \mathcal{O}\left(k^5 a^5\right). \tag{8.11}$$

and from (8.10) it is evident that the simple expression for dielectric spheres (8.1) is non-passive unless higher-order terms are included. A simulation of a single scatterer is seen in Fig. 38 where the right figure displays the total power flow of the scattered field for different values of τ. This is identical to the description in (8.10), values of τ on a circle centered at $-1/2$ with radius $1/2$ in the complex plane gives a passive scatterer. Any point outside the circle corresponds to active scatterers and within are absorbing scatterers, with peak absorption at $\tau = -1/2$. The left graph displays the scattering cross section, as expected from (8.9), scales only with the real part. Thus maximal scattering from passive scatterers occurs for $\tau = -1$.

For a single point scatterer, m, in a collection of several point scatterers, M, we can, in a similar manner to (8.8), write the scattered field from one scatter as,

$$E_m^\text{s}(\boldsymbol{r}) = \tau_m \left(E^\text{i}(\boldsymbol{r}_m) + \sum_{n \neq m} E_n^\text{s}(\boldsymbol{r}_m) \right) G(\boldsymbol{r}, \boldsymbol{r}_m), \tag{8.12}$$

where $E_m^\text{s}(\boldsymbol{r})$ is the scattered field from scatterer m, $E^\text{i}(\boldsymbol{r}_m)$ is the incident field from the sources at the position of the scatterer $\boldsymbol{r}_m$ and $E_n^\text{s}(\boldsymbol{r}_m)$ is the electric field from scatterer n at the position of scatterer m. Analogous to the currents

in the method of moments formulation we can describe the relation in terms of the strength of the scatterers, $\boldsymbol{I}^{\mathrm{s}}$,

$$I_m^{\mathrm{s}}(\boldsymbol{r}) = \tau_m \left(E_m^{\mathrm{i}} + \sum_{n \neq m} I_n^{\mathrm{s}} G(\boldsymbol{r}_m, \boldsymbol{r}_n) \right). \tag{8.13}$$

This expression can be rearranged to relate the strength of each scatterer to the incident electric field on a matrix form,

$$\boldsymbol{E}^{\mathrm{i}} = \mathbf{A} \boldsymbol{I}^{\mathrm{s}}, \tag{8.14}$$

$$\mathbf{A} = \begin{pmatrix} 1/\tau_1 & -G(\boldsymbol{r}_1, \boldsymbol{r}_2) & \cdots & -G(\boldsymbol{r}_1, \boldsymbol{r}_M) \\ -G(\boldsymbol{r}_2, \boldsymbol{r}_1) & 1/\tau_2 & \dots & -G(\boldsymbol{r}_2, \boldsymbol{r}_M) \\ \vdots & \vdots & \ddots & \vdots \\ -G(\boldsymbol{r}_M, \boldsymbol{r}_1) & -G(\boldsymbol{r}_M, \boldsymbol{r}_2) & \cdots & 1/\tau_M \end{pmatrix}. \tag{8.15}$$

The incident electric field is in this work often generated by a collection of densely placed point sources, K, over some aperture. The incident field at scatterer m can then be written similar to (8.12),

$$E_m^{\mathrm{i}} = \sum_k I_k^{\mathrm{i}} G(\boldsymbol{r}_m, \boldsymbol{r}_k), \tag{8.16}$$

where I_k^{i} is the source excitation for source k and $\boldsymbol{r}_k$ is the position of the source k. In matrix from this becomes,

$$\boldsymbol{E}^{\mathrm{i}} = \mathbf{P}^{\mathrm{s,i}} \boldsymbol{I}^{\mathrm{i}}, \tag{8.17}$$

where $\mathbf{P}^{\mathrm{s,i}}$ is a propagation matrix from the incident sources (i) to the scatterers (s),

$$\mathbf{P}^{\mathrm{s,i}} = \begin{pmatrix} G(\boldsymbol{r}_{m=1}, \boldsymbol{r}_{k=1}) & G(\boldsymbol{r}_1, \boldsymbol{r}_2) & \cdots & G(\boldsymbol{r}_1, \boldsymbol{r}_K) \\ G(\boldsymbol{r}_2, \boldsymbol{r}_1) & 1/\tau_2 & \dots & G(\boldsymbol{r}_2, \boldsymbol{r}_K) \\ \vdots & \vdots & \ddots & \vdots \\ G(\boldsymbol{r}_M, \boldsymbol{r}_1) & G(\boldsymbol{r}_M, \boldsymbol{r}_2) & \cdots & G(\boldsymbol{r}_M, \boldsymbol{r}_K) \end{pmatrix}. \tag{8.18}$$

This implementation is a Foldy-Lax type formulation [76, 139, 140]. The total strength for a given incident field can now be computed and thus the total field at any given position using the scatterer strengths and the Green's function, which differ in 2D and 3D. For a 3D case, the Green's function is as stated earlier,

$$G^{(3)}(\boldsymbol{r}, \boldsymbol{r}') = \frac{\mathrm{e}^{-\mathrm{j}kr}}{4\pi r}, \tag{8.19}$$

where $|\boldsymbol{r} - \boldsymbol{r}'| = r$ and the superscript indicates the dimensionality. The 2D Green's function can be obtained by reducing the dimension of (8.19). Placing

the source in the center,

$$G^{(2)}(\boldsymbol{r}, \boldsymbol{r}') = \int\limits_{-\infty}^{\infty} G^{(3)}(\boldsymbol{r}, \boldsymbol{r}')\, \mathrm{d}z = \frac{1}{4\pi} \int\limits_{-\infty}^{\infty} \frac{\mathrm{e}^{-\mathrm{j}kr}}{r}\, \mathrm{d}z. \tag{8.20}$$

Introduce $[\rho^2 = x^2 + y^2,\ b = \sqrt{\rho^2 + z^2},\ \mathrm{d}z = b/\sqrt{b^2 - \rho^2}\, db]$,

$$G^{(2)}(\boldsymbol{r}, \boldsymbol{r}') = \frac{2}{4\pi} \int\limits_{\rho}^{\infty} \frac{\mathrm{e}^{-\mathrm{j}kb}}{\sqrt{b^2 - \rho^2}}\, \mathrm{d}b, \tag{8.21}$$

finally with $[b = \rho \cosh(\theta), \mathrm{d}b = \rho \sinh(\theta)\, \mathrm{d}\theta]$ and known integrals [4]

$$G^{(2)}(\boldsymbol{r}, \boldsymbol{r}') = \frac{1}{2\pi} \int\limits_{\rho}^{\infty} \frac{\mathrm{e}^{-\mathrm{j}kb}}{\sqrt{b^2 - \rho^2}}\, \mathrm{d}b = \frac{1}{2\pi} \int\limits_{0}^{\infty} \mathrm{e}^{-\mathrm{j}k\cosh(\theta)}\, \mathrm{d}\theta$$

$$= -\frac{\mathrm{j}\pi}{2} \int\limits_{0}^{\infty} \sin(k\cosh(\theta)) + \mathrm{j}\cos(k\cosh(\theta))\, \mathrm{d}\theta = -\frac{\mathrm{j}}{4} \mathrm{H}_0^{(2)}(kr), \tag{8.22}$$

where $\mathrm{H}_0^{(2)}$ is the Hankel function of the second kind (the Hankel function of the first kind describes ingoing waves, or outgoing if another time convention is used). Alternatively, it can be obtained from the 2D scalar equation with radiation condition [223]. One important difference with the scalar equation to remember is the expression for power flow. In 3D it is described by Poynting vector (2.20). Instead with the scalar equation, it is proportional to $E\boldsymbol{\nabla}E$ which for instance follows from the continuity equation, Cauchy's equation along with Euler equations for fluid dynamics.

This technique uses minimal memory consumption to achieve maximal scattering. Regions of any size can be simulated as the only stored information in the system are the positions of the scatterers and their value of τ, which is set to -1 for maximal scattering, or $-1/2$ for absorption. The computational cost in the technique lies within the matrix $\mathbf{A}$. A solution typically requires an inversion of this matrix, an operation that scales as the cube of the number of scatterers M. Iterative techniques such as conjugate gradient, biconjugate, preconditioner, *etc.* can be further investigated to trade memory allocation for time [117]. In a brute force setting $40 - 100$k scatterers can be included in a system solved on a central processing unit (CPU). Graphics processing unit (GPU) solvers can be faster but must be segmented into parts as the current memory sizes of GPUs are much smaller than the available RAM. Segmentation, or cascading the region into several sub-slabs, will influence the scattering properties and is a subject for further investigation.

With this model or full-wave toolbox, we can describe and investigate several scenarios, not just the problem of focusing through and into regions of highly scattering medium. We shall now make a brief comparison with an analytical solution and then display some examples of focusing.

8.2   Comparison with Diffusion Theory

Before investigating transmission and focusing through random media, it is of interest to compare with analytical expressions of approximate models. Dealing with electromagnetic waves and materials with a high density of scattering effects, first-order multiple scattering effects or approximations such as the Rytov approximations can no longer be utilized [93]. One approach to approximate multiple scattering is through transport theory [47, 110, 212]. Instead of starting with the wave equation, this model starts with the transport of energy through a medium with particles. It is also called radiative power transport theory or radiative transport theory [47]. It is a heuristic model in which the addition of power holds instead of the addition of fields [110]. This is the situation modeled by typical Monte Carlo simulations. From the radiative transport theory, one can approximate further and arrive at the diffusion model[3]. We shall focus on the important results and for further information see for instance [110, 249]. It is assumed in the following case that the average diffuse intensity, U_d, encounters many particles and that they are uniformly distributed. For a homogeneous background material in 2D, the diffusion equation is,

$$\nabla^2 U_\mathrm{d}(\boldsymbol{r}) - 2\rho\sigma_\mathrm{a}\rho\sigma_{tr}U_\mathrm{d}(\boldsymbol{r}) = -2\rho\sigma_\mathrm{s}\rho\sigma_{tr}U_\mathrm{ri}(\boldsymbol{r}) - \frac{1}{\pi}\rho\sigma_{tr}Q_\mathrm{d}(\boldsymbol{r})$$
$$+ \frac{1}{\pi}\nabla \cdot \int_{2\pi} \varepsilon_\mathrm{ri}(\boldsymbol{r}, \hat{\boldsymbol{s}})\hat{\boldsymbol{s}}\, \mathrm{d}\omega + \frac{1}{\pi}\nabla \cdot \int_{2\pi} \varepsilon(\boldsymbol{r}, \hat{\boldsymbol{s}})\hat{\boldsymbol{s}}\, \mathrm{d}\omega, \quad (8.23)$$

where U_d is the average diffuse intensity, U_ri is the average reduced intensity, ρ is the density of scatterers, σ_a the absorption cross section, σ_s the scattering cross section, σ_tr the effective scattering, $Q_\mathrm{d}(\boldsymbol{r})$ is power generated per unit area per unit frequency interval, ε_ri is a source related to the reduced intensity and ε is a source term [110]. The terms are often gathered and commonly written as,

$$\mu_\mathrm{a}\Phi - D\nabla^2\Phi = A(\boldsymbol{r}), \tag{8.24}$$

where Φ ($\propto U_d$) is the average intensity, in this case, similar to the squared absolute value of the electric field, D is a material parameter describing the effective scattering cross section and absorption in the media which can be related to the scattering parameters previously discussed through,

$$\sigma_\mathrm{tr} = \sigma_\mathrm{s}(1 - \bar{\mu}) + \sigma_\mathrm{a}, \tag{8.25}$$

where, σ_tr is the effective scattering, $\bar{\mu}$ describe the anisotropy of the scatterers ($\bar{\mu}=0$ in this case for isotropic scatterers), and σ_a is the absorption cross section.

---

[3]A brief remark regarding notation; Electromagnetics, radiative transport theory and diffusion theory have many different parameters and quantities with different names and symbols. Some symbols are reoccurring through the different theories albeit with a completely different meaning. We try to keep the notation as close to the relevant theory as possible, with some slight changes to avoid confusion.
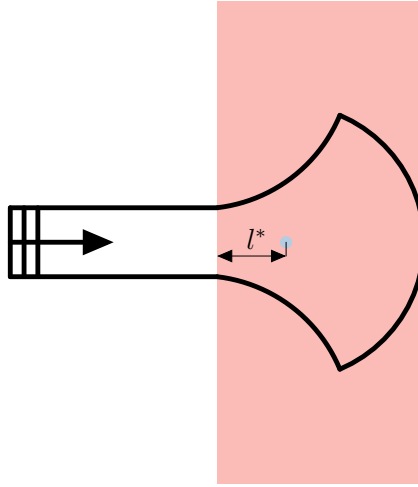
Figure 39: Illustration of an incident wave impinging on a scattering medium. After a distance l^* the field within the medium appears to originate from a point source shown by the blue circle.

It is convenient to use the length scale of l^*, which is the distance after which directionality is lost in the medium, *i.e.* an input beam outside the medium will appear to stem from an isotropic source placed l^* within the medium, illustrated in Fig. 39. Where l^* can be expressed as,

$$l^* = \frac{1}{\rho \sigma_{\mathrm{tr}}} = \frac{1}{\mu_{\mathrm{tr}}}. \tag{8.26}$$

The diffusion constant can be written as,

$$D = \frac{1}{2\mu_{\mathrm{tr}}} = \frac{1}{2(\mu_{\mathrm{s}}' + \mu_{\mathrm{a}})}. \tag{8.27}$$

Even though the diffusion equation is an approximation the solution quickly becomes cumbersome to write in an analytical setting. One simple case for which a simple analytical solution exists is illustrated in Fig. 40. The region is a disc of radius a in 2D filled with non-absorbing scatterers and an isotropic point source in the center

The form of the solution is,

$$U_{\mathrm{d}}(\boldsymbol{r}) = -\frac{C_{\mathrm{a}}}{l^*}\ln\left\{\frac{r}{a}\right\} - \frac{C_{\mathrm{b}}}{a}, \tag{8.28}$$

where C_{a} and C_{b} are real-valued constants depending on input power and the boundary condition. The diffuse intensity is not a quantity used in other simulation setting and to put it into quantities of electromagnetic scattering we write a relation with power flow ($\boldsymbol{S}$),

$$\langle |\boldsymbol{S}| \rangle = \frac{C_1}{a} - \frac{C_2}{l^*}\ln\left\{\frac{r}{a}\right\} + \frac{C_3}{r}. \tag{8.29}$$
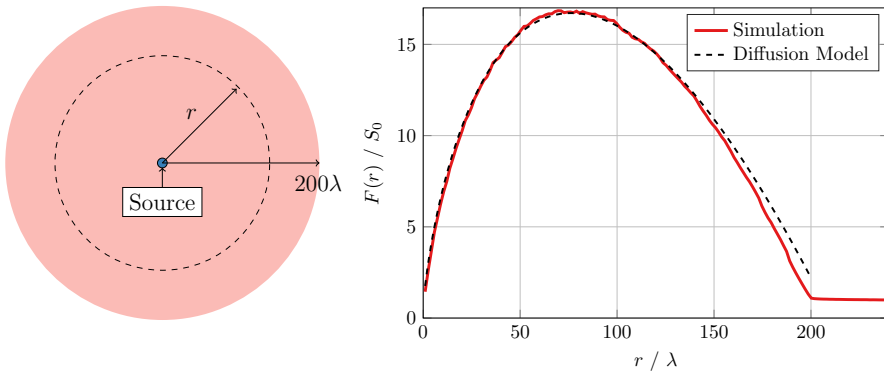
Figure 40: The geometry of the scattering problem (left) with a source in the center (blue). The right graph displays the total average power flow multiplied with the radial value on concentrical circles.

This is the average value of the total power flow, where C_1, C_2, and C_3 are real-valued constants. In the right graph in Fig. 40 is a comparison of the average value of the total power flow multiplied with the radial coordinate.

$$F(r) = \frac{1}{2\pi} \int\limits_0^{2\pi} \langle |\boldsymbol{S}| \rangle r \, \mathrm{d}\phi. \tag{8.30}$$

This highlights that the total intensity per circle around the source is increasing. However, the outgoing power is constant for each circle, as expected by power conservation. This is particular to 2D, where intensity scales as $\ln(r)$ and power density as $1/r$. As seen from the right of Fig. 40, the models compare reasonably well. The validity of the diffusion model holds within the medium and closer to the edge we can see larger disagreement to be expected as the model is no longer as valid.

Transmission in these situations is heavily dependant on the geometry, boundary condition, and scattering properties. Diffusion has sources within the medium and is only valid for specific cases in specific regions and cannot be used to simulate focusing within media. This comparison gives some faith to the modeling technique but is an analytical construction difficult to recreate in measurement scenarios. Comparisons with measurements are the next step in validating this technique.

Nonetheless, we can continue to use the strengths of the technique. Full-wave information to focus the electric field through and into random media.
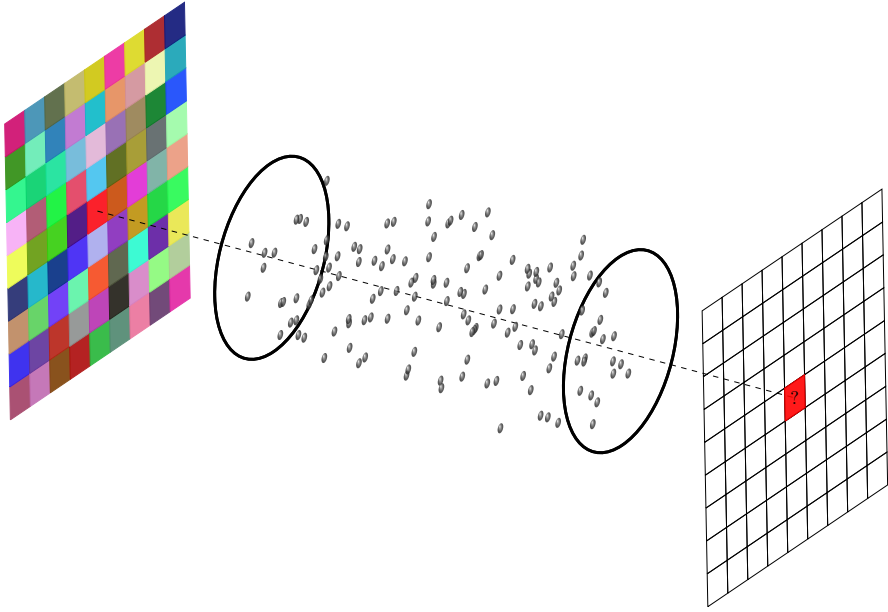
Figure 41: The geometry of a 3D scattering problem. Sources are placed in the left of the illustration in an array configuration. The amplitude and phase can be controlled as illustrated by the varying colors. On the right-hand side is a detector, also divided in an array configuration and the center pixel is the region of interest. In between is a scattering medium of randomly placed scatterers.

8.3 Focus Through Random Media

A typical setup when focusing through media can be seen illustrated for 3D in Fig. 41. There is an array of elements to the left which represent the sources. They can, mathematically, be controlled to amplitude and phase, represented by the different colors and intensities. As they radiate some energy propagates through the medium and reaches the right side where there is a detector. We can consider the electric field at these points, in amplitude only or amplitude and phase as well as the incident power density. In a real-life setting, there is an incident beam of laser light. This laser light can be controlled for instance through a spatial light modulator (SLM) [146,189] or a digital micromirror device (DMD) [60,196]. An SLM can be described as a large pixelized mirror that has individual control of each pixel to modulate the phase whereas a DMD can turn the signal on or off. There exist a plethora of devices with varying adjustability, phase control, and number of pixels which is discussed in [60,189]. The information carried forward to the numerical implementation is that the input light can be modulated.

The receiver can be a traditional detector, such as a CCD detector, but can also consist of a system collecting both amplitude and phase through hologra-

phy [18] or utilizing the formed speckles pattern [29]. Other interesting objects in this measurement setting are phase conjugating mirrors. The name is self-explanatory, an incoming wave gets phase conjugated and sent back in the direction it came from [30, 189]. Phase conjugation over an aperture is something we demonstrate in this work.

2D and 3D only differ in their respective Green's functions and most of the results here are from 2D, as larger structures can be simulated. The results in this section are just demonstrations of the technique and much larger regions can be simulated. Regardless of the dimension and position of the scatterers and sources, we wish to obtain the map which takes us from the input fields, or source excitations, to the output (receivers). The singular values of this mapping provide, in some regards, the optimal solution. First, consider an array of several input sources and a single receiver at the other side of a slab filled with randomly placed scatterers. Each source array element is a point source that can be modulated in amplitude and phase. We shall now consider optimizing the electric field values at the receivers, but similar can be done for power flow as well. In a simulation of the experimental setting we control the source excitation in amplitude and phase,

$$I_k^i \in \mathbb{C}^1 \tag{8.31}$$

Multiple sources could be grouped together to form larger pixels similar to an SLM. If we consider a single receiver, it will collect a complex signal, $R \in \mathbb{C}^1$, and the mapping,

$$\boldsymbol{V} \in \mathbb{C}^{1,K}, \tag{8.32}$$

takes us from the exited sources to the field at the receiver,

$$R = \boldsymbol{V} \cdot \boldsymbol{I}^i. \tag{8.33}$$

The problem to maximize the received field can be formulated as,

$$\underset{\boldsymbol{I}^i}{\text{maximize}} \ \left\{ \left| \boldsymbol{V} \cdot \boldsymbol{I}^i \right| \right\}, \tag{8.34}$$

$$\text{subject to } ||\boldsymbol{I}^i||_2^2 = \beta, \tag{8.35}$$

and the solution can be written immediately as,

$$\boldsymbol{I}^{i,\text{opt}} = \frac{\sqrt{\beta}}{||\boldsymbol{V}||_2} e^{j\theta} \boldsymbol{V}^\dagger, \tag{8.36}$$

where the first part is for normalization purposes and θ is an arbitrary phase and $.^\dagger$ is the Hermitian transpose. The problem changes little if one wishes to focus down on several points, the mapping is now a matrix and the problem becomes,

$$\underset{\boldsymbol{I}^i}{\text{maximize}} \ \left\{ \left| \mathbf{M} \cdot \boldsymbol{I}^i \right| \right\}, \tag{8.37}$$

$$\text{subject to } ||\boldsymbol{I}^i||_2^2 = \beta, \tag{8.38}$$

where $\mathbf{M} \in \mathbb{C}^{L,K}$ is the mapping matrix between K sources and L receivers. The maximum is given through the singular vector corresponding to the maximal singular value, as evident by the Rayleigh quotient.

For a problem of K sources, L receivers and M scatterers, the mapping is described by the previously introduced matrices (8.14)–(8.18),

$$\mathbf{M} = \mathbf{P}^{\mathrm{r,i}} + \mathbf{P}^{\mathrm{r,s}}\mathbf{A}^{-1}\mathbf{P}^{\mathrm{s,i}}, \tag{8.39}$$

where $\mathbf{P}^{\mathrm{r,i}} \in \mathbb{C}^{L,K}$ is the matrix relating the source excitations to the electric field at the receivers, $\mathbf{P}^{\mathrm{s,i}} \in \mathbb{C}^{M,K}$ describes the relation between the sources and the positions of the scatterers, $\mathbf{A} \in \mathbb{C}^{M,M}$ describes the scatterers (8.15) and $\mathbf{P}^{\mathrm{r,s}} \in \mathbb{C}^{L,M}$ the relation between the scatterer and receivers. In large scattering problems $M \gg K \geq L$ the matrix $\mathbf{A}$ and its inversion is the bottleneck of the computation. The mapping itself is often of a much smaller size. If only the field information at the source positions is of interest then the mapping, $\mathbf{M}$, is all we need to investigate different phase and amplitude control of the sources.

Obtaining the mapping numerically is as simple as implementing the above-stated code, but obtaining it experimentally is a different matter. If the experimentalist has complete control of the system, then the mapping can be probed by using one source at a time, mathematically carrying out M controlled measurements,

$$\mathbf{R}_{\mathrm{data}} = \mathbf{M}\mathbf{I}^{\mathrm{i}}, \tag{8.40}$$

where $\mathbf{R}_{\mathrm{data}}$ is a matrix of the collected data and $\mathbf{V}_{\mathrm{i}}$ is a matrix of the source excitations given. If the sources can individually be turned off, we can simply let the source excitation matrix be the identity matrix. In a more realistic scenario, when only the phase is controlled, we can use random excitations. Every element in the excitation matrix is taken randomly from the set $\{x \in \mathbb{C} : |x| = 1\}$. This results in a random matrix that is almost surely full rank, thus invertible, yielding the mapping through inversion, at least in a noise-free environment.

In cases where the phase cannot be measured, more measurements can be added to estimate the phase. In an otherwise perfect environment, this would triple the number of needed measurements.

Optimal focus through the medium is, as discussed, described by the singular value decomposition of the mapping. Experimentally, this mapping is unknown and the random excitation process described above is not used. Instead, iterative schemes are employed [29, 242, 243]. Such as optimizing each pixel, or subregion on an SLM, one by one described by,

1. Start with a random excitation

2. Measure the output signal

3. Optimize over one element in the input signal

4. Go through all elements as many times as desirable

With the complete mapping known in the numerical case, we can study these techniques and investigate their performances. There is an alternative first step in the process. Instead of utilizing random excitations one can estimate the highest singular value and singular vector using probabilistic algorithms for matrix approximation [89]. This routine is summarized in the following steps. Given an $m \times n$ complex matrix $\mathbf{M}$,

1. Create a Gaussian test matrix Ω of dimension $n \times \min\{2b, n\}$ where b is the number of singular values sought for.

2. Form $\mathbf{Y} = \mathbf{M}\Omega$

3. Construct a matrix $\mathbf{Q}$ whose columns form an orthogonal basis for the range of $\mathbf{Y}$

4. Form $\mathbf{B}^{\mathrm{T}} = \mathbf{M}^{\mathrm{T}}(\mathbf{Q}^{\dagger})^{\mathrm{T}}$

5. Compute the SVD of the small matrix $\mathbf{B} = \widetilde{\mathbf{U}}\mathbf{\Sigma}\mathbf{V}^{\dagger}$

6. Set $\mathbf{U} = \mathbf{Q}\widetilde{\mathbf{U}}$

The technique is now demonstrated for a 2D slab of height $110\,\lambda$ and width $60\,\lambda$ filled with 4000 scatterers with $\tau = -1$, corresponding to a total effective length of the slab of 6 in terms of l^*. The incident array covers 80% of the slab and the receiver is one-tenth of the source array size. The geometry is illustrated in Fig. 42. Displayed in this figure is the total power flow, on a 30 dB dynamic range, through the structure for an incident beam and the optimal signal, both the pure source input, right column, and the resulting total power, left column. One can visually see a higher power flow within the medium and at the receiver in the optimal setting, bottom left, compared to the uniform input, top left.

The setup illustrated in Fig. 42 consists of 350 sources with 35 receivers and can be used to investigate the iterative optimization scheme presented above. Each source, or pixel, is optimized using a golden section search and all sources are optimized for in total five times [126]. In Fig. 43 the results are shown in solid line with the x-axis labeling how many times each pixel has been optimized, called iteration. The output is normalized to the output of the first realization, displaying the enhancement through optimization [242]. The alternative starting point following the estimation of the singular value is displayed in the dashed line, normalized to the starting value of the black line. This optimization was done over the electric field values and similar can be done for incident power flow, seen in the right of Fig. 43.

The realization of the random media was identical in this run as the results can differ significantly for different runs, depending on geometry and source/receiver relations. The optimization in power flow and electric field differs somewhat for this realization. Depending on the geometry, boundary conditions, and the numbers of sources, receivers, and their ratio, different enhancement factors could be expected along with distributions over the open/closed channels [82, 103, 242].
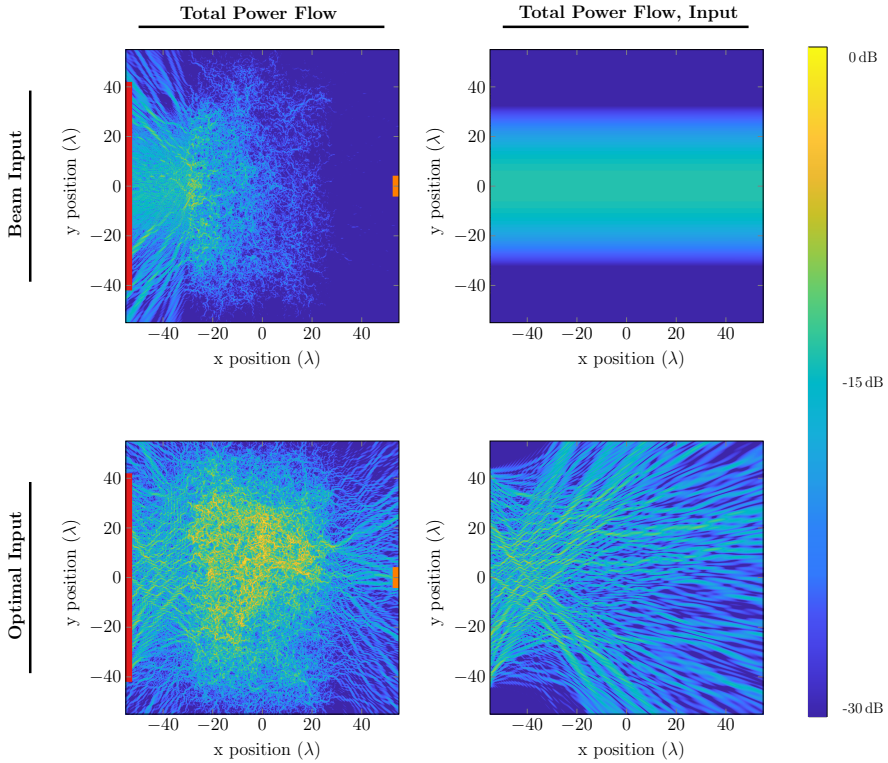
Figure 42: Total power flow for the input sources (right column) and through the scattering medium (left column) for a beam input (top row) and the optimal input (bottom row). The region of sources is marked by a red bar and the receiving region by an orange bar. The dynamic range of the figures is 30 dB

An interesting alternative technique is to use phase conjugating mirrors instead of an SLM. Instead of iterating through the pixels, we count the number of bounces between the source plane and receive plane, now replaced with phase conjugating mirrors. One bounce consists of source → receiver → source. We consider each of the mirrors to be capable of enhancing the signal such that the same input power is transmitted each bounce. In Fig. 44 the enhancement factor for electric field (left) and incident power density (right) each x-axis point marks one full bounce. Similar to Fig. 43 the enhancement factor is normalized to the value of the initial randomized input. This technique rapidly converges on a focus. The process can in this case be described by,

$$\mathbf{M}\left(\mathbf{M}^{\dagger}\mathbf{M}\right)^{n}\boldsymbol{I}^{\mathrm{i}}, \tag{8.41}$$

where n is the number of bounces. This expression focuses on a singular vector corresponding to the highest singular value rapidly as the number of high transmission channels are few [82].
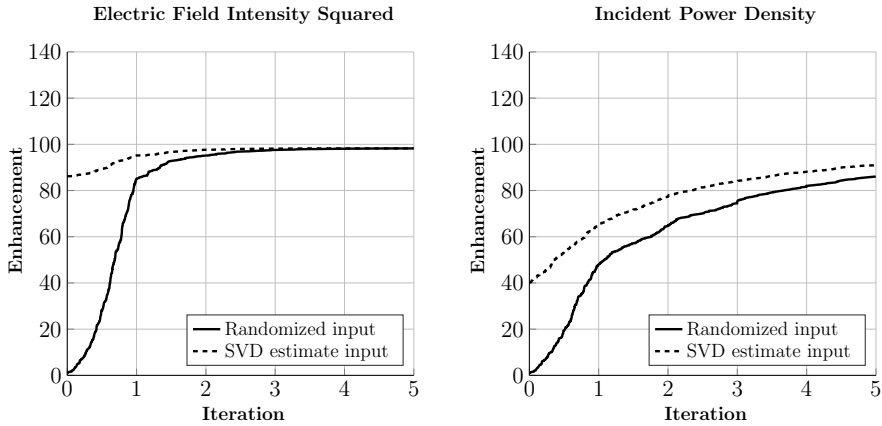
Figure 43: Enhancement factor of iterative pixel by pixel optimization in phase for electric field intensity (left) and incident power density (right). Solid lines use a randomized input and the dashed line estimates of an optimal input.
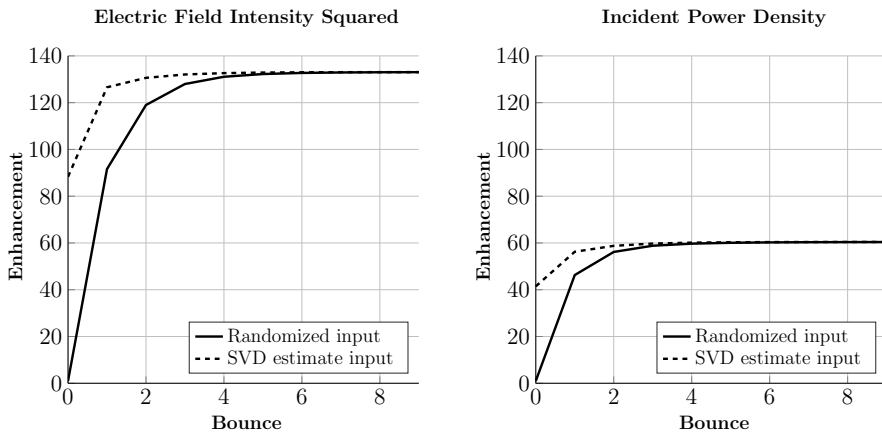
Figure 44: Enhancement factor of focusing using phase conjugation for electric field intensity (left) and incident power density (right). Solid lines use a randomized input and the dashed line estimates of an optimal input.
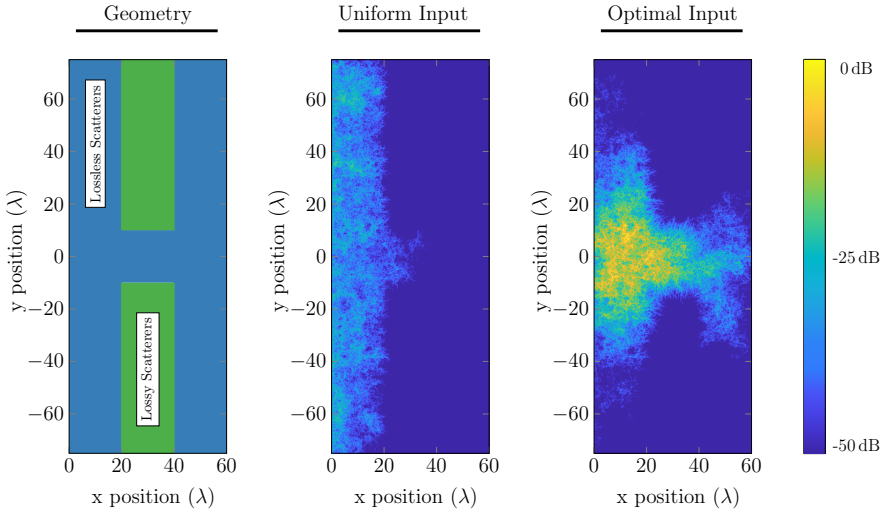
Figure 45: The geometry of the absorbing and scattering regions (left) and total power flow for a uniform input (center) and optimal input (right). The sources and receivers cover the entire left and right side of the slab, respectively. The dynamic range of the figures is 50 dB.

8.4   Focus into Random Media

It is also interesting to simulate focusing within media. In the implementation, this shares several similarities with the previous subsection and we can direct attention to presenting one type of result.

Focusing into random media can be done in several ways using this numerical technique. Examples include placing a receiver within the media, mark certain scatterers and emulate ultrasound focus, or adding absorbing points in regions to avoid ($\tau = -1/2$). The numerical technique chosen depends on the measurement setup one is trying to emulate. One technique places a point-like source within the medium which either transmits or relays a signal which the transmitter can focus on, using, for instance, phase conjugation as wavefront shaping [12, 46, 121, 244, 254, 264]. Consider instead the option of adding several absorbing points. The geometry of this example is displayed on the left of Fig. 45. The sources cover the entirety of the 150 λ high slab ($x = 0\,\lambda$), and the receivers similarly cover the entirety of the output side ($x = 60\,\lambda$). The slab is 60 λ thick, and parts of the slab is filled with absorbing points (green region) and the remaining region (blue) is covered with scatterers ($\tau = -1$). In total, there were ∼1700 sources, ∼1700 receivers, and ∼41000 scattering/absorbing objects uniformly distributed. In the center of Fig. 45 the total power flow for a uniform input signal is seen throughout the medium with the absorption clearly seen in the top and bottom of the center figure. In the right figure, the optimal input is displayed where much more power is being transmitted through the system. The images both use

the same dynamic range of 50 dB.

In this section, we have presented a numerical technique to simulate random media in a full-wave setting. There are several interesting scenarios and properties to investigate and we have only presented a very narrow selection. Using this technique to model noise in the system, aspect ratios of the geometry, scaling of intensity through the medium due to scatterer strength, sizes of focus and speckles, eigenvalue distributions of the mapping to mention a few. With experimental data and specific setups, we can construct a numerical model and compare these simulation results to real-world cases.

9 Conclusions

Electromagnetic waves have always intrigued mankind, and interesting concepts are continuously discovered. In this thesis, new functional structures are developed through physical understanding and optimization techniques. With emerging communication technologies utilizing higher frequency bands and the need to measure near-field devices, this thesis also investigates measurement techniques. In the work, new possibilities for functional structures as an integral part of the solution are displayed. The topics and use cases in this thesis cover a wide scientific spectrum, and as a general summary, Paper I–II,V–VI focuses on the use of functional structures, and in Paper III–VI electromagnetic measurements techniques are used and developed.

The functional structure in Paper I is developed to study fundamental limitations of transmission through arrays of periodic sub-wavelength apertures. We design the structure to have large polarizability and optimize it to maximize the obtainable bandwidth within the first resonance peak.

In Paper II and III, we investigate circular polarization selective structures for a space communication application. The design concept is based on polarization selectivity from cascaded anisotropic sheets. The separation between the two bands is governed by the rotation and separation between the layers. With performance requirement, the design is optimized based using a combination of genetic algorithm, Nelder-Mead simplex method, and trust-region technique [220]. The design is characterized in measurements for both transmission and reflection through the measurement technique presented in Paper III, using linearly-polarized single-polarized antennas, time gating, and reference measurements.

Measurement of electromagnetic fields from scattering and radiating objects is investigated in Paper IV where a reflection-based reference-free measurement setup is developed to simplify measurements of defect detection of composite structures at 60 GHz.

In Paper V, a novel technique to measure near-field regions of antennas using a small aperture as a setup calibration is presented and demonstrated for 28 GHz and 60 GHz. The technique requires two measurements, one of the device of interest and one of a small aperture. The small aperture measurement calibrates

the setup and the measurement of the device is used to reconstruct sources on a pre-defined surface. These reconstructed sources are used to compute the fields on a plane of interest.

A multi-physical measurement technique of electromagnetic waves using a metasurface is introduced in Paper VI. The metasurface consists of thermally isolated electromagnetic elements designed to absorb power and generate heat, which is detected by an infrared camera, enabling real-time visualization. The technique is intended to be used for communication devices. Other IR-based methods typically require a high power density, whereas this technique handles the low power density levels of consumer devices.

Finally, a full-wave numerical model for investigating control of wave propagation through random media was presented, in Sec. 8. The technique is based on describing the scatterers in a simple manner with optimal scattering characteristics to conserve memory and allow for large scattering configurations. The technique is not restricted in the physical size of the simulation region, only the number of scatterers. A selection of results was presented for focusing through and into a slab of random media, both optimally and iteratively. Different measurement scenarios can be simulated and we await measurement results for further comparisons.

10   Future Work

This thesis spans several subjects, and techniques pulled together by functional structures and measurement techniques. Much of the work done has been on developing these structures or techniques from unconventional approaches, which undeniably provided further regions to explore in a continuation of the work. In this last section, I will outline some ideas and thoughts of future continuation in relation to the work presented in this thesis.

The computational power and optimization toolboxes are increasing at a rapid pace. In the development of the functional structures in Paper III, we were limited by the inherent unit cell restrictions. The complexity of the structure increase, both from a manufacturing and a simulation point of view, with the addition of layers and it is therefore of interest to investigate if similar performance is achievable in structures with fewer layers. The symmetry of the layers could be broken and a rotation of arbitrary rotational angles included. The functional structure design in Paper III is interesting, even outside of space applications, and could be interesting to include in situations utilizing ground planes to investigate possible reflector performance.

The measurements and techniques presented in Papers IV–V have improvements in hardware. A significant reduction in measurement time would be achieved with a multi-probe setup. In Paper IV, multiple frequencies can be used to potentially enable a sparser measurement sampling.

The aperture technique in Paper V has several interesting regions of continuing work. Currently, only single-polarization measurements were used and

dual-polarization is something that potentially could increase performance. The technique is demonstrated and further rigorous investigation into details such as sampling, transverse distances between the aperture and source could be investigated. The calibration part of the measurements uses first-order corrections, which could be improved with, for instance, spherical wave expansions of the receiving port.

Regarding the multi-physical metasurface presented in Paper VI there are aspects within the measurement technique, element construction, manufacturing and signal processing to expand and further investigate. The technique was demonstrated at $10\,\mathrm{GHz}$ and it is interesting to explore the possibilities to go much higher as well as lower in frequency by utilizing different materials and designs along with altering the signals to obtain positive trade-offs in the signal strength. A currently unexplored, but possible path, is to create large non-planar surfaces.

Finally, the numerical toolbox for full-wave simulations of random media presented in Sec. 8 could be further improved to handle larger regions and smaller regions faster using GPU acceleration, iterative solvers, and cascading of slabs. With future measurement results and comparisons, one can expand the model to better fit the needs of a specific case and tweak the code accordingly. Currently operating in 2D and 3D for a scalar case, eventually, the code can be expanded to include vector waves in 3D.

References

[1] Guidance for evaluating exposure from multiple electromagnetic sources, iec/tr 62630, 2010.

[2] S. M. A. M. H. Abadi and N. Behdad. A broadband, circular-polarization selective surface. *Journal of Applied Physics*, **119**(24), pp. 244901, 2016.

[3] S. M. A. M. H. Abadi and N. Behdad. Wideband linear-to-circular polarization converters based on miniaturized-element frequency selective surfaces. *IEEE Trans. Antennas Propag.*, **64**(2), pp. 525–534, 2016.

[4] M. Abramowitz and I. Stegun. *Handbook of Mathematical Functions with Formulas.* United States Department of Commerce, National Bureau of Standards, 1964.

[5] K. Achouri and C. Caloz. *Electromagnetic Metasurfaces: Theory and Applications.* Wiley-IEEE Press, 2021.

[6] S. S. Ahmed, A. Schiessl, F. Gumbmann, M. Tiebout, S. Methfessel, and L.-P. Schmidt. Advanced microwave imaging. *IEEE Microw. Mag.*, **13**(6), pp. 26–43, 2012.

[7] M. Albani, P. Balling, L. Datashvili, G. Gerini, P. Ingvarson, K. Pontoppidan, M. Sabbadini, D. Sjöberg, S. Skokic, and G. Vecchi. Concepts for polarising sheets & "dual-gridded" reflectors for circular polarisation. In *ICECom Proceedings*, pp. 1–4, 2010.

[8] J. Allday. *Quarks, Leptons, and the Big Bang.* Taylor & Francis, New York, 2002.

[9] S. A. Altair Development S.A. (Pty) Ltd Stellenbosch. Altair Feko™ applications. https://www.altair.com/feko-applications/, 2021. Accessed April, 2021.

[10] K. Appel and W. Haken. Every planar map is four-colorable. *Contemporary Mathematics*, **98**, 1989.

[11] R. Aster, B. Borchers, and C. Thurber. *Parameter Estimation and Inverse Problems.* Academic Press, New York, NY, 2005.

[12] J. Aulbach, B. Gjonaj, P. Johnson, and A. Lagendijk. Spatiotemporal focusing in opaque scattering media by wave front shaping with nonlinear feedback. *Opt. Express*, **20**(28), pp. 29237–29251, Dec 2012.

[13] S. N. Azemi, K. Ghorbani, and W. S. Rowe. 3D frequency selective surfaces. *Progress in Electromagnetics Research C*, **29**, pp. 191–203, 2012.

[14] D. Balageas and P. Levesque. EMIR: a photothermal tool for electromagnetic phenomena characterization. *Revue générale de Thermique*, **37**(8), pp. 725–739, 1998.

[15] D. L. Balageas, P. Levesque, and A. A. Deom. Characterization of electromagnetic fields using a lock-in infrared thermographic system. In *Thermosense XV: An International Conference on Thermal Sensing and Imaging Diagnostic Applications*, volume 1933, pp. 274–285. International Society for Optics and Photonics, 1993.

[16] C. A. Balanis. *Antenna Theory: Analysis and Design, 4th Edition*. Wiley, 2016.

[17] H. U. Baranger, D. P. DiVincenzo, R. A. Jalabert, and A. D. Stone. Classical and quantum ballistic-transport anomalies in microjunctions. *Phys. Rev. B*, **44**, pp. 10637–10675, Nov 1991.

[18] K. Barjean, K. Contreras, J.-B. Laudereau, Éric Tinet, D. Ettori, F. Ramaz, and J.-M. Tualle. Fourier transform acousto-optic imaging with a custom-designed cmos smart-pixels array. *Opt. Lett.*, **40**(5), pp. 705–708, 2015.

[19] M. Baunge, H. Ekström, P. Ingvarson, and M. Petersson. A new concept for dual gridded reflectors. In *Proceedings of the fourth European Conference on Antennas and Propagation (EuCAP)*, pp. 1–5. IEEE, 2010.

[20] A. G. Bell. Improvement in telegraphy, February 14 1876. US Patent 174465A.

[21] A. G. Bell and S. Tainter. Photo phone-transmitter, December 14 1880. US Patent 235496A.

[22] A. Bengtsson, D. Hill, M. Li, M. Di, M. Cinthio, T. Erlöv, S. Andersson-Engels, N. Reistad, A. Walther, L. Rippe, and S. Kröll. Characterization and modeling of acousto-optic signal strengths in highly scattering media. *Biomedical Optics Express*, **10**(11), pp. 5565–5584, 2019.

[23] M. Bertolotti. *The History of the Laser*. CRC press, 2004.

[24] D. Bertsimas and J. N. Tsitsiklis. *Introduction to Linear Optimization*, volume 6. Athena Scientific Belmont, MA, 1997.

[25] B. Blochet, L. Bourdieu, and S. Gigan. Focusing light through dynamical samples using fast continuous wavefront optimization. *Opt. Lett.*, **42**(23), pp. 4994–4997, 2017.

[26] D. Boas, C. Pitris, and N. Ramanujam. *Handbook of Biomedical Optics*. CRC Press, 2016.

[27] F. Boccardi, R. W. Heath, A. Lozano, T. L. Marzetta, and P. Popovski. Five disruptive technology directions for 5G. *IEEE Commun. Mag.*, **52**(2), pp. 74–80, 2014.

[28] A. Bondeson, T. Rylander, and P. Ingelström. *Computational Electromagnetics.* Springer-Verlag, Berlin, 2005.

[29] A. Boniface, B. Blochet, J. Dong, and S. Gigan. Noninvasive light focusing in scattering media using speckle variance optimization. *Optica*, **6**(11), pp. 1381–1385, 2019.

[30] A. Boniface, M. Mounaix, B. Blochet, R. Piestun, and S. Gigan. Transmission-matrix-based point-spread-function engineering through a complex medium. *Optica*, **4**(1), pp. 54–59, 2017.

[31] L. Borcea. *Imaging in Random Media*, pp. 1279–1340. Springer New York, New York, NY, 2015.

[32] M. Born and E. Wolf. *Principles of Optics: Electromagnetic Theory of Propagation, Interference and Diffraction of Light.* Elsevier, 2013.

[33] M. Bosiljevac, M. Casaletti, F. Caminita, Z. Sipus, and S. Maci. Non-uniform metasurface Luneburg lens antenna design. *IEEE Trans. Antennas Propag.*, **60**(9), pp. 4065–4073, 2012.

[34] P. Bossuet and F. Gautier. Electromagnetic wave spatial filter with circular polarization, 1987. US Patent 4,652,891.

[35] P. Bossuet and F. Gautier. Electromagnetic wave spatial filter with circular polarization and a cassegrain antenna comprising such a filter, 1988. US Patent 4,728,961.

[36] J. Brake, M. Jang, and C. Yang. Analyzing the relationship between decorrelation time and tissue thickness in acute rat brain slices using multispeckle diffusing wave spectroscopy. *J. Opt. Soc. Am. A*, **33**(2), pp. 270–275, 2016.

[37] Brillouin, Léon. Diffusion de la lumière et des rayons x par un corps transparent homogène - influence de l'agitation thermique. *Ann. Phys.*, **9**(17), pp. 88–122, 1922.

[38] K. Brown. Far-field antenna pattern measurement using near-field thermal imaging. *IEEE Trans. Antennas Propag.*, **66**(3), pp. 1488–1496, 2018.

[39] O. M. Bucci and T. Isernia. Electromagnetic inverse scattering: Retrievable information and measurement strategies. *Radio Science*, **32**(6), pp. 2123–2137, 1997.

[40] E. Bullard, B. Lovell, and G. Deacon. The effect of world war II on the development of knowledge in the physical sciences [and discussion]. *Proceedings of the Royal Society of London. Series A, Mathematical and Physical Sciences*, **342**(1631), pp. 519–536, 1975.

[41] W. Cai and V. Shalaev. *Optical Metamaterials: Fundamentals and Applications*. Springer Science & Business Media, 2009.

[42] W. A. Campbell Jr, R. S. Marriott, and J. J. Park. Outgassing data for selecting spacecraft materials. Technical Report NASA-RP-1124, NASA, Washington DC 20546-0001, 1984.

[43] E. J. Candès and M. B. Wakin. An introduction to compressive sampling. *IEEE Signal Process. Mag.*, **25**(2), pp. 21–30, 2008.

[44] F. Capolino, editor. *Metamaterials Handbook*. CRC press, Boca Raton, FL, 2009.

[45] C. Cattani. *Wavelet and Wave Analysis as Applied to Materials with Micro or Nanostructure*, volume 74. World Scientific, 2007.

[46] T. Chaigne, O. Katz, A. C. Boccara, M. Fink, E. Bossy, and S. Gigan. Controlling light in scattering media non-invasively using the photoacoustic transmission matrix. *Nature Photonics*, **8**(1), pp. 58–64, 2014.

[47] S. Chandrasekhar. *Radiative Transfer*. Dover Publications, New York, NY, 1960.

[48] W. C. Chew, M. S. Tong, and B. Hu. *Integral Equation Methods for Electromagnetic and Elastic Waves*, volume 12. Morgan & Claypool, 2008.

[49] W. C. Chew, E. Michielssen, J. Song, and J. Jin. *Fast and Efficient Algorithms in Computational Electromagnetics*. Artech House, Inc., 2001.

[50] D. Colombi, B. Thors, and C. Törnevik. Implications of EMF exposure limits on output power levels for 5G devices above 6 GHz. *IEEE Antennas and Wireless Propagation Letters*, **14**, pp. 1247–1249, 2015.

[51] D. Colton and R. Kress. *Inverse Acoustic and Electromagnetic Scattering Theory*. Springer-Verlag, Berlin, 1992.

[52] COMSOL. Understand, predict, and optimize physics-based designs and processes with COMSOL multiphysics. COMSOL Inc, Available online at https://www.comsol.com/comsol-multiphysics/, Accessed April, 2021.

[53] R. Cornelius, D. Heberling, N. Koep, A. Behboodi, and R. Mathar. Compressed sensing applied to spherical near-field to far-field transformation. In *2016 10th European Conference on Antennas and Propagation (EuCAP)*, pp. 1–4, 2016.

[54] T. J. Cui, D. R. Smith, and R. Liu, editors. *Metamaterials: Theory, Design, and Applications*. Springer-Verlag, Berlin, 2010.

[55] O. Darrigol. *A History of Optics From Greek Antiquity to the Nineteenth Century*. OUP Oxford, 2012.

[56] S. Datta. *Electronic Transport in Mesoscopic Systems.* Cambridge Studies in Semiconductor Physics and Microelectronic Engineering. Cambridge University Press, 1995.

[57] D. B. Davidson. *Computational Electromagnetics for RF and Microwave Engineering.* Cambridge University Press, 2005.

[58] A. Devaney. Inverse-scattering theory within the Rytov approximation. *Opt. Lett.*, **6**(8), pp. 374–376, 1981.

[59] J.-B. Doré, D. Belot, E. Mercier, S. Bicaïs, G. Gougeon, Y. Corre, B. Miscopein, D. Kténas, and E. C. Strinati. Technology roadmap for beyond 5G wireless connectivity in D-band. In *2020 2nd 6G Wireless Summit (6G SUMMIT)*, pp. 1–5, 2020.

[60] A. Drémeau, A. Liutkus, D. Martina, O. Katz, C. Schülke, F. Krzakala, S. Gigan, and L. Daudet. Reference-less measurement of the transmission matrix of a highly scattering material using a DMD and phase retrieval techniques. *Opt. Express*, **23**(9), pp. 11898–11911, 2015.

[61] T. Durduran, R. Choe, W. B. Baker, and A. G. Yodh. Diffuse optics for tissue monitoring and tomography. *Reports on Progress in Physics*, **73**(7), pp. 076701, 2010.

[62] T. W. Ebbesen, H. J. Lezec, H. F. Ghaemi, T. Thio, and P. A. Wolff. Extraordinary optical transmission through sub-wavelength hole arrays. *Nature*, **391**, pp. 667–669, 1998.

[63] T. F. Eibert, E. Kaliyaperumal, and C. H. Schmidt. Inverse equivalent surface current method with hierarchical higher order basis functions, full probe correction and multilevel fast multipole acceleration. *Progress In Electromagnetics Research*, **106**, pp. 377–394, 2010.

[64] N. Engheta and R. W. Ziolkowski. *Metamaterials: Physics and Engineering Explorations.* John Wiley & Sons, 2006.

[65] J. M. Enoch. Archeological optics: the very first known mirrors and lenses. *Journal of Modern Optics*, **54**(9), pp. 1221–1239, 2007.

[66] J. Epis. Broadband antenna polarizer, August 21 1973. US Patent 3,754,271.

[67] Ericsson. 5G radio access. Technical report, Ericsson white paper, Ericsson AB, Stockholm, Sweden, 2016.

[68] A. Ericsson, J. Lundgren, and D. Sjöberg. Experimental characterization of circular polarization selective structures using linearly single-polarized antennas. *IEEE Trans. Antennas Propag.*, **65**(8), pp. 4239–4249, 2017.

[69] A. Ericsson and D. Sjöberg. A performance study of circular polarization selective structures. In *Proceedings of the 9th European Conference on Antennas and Propagation (EuCAP)*. IEEE, 2015.

[70] A. Ericsson and D. Sjöberg. Design and analysis of a multilayer meander line circular polarization selective structure. *IEEE Trans. Antennas Propag.*, **65**(8), pp. 4089–4101, 2017.

[71] L. Eyges. *The Classical Electromagnetic Field*. Courier Corporation, June 1972.

[72] K. Fan, J. Y. Suen, X. Liu, and W. J. Padilla. All-dielectric metasurface absorbers for uncooled terahertz imaging. *Optica*, **4**(6), pp. 601–604, 2017.

[73] S. Flock, M. Patterson, B. Wilson, and D. Wyman. Monte carlo modeling of light propagation in highly scattering tissues. I. model predictions and comparison with diffusion theory. *IEEE Transactions on Biomedical Engineering*, **36**(12), pp. 1162–1168, 1989.

[74] G. Floquet. Sur les équations différentielles linéaries à coefficients périodique. *Ann. École Norm. Sup.*, **12**, pp. 47–88, 1883.

[75] L. J. Foged, G. Barone, and F. Saccardi. Antenna measurement systems using multi-probe technology. In *2015 IEEE Conference on Antenna Measurements Applications (CAMA)*, pp. 1–3, 2015.

[76] L. L. Foldy. The multiple scattering of waves. I. general theory of isotropic scattering by randomly distributed scatterers. *Phys. Rev.*, **67**, pp. 107–119, 1945.

[77] M. J. Franco. A high-performance dual-mode feed horn for parabolic reflectors with a stepped-septum polarizer in a circular waveguide [antenna designer's notebook]. *IEEE Antennas and Propagation Magazine*, **53**(3), pp. 142–146, 2011.

[78] V. Fusco and B. Nair. Circular polarisation selective surface characterisation and advanced applications. *IEE Proceedings Microwaves Antennas and Propagation*, **153**(3), pp. 247–252, 2006.

[79] S. S. Gao, Q. Luo, and F. Zhu. *Circularly Polarized Antennas*. John Wiley & Sons, 2013.

[80] W. C. Gibson. *The Method of Moments in Electromagnetics*, volume 1. Chapman & Hall/CRC London, UK, 2008.

[81] S. Gigan. Optical microscopy aims deep. *Nature Photonics*, **11**(1), pp. 14–16, 2017.

[82] A. Goetschy and A. D. Stone. Filtering random matrices: The effect of incomplete channel control in multiple scattering. *Phys. Rev. Lett.*, **111**, pp. 063901, 2013.

[83] L. Goldstone. MM wave transmission polarizer. In *Antennas and Propagation Society International Symposium, 1979*, volume 17, pp. 606–609. IEEE, 1979.

[84] J. A. J. Gowlett. The discovery of fire by humans: a longand convoluted process. *Philosophical Transactions of the Royal Society B: Biological Sciences*, **371**(1696), pp. 20150164, 2016.

[85] L. G. Gregoris and K. Iizuka. Thermography in microwave holography. *Applied optics*, **14**(7), pp. 1487–1489, 1975.

[86] J. Gubbi, R. Buyya, S. Marusic, and M. Palaniswami. Internet of things (IoT): A vision, architectural elements, and future directions. *Future Generation Computer Systems*, **29**(7), pp. 1645–1660, 2013.

[87] J. Gunther and S. Andersson-Engels. Review of current methods of acousto-optical tomography for biomedical applications. *Front. Optoelectron*, **10**, pp. 211–238, 2017.

[88] M. Gustafsson and D. Sjöberg. Sum rules and physical bounds on passive metamaterials. *New Journal of Physics*, **12**, pp. 043046, 2010.

[89] N. Halko, P. G. Martinsson, and J. A. Tropp. Finding structure with randomness: Probabilistic algorithms for constructing approximate matrix decompositions. *SIAM Review*, **53**(2), pp. 217–288, 2011.

[90] P. C. Hansen. *Discrete Inverse Problems: Insight and Algorithms*, volume 7. Society for Industrial & Applied Mathematics, 2010.

[91] R. Hansen and L. Bailin. A new method of near field analysis. *IRE Transactions on Antennas and Propagation*, **7**(5), pp. 458–467, 1959.

[92] Q. He, S. Sun, and L. Zhou. Tunable/Reconfigurable Metasurfaces: Physics and Applications. *Research*, **2019**, 2019.

[93] G. R. Heidbreder. Multiple scattering and the method of rytov∗. *J. Opt. Soc. Am.*, **57**(12), pp. 1477–1479, 1967.

[94] J. Helander, A. Ericsson, M. Gustafsson, T. Martin, D. Sjöberg, and C. Larsson. Compressive sensing techniques for mm-wave nondestructive testing of composite panels. *IEEE Trans. Antennas Propag.*, **65**(10), pp. 5523–5531, 2017.

[95] W. Herschel. Experiments on the solar, and on the terrestrial rays that occasion heat; with a comparative view of the laws which occasion them, are subject, in order to determine whether they are the same, or different. part I and part II. **90**, pp. 296–326 and 437–538, 1800.

[96] H. Hertz. On electromagnetic waves in air and their reflection. *Heinrich Rudolph Hertz. Electrical waves*, pp. 124–136, 1888.

[97] N. Heuveldop et al. Ericsson mobility report. Technical Report EAB-17 5964, Technol. Emerg. Bus., Ericsson AB, Stockholm, Sweden, 2017.

[98] D. Hill, A. Bengtsson, T. Erlöv, M. Cinthio, and S. Kröll. Acousto-optic interaction strengths in optically scattering media using high pressure acoustic pulses. *Biomed. Opt. Express*, **12**(6), pp. 3196–3213, 2021.

[99] R. L. Hobbie and B. J. Roth. *Intermediate Physics for Medicine and Biology.* Springer-Verlag, Berlin, 2007.

[100] C. L. Holloway, E. F. Kuester, J. A. Gordon, J. O'Hara, J. Booth, and D. R. Smith. An overview of the theory and applications of metasurfaces: The two-dimensional equivalents of metamaterials. *IEEE Antennas and Propagation Magazine*, **54**(2), pp. 10–35, 2012.

[101] H. Holter and H. Steyskal. On the size requirement for finite phased-array models. *IEEE Trans. Antennas Propag.*, **50**(6), pp. 836–840, June 2002.

[102] J. R. Howell, M. P. Menguc, and R. Siegel. *Thermal Radiation Heat Transfer.* CRC Press, 2010.

[103] C. W. Hsu, S. F. Liew, A. Goetschy, H. Cao, and A. Douglas Stone. Correlation-enhanced control of wave focusing in disordered media. *Nature Physics*, **13**(5), pp. 497–502, 2017.

[104] C. Hülsmeyer. Verfahren, um metallische Gegenstände mittels elektrischer Wellen einem Beobachter zu melden, 30. April 1904. German patent: Reichspatent Nr. 165546.

[105] B. J. Hunt. *The Maxwellians.* Cornell University Press, Ithaca, 1991.

[106] P. T. Hutchison and R. A. Swift. Results of the Telstar satellite space experiments. *The Bell System Technical Journal*, **42**(4), pp. 1475–1504, 1963.

[107] IEEE Future Networks. IEEE 5G and beyond technology roadmap, white paper. *IEEE, Tech. Rep.*, 2017.

[108] W. A. Imbriale, S. S. Gao, and L. Boccia, editors. *Space Antenna Handbook.* Wiley, 2012.

[109] International Commission on Non-Ionizing Radiation Protection (IC-NIRP). Guidelines for limiting exposure to electromagnetic fields (100 kHz to 300 GHz). *Health Phys.*, **118**(5), pp. 483–524, 2020.

[110] A. Ishimaru. *Wave Propagation and Scattering in Random Media. Volume 1. Single Scattering and Transport Theory.* Academic Press, New York, NY, 1978.

[111] A. Ishimaru. *Electromagnetic Wave Propagation, Radiation, and Scattering.* Prentice-Hall, Inc., Englewood Cliffs, New Jersey, 1991.

[112] M. Izzetoglu, S. C. Bunce, K. Izzetoglu, B. Onaral, and K. Pourrezaei. Functional brain imaging using near-infrared technology. *IEEE engineering in medicine and biology magazine: the quarterly magazine of the Engineering in Medicine & Biology Society*, **26**(4), pp. 38–46, 2007.

[113] G. W. J. Frercksa, H. Weberb. Reception and discovery: the nature of johann wilhelm ritter's invisible rays. **340**(2), pp. 143–156, 2009.

[114] J. D. Jackson. *Classical Electrodynamics.* John Wiley & Sons, New York, NY, third edition, 1999.

[115] J. Jin. *The Finite Element Method in Electromagnetics.* John Wiley & Sons, New York, NY, 1993.

[116] J. M. Jin. *Theory and Computation of Electromagnetic Fields.* Wiley, 2011.

[117] P. Joly and G. Meurant. Complex conjugate gradient methods. *Numerical Algorithms*, **4**(3), pp. 379–406, 1993.

[118] M. Joyal and J. Laurin. A cascaded circular-polarization-selective surface at K band. In *Antennas and Propagation (APSURSI), 2011 IEEE International Symposium on*, pp. 2657–2660. IEEE, 2011.

[119] M. Joyal and J. Laurin. Analysis and design of thin circular polarizers based on meander lines. *IEEE Trans. Antennas Propag.*, **60**(6), pp. 3007–3011, 2012.

[120] M. Joyal and J. Laurin. Design and analysis of a cascade circular-polarization-selective surface at K band. *IEEE Trans. Antennas Propag.*, **62**(6), pp. 3043–3052, 2014.

[121] B. Judkewitz, Y. M. Wang, R. Horstmeyer, A. Mathy, and C. Yang. Speckle-scale focusing in the diffusive regime with time reversal of variance-encoded light (TROVE). *Nature Photonics*, **7**(4), pp. 300–305, 2013.

[122] G. Julian H. *Introduction to Thermoelectricity.* Springer-Verlag, Berlin Heidelberg, 2010.

[123] A. Karlsson and G. Kristensson. Constitutive relations, dissipation and reciprocity for the Maxwell equations in the time domain. *J. Electromagnet. Waves Appl.*, **6**(5/6), pp. 537–551, 1992.

[124] S. Kharkovsky and R. Zoughi. Microwave and millimeter wave nondestructive testing and evaluation - overview and recent advances. *IEEE Instrum. Meas. Mag.*, **10**(2), pp. 26–38, 2007.

[125] A. Kiamanesh. In-situ tuned microwave oil extraction process, January 21 1992. US Patent 5,082,054.

[126] J. Kiefer. Sequential minimax search for a maximum. *Proceedings of the American Mathematical Society*, **4**(3), pp. 502–506, 1953.

[127] H. Kirschbaum and S. Chen. A method of producing broad-band circular polarization employing an anisotropic dielectric. *IRE Transactions on Microwave Theory and Techniques*, **5**(3), pp. 199–203, 1957.

[128] C. Kittel. *Introduction to Solid State Physics*. John Wiley & Sons, New York, NY, 8 edition, 2005.

[129] M. Kline and I. W. Kay. *Electromagnetic Theory and Geometrical Optics*. John Wiley & Sons, New York, NY, 1965.

[130] K. J. K. Koerkamp, S. Enoch, F. B. Segerink, N. F. van Hulst, and L. Kuipers. Strong influence of hole shape on extraordinary transmission through periodic arrays of subwavelength holes. *Phys. Rev. Lett.*, **92**(18), pp. 183901, 2004.

[131] N. V. Korovkin, V. L. Chechurin, and M. Hayakawa. *Inverse Problems in Electric Circuits and Electromagnetics*. Springer Science & Business Media, 2007.

[132] D. J. Kozakoff. *Analysis of Radome-Enclosed Antennas*. Artech House, 2010.

[133] G. Kristensson. *Scattering of Electromagnetic Waves by Obstacles*. SciTech Publishing, an imprint of the IET, Edison, NJ, 2016.

[134] I. Kuzle, H. Pandzic, and D. Bosnjak. The true inventor of the radio communications. In *2008 IEEE History of Telecommunications Conference*, pp. 20–23, 2008.

[135] S. A. Kuznetsov, A. G. Paulish, M. Navarro-Cía, and A. V. Arzhannikov. Selective pyroelectric detection of millimetre waves using ultra-thin metasurface absorbers. *Scientific reports*, **6**, pp. 21079, 2016.

[136] S. A. Kuznetsov, A. G. Paulish, A. V. Gelfand, P. A. Lazorskiy, and V. N. Fedorinin. Bolometric THz-to-IR converter for terahertz imaging. *Applied Physics Letters*, **99**(2), pp. 023501, 2011.

[137] A. Lait. Broadband circular polarisers. *Marconi Review*, **32**(173), pp. 159, 1969.

[138] T. Laitinen, S. Pivnenko, and O. Breinbjerg. Iterative probe correction technique for spherical near-field antenna measurements. *IEEE Antennas and Wireless Propagation Letters*, **4**, pp. 221–223, 2005.

[139] M. Lax. Multiple scattering of waves. *Reviews of Modern Physics*, **23**(4), pp. 287–310, 1951.

[140] M. Lax. Multiple scattering of waves. II. The effective field in dense systems. *Phys. Rev.*, **85**, pp. 621–629, Feb 1952.

[141] C. A. Leal-Sevillano, J. A. Ruiz-Cruz, J. R. Montejo-Garai, and J. M. Rebollar. Wide-band compact antenna feed for multi-beam satellite communications. In *Antennas and Propagation (EuCAP), 2015 9th European Conference on*, pp. 1–4. IEEE, 2015.

[142] D. Lerner. A wave polarization converter for circular polarization. *IEEE Trans. Antennas Propag.*, **13**(1), pp. 3–7, 1965.

[143] J. L.-W. Li, W.-L. Ong, and K. H. R. Zheng. Anisotropic scattering effects of a gyrotropic sphere characterized using the T-matrix method. *Phys. Rev. E*, **85**, pp. 036601, 2012.

[144] S.-Q. Li, X. Xu, R. Maruthiyodan Veetil, V. Valuckas, R. Paniagua-Domínguez, and A. I. Kuznetsov. Phase-only transmissive spatial light modulator based on tunable dielectric metasurface. *Science*, **364**(6445), pp. 1087–1090, 2019.

[145] Y. Liu, P. Lai, C. Ma, X. Xu, A. A. Grabar, and L. V. Wang. Optical focusing deep inside dynamic scattering media with near-infrared time-reversed ultrasonically encoded ([true]) light. *Nat Commun*, **19**, 2015.

[146] A. Liutkus, D. Martina, S. Popoff, G. Chardon, O. Katz, G. Lerosey, S. Gigan, L. Daudet, and I. Carron. Imaging With Nature: Compressive Imaging Using a Multiply Scattering Medium. *Scientific Reports*, **4**(1), pp. 5552, 2014.

[147] I. Lopez and J. Laurin. A circular polarization selective surface implemented on a flexible substrate. *IEEE Trans. Antennas Propag.*, **62**(7), pp. 3847–3852, 2014.

[148] I. Lopez and J.-J. Laurin. Alternative topologies of circular polarization selective surfaces based on modifications of the Pierrot cell. *IEEE Trans. Antennas Propag.*, **63**(4), pp. 1465–1472, 2015.

[149] V. Lucarini, J. J. Saarinen, K.-E. Peiponen, and E. M. Vartiainen. *Kramers-Kronig Relations in Optical Materials Research*. Springer-Verlag, Berlin, 2005.

[150] S. Lucero. IoT platforms: Enabling the Internet of Things. Technical report, IHSTechnol., London, U.K., White Pape, 2016.

[151] A. Ludvig-Osipov, J. Lundgren, C. Ehrenborg, Y. Ivanenko, A. Ericsson, M. Gustafsson, B. L. G. Jonsson, and D. Sjöberg. Fundamental bounds on transmission through periodically perforated metal screens with experimental validation. *IEEE Transactions on Antennas and Propagation*, **68**(2), pp. 773–782, 2020.

[152] J. Lundgren, A. Ericsson, and D. Sjöberg. Design, optimization and verification of a dual band circular polarization selective structure. *IEEE Transactions on Antennas and Propagation*, **66**(11), pp. 6023–6032, 2018.

[153] J. Lundgren. Dual band circular polarization selective structures for space applications. Master's thesis, Lund University, Department of Electrical and Information Technology, P.O. Box 118, SE-221 00 Lund, Sweden, 2016. Rep. No. LU/LTH-EIT 2016-540.

[154] J. Lundgren, M. Gustafsson, D. Sjöberg, and M. Nilsson. IR and metasurface based mm-wave camera. *Applied Physics Letters*, **118**(18), pp. 184104, 2021.

[155] J. Lundgren, J. Helander, M. Gustafsson, D. Sjöberg, B. Xu, and D. Colombi. Near-field measurement and calibration technique for rf emf exposure assessment of mm-wave 5G devices. Technical Report LUTEDX/(TEAT-7267)/1–30/(2019), Lund University, Department of Electrical and Information Technology, P.O. Box 118, S-221 00 Lund, Sweden, 2019.

[156] J. Lundgren, J. Helander, M. Gustafsson, D. Sjoberg, B. Xu, and D. Colombi. A near-field measurement and calibration technique: Radio-frequency electromagnetic field exposure assessment of millimeter-wave 5G devices. *IEEE Antennas and Propagation Magazine*, pp. 0–0, 2020.

[157] S. A. Maier. *Plasmonics: Fundamentals and Applications.* Springer-Verlag, Berlin, 2007.

[158] N. Marcuvitz. *Waveguide Handbook.* McGraw-Hill, New York, NY, 1951.

[159] R. J. I. Marks. *Introduction to Shannon Sampling and Interpolation Theory.* Springer Science & Business Media, 2012.

[160] L. Martín-Moreno, F. J. García-Vidal, H. J. Lezec, K. M. Pellerin, T. Thio, J. B. Pendry, and T. W. Ebbesen. Theory of extraordinary optical transmission through subwavelength hole arrays. *Phys. Rev. Lett.*, **86**(6), pp. 1114–1117, 2001.

[161] A. Massa, P. Rocca, and G. Oliveri. Compressive sensing in electromagnetics – a review. *IEEE Antennas Propag. Mag.*, **57**(1), pp. 224–238, 2015.

[162] J. C. Maxwell. A dynamical theory of the electromagnetic field. *Philos. Trans. R. Soc. London*, **155**, pp. pp. 459–512, 1865.

[163] J. C. Maxwell. *A Treatise on Electricity and Magnetism*, volume 1. Dover Publications, New York, NY, 1954.

[164] J. C. Maxwell. *A Treatise on Electricity and Magnetism*, volume 2. Dover Publications, New York, NY, 1954.

[165] G. Minatti, M. Faenzi, E. Martini, F. Caminita, P. D. Vita, D. G. lez Ovejero, M. Sabbadini, and S. Maci. Modulated metasurface antennas for space: Synthesis, analysis and realizations. *IEEE Trans. Antennas Propag.*, **63**(4), pp. 1288–1300, 2015.

[166] G. Minatti, S. Maci, P. D. Vita, A. Freni, and M. Sabbadini. A circularly-polarized isoflux antenna based on anisotropic metasurface. *IEEE Trans. Antennas Propag.*, **60**(11), pp. 4998–5009, 2012.

[167] M. I. Mishchenko, L. D. Travis, and A. A. Lacis. *Multiple Scattering of Light by Particles: Radiative Transfer and Coherent Backscattering.* Cambridge University Press, Cambridge, 2006.

[168] M. I. Mishchenko, G. Videen, V. A. Babenko, N. G. Khlebtsov, and T. Wriedt. T-matrix theory of electromagnetic scattering by particles and its applications: a comprehensive reference database. *J. Quant. Spectrosc. Radiat. Transfer*, **88**(1-3), pp. 357–406, 2004.

[169] G. A. Morin. A simple circular polarization selective surface (CPSS). In *Antennas and Propagation Society International Symposium, 1990. AP-S. Merging Technologies for the 90's. Digest.*, pp. 100–103. IEEE, 1990.

[170] G. Morin. Circular polarization selective surface made of resonant spirals, 1994. US Patent 5,280,298.

[171] G. A. Morin. A circular polarization selective surface made of resonant helices. Technical report, DTIC Document, 1995.

[172] A. Motevasselian and B. L. G. Jonsson. Design of a wideband rasorber with a polarisation-sensitive transparent window. *IET Microwaves, Antennas Propagation*, **6**(7), pp. 747–755, 2012.

[173] B. Munk. *Frequency Selective Surfaces: Theory and Design.* John Wiley & Sons, New York, NY, 2000.

[174] K. Muzaffar, L. I. Giri, K. Chatterjee, S. Tuli, and S. Koul. Fault detection of antenna arrays using infrared thermography. *Infrared Physics & Technology*, **71**, pp. 464–468, 2015.

[175] K. Muzaffar, S. Tuli, and S. Koul. Beam width estimation of microwave antennas using lock-in infrared thermography. *Infrared Physics & Technology*, **72**, pp. 244–248, 2015.

[176] J. Neff, R. Athale, and S. Lee. Two-dimensional spatial light modulators: a tutorial. *Proceedings of the IEEE*, **78**(5), pp. 826–855, 1990.

[177] J. Norgard and R. Musselman. Direct infrared measurements of phased array near-field and far-field antenna patterns. *Quantitative InfraRed Thermography Journal*, **2**(1), pp. 113–126, 2005.

[178] V. Ntziachristos. Going deeper than microscopy: the optical imaging frontier in biology. *Nature Methods*, **7**(8), pp. 603–614, 2010.

[179] H. M. Nussenzveig. *Causality and Dispersion Relations*. Academic Press, London, 1972.

[180] S. J. Orfanidis. Electromagnetic Waves and Antennas, 2016. Available online at http://www.ece.rutgers.edu/ orfanidi/ewa/.

[181] S. V. Parekh. Dual gridded reflector structure, November 25 1986. US Patent 4,625,214.

[182] D. Paris, W. Leach Jr, and E. Joy. Basic theory of probe-compensated near-field measurements. *IEEE Trans. Antennas Propag.*, **26**(3), pp. 373–379, 1978.

[183] B. E. Penprase. *The Power of Stars: How Celestial Observations Have Shaped Civilization*. Springer-Verlag, New York, 1 edition, 2011.

[184] L. Petersson and G. Smith. On the use of a gaussian beam to isolate the edge scattering from a plate of finite size. *IEEE Transactions on Antennas and Propagation*, **52**(2), pp. 505–512, 2004.

[185] S. Pfeifer, E. Carrasco, P. Crespo-Valero, E. Neufeld, S. Kühn, T. Samaras, A. Christ, M. H. Capstick, and N. Kuster. Total field reconstruction in the near field using pseudo-vector E-field measurements. *IEEE Trans. Electromagn. Compat.*, **61**, pp. 476–486, 2019.

[186] R. Pierrot. Reflector for circularly polarized waves, 1970. US Patent 3,500,420.

[187] L. Poli, G. Oliveri, and A. Massa. Microwave imaging within the first-order born approximation by means of the contrast-field bayesian compressive sensing. *IEEE Trans. Antennas Propag.*, **60**(6), pp. 2865–2879, 2012.

[188] C. Polk. Optical fresnel-zone gain of a rectangular aperture. *IRE Transactions on Antennas and Propagation*, **4**(1), pp. 65–69, 1956.

[189] S. M. Popoff, G. Lerosey, R. Carminati, M. Fink, A. C. Boccara, and S. Gigan. Measuring the transmission matrix in optics: An approach to the study and control of light propagation in disordered media. *Phys. Rev. Lett.*, **104**, pp. 100601, 2010.

[190] S. Poulsen. Artificial puck plate radomes. In *Proc. International Confer-
ence on Electromagnetics in Advanced Applications (ICEAA'05)*, Torino,
Italy, 2005.

[191] S. Poulsen. *Stealth Radomes*. PhD thesis, Lund University, Department
of Electroscience, Lund University, P.O. Box 118, S-221 00 Lund, Sweden,
2006.

[192] D. M. Pozar. *Microwave Engineering*. John Wiley & Sons, New York, NY,
third edition, 2005.

[193] D. Prost, F. Issac, and M. Romier. Imaging electric and magnetic near field
of radiating structures by infrared thermography. In *2019 International
Symposium on Electromagnetic Compatibility-EMC EUROPE*, pp. 311–
314. IEEE, 2019.

[194] O. Quevedo-Teruel, H. Chen, A. Díaz-Rubio, G. Gok, A. Grbic, G. Minatti,
E. Martini, S. Maci, G. V. Eleftheriades, M. Chen, et al. Roadmap on
metasurfaces. *Journal of Optics*, **21**(7), pp. 073002, 2019.

[195] Y. Ra'di. *Functional Metasurfaces*. PhD thesis, Aalto University, 2015.

[196] B. Rajaei, E. W. Tramel, S. Gigan, F. Krzakala, and L. Daudet. Intensity-
only optical compressive imaging using a multiply scattering material and
a double phase retrieval approach. In *2016 IEEE International Conference
on Acoustics, Speech and Signal Processing (ICASSP)*, pp. 4054–4058.
IEEE, 2016.

[197] S. M. Rao. *Time Domain Electromagnetics*. Academic Press, 1999.

[198] S. Rao, L. Shafai, and S. K. Sharma. *Handbook of Reflector Antennas and
Feed Systems Volume III: Applications of Reflectors*. Artech house, 2013.

[199] T. S. Rappaport, S. Sun, R. Mayzus, H. Zhao, Y. Azar, K. Wang, G. N.
Wong, J. K. Schulz, M. Samimi, and F. Gutierrez. Millimeter wave mobile
communications for 5G cellular: It will work! *Access, IEEE*, **1**, pp. 335–
349, 2013.

[200] A. K. Rashid, B. Li, and Z. Shen. An overview of three-dimensional
frequency-selective structures. *IEEE Antennas and Propagation Magazine*,
56(3), pp. 43–67, 2014.

[201] A. K. Rashid and Z. Shen. A novel band-reject frequency selective sur-
face with pseudo-elliptic response. *IEEE Trans. Antennas Propag.*, **58**(4),
pp. 1220–1226, 2010.

[202] S. G. Resink, A. C. Boccara, and W. Steenbergen. State-of-the art of
acousto-optic sensing and imaging of turbid media. *Journal of Biomedical
Optics*, **17**(4), pp. 040901, 2012.

[203] A. G. Roederer and G. A. Crone. Double grid reflector antenna, March 3 1987. US Patent 4,647,938.

[204] W. C. Röntgen. On a new kind of rays. **3**(59), pp. 227–231, 1896.

[205] S. Rotter and S. Gigan. Light fields in complex media: Mesoscopic scattering meets wave control. *Rev. Mod. Phys.*, **89**, pp. 015005, 2017.

[206] J. E. Roy and L. Shafai. Reciprocal circular-polarization-selective surface. *Antennas and Propagation Magazine, IEEE*, **38**(6), pp. 18–33, 1996.

[207] A. V. Ruban. Evolution under the sun: optimizing light harvesting in photosynthesis. *Journal of Experimental Botany*, **66**(1), pp. 7–23, 2014.

[208] B. E. A. Saleh and M. C. Teich. *Fundamentals of Photonics.* John Wiley & Sons, New York, NY, 1991.

[209] J. Sanz-Fernandez, E. Saenz, and P. de Maagt. A circular polarization selective surface for space applications. *IEEE Trans. Antennas Propag.*, **63**(6), pp. 2460–2470, 2015.

[210] J. Sanz-Fernandez, E. Saenz, P. de Maagt, and C. Mangenot. Circular polarization selective surface for dual-optics CP offset reflector antennas in Ku-band. In *Proceedings of the 6th European Conference on Antennas and Propagation (EuCAP)*, pp. 2683–2687. IEEE, 2012.

[211] J. W. Schultz. *Focused Beam Methods: Measuring Microwave Materials in Free Space.* John Schultz, 2012.

[212] A. Schuster. Radiation through a foggy atmosphere. *The astrophysical journal*, **21**, pp. 1, 1905.

[213] I. Schwab. The evolution of eyes: major steps. *The Keeler lecture 2017: centenary of Keeler Ltd*, **32**, pp. 302–313, 2018.

[214] K. T. Selvan and R. Janaswamy. Fraunhofer and Fresnel distances : Unified derivation for aperture antennas. *IEEE Antennas and Propagation Magazine*, **59**(4), pp. 12–15, 2017.

[215] M. Shafi, A. F. Molisch, P. J. Smith, T. Haustein, P. Zhu, P. De Silva, F. Tufvesson, A. Benjebbour, and G. Wunder. 5g: A tutorial overview of standards, trials, challenges, deployment, and practice. *IEEE Journal on Selected Areas in Communications*, **35**(6), pp. 1201–1221, 2017.

[216] K. Shafique, B. A. Khawaja, F. Sabir, S. Qazi, and M. Mustaqim. Internet of Things (IoT) for next-generation smart systems: A review of current challenges, future trends and prospects for emerging 5G-IoT scenarios. *IEEE Access*, **8**, pp. 23022–23040, 2020.

[217] A. M. Shaltout, V. M. Shalaev, and M. L. Brongersma. Spatiotemporal light control with active metasurfaces. *Science*, **364**(6441), 2019.

[218] A. Sihvola. Metamaterials in electromagnetics. *Metamaterials*, **1**(1), pp. 2–11, 2007.

[219] S. Silver. *Microwave Antenna Theory and Design*, volume 12 of *Radiation Laboratory Series*. McGraw-Hill, New York, NY, 1949.

[220] Simulia. Automatic Optimization, CST Studio Suite, 2021. Available at https://www.3ds.com/products-services/simulia/products/cst-studio-suite/optimization/, accessed 2021-04-08.

[221] J. O. Smith. *Mathematics of the Discrete Fourier Transform*. W3K Publishing, 2. ed. edition, 2007.

[222] L. Solymar and E. Shamonina. *Waves in Metamaterials*. Oxford University Press, 2009.

[223] A. Sommerfeld. *Partial Differential Equations in Physics*. Academic Press, New York, NY, 1949.

[224] E. M. Soop. *Handbook of Geostationary Orbits*, volume 3. Springer Science & Business Media, 1994.

[225] SPEAG. EUmmWVx / 5G ProbeE-Field mm-Wave Probe for General Near-Field Measurements. Schmid & Partner Engineering AG, Zurich, Switzerland, [Online] https://speag.swiss/products/dasy6/probes/new-eummwvx-vector-e-probe/, Retrieved: Jan. 2019.

[226] M. Stichs. Introduction to NVIDIA RTX and DirectX ray tracing, 2018. Available at: https://developer.nvidia.com/blog/introduction-nvidia-rtx-directx-ray-tracing/, accessed 2021-04-22.

[227] M. I. Stockman. Nanoplasmonics: The physics behind the applications. **64**, pp. 39–44, 2011.

[228] W. L. Stutzman and G. A. Thiele. *Antenna Theory and Design*. John Wiley & Sons, New York, NY, second edition, 1998.

[229] A. Taflove and S. C. Hagness. *Computational electrodynamics: The Finite-Difference Time-Domain Method*. Artech House, Boston, MA, 2000.

[230] T. Tao. *Topics in Random Matrix Theory*. American Mathematical Society, 2012.

[231] H. Tataria, M. Shafi, A. F. Molisch, M. Dohler, H. Sjöland, and F. Tufvesson. 6G wireless systems: Vision, requirements, challenges, insights, and opportunities. *Proceedings of the IEEE*, pp. 1–34, 2021.

[232] The MathWorks, Inc. MATLAB. https://se.mathworks.com/products/matlab.html, 2021. Accessed April, 2021.

[233] S. E. Thompson and S. Parthasarathy. Moore's law: the future of si microelectronics. *Materials Today*, **9**(6), pp. 20–25, 2006.

[234] W. V. Tilston, T. Tralman, and S. M. Khanna. A polarization selective surface for circular polarization. In *Antennas and Propagation Society International Symposium, 1988. AP-S. Digest*, pp. 762–765. IEEE, 1988.

[235] S. Tretyakov, I. Nefedov, A. Sihvola, S. Maslovski, and C. Simovski. Waves and energy in chiral nihility. *Journal of electromagnetic waves and applications*, **17**(5), pp. 695–706, 2003.

[236] P. Y. Ufimtsev. *Fundamentals of the Physical Theory of Diffraction.* John Wiley & Sons, 2007.

[237] P. L. E. Uslenghi, editor. *Electromagnetic Scattering.* Academic Press, New York San Fransisco London, 1978.

[238] J. G. van Bladel. *Electromagnetic Fields.* IEEE Press, Piscataway, NJ, second edition edition, 2007.

[239] P. M. van den Berg and R. E. Kleinman. A contrast source inversion method. *Inverse Problems*, **13**, pp. 1607–1620, 1997.

[240] D. F. Vanderwerf. *The Story of Light Science.* Springer International Publishing, 2017.

[241] J. C. Vardaxoglou. *Frequency Selective Surfaces (Analysis and Design).* Research Studies Press, 1997.

[242] I. M. Vellekoop, A. Lagendijk, and A. P. Mosk. Exploiting disorder for perfect focusing. *Nature Photonics*, **4**(5), pp. 320–322, 2010.

[243] I. M. Vellekoop and A. P. Mosk. Focusing coherent light through opaque strongly scattering media. *Opt. Lett.*, **32**(16), pp. 2309–2311, 2007.

[244] I. M. Vellekoop, E. G. van Putten, A. Lagendijk, and A. P. Mosk. Demixing light paths inside disordered metamaterials. *Opt. Express*, **16**(1), pp. 67–80, 2008.

[245] C. Venet, M. Bocoum, J.-B. Laudereau, T. Chaneliere, F. Ramaz, and A. Louchet-Chauvet. Ultrasound-modulated optical tomography in scattering media: flux filtering based on persistent spectral hole burning in the optical diagnosis window. *Opt. Lett.*, **43**(16), pp. 3993–3996, 2018.

[246] V. G. Veselago. The electrodynamics of substances with simultaneously negative values of ϵ and μ. *Sov. Phys. Usp.*, **10**(4), pp. 509–514, 1968.

[247] A. Walther, L. Rippe, L. V. Wang, S. Andersson-Engels, and S. Kröll. Analysis of the potential for non-invasive imaging of oxygenation at heart depth, using ultrasound optical tomography (UOT) or photo-acoustic tomography (PAT). *Biomedical Optics Express*, **8**(10), pp. 4523–4536, 2017.

[248] L. V. Wang. Ultrasound-mediated biophotonic imaging: a review of acousto-optical tomography and photo-acoustic tomography. *Disease Markers*, **19**(2-3), pp. 123–138, 2003.

[249] L. Wang and H.-I. Wu. *Radiative Transfer Equation and Diffusion Theory*, chapter 5, pp. 83–118. John Wiley & Sons, Ltd, 2009.

[250] J. Wells. Faster than fiber: the future of multi-Gb/s wireless. *IEEE Microw. Mag.*, **10**(3), pp. 104–112, 2009.

[251] D. H. Werner and D.-H. Kwon. *Transformation Electromagnetics and Metamaterials.* Springer, 2015.

[252] T. K. Wu. *Frequency Selective Surface and Grid Array.* New York, John Wiley & Sons Inc., 1995.

[253] B. Xu, K. Zhao, B. Thors, D. Colombi, O. Lundberg, Z. Ying, and S. He. Power density measurements at 15 GHz for RF EMF compliance assessments of 5G user equipment. *IEEE Trans. Antennas Propag.*, **65**(12), pp. 6584–6595, 2017.

[254] X. Xu, H. Liu, and L. V. Wang. Time-reversed ultrasonically encoded optical focusing into scattering media. *Nature Photonics*, **5**(3), pp. 154–157, 2011.

[255] A. Yadav, P. Deshmukh, K. Roberts, N. Jisrawi, and S. Valluri. An analytic study of the Wiedemann–Franz law and the thermoelectric figure of merit. *Journal of Physics Communications*, **3**(10), pp. 105001, 2019.

[256] A. D. Yaghjian. Approximate formulas for the far field and gain of open-ended rectangular waveguide. *IEEE Trans. Antennas Propag.*, **32**(4), pp. 378–384, 1984.

[257] A. D. Yaghjian. Equivalence of surface current and aperture field integrations for reflector antennas. *IEEE Trans. Antennas Propag.*, **32**(12), pp. 1355–1358, 1984.

[258] A. D. Yaghjian. An overview of near-field antenna measurements. *IEEE Trans. Antennas Propag.*, **34**(1), pp. 30–45, January 1986.

[259] H. Yılmaz, W. C. Hsu, A. Yamilov, and H. Cao. Transverse localization of transmission eigenchannels. *Nat. Photonics*, **13**, pp. 352–358, 2019.

[260] A. H. Zemanian. *Distribution Theory and Transform Analysis: an Introduction to Generalized Functions, with Applications.* Dover Publications, New York, NY, 1987.

[261] S. Zhang, Y.-S. Park, J. Li, X. Lu, W. Zhang, and X. Zhang. Negative refractive index in chiral metamaterials. *Phys. Rev. Lett.*, **102**, pp. 023901, 2009.

[262] X. Zhang, Q. Li, F. Liu, M. Qiu, S. Sun, Q. He, and L. Zhou. Controlling angular dispersions in optical metasurfaces. *Light: Science & Applications*, **9**(76), 2020.

[263] K. Zhao, M. N. Vouvakis, and J.-F. Lee. The adaptive cross approximation algorithm for accelerated method of moments computations of EMC problems. *IEEE Trans. Electromagn. Compat.*, **47**(4), pp. 763–773, 2005.

[264] E. H. Zhou, H. Ruan, C. Yang, and B. Judkewitz. Focusing on moving targets through scattering samples. *Optica*, **1**(4), pp. 227–232, 2014.

Part II: Included Papers

Fundamental Bounds on Transmission Through Periodically Perforated Metal Screens with Experimental Validation

Andrei Ludvig-Osipov, Johan Lundgren, Casimir Ehrenborg, Yevhen Ivanenko, Andreas Ericsson, Mats Gustafsson, B.L.G Jonsson, and Daniel Sjöberg

Abstract

This paper presents a study of transmission through arrays of periodic sub-wavelength apertures. Fundamental limitations for this phenomenon are formulated as a sum rule, relating the transmission coefficient over a bandwidth to the static polarizability. The sum rule is rigorously derived for arbitrary periodic apertures in thin screens. By this sum rule we establish a physical bound on the transmission bandwidth which is verified numerically for a number of aperture array designs. We utilize the sum rule to design and optimize sub-wavelength frequency selective surfaces with a bandwidth close to the physically attainable. Finally, we verify the sum rule and simulations by measurements of an array of horseshoe-shaped slots milled in aluminum foil.

1   Introduction

High transmission through periodically perforated metal screens occurs at certain frequencies associated with various resonance phenomena. Those can be intrinsic resonances of the apertures, related to their size and geometry, or resonances related to the periodicity. Some transmission peaks, referred to as extraordinary transmission [9, 24, 27], have been explained from a theoretical perspective by surface plasmon polaritons at optical frequencies [12, 24], and by spoof plasmons at radio frequencies [34]. From the practical perspective it is desirable to know what is the maximum attainable transmission bandwidth, regardless of the nature of the transmission. Here, we formulate a fundamental bound on the transmission bandwidth in the form of a sum rule.

Applications of such structures include spatially tunable filters, near-field imaging and modulators as well as negative refractive index metamaterials [11]. In frequency selective surface (FSS) design subwavelength apertures are commonly used [30]. A proposed FSS application is slotted infrared-protective metalized windows [13]. These would be transparent for cell phone signals, to increase coverage inside of buildings, while serving as a barrier for infrared waves. Also, such structures localize high power flow within the apertures [3]. This effect can be additionally increased by designing apertures with narrow slots. This can be used to create nonlinear devices with strong concentration of fields. A further application is the Bethe-hole directional coupler [4, 20], where a periodic sequence of apertures in a wall joining two waveguides is designed to provide a coupling mechanism in the band of interest. Extraordinary transmission (EoT) is an interesting phenomenon, when transmissivity exceeds the predictions of a classical diffraction theory [4, 20]. Originally discovered and analyzed in optics [9], it has been observed and discussed also for electromagnetic millimeter waves, see *e.g.*, [2, 28], and in acoustics [26].

A limiting factor of many FSS and EoT applications is that the frequency bands where a high transmission occurs are rather narrow. Naturally, it is desirable to understand the limitations of this effect; how much bandwidth is achievable and at what frequencies. The tuning of the transmission bandwidth is

an iterative trial-and-error procedure, usually assisted by heuristically reasoned guidelines [30]. To facilitate this procedure, a physical bound in the form of a sum rule is proposed. Sum rules have been derived for different types of periodic structures, such as transmission blockage [15, 36], extinction cross section [19], high-impedance surfaces [17], and antennas [8, 22]. The transmission cross section sum rule [16] produces a bound on the bandwidth transmission cross section product for single apertures. These sum rules are targeted for their particular applications and cannot be used to determine bounds on the perforated screen's transmission bandwidth.

In this paper, we present a derivation of a sum rule for perforated screens, which shows that the total transmission bandwidth is limited from above by the normalized static polarizability of the structure. We validate the sum rule by comparison both with simulated periodic structures, and also with measurements. We illustrate how the sum rule can be utilized in the design and bandwidth optimization of FSS. The sum rule is derived here for structures consisting of an infinitely thin perfect electric conductor (PEC) screen. We show by simulations that the transmitted power and bandwidth of a generic periodic design is not greatly affected by a finite thickness and conductivity up to certain limits. This motivates the use of the sum rule in evaluation of real structures as well as in a penalty function in optimization. The sum rule is valid for all types of transmission peaks for periodically perforated metal screens.

In the presented examples, we consider transmission peaks, associated with resonances of sub-wavelength apertures. A horseshoe slot aperture was designed and optimized utilizing the sum rule to maximize the transmission bandwidth in the lowest frequency peak. This design was manufactured in aluminum foil and measured in the frequency range $10\,\text{GHz}$ to $20\,\text{GHz}$.

The rest of the paper is organized as follows. Section 2 formulates the problem of scattering against periodic screens, and Section 3 gives a derivation of the sum rule for periodic structures. Numerical examples validating and illustrating the sum rule are presented in Section 4 along with a demonstration of how the sum rule is used in the design process. Section 5 investigates the applicability of the sum rule for non-ideal structures. Section 6 provides the details of the manufacturing process and the measurement setup, and presents the measured transmission coefficient, which is also compared to the theoretical predictions. Finally, the results of this paper are summarized and discussed in Section 7.

2   Scattering by Periodic Perforated Screens

We consider the scattering of a linearly polarized electromagnetic plane wave by a periodically perforated metal screen in free space, see Figure 1. The goal is to quantify the amount of transmitted power that passes through the structure and continues to propagate as a wave of the same frequency, polarization and direction

as the incident wave. To accomplish this, we extend the initial theoretical results reported in [18], and use them to impose a bandwidth bound on the power transmission of such structures. The theory is derived under the assumption that the structure is an infinitely thin two-dimensional periodic PEC screen of infinite extent in the plane normal to the incident wave direction. In Sections 5 and 6, these assumptions are validated to be reasonable approximations for power transmission through real structures.

The screen is placed in the xy-plane at $z = 0$, and the unit cell is defined by the lattice vectors $l_x \hat{\boldsymbol{x}}$ and $l_y \hat{\boldsymbol{y}}$. The incoming wave with the associated electric field $\boldsymbol{E}^{(i)}(k, \boldsymbol{r}) = E^{(i)} \mathrm{e}^{\mathrm{i}\boldsymbol{k} \cdot \boldsymbol{r}} \hat{\boldsymbol{e}}$ is propagating in the positive z-direction, where $\hat{\boldsymbol{e}}$ is the polarization unit vector, $k = \omega/c_0$ is the wave number in free space with ω and c_0 being the angular frequency and the speed of light in vacuum, respectively, $\boldsymbol{k} = k\hat{\boldsymbol{z}}$ is the wavevector, $\boldsymbol{r}$ is the field position vector, and the time convention $\mathrm{e}^{-\mathrm{i}\omega t}$ is used. Interaction between the incident wave and the structure gives rise to the scattered field. We denote the scattered field in $z < 0$ as the reflected field $\boldsymbol{E}^{(r)}(k, \boldsymbol{r})$, and the total field in $z > 0$ as the transmitted field $\boldsymbol{E}^{(t)}(k, \boldsymbol{r})$. A spectral decomposition of the transmitted field in Floquet modes is

$$\boldsymbol{E}^{(t)}(k, \boldsymbol{r}) = \sum_{m,n=-\infty}^{\infty} \boldsymbol{E}_{mn}^{(t)}(k) \mathrm{e}^{\mathrm{i}\boldsymbol{k}_{mn} \cdot \boldsymbol{r}}, \tag{2.1}$$

where $\boldsymbol{k}_{mn} = k_{x,n}\hat{\boldsymbol{x}} + k_{y,m}\hat{\boldsymbol{y}} + k_{z,mn}\hat{\boldsymbol{z}}$ are the modal wave vectors with $k_{x,n} = 2\pi n/l_x$, $k_{y,m} = 2\pi m/l_y$, $k_{z,mn} = \sqrt{k^2 - k_{x,n}^2 - k_{y,m}^2}$ and $\boldsymbol{E}_{mn}^{(t)}(k)$ are the expansion coefficients. The latter are related to the incident field through a linear mapping

$$\boldsymbol{E}_{mn}^{(t)}(k) = \mathbf{T}_{mn}(k) \cdot \boldsymbol{E}^{(i)}(k, z = 0), \tag{2.2}$$

where $\mathbf{T}_{mn}(k)$ are the transmission dyadic tensors. For frequencies below the first grating lobe, $f < c_0/\max\{l_x, l_y\}$ [30], only the fundamental mode is propagating. We define the co-polarized transmission coefficient for the fundamental mode as $T(k) = \hat{\boldsymbol{e}} \cdot \mathbf{T}_{00}(k) \cdot \hat{\boldsymbol{e}}$.

Given a transmission threshold T_0 we define the transmission bands as intervals of k, where $|T(k)| > T_0$. For the largest such interval (the main band) with endpoints k_1 and k_2, the fractional bandwidth is

$$B = 2\frac{k_2 - k_1}{k_1 + k_2}. \tag{2.3}$$

In this paper, we characterize how the fractional bandwidth depends on various perforation shapes with respect to different metrics, such as aperture area, or size of a minimal enclosing square, see S_p and a respectively, in Figure 2a. In the design examples, we strive towards having the bandwidth of the lowest-frequency transmission peak to be as close to the maximum attainable as possible.
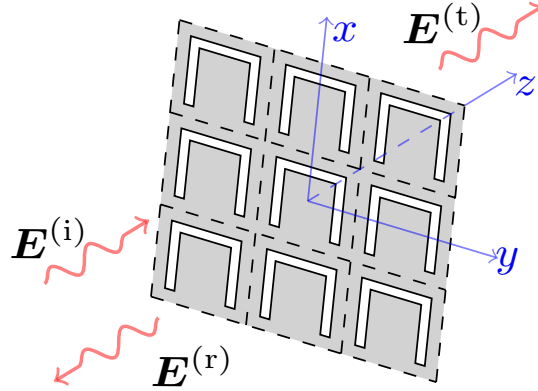
Figure 1: A periodic planar array with normally incident (i), reflected (r) and transmitted (t) waves.

3   Derivation of the Sum Rule

In this section, the derivation of the sum rule is presented. It is based on the passive properties of the screen [39], with an associated system response that can be transformed into a Herglotz function [1, 31], associated with the scattering system. An integral identity is applied to this function to obtain the extraordinary-transmission sum rule. The main theoretical result is the sum rule in (3.7), from which an upper bound of (2.3) is obtained in (3.9).

Passivity of the scattering configuration [15,33,39] allows an analytical extension of $T(k)$ for $k \in \mathbb{C}^+$, where $\mathbb{C}^+ = \{k \in \mathbb{C} : \operatorname{Im} k > 0\}$ is the upper half plane. Apart from analyticity, a few additional properties are required to construct a physical bound in the form of a sum rule. The impinging wave generates electric currents on the screen. From the assumption of negligible thickness of the screen it follows that the scattered field is symmetric relative to the screen, *i.e.*, $\boldsymbol{E}^{(\mathrm{t})} - \boldsymbol{E}^{(\mathrm{i})} = \boldsymbol{E}^{(\mathrm{r})}$ at $z = 0$. This can be rewritten as $T(k) = 1 + R(k)$, where $R(k)$ is the reflection coefficient defined for $\boldsymbol{E}^{(\mathrm{r})}$ similarly as $T(k)$ is defined for $\boldsymbol{E}^{(\mathrm{t})}$. This, combined with conservation of power $|T(k)|^2 + |R(k)|^2 \leq 1$, yields $|T(k) - 1/2| \leq 1/2$. Thus, the transmission coefficient is a holomorphic mapping from the upper complex half-plane $\mathbb{C}^+$ to the closed disc D with center at $1/2$ and radius $1/2$ in the complex plane, see the green disc in Figure 2b.

In order to obtain the sum rule, we transform the system response $T(k)$ in such a way that it becomes a Herglotz function, which is a mapping from the upper complex half-plane to its closure. Details about Herglotz functions and the associated integral identity used here are stated in Appendix 8.1.

Here, we consider a Möbius transform [7], $m(\zeta) = \mathrm{i}(1 - \zeta)/\zeta$, which maps the disc D to the closed upper complex half-plane. We compose it with the
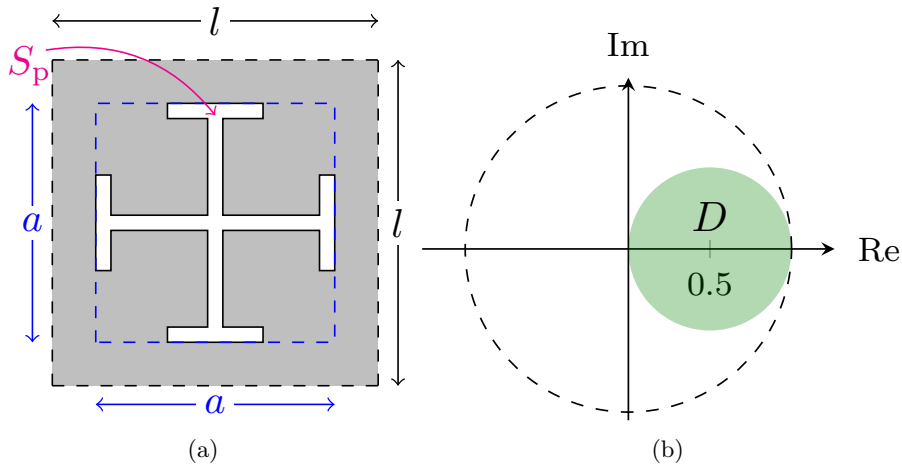
Figure 2: (a) An example of the unit cell geometry, with perforated area S_p, contained in a minimal enclosing square of size a, and the unit cell size $l = l_\mathrm{x} = l_\mathrm{y}$; (b) Range of the transmission coefficient $T(k) \in D$ in the complex plane.

transmission coefficient to obtain a symmetric Herglotz function

$$g(k) = m(T(k)) = \mathrm{i}\frac{1 - T(k)}{T(k)}. \tag{3.1}$$

A key element to derive the sum rule is the high and low frequency behavior of the transmission coefficient T, see (8.2) in Appendix 8.1. To determine the low-frequency behavior we utilize Babinet's principle: the field $\boldsymbol{E}^{(\mathrm{t})}$ transmitted through an aperture screen and the field $\boldsymbol{E}_\mathrm{c}^{(\mathrm{t})}$ transmitted through the complementary structure are related as $\boldsymbol{E}^{(\mathrm{t})} + \boldsymbol{E}_\mathrm{c}^{(\mathrm{t})} = \boldsymbol{E}^{(\mathrm{i})}$ [25, 38], where $\boldsymbol{E}^{(\mathrm{i})}$ is the incident field in both cases, see also a single aperture case in [16]. Hence, the low-frequency expansion (*i.e.*, $k \hat{\rightarrow} 0$) can be found by investigating the complementary structure. In the complementary structure, the perforations are filled with perfect magnetic conductor (PMC) in the xy-plane and the PEC is removed. The transmission coefficient of the complementary structure is $T_\mathrm{c}(k) = 1 - T(k)$ [16]. Its low-frequency expansion is [15, 17, 23, 37]

$$T_\mathrm{c}(k) \sim 1 + \frac{\mathrm{i}k\gamma}{2A} \qquad \text{as } k \hat{\rightarrow} 0, \tag{3.2}$$

where $\gamma = (\hat{\boldsymbol{e}} \cdot \mathbf{b}_\mathrm{m}\gamma_\mathrm{e} \cdot \hat{\boldsymbol{e}} + (\hat{\boldsymbol{k}} \times \hat{\boldsymbol{e}}) \cdot \mathbf{b}_\mathrm{m}\gamma_\mathrm{m} \cdot (\hat{\boldsymbol{k}} \times \hat{\boldsymbol{e}}))$, $\hat{\boldsymbol{k}} = \hat{\boldsymbol{z}}$ is the wave propagation direction, $\mathbf{b}_\mathrm{m}\gamma_\mathrm{e}$ and $\mathbf{b}_\mathrm{m}\gamma_\mathrm{m}$ are the electric and the magnetic polarizability tensors of the complementary structure, respectively, and $A = l_\mathrm{x}l_\mathrm{y}$ is the area of the unit cell. This gives us the expansion for the perforated PEC screen

$$T(k) \sim -\frac{\mathrm{i}k\gamma}{2A} \qquad \text{as } k \hat{\rightarrow} 0. \tag{3.3}$$

Note that the polarizabilities used here are the polarizabilities for the complementary structure. Furthermore, for a planar PMC array and the electric field direction $\hat{e}$ parallel to the array plane, the term $\hat{e} \cdot \mathbf{b}_{\mathrm{m}} \gamma_{\mathrm{e}} \cdot \hat{e}$ vanishes, and thus we only need to calculate the magnetic polarizability. The magnetic polarizability of a PMC structure can be calculated as the electric polarizability of a PEC structure of the same shape, see *e.g.*, [15, 36].

To construct the desired sum rule, we apply a Herglotz function with specific properties to $g(k)$ in (3.1). The resulting function is a Herglotz function, as non-zero Herglotz functions satisfy the property that a composition of two Herglotz functions is a Herglotz function [1]. To obtain an effective sum rule, we want to characterize the total attainable bandwidth. To do this, we need to emphasize the bands where the transmission is higher than a chosen threshold T_0 and to disregard the rest of the spectrum. The desired function h_Δ should have the properties $\operatorname{Im} h_\Delta(g(k)) = 1$ when $|T| \geq T_0$ and zero otherwise. The pulse Herglotz function [1]

$$h_\Delta(\zeta) = \frac{1}{\pi} \ln \frac{\zeta - \Delta}{\zeta + \Delta} \sim \begin{cases} \mathrm{i} & \text{as } \zeta \to 0 \\ -\frac{2\Delta}{\pi \zeta} & \text{as } \zeta \to \infty, \end{cases} \tag{3.4}$$

satisfies these criteria and has previously been used to construct sum rules for passive metamaterials [14] and high-impedance surfaces [17]. For any real-valued argument x this function has the property $\operatorname{Im} h_\Delta(x) = 1$ for $|x| < \Delta$ and $\operatorname{Im} h_\Delta(x) = 0$ for $|x| > \Delta$. We use this property later to relate the resulting integral identity with the fractional bandwidth (2.3) for the lossless case. For the composed function $h_\Delta(g(k))$, the connection between the parameter Δ and the threshold T_0 is found from relating Δ to a threshold value of $g(k)$ (i.e., when $|T(k)| = T_0$)

$$\Delta^2 = \frac{1 - T_0^2}{T_0^2}. \tag{3.5}$$

Finally, we apply the integral identity (8.2) to the function $h_\Delta(g(k))$. From (3.3) we obtain that $T(k) \sim -\mathrm{i}k\gamma/(2A)$ for $k \hat{\to} 0$. Combining this result and the low-frequency asymptote of (3.1), we get $g(k) \sim -2A/(\gamma k)$ as $k \hat{\to} 0$. Consequently, the function $h_\Delta(g(k))$ has the low-frequency expansion $h_\Delta(g(k)) \sim k\gamma\Delta/(A\pi)$ for $k \hat{\to} 0$. Performing the same steps for the high frequency limit yields $h_\Delta(g(k)) \sim o(k)$ as $k \hat{\to} \infty$. Thus, according to (8.2) we find the sum rule

$$\int_0^\infty \frac{\operatorname{Im} h_\Delta(g(k))}{k^2} \, \mathrm{d}k = \frac{\gamma\Delta}{2A}. \tag{3.6}$$

After substituting $\lambda = 2\pi/k$ and reusing $g(\lambda)$ for (3.1) as a function of wavelength, an alternative form of the sum rule is

$$\int_0^\infty \operatorname{Im} h_\Delta(g(\lambda)) \, \mathrm{d}\lambda = \frac{\gamma\Delta\pi}{A}. \tag{3.7}$$

From this sum rule expression we deduce the upper bound of (2.3) convenient for practical use. The sum rule shows that the total sum of transmission bands of an aperture array is determined by the array's polarizability per unit area. Note that the right-hand side of (3.7) is always strictly positive and hence there must exist intervals with non-zero transmission. Moreover, the transmission is perfect, $|T(\lambda_0)| = 1$, for some wavelength λ_0 if the structure is resonant below the onset of grating lobes and the cross polarization is negligible. This is a consequence of a lossless scattering system with $|T|^2 + |R|^2 = 1$, for which T is located on the boundary circle of D, in Figure 2b. This implies that $\operatorname{Im} h_\Delta(g(\lambda)) = 1$ for some wavelength interval of nonzero length, *i.e.*, there always exists a transmission band with an arbitrarily high level of transmission.

Note that, although ohmic losses are eliminated for screens made of PEC material, the scattering system is in general lossy due to radiation in other modes than the co-polarized fundamental mode in (2.2). Such radiation is perceived as losses from the system point of view, and includes higher-order modes radiating above the grating lobe frequency, as well as the cross-polarized mode below the first grating lobe. We refrain here from considering lossy materials and impedance surfaces from a theoretical perspective, as the resulting lossy case bound is in general not tight. Instead, we treat our lossless PEC model as an approximation of a highly conductive low-loss screen. Further discussion on the validity of the model is provided in Sections 5-6.

For practical applications the integration over a finite interval of wavelengths $[\lambda_a, \lambda_b]$ is performed (*e.g.*, see Figure 3 with $[\lambda_a, \lambda_b] = [0.6l, 5.2l]$, where l is the unit cell size)

$$\int_{\lambda_a}^{\lambda_b} \operatorname{Im} h_\Delta(g(\lambda)) \, \mathrm{d}\lambda \leq \frac{\gamma \pi \Delta}{A}. \tag{3.8}$$

Assume now that within the interval $[\lambda_a, \lambda_b]$ there are a number of mutually disjoint subintervals, where $|T| \geq T_0$. As an example, in Figure 3 we observe two intervals for $\lambda/l > 0.9$ with transmittance higher than $T_0^2 = 0.8$, where the widest is located around $\lambda/l = 3$. In this paper, we focus mainly on the bandwidth of the widest transmission band even though the sum rule includes all the transmission windows. If we retain only the contribution of the largest transmission band with endpoints λ_1 and λ_2, and normalize (3.8) with the central wavelength $\lambda_0 = (\lambda_1 + \lambda_2)/2$ of the corresponding band, we obtain a bound for the fractional bandwidth

$$B = 2\frac{\lambda_1 - \lambda_2}{\lambda_1 + \lambda_2} \leq \frac{\gamma \pi \Delta}{A \lambda_0}. \tag{3.9}$$

Note that due to the relation $|T|^2 + |R|^2 = 1$ below the first grating lobe frequency and assuming negligible cross polarization, the numerical results can be equivalently presented in the reflectance. We, however, focus on transmission bandwidth in this paper.
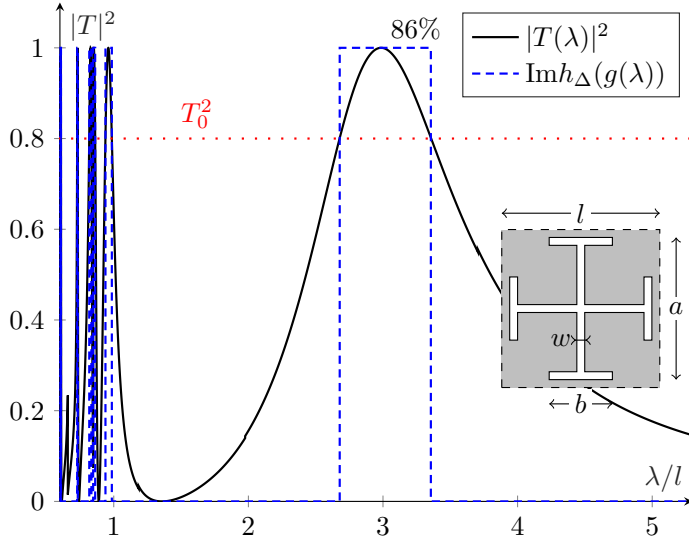
Figure 3: Cross potent: transmittance as a function of wavelength and the unit cell geometry. Transmission bands with respect to the transmittance threshold level $T_0^2 = 0.8$ (dotted line) are shown by the integrand function $\operatorname{Im} h_\Delta(g(\lambda))$ of (3.7).

4 Numerical Examples and Applications of the Bound

We begin this section with illustrating the sum rule (3.7) by analyzing a given FSS design. The numerical example in Figure 3 shows the transmittance $|T|^2$ through an array of cross-potent (sometimes referred to as Jerusalem cross) [29,30] shaped apertures as a function of the normalized wavelength. The assumptions of the idealized model are retained: the screen is infinitely thin and made of PEC material, and the array of perforations is infinitely periodic. The unit cell geometry is given, with $l_x = l_y = l$, slot width $w = l/20$, and parameters $a = 0.9l$ and $b = 0.4l$. The numerical analysis was performed in CST MW Studio using the frequency domain solver and Floquet mode ports. The results show the main transmission band (transmittance threshold level $T_0^2 = 0.8$) centered at $\lambda = 2.9l$, with the fractional bandwidth $B = 0.24$. This accounts for 86% of the upper bound limit in (3.9). For the wavelengths shorter than 0.9λ, we observe multiple narrower peaks. Due to the resonance nature of the phenomenon, an infinite number of such peaks is expected in the short wavelength limit. The contributions from these peaks, along with the grating lobes, are also accounted for in the left hand side of the sum rule (3.7).

In the above cross-potent example, the sum rule is used to analyze a given

FSS design. Additionally, the sum rule is instrumental to design and optimize FSS, which we discuss and illustrate in the remainder of this section. One of the most crucial performance parameters of a periodically perforated screen is the frequency bandwidth over which the screen is transparent. The bandwidth optimization of periodic screens typically involves a considerable amount of full-wave numerical simulations in order to tune the design. Thus, tools that guide the optimization process and reduce the number of simulations are desired. The sum rule (3.9) is such a tool, as it provides a quantitative estimate of the total attainable bandwidth. This can be used in two ways. First, the total attainable bandwidth is bounded by the static polarizability of a perforation element according to (3.9). Testing the static polarizability for each design candidate can thus replace numerically costly wide-frequency-range full-wave simulations in the search of preliminary structure. Second, the total attainable bandwidth, obtained from the polarizability, can serve as a reference for the fraction of the total bandwidth in the main frequency band. Using this reference, we can optimize the main frequency band to utilize most of the physically attainable bandwidth. In this section, we demonstrate an optimization procedure by maximizing the frequency bandwidth of a transmission window through a perforated screen, while keeping the area of perforations S_{p} low ($1 - 5\%$ of the total screen area). In general, different metrics can be considered instead of S_{p}, for example, the size of the smallest enclosing square.

The total achievable bandwidth is determined by the polarizability of the corresponding complementary structure according to (3.9), as discussed above. We use this as a guideline to choose the preliminary perforation design. Figure 4 compares the normalized polarizability γ/l^3 of an array of square PEC patches of size $a \times a$ and period $l_{\mathrm{x}} = l_{\mathrm{y}} = l$ with periodic PEC arrays, tightly enclosed by the square patch structure. Three shapes of enclosed unit cell designs are considered: a cross potent, a horseshoe and a split ring resonator. According to the monotonic growth of polarizabilities with volume, the polarizability of an enclosed object cannot exceed the polarizability of an enclosing object [35, 37]. Thus, the polarizability of the square patches is the upper bound for the enclosed designs. We observe in Figure 4 that the horseshoe and the split ring designs approach the upper bound, and thus make a good use of the unit cell geometry. The split-ring-resonator unit cell outperforms the horseshoe-shaped design when they are compared with respect to normalized distance $(l - a)/l$ between the adjacent perforations.

As an alternative evaluation of performance, we can investigate how the shapes perform with respect to the perforation area. Figure 5 shows the normalized static polarizability γ/l^3 as a function of the percentage of perforation area in the total area of the screen $\alpha = S_{\mathrm{p}}/A$, where $l = l_{\mathrm{x}} = l_{\mathrm{y}}$ is the size of a unit cell, see Figure 2a. Here, solid, $\circ$-dashed, $\square$-dashed and $\star$-dashed lines correspond to square hole, cross potent, horseshoe and split ring resonator designs, respectively. All the designs were contained within the square of size a, and the slot width for the cross potent, horseshoe and split ring was fixed at $w = a/17$, see *e.g.*, Figures 3 and 6, while the unit cell size l was varied in
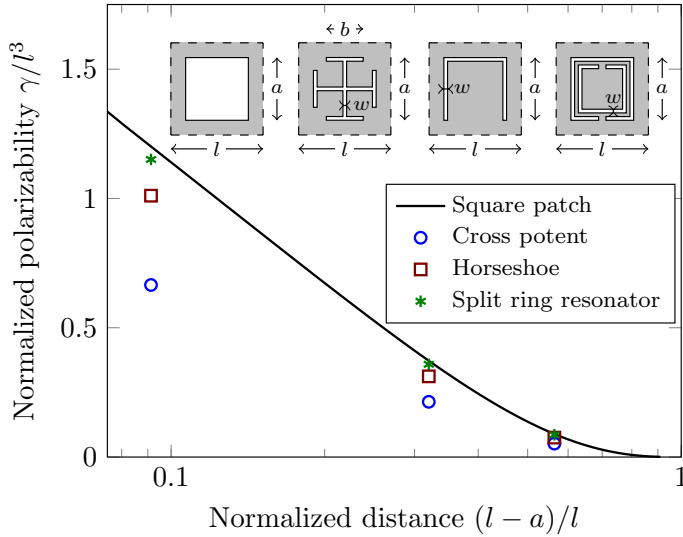
Figure 4: Normalized polarizability γ/l^3 of infinitely thin PEC periodic structures as a function of the normalized distance between two adjacent square patches, $l \in \{1.1a, \; 1.47a, \; 2.29a\}$. The external applied field for polarizability calculation is directed vertically with respect to the unit cells in the inset.

the range $[1.03a, 11.15a]$, $[1.04a, 4.67a]$, $[1.03a, 4.12a]$ and $[1.38a, 6.17a]$ for the corresponding design, respectively. The evaluation of static polarizabilities was performed via a variational approach [37] in COMSOL Multiphysics electrostatic solver.

We observe among all considered shapes that the horseshoe utilizes the perforation area better than the other shapes, in the sense of the upper bound γ/l^3 of the total attainable bandwidth. The square hole perforations are given as a reference, and all the suggested designs outperform it. The same total bandwidth, as achieved by cutting out 15% of the screen with square-shaped perforations, can be attained by cutting out only 2.5% of the screen with the horseshoe-shaped perforations. Additionally, the horseshoe-shaped perforations have better mechanical stability compared to the other considered designs, which finalizes the choice of the preliminary structure.

Having chosen a horseshoe design as a preliminary structure, we perform optimization of its geometrical parameters with respect to its transmission bandwidth. Consider the following optimization problem. For a given upper limit α_0 of $\alpha = S_p/A$, make the fractional bandwidth B as close as possible to its upper bound given by the right hand side of (3.9). We denote the ratio between the bandwidth and its upper bound as $\eta(\Omega, \Delta) = B/(\gamma \pi \Delta/A\lambda_0)$. The optimization
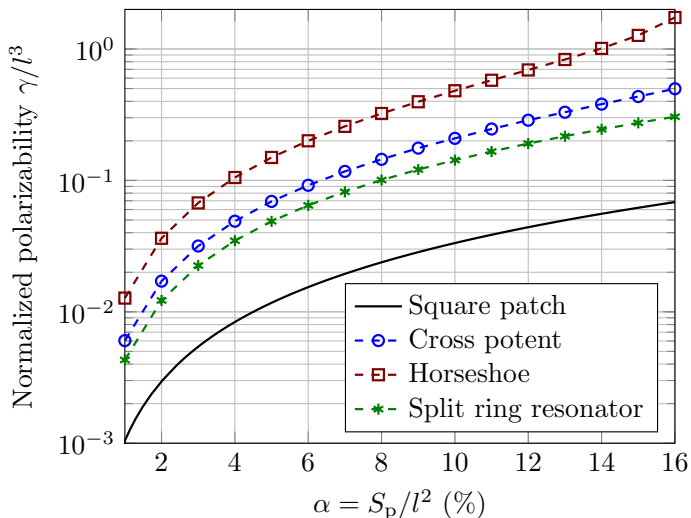
Figure 5: Normalized polarizability γ/l^3 of infinitely thin PEC periodic structures as a function of perforated area. The external applied field for polarizability calculation is directed vertically with respect to the unit cells in the inset of Figure 4.
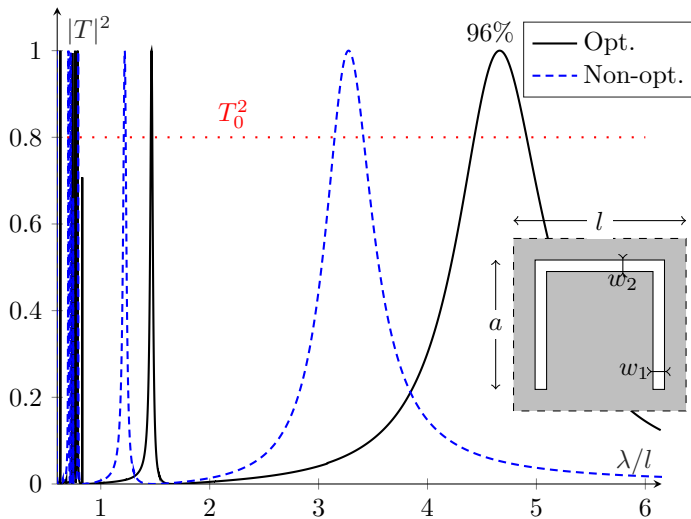
Figure 6: Horseshoe transmittance, optimized (black curve) and non-optimized (dash-dotted) designs. In both cases $\alpha = S_{\mathrm{p}}/A = 5\%$.

problem is formulated as follows for a given Δ

$$
\begin{aligned}
&\underset{\Omega}{\text{maximize}} \quad \eta(\Omega, \Delta) \\
&\text{subject to} \quad \alpha(\Omega) \leq \alpha_0,
\end{aligned}
\tag{4.1}
$$

where the optimization is performed over the parametrized geometry Ω of the aperture. We use a genetic algorithm optimization for geometric parameters of a horseshoe shaped aperture (the shape choice is motivated by Figure 5).

Figure 6 shows the results of optimization of the horseshoe perforation geometry with $\alpha_0 = 5\%$. We start with a non-optimized design given by the size a, and $l = 1.69a$, $w_1 = w_2 = 0.049a$. Optimization (4.1) yields the design given by $l = 1.43a$, $w_1 = 0.049a$, and $w_2 = 0.0047a$. We observe that the bandwidth is improved approximately twice, and the main peak contains 96% of the attainable bandwidth, according to (3.9).

5 Implementation of Real Structures

In Sections 2-4, the theoretical and numerical evaluation of the screen were performed under certain assumptions. Here, we investigate the validity of these results when the assumptions are relaxed. One of the key assumptions was that the screen is infinitely thin. Figure 7 illustrates how the screen thickness d affects the screen's transmission characteristics. We consider transmission through a screen with horseshoe-shaped apertures, with slot width $w_1 = w_2 = w$, see Figure 6 for the unit cell geometry. The transmission through an infinitely thin screen is compared with three screens with width-to-thickness ratios $w/d = \{1, 5, 10\}$. For $w/d = 1$, we observe a noticeable bandwidth reduction in comparison with the infinitely thin case. However, when $w/d = 10$, the difference between the transmittance of the infinitely thin screen and the screen of thickness d is negligible, resulting in a bandwidth reduction of about 2% (with the threshold $T_0^2 = 0.8$). Figure 7 shows that the transmission bandwidth is reduced with decreasing w/d ratio. This implies that the inequality in (3.9) is still valid for cases with a finite thickness. However, when the slot width becomes comparable to the slot thickness, the bound is not tight.

The second crucial assumption made in the derivation of the sum rule was the PEC material of the screen. Therefore, candidates for screen material should be highly conductive low-loss metals. To reconcile this requirement with limitations put on thickness and mechanical stability, aluminum foil was chosen. Alternative options were metalized dielectric substrate, copper sheet and silver foil. However, these options impose issues which are hard to resolve in the sum rule or fabrication. Figure 8 shows the simulated transmittance for a perforated screen made of PEC or aluminum. The geometrical parameters of the screen are the same as of the manufactured sample, to be discussed in the next section. The aluminum screen has slightly lower amplitude (about 5%) in the transmission peak in comparison with the PEC screen. However, the bandwidth reduction is negligible.
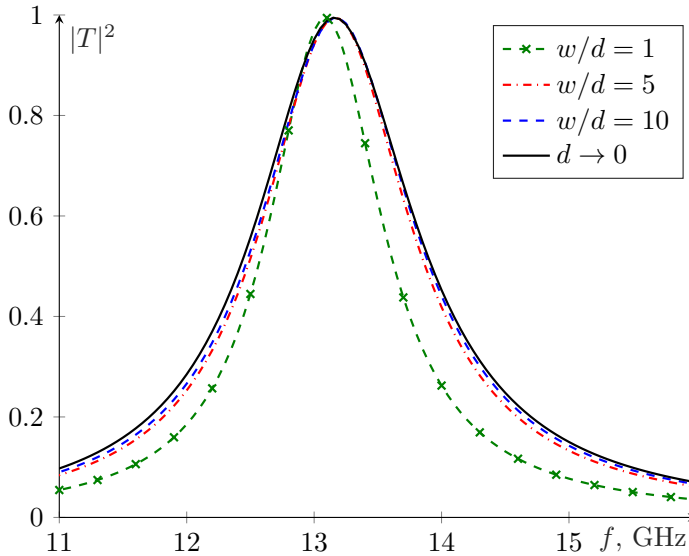
Figure 7: Simulated transmittance through an array of horseshoe apertures for different ratios of the slot width to the screen thickness.

Thus, the sum rule is applicable to aluminum screens and it is relatively tight.

In the sum rule we also considered an infinite periodicity of the screen. Ref. [6] reports that 30 periods in both dimensions of the screen is sufficient to ensure a negligible difference in transmission between finite and infinite structures. The edge effects can be compensated by time-gating.

6   Measurements

The final manufactured sample had the unit cell geometry given by the inset in Figure 6 with $l = 6.57\,\text{mm}$, $a = 3.43\,\text{mm}$, $w_1 = 0.3\,\text{mm}$, and $w_2 = 0.06\,\text{mm}$. The aperture array was laser milled by a ProtoLaser U3 machine in a sheet of aluminum foil of thickness $d = 0.018\,\text{mm}$. The array consisted of $34 \times 45 = 1530$ apertures, and $\alpha = 5\%$; see Figure 9 for the manufactured sample.

The measurement setup is shown in Figure 10. The sample was fixed in a polymethyl methacrylate (PMMA) frame fastened by two plastic stands equidistant to the transmitting and receiving antennas. Standard gain horn Satimo SGH1240 antennas were used, with the nominal frequency range $12.4 - 18.0\,\text{GHz}$. The antennas were installed at the distance of $1\,\text{m}$ from each other. The reference transmission measurements were performed with the empty PMMA frame instead of the sample and multipath reflections from the surrounding objects and surfaces were filtered out in the time domain by using time-gating [5,10] utilizing a tapered cosine window.
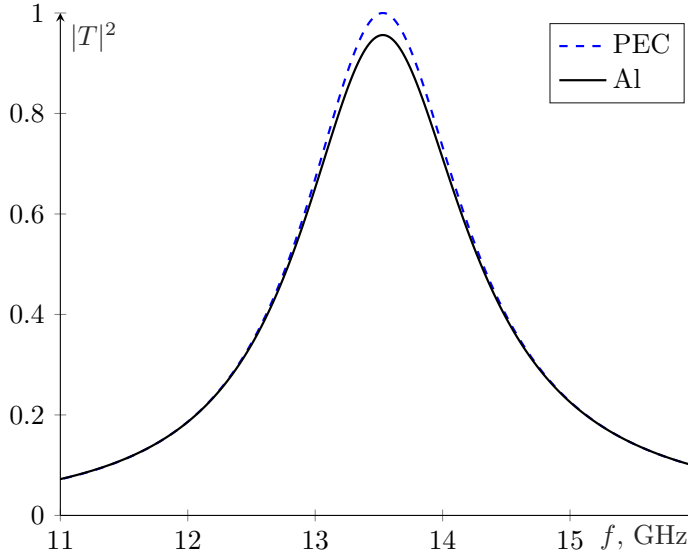
Figure 8: Simulated transmittance of the horseshoe design for manufactured sample, PEC and Al comparison.

The transmission through the manufactured sample was measured in the frequency range $10 - 20$ GHz to capture the first transmission peak and to filter multipath components in an efficient manner. In Figure 11, the red and black solid curves correspond to the raw data of the measured transmittance and the processed data obtained by filtering out multipath propagation components using time gating, respectively, and the dashed curve corresponds to the simulated transmittance of the infinitely-periodic model of the sample. We observe a fine agreement between the measured and simulated transmittances in the whole frequency range. The magnitude and the frequency of the resonance perfectly coincide for simulation and measurements.

The optimized PEC-bandwidth of the lowest-frequency peak, as shown in Section 4, reaches 96% of the available physical bandwidth, based on the sum rule utilizing the polarizability of the perforation (3.9). As we saw in Section 5, a finite thickness, but small in comparison with the perforation size, together with a finite but high conductivity made small perturbations to the transmission peak.

By comparing the measured result with the PEC-simulated results at the 80% transmittance threshold level, we find that the time-gated measured transmission peak has 98% of the available bandwidth of a PEC-based structure. The measured transmission peak is centered at the frequency of 13.52 GHz with the fractional bandwidth of 5.83%.

The remarkable agreement between measured and PEC-simulated results validate the use of the PEC-based sum rule as a tool to predict the physically
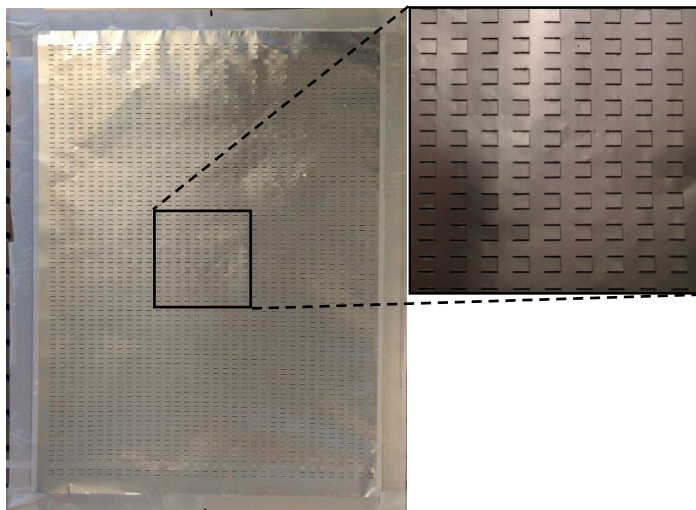
Figure 9: Sample manufactured in aluminium foil: the entire sample of the size 238 mm×320 mm and a close up of the manufactured horseshoe design.
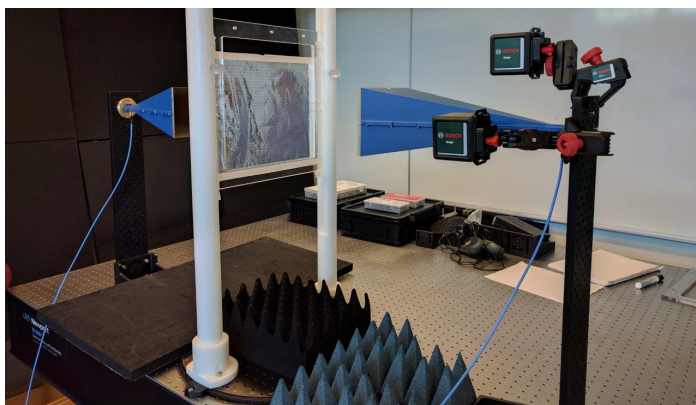
Figure 10: Measurement setup mounted on an optical table. Two blue standard gain, horn MVG SGH1240 antennas were used as both receiver and transmitter. The horns were aligned using two Bosch Quigo Cross line lasers, seen here mounted on the right antenna. The sample was mounted on a custom made polymethyl methacrylate frame and held up by two plastic stands.
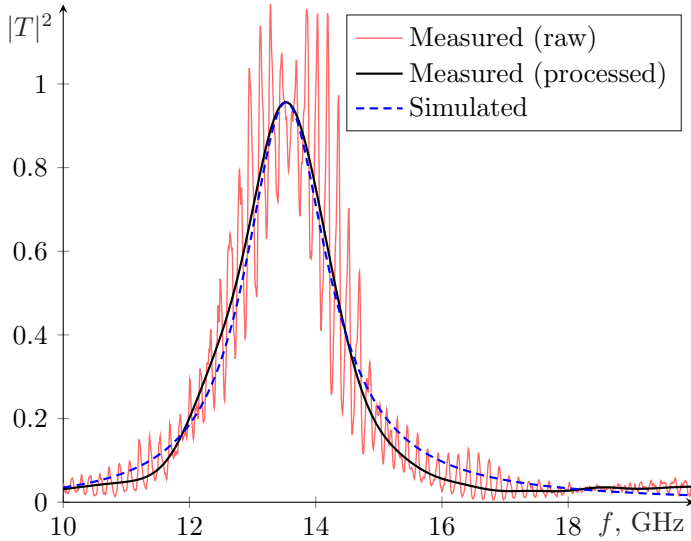
Figure 11: Horseshoe slot array: comparison between measured raw data (red), processed data (black solid) and simulated (blue dashed) transmittance.

maximum available bandwidth in thin and highly conductive EoT-screens. We further note that the PEC-based upper bound solely utilizes the observation that the screen is a passive system.

7   Conclusions

In this paper we have derived a sum rule for periodic structures and applied it to an FSS design problem. We have shown numerically, that a periodic PEC-like infinitely thin screen with 5% of its total area cut out as horseshoe shaped perforations can have up to 96% of its physically attainable bandwidth in its largest transmission window. The transmittance threshold of this study was set to 80%. Our numerical investigations illustrate that small perturbations of the PEC-screen accounting for a finite thickness and a finite but high conductivity marginally perturbed the transmission result. This indicates the validity of the sum rule for real applications, even though it was derived for an ideal model.

We have experimentally validated our results by showing that the transmission characteristics of the first transmission window of a horseshoe design, optimized with the use of the sum rule, fabricated in a 0.018 m m thick highly conducting aluminum foil with horseshoe perforations, accurately matches the corresponding simulations. The mutual agreement between the theoretical limitations, numerical and experimental validation is high. The choice of frequency band was selected to fully utilize the range of the experimental equipment. We

conclude that the sum rule can be used to predict the results of transmission experiments with highly conductive metal films in the GHz range, and may be of use in understanding the phenomena at other frequencies. We have also observed that the perforation shape needed to maximize the performance of this phenomenon can be rather simple and still gather a high degree of transmission in one transmission window.

The theoretical sum rule result (3.7) shows that a transmission band at long (in comparison to the periodicity of the structure) wavelengths exists for any type of perforations, even infinitely small ones ($\alpha \to 0$). However, the bandwidth of the transmission peak is proportional to the polarizability, closely related to the shape and size of the perforations. As a result, it is shown that the static polarizability, and hence, the transmission bandwidth of an array of square apertures can be attained by periodic perforations of much smaller relative area α, see Figures 4 and 5. The sum rule (3.7) implicates that in the ideal setting the ratio T/α can be infinitely large.

The good agreement between the measured transmission peak and the corresponding PEC simulations was enabled by a careful choice of material. By utilizing aluminum foil we stayed relatively close to the idealized PEC case. There was no dielectric material supporting the metal, and the foil had high conductivity, which ensured a high value of transmittance in the transmission peak. The foil was also thinner than the smallest slot in the design. This meant that there was no waveguide-like phenomenon occurring in the slots. Such an effect has a tendency to shift the spectral localization of resonances. This can be compared to the initial investigation performed at optical frequencies [9, 24, 27], where the aperture sizes are small compared to the thickness of the materials they are etched in. This explains why these studies exhibit deviations from ideal models.

The derived sum rule (3.7) provides an upper bound on the bandwidth, which determines the largest attainable bandwidth for any aperture, enclosed in *e.g.*, a square of a given size. Additionally, it allows us to verify that the total bandwidth for a given aperture cannot be improved by redesigning the aperture within the enclosing square. In this paper, we have shown an example of how the sum rule can be used in the design process of a perforated screen. Given maximal transmission bandwidth as the design goal, while having constrained fractional aperture area, the sum rule serves as an upper limit to optimize towards. However, other constraints and optimization goals are possible. The optimization problem might be formulated as maximization of the bandwidth of transmission peaks at wavelengths closest to the array period. Here, the sum rule can serve as a reference to maximally attainable bandwidth.

An interesting continuation of this work might be a theoretical investigation of transmission through infinitely-thin perforated impedance surface. However, the approach of this paper does not directly translate to the impedance-surface case. The impedance surface does not have zero transmission in low-frequency limit, which is one of the key elements used in the derivation of the presented sum rule, and therefore requires further investigation. One of the possible alternatives

here is to use numerical techniques, approximating the system function with a linear combination of Herglotz functions [21, 32].

8   Appendices

8.1   Herglotz Functions

A Herglotz function is a holomorphic function $h(\zeta)$ such that $\operatorname{Im} h(\zeta) \geq 0$ whenever $\operatorname{Im} \zeta > 0$, *i.e.*, it is a mapping from the upper complex half plane to its closure. Functions of this class can have a family of integral identities [1], also known as sum rules.

Consider a Herglotz-function such that

$$h(\zeta) = \begin{cases} a_{-1}\zeta^{-1} + a_1\zeta + o(\zeta) & \text{as } \zeta \,\hat{\to}\, 0, \\ b_1\zeta + o(\zeta^{-1}) & \text{as } \zeta \,\hat{\to}\, \infty, \end{cases} \tag{8.1}$$

where the coefficients a_{-1}, a_1 and b_1 are real-valued. Here $\zeta = x + \mathrm{i}y$. A sum rule [1, 31] for the Herglotz function h with the above expansion is:

$$\frac{2}{\pi} \int\limits_{0+}^{\infty} \frac{\operatorname{Im} h(x)}{x^2} \, \mathrm{d}x \overset{\mathrm{def}}{=} \lim_{\varepsilon \to 0+} \lim_{y \to 0+} \frac{2}{\pi} \int\limits_{\varepsilon}^{1/\varepsilon} \frac{\operatorname{Im} h(x + \mathrm{i}y)}{x^2} \, \mathrm{d}x$$

$$= a_1 - b_1. \quad (8.2)$$

Above, $\hat{\to}$ denotes the limit in a cone $\alpha \leq \arg(\zeta) \leq (\pi - \alpha)$ for some $\alpha > 0$. Throughout this paper, we utilize the symmetry $h(\zeta) = -h^*(-\zeta^*)$, which follows from the real-valuedness of the function in the time domain.

Acknowledgments

References

[1] A. Bernland, A. Luger, and M. Gustafsson. Sum rules and constraints on passive systems. *J. Phys. A: Math. Theor.*, **44**(14), pp. 145205, 2011.

[2] M. Beruete, M. Sorolla, I. Campillo, J. S. Dolado, L. Martín-Moreno, J. Bravo-Abad, and F. J. García-Vidal. Enhanced millimeter-wave transmission through subwavelength hole arrays. *Opt. Lett.*, **29**(21), pp. 2500–2502, Nov 2004.

[3] M. Beruete, M. Sorolla, and I. Campillo. Left-handed extraordinary optical transmission through a photonic crystal of subwavelength hole arrays. *Optics Express*, **14**(12), pp. 5445–5455, 2006.

[4] H. A. Bethe. Theory of diffraction by small holes. *Phys. Rev.*, **66**(7&8), pp. 163–182, 1944.

[5] G. H. Bryant. *Principles of microwave measurements*, volume 5. IET, 1993.

[6] M. Camacho, R. Boix, and F. Medina. Computationally efficient analysis of extraordinary optical transmission through infinite and truncated subwavelength hole arrays. *Physical Review E*, **93**(6), pp. 063312, 2016.

[7] J. B. Conway. *Functions of One Complex Variable*. Springer, New York, NY, 1973.

[8] J. P. Doane, K. Sertel, and J. L. Volakis. Matching bandwidth limits for arrays backed by a conducting ground plane. *IEEE Trans. Antennas Propag.*, **61**(5), pp. 2511–2518, 2013.

[9] T. W. Ebbesen, H. J. Lezec, H. F. Ghaemi, T. Thio, and P. A. Wolff. Extraordinary optical transmission through sub-wavelength hole arrays. *Nature*, **391**, pp. 667–669, 1998.

[10] A. Ericsson, J. Lundgren, and D. Sjöberg. Experimental characterization of circular polarization selective structures using linearly single-polarized antennas. *IEEE Trans. Antennas Propag.*, **65**(8), pp. 4239–4249, 2017.

[11] C. García-Meca, R. Ortuño, F. Rodríguez-Fortuño, J. Martí, and A. Martínez. Negative refractive index metamaterials aided by extraordinary optical transmission. *Opt. Express*, **17**(8), pp. 6026–6031, Apr 2009.

[12] C. Genet and T. W. Ebbesen. Light in tiny holes. *Nature*, **445**, pp. 39–46, 2007.

[13] M. Gustafsson, A. Karlsson, A. P. Rebelo, and B. Widenberg. Design of frequency selective windows for improved indoor outdoor communication. *IEEE Trans. Antennas Propag.*, **54**, pp. 1897–1900, 2006.

[14] M. Gustafsson and D. Sjöberg. Sum rules and physical bounds on passive metamaterials. *New Journal of Physics*, **12**, pp. 043046, 2010.

[15] M. Gustafsson, C. Sohl, and G. Kristensson. Physical limitations on scattering and absorption of antennas. In *Proceedings of the Second European Conference on Antennas and Propagation*. The Institution of Engineering and Technology, 2007.

[16] M. Gustafsson. Sum rule for the transmission cross section of apertures in thin opaque screens. *Opt. Lett.*, **34**(13), pp. 2003–2005, 2009.

[17] M. Gustafsson and D. Sjöberg. Physical bounds and sum rules for high-impedance surfaces. *IEEE Trans. Antennas Propag.*, **59**(6), pp. 2196–2204, 2011.

[18] M. Gustafsson, D. Sjöberg, and I. Vakili. On the extraordinary transmission through sub-wavelength apertures in perfectly conducting sheets. In *International Conference on Electromagnetics in Advanced Applications (ICEAA)*, Turin, Italy, September 12–16 2011.

[19] M. Gustafsson, I. Vakili, S. E. B. Keskin, D. Sjöberg, and C. Larsson. Optical theorem and forward scattering sum rule for periodic structures. *IEEE Trans. Antennas Propag.*, **60**(8), pp. 3818–3826, 2012.

[20] T. K. Ishii. *Handbook of microwave technology.* Elsevier, 1995.

[21] Y. Ivanenko, M. Gustafsson, B. L. G. Jonsson, A. Luger, B. Nilsson, S. Nordebo, and J. Toft. Passive approximation and optimization using B-splines. *SIAM Journal on Applied Mathematics*, **79**(1), pp. 436–458, 2019.

[22] B. L. G. Jonsson, C. I. Kolitsidas, and N. Hussain. Array antenna limitations. *Antennas and Wireless Propagation Letters, IEEE*, **12**, pp. 1539–1542, 2013.

[23] R. E. Kleinman and T. B. A. Senior. Rayleigh scattering. In V. V. Varadan and V. K. Varadan, editors, *Low and high frequency asymptotics*, volume 2 of *Handbook on Acoustic, Electromagnetic and Elastic Wave Scattering*, chapter 1, pp. 1–70. Elsevier Science Publishers, Amsterdam, 1986.

[24] K. J. K. Koerkamp, S. Enoch, F. B. Segerink, N. F. van Hulst, and L. Kuipers. Strong influence of hole shape on extraordinary transmission through periodic arrays of subwavelength holes. *Phys. Rev. Lett.*, **92**(18), pp. 183901, 2004.

[25] L. D. Landau, E. M. Lifshitz, and L. P. Pitaevskii. *Electrodynamics of Continuous Media.* Pergamon, 1984.

[26] M.-H. Lu, X.-K. Liu, L. Feng, J. Li, C.-P. Huang, Y.-F. Chen, Y.-Y. Zhu, S.-N. Zhu, and N.-B. Ming. Extraordinary Acoustic Transmission through a 1D Grating with Very Narrow Apertures. *Phys. Rev. Lett.*, **99**, pp. 174301, Oct 2007.

[27] L. Martín-Moreno, F. J. García-Vidal, H. J. Lezec, K. M. Pellerin, T. Thio, J. B. Pendry, and T. W. Ebbesen. Theory of extraordinary optical transmission through subwavelength hole arrays. *Phys. Rev. Lett.*, **86**(6), pp. 1114–1117, 2001.

[28] F. Medina, F. Mesa, and R. Marques. Extraordinary transmission through arrays of electrically small holes from a circuit theory perspective. *IEEE Transactions on Microwave Theory and Techniques*, **56**(12), pp. 3108–3120, 2008.

[29] R. Mittra, C. H. Chan, and T. Cwik. Techniques for analyzing frequency selective surfaces-a review. *Proceedings of the IEEE*, **76**(12), pp. 1593–1615, 1988.

[30] B. Munk. *Frequency Selective Surfaces: Theory and Design*. John Wiley & Sons, New York, NY, 2000.

[31] M. Nedic, C. Ehrenborg, Y. Ivanenko, A. Ludvig-Osipov, S. Nordebo, A. Luger, B. L. G. Jonsson, D. Sjöberg, and M. Gustafsson. *Herglotz functions and applications in electromagnetics*. IET, 2019.

[32] S. Nordebo, M. Gustafsson, B. Nilsson, and D. Sjoberg. Optimal realizations of passive structures. *IEEE Trans. Antennas Propag.*, **62**(9), pp. 4686–4694, 2014.

[33] H. M. Nussenzveig. *Causality and Dispersion Relations*. Academic Press, London, 1972.

[34] J. B. Pendry, L. Martín-Moreno, and F. J. Garcia-Vidal. Mimicking surface plasmons with structured surfaces. *Science*, **305**(5685), pp. 847–848, 2004.

[35] M. Schiffer and G. Szegö. Virtual mass and polarization. *Trans. Amer. Math. Soc.*, **67**(1), pp. 130–205, 1949.

[36] D. Sjöberg, M. Gustafsson, and C. Larsson. Physical bounds on the all-spectrum transmission through periodic arrays: Oblique incidence. *EPL Europhysics Letters*, **92**, pp. 34009 (6pp), 2010.

[37] D. Sjöberg. Variational principles for the static electric and magnetic polarizabilities of anisotropic media with perfect electric conductor inclusions. *J. Phys. A: Math. Theor.*, **42**, pp. 335403, 2009.

[38] J. G. van Bladel. *Electromagnetic Fields*. IEEE Press, Piscataway, NJ, second edition edition, 2007.

[39] A. H. Zemanian. *Distribution Theory and Transform Analysis: An Introduction to Generalized Functions, with Applications*. McGraw-Hill, New York, NY, 1965.

Design, Optimization and Verification of a Dual Band Circular Polarization Selective Structure

Paper II

Johan Lundgren, Andreas Ericsson and Daniel Sjöberg

Abstract

We present a non-resonant, dual band circular polarization selective structure (CPSS) for satellite communication applications in the K- and K_a-bands. The structure consists of multiple layers of cascaded anisotropic sheets, with printed meander lines, separated by low permittivity spacers. It reflects right handed circular polarization and transmits left handed circular polarization in the lower frequency band. In the upper frequency band the opposite polarization selectivity is achieved. The theory of dual band circular polarization selectivity from cascaded anisotropic sheets is presented. The separation between the frequency bands of operation is shown to be governed by the relative rotation between subsequent layers. An optimization routine for synthesizing dual band CPSSs from predefined design requirements is introduced, utilizing several different optimization algorithms. A simulated design is presented which fulfills the strict requirements of insertion loss and return loss less than 0.5 dB, and axial ratio less than 0.78 dB, in the frequency bands 17.7–20.2 GHz and 27.5–30.0 GHz. A prototype of the optimized design is fabricated and characterized experimentally, both in transmission and reflection. Good agreement is observed between simulated and experimental results. This type of structure is a potential candidate for implementation in dual band multiple spot beam systems utilizing frequency and polarization reuse schemes.

1   Introduction

Key components in today's interconnected world are communication satellites positioned in crowded orbits [7]. In order to utilize the available satellite aperture in a more efficient manner, frequency and polarization reuse schemes can be utilized [14]. The number of reflectors needed for a satellite communication (SATCOM) system can be reduced by a factor of two by using polarizing surfaces [2]. An example of such a system was recently presented in [17], where a dual band polarizing surface converting linear polarization (LP) to circular polarization (CP) was used as a reflector in the K_u-band. Alternative solutions to this system can be achieved using dual band circular polarization selective structures (CPSSs), either as diplexers or reflectors. A dual band CPSS will for the lower frequency band reflect one handedness of CP while transmitting the orthogonal circular polarization, and do the converse for the higher frequency band [11].

In the last century, many different CPSS designs have been presented with various performance levels [1, 8, 12, 13, 16, 18, 20–22]. An overview of the CPSSs presented up to date is presented in [5], where these structures are evaluated with respect to relevant performance requirements. Recently, a high performing, wide band CPSS concept based on non resonant elements was presented [3–5, 15]. These designs all consist of multiple sheets of meander lines stacked and rotated after one another. Each layer is perceived as an effective capacitance/inductance in linear polarization by incident waves. A shortcoming of previously presented CPSSs is that the design and optimization have been carried out to obtain operation in a single frequency band. In the same manner as in a frequency selective

structure, higher order resonances can be observed in a CPSS. However, the frequency separation between these resonances is generally much larger than what is desirable, and to optimize a CPSS for dual band operation is a challenging task.

To this end, we present a design procedure for dual band CPSSs consisting of multiple layers of anisotropic sheets. In the same manner as in [3–5, 15], sub-wavelength meander lines are used to achieve a strong anisotropic response in the sheets. The frequency bands of interest in this work are the SATCOM downlink band 17.7–20.2 GHz and the uplink band 27.5–30.0 GHz, located in the K- and K_a-bands. To the authors' knowledge, this is the first time a dual band CPSS is presented with performance levels applicable to real world configurations.

The paper is organized as follows: in Section 2 the theory of scattering in circular polarization from anisotropic sheets is presented. It is shown that the optimal number of layers of a CPSS can be found in order to achieve CP selectivity in multiple frequency bands, and to reduce the cross polarization scattering. A detailed optimization procedure is introduced in Section 3, where a dual band CPSS is designed based on predefined performance requirements. Simulation results of the optimized design are presented in Section 4. A prototype was manufactured and the details of this test panel are presented in Section 5, and experimental results of this structure are evaluated in Section 6. Finally, some concluding remarks are presented in Section 7.

2 Theory - Dual Band Circular Polarization Selectivity from Linear Elements

The scattering matrix in circular polarization of a system with two ports, located on each side of the sample, is

$$\mathbf{S}^{\mathrm{CP}} = \begin{pmatrix} S_{11}^{\mathrm{RR}} & S_{11}^{\mathrm{RL}} & S_{12}^{\mathrm{RR}} & S_{12}^{\mathrm{RL}} \\ S_{11}^{\mathrm{LR}} & S_{11}^{\mathrm{LL}} & S_{12}^{\mathrm{LR}} & S_{12}^{\mathrm{LL}} \\ S_{21}^{\mathrm{RR}} & S_{21}^{\mathrm{RL}} & S_{22}^{\mathrm{RR}} & S_{22}^{\mathrm{RL}} \\ S_{21}^{\mathrm{LR}} & S_{21}^{\mathrm{LL}} & S_{22}^{\mathrm{LR}} & S_{22}^{\mathrm{LL}} \end{pmatrix}, \tag{2.1}$$

where the superscript R stands for right handed circular polarization (RHCP) and similarly L stands for left handed circular polarization (LHCP). The subscripts 1 and 2 indicate the number of the receiving and transmitting port. Throughout this work, the time convention $e^{j\omega t}$ is used, and for the definition of circular polarization the IEEE definition is followed [6]. An ideal right handed circular polarization selective structure (RHCPSS) should reflect RHCP waves and transmit LHCP waves, while maintaining the polarization state of the signals, and is

described by

$$
\mathbf{S}^{\text{RHCPSS}} = \begin{pmatrix} e^{-j\phi_r} & 0 & 0 & 0 \\ 0 & 0 & 0 & e^{-j\phi_t} \\ 0 & 0 & e^{-j\phi_r} & 0 \\ 0 & e^{-j\phi_t} & 0 & 0 \end{pmatrix},
\tag{2.2}
$$

where ϕ_t and ϕ_r are the phases of the transmission and reflection coefficients, respectively. Similarly, an ideal left handed circular polarization selective structure (LHCPSS) is described by

$$
\mathbf{S}^{\text{LHCPSS}} = \begin{pmatrix} 0 & 0 & e^{-j\phi_t} & 0 \\ 0 & e^{-j\phi_r} & 0 & 0 \\ e^{-j\phi_t} & 0 & 0 & 0 \\ 0 & 0 & 0 & e^{-j\phi_r} \end{pmatrix}.
\tag{2.3}
$$

The scattering matrix of an ideal dual band CPSS will be represented by either (2.2) or (2.3) for a certain frequency f_1 and the other for frequency f_2.

A layer of infinite extent in the plane, perpendicular to the direction of propagation and of infinitesimal thickness, with certain reflection coefficients (r_x, r_y) and transmission coefficients $(t_x = 1 + r_x, t_y = 1 + r_y)$ for linear polarization can be represented by a scattering matrix in circular polarization [11]. The scattering matrix for this linear element is given by

$$
\mathbf{S}_{\text{Linear}}^{\text{CP}} = \frac{r_x + r_y}{2} \begin{pmatrix} 0 & 1 & 1 & 0 \\ 1 & 0 & 0 & 1 \\ 1 & 0 & 0 & 1 \\ 0 & 1 & 1 & 0 \end{pmatrix} + \begin{pmatrix} 0 & 0 & 1 & 0 \\ 0 & 0 & 0 & 1 \\ 1 & 0 & 0 & 0 \\ 0 & 1 & 0 & 0 \end{pmatrix}
$$
$$
+ \frac{r_x - r_y}{2} \begin{pmatrix} e^{-2j\theta_i} & 0 & 0 & e^{-2j\theta_i} \\ 0 & e^{2j\theta_i} & e^{2j\theta_i} & 0 \\ 0 & e^{2j\theta_i} & e^{2j\theta_i} & 0 \\ e^{-2j\theta_i} & 0 & 0 & e^{-2j\theta_i} \end{pmatrix}, \tag{2.4}
$$

where θ_i is the rotation of the element in the plane. A single layer cannot be reduced to any of the ideal cases (2.2) or (2.3), but these properties can be achieved by stacking several layers each rotated with respect to the previous layer and separated by a distance d. Assuming $r_y = 0$, $r_x = r$ and using the Born approximation treating the elements as weak scatterers [10], the scattering matrix for multiple layers of linear elements can be shown to be

$$
\mathbf{S}_{\text{Linear}} = e^{-jkd} \begin{pmatrix} 0 & 0 & 1 & 0 \\ 0 & 0 & 0 & 1 \\ 1 & 0 & 0 & 0 \\ 0 & 1 & 0 & 0 \end{pmatrix} +
$$
$$
\sum_{n=1}^{N} \frac{r}{2} \begin{pmatrix} e^{-2j(kz_n+\theta_n)} & e^{-jkz_n} & e^{-jkd} & e^{-j(kd+2\theta_n)} \\ e^{-2jkz_n} & e^{-2j(kz_n-\theta_n)} & e^{-j(kd-2\theta_n)} & e^{-jkd} \\ e^{-jkd} & e^{-j(kd-2\theta_n)} & e^{-2j(kz_n+\theta_n)} & e^{-2jkz_n} \\ e^{-j(kd+2\theta_n)} & e^{-jkd} & e^{-2jkz_n} & e^{-2j(kz_n-\theta_n)} \end{pmatrix}, \tag{2.5}
$$

where N is the number of layers, z_n is the position of the n:th layer and θ_n is the rotation of the n:th layer. With equidistant placement and the same rotation between each layer the relevant reflection parameters in the scattering matrix can be described by

$$S_{11}^{\mathrm{RR}} = \frac{r}{2} \sum_{n=1}^{N} \mathrm{e}^{-\mathrm{j}2n(kd+\theta)}, \tag{2.6}$$

$$S_{11}^{\mathrm{LL}} = \frac{r}{2} \sum_{n=1}^{N} \mathrm{e}^{-\mathrm{j}2n(kd-\theta)}, \tag{2.7}$$

$$S_{11}^{\mathrm{RL}} = S_{11}^{\mathrm{LR}} = \frac{r}{2} \sum_{n=1}^{N} \mathrm{e}^{-\mathrm{j}2nkd}. \tag{2.8}$$

When the phase distance between two layers equals the relative rotation of the linear elements, $k_1 d = \theta$, (2.7) is maximized and LHCP waves are reflected. If the direction of rotation between the layers is mirrored, $i.e.$ $\theta = -k_1 d$, (2.6) is instead maximized and thus the opposite polarization (RHCP) is reflected. Given that either (2.6) or (2.7) is maximized, the number of layers N can be chosen to minimize the reflection of the orthogonal co-polarized component as well as the cross polarization terms (2.8). A detailed derivation of the lowest optimal number of layers (N_{opt}) is presented in [11], where it is concluded that this quantity is given by the smallest denominator of θ/π, when this is a rational number. To summarize, if $\theta = -k_1 d < 0$ the structure is an RHCPSS at the frequency f_1, corresponding to the wave number k_1. Another solution is achieved when $k_2 d = \pi + \theta = \pi - k_1 d$. Then (2.7) is maximized and for the previously chosen N_{opt} (2.6) and (2.8) are still minimized. This indicates that the structure is an LHCPSS at the frequency f_2, corresponding to the wave number k_2, and the relation between the two bands is given by,

$$f_2 = \frac{\pi - |\theta|}{|\theta|} f_1. \tag{2.9}$$

A physical explanation of these two solutions, and thus the dual band behavior, is as follows. At a fixed instant in time, an electromagnetic CP wave with frequency f_1 propagating in the z-direction through a multilayered CPSS will have a certain phase distribution as it interacts with each of the anisotropic layers, as in Figure 1. If the polarization of the wave rotates in a certain direction in space as a function of the distance z, and the rotation between each layer of the structure θ matches this rotation, the wave will align with the layers and be reflected. This situation is described by the relation $k_1 d = -\theta$. The orthogonal polarization will be misaligned with each layer and thus will be transmitted. However, if another wave at a different frequency f_2 rotates in the opposite direction in space it would also align with the layers the same way if the change of phase between the layers was $k_2 d = \pi + \theta = \pi - k_1 d$. Thus, dual band CP selectivity is achieved with interchanged reflection and transmission properties in the two bands, and the two reflected waves are illustrated in Figure 1.
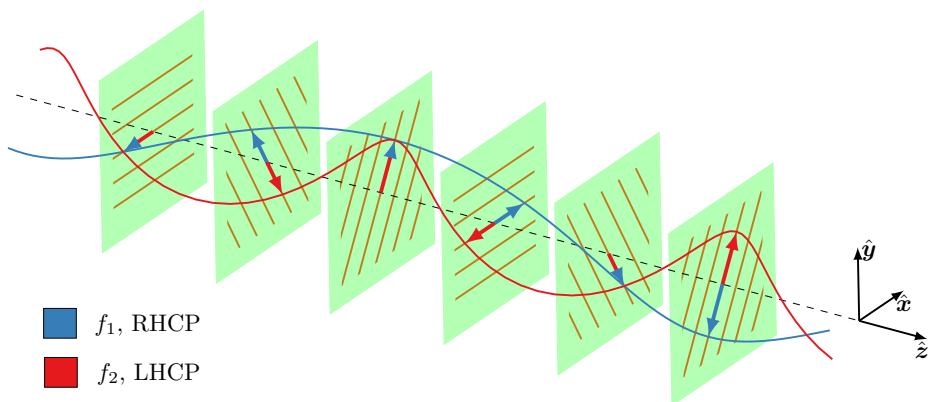
Figure 1: The principle of operation of a dual band CPSS illustrated at a fixed instant in time t, where RHCP waves at frequency f_1 rotate $\theta = -\pi/3$ radians between each layer and LHCP waves at frequency f_2 rotate $\pi + \theta = 2\pi/3$ radians (in the opposite direction).

The selectivity in transmission is not treated by the theory of weak scattering in (2.5)–(2.8), but can be motivated from a power conservation point of view. The co-polarized transmission amplitude is bounded by $|S_{mn}^{ll}|^2 \leq 1 - |S_{nn}^{ll}|^2 - |S_{nn}^{kl}|^2 - |S_{mn}^{kl}|^2$, where $m, n \in \{1, 2\}$ are the receiving and transmitting ports, and $k, l \in \{\text{RHCP}, \text{LHCP}\}$ are the polarization state of the received and transmitted waves. If the co-polarized reflection amplitude $|S_{nn}^{ll}|$ is close to one the co-polarized transmission amplitude $|S_{mn}^{ll}|$ will be small. Conversely, if the co-polarized reflection amplitude is weak, the co-polarized transmission amplitude will be strong, provided weak cross-polarization scattering and low losses.

The choice of the rotation angle θ between the CPSS layers will depend on the desired frequency separation of the bands and the optimal number of layers. In Table 1 different feasible values of θ, the corresponding lowest optimal number of layers, and the frequency separation of the two bands are shown. A general pattern that can be observed is that smaller relative rotations result in larger separations between the frequency bands, and vice versa.

For the proposed frequency bands of $17.7 - 20.2\,\text{GHz}$ and $27.5 - 30.0\,\text{GHz}$ a rotation of $\theta = 76.3°$ would be preferable. This is illustrated in Figure 2, where the reflection of a dual band CPSS consisting of five equidistantly placed layers of linear elements, each rotated $\theta = 76.3°$ with respect to the previous layer, has been simulated using the expressions (2.6)–(2.8). The cross polarization is not minimized with this number of layers but it is low. However, this choice of θ cannot be implemented in a full wave simulation model as the unit cell construction using periodic boundary conditions is infeasible if the number of layers is larger than three. For such a periodic structure consisting of connected elements, modeled with periodic boundary conditions, the feasible choices of θ

Table 1: The number of layers and for what frequencies the dual band CPSS is operating for a certain rotation between layers.

Rotation - degree / (radian)	$N_{\min}$	f_2
18° / ($\pi/10$)	10	$9f_1$
20° / ($\pi/9$)	9	$8f_1$
22.5° / ($\pi/8$)	8	$7f_1$
24° / ($2\pi/15$)	15	$6.5f_1$
30° / ($\pi/6$)	6	$5f_1$
36° / ($\pi/5$)	5	$4f_1$
40° / ($2\pi/9$)	9	$3.5f_1$
45° / ($\pi/4$)	4	$3f_1$
60°/ ($\pi/3$)	3	$2f_1$
72° / ($2\pi/5$)	5	$1.5f_1$

are $\{45°, 60°\}$ [11]. To this end, $\theta = 60°$ is used in this work as the frequency separation of the two bands is better suited than that of $\theta = 45°$.

3 Design and Optimization

A multitude of dual band CPSS designs, consisting of different numbers of meander line sheets, were optimized and evaluated in [11]. There it was observed that adding more layers to the structure increases the potential bandwidth of the CPSS, but also increases the design complexity of the structure. It was shown that the wide bandwidth displayed in [5] can be traded for improved dual band performance by relocating the frequency bands of operation closer to each other. The study in [11] provided a starting point for designing and optimizing a dual band CPSS in this work. As was mentioned in Section 2, the rotation angle $\theta = 60°$ is used and meander lines are utilized as linear elements as they previously have been successfully used to simulate and manufacture a single band wide band CPSS [4, 5]. However, the optimization procedure presented in this section can be used to design dual band CPSS with any kind of elements. Realistic materials were implemented in the simulation model, where copper meander lines were printed on thin substrates, separated by low permittivity spacers and assembled together using thin bonding films. Further details of the materials used are presented in Sections 4–5.
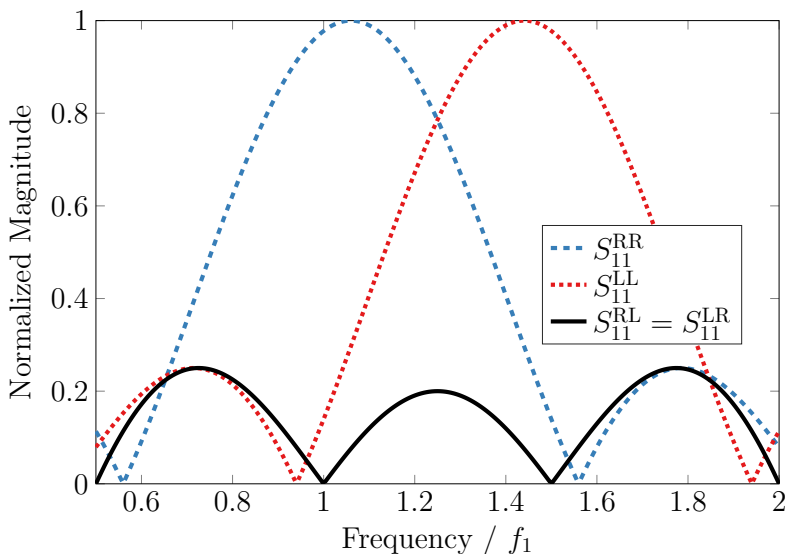
Figure 2: Reflection simulations of a five layer dual band CPSS using the weak scattering approximation. Scattering parameters of normalized magnitude are presented as a function of normalized frequency.

The meander line geometry for a single layer is depicted in Figure 3, where a unit cell is shown and design parameters are introduced to describe the unit cell and the meander line. Each meander line is described by a width, w_n, a height, h_n and a periodicity, P, which is the same for all layers. There are two periods of the meander line in the unit cell to enforce correct alignment in the infinite structure. The three dimensional unit cell has the shape of a parallelepiped and the periodicity of the unit cell is shared between all layers.

Increasing the number of layers, given $N = aN_{\text{opt}}$ ($a \in \mathbb{N}$), increases control of the polarization purity of reflected and transmitted CP waves. However, in a realistic design increasing the number of layers is problematic as the losses in the materials become more significant and the fabrication of the design becomes more challenging. Moreover, each additional layer of meander lines adds to the dimension of the parameter space, resulting in higher complexity of the optimization problem.

Due to the high number of degrees of freedom in the design, multilayer CPSS are quite complex from an optimization point of view. Thus, symmetry around the center of the structure in the $\hat{\boldsymbol{z}}$-direction is enforced in order to reduce the design complexity. This roughly reduces the dimension of the problem by half. The design parameters used are the width, w_n, and height, h_n, of the meander lines (as illustrated in Figure 3), the thickness, d_n, of each spacer between the layers and the periodicity of the meander lines, P. For a design with an even number of layers this results in $\frac{3}{2}N + 1$ optimization parameters where N is the
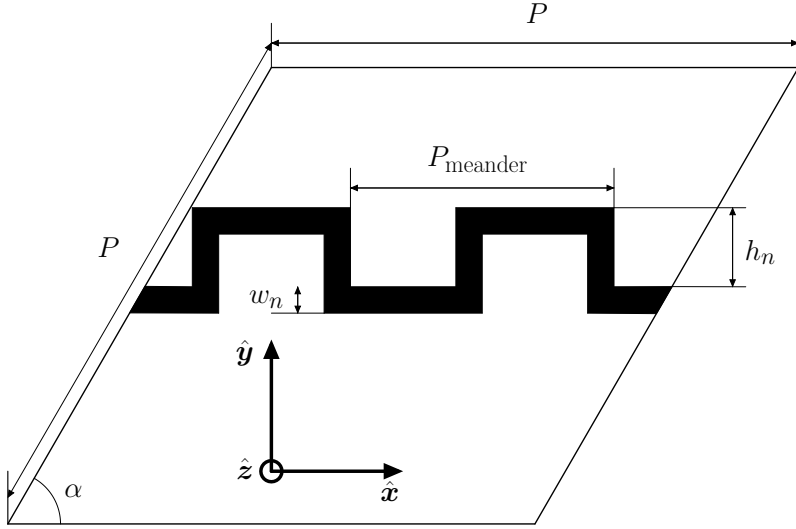
Figure 3: Geometry of a meander line unit cell. The tilt angle of the unit cell α is chosen to be equal to $\theta = 60°$.

number of layers, similarly for a design with an odd number of layers the number of optimization parameters are $\frac{3}{2}(N+1)$. In this work, six layers were chosen for the design based on a compromise between performance and design complexity.

To evaluate the designs during the optimization process a number of performance parameters are introduced. For a CPSS the relevant properties to examine are the losses in transmission and reflection as well as the purity of the circular polarization in both reflection and transmission for the relevant polarization. These parameters are quantified as insertion loss (IL), return loss (RL) and axial ratio (AR). The definition of these parameters, in dB, is

$$\mathrm{IL} = -20\log 10(|S_{mn}^{ll}|), \quad m \neq n, \tag{3.1}$$

$$\mathrm{RL} = -20\log 10(|S_{nn}^{ll}|), \tag{3.2}$$

$$\mathrm{AR_t} = 20\log 10\left(\left|\frac{|S_{mn}^{kl}| + |S_{mn}^{ll}|}{|S_{mn}^{kl}| - |S_{mn}^{ll}|}\right|\right), k \neq l, \ m \neq n, \tag{3.3}$$

$$\mathrm{AR_r} = 20\log 10\left(\left|\frac{|S_{nn}^{kl}| + |S_{nn}^{ll}|}{|S_{nn}^{kl}| - |S_{nn}^{ll}|}\right|\right), k \neq l, \tag{3.4}$$

where, as previously introduced in Section 2, $m, n \in \{1, 2\}$ are the receiving and transmitting ports, and $k, l \in \{\mathrm{RHCP}, \mathrm{LHCP}\}$ are the polarization state of the received and transmitted waves.

The targeted goals to be fulfilled in both frequency bands, are IL and RL less than 0.5 dB for the relevant polarization, and AR less than 0.78 dB. These

performance levels were previously introduced in an analogous project involving a single band CPSS [2]. For a dual band CPSS there are in total eight target goals to fulfill, summarized in Table 2. In this project, the structure was designed to reflect RHCP in the lower frequency band and LHCP in the upper frequency band, which could easily be interchanged by mirroring the structure.

Table 2: Performance parameters for each polarization and frequency band. The subscripts on AR indicate transmission (t) or reflection (r). The requirements to be fulfilled in this work are IL and RL less than 0.5 dB and AR less than 0.78 dB.

	$17.7 - 20.2\,\text{GHz}$	$27.5 - 30.0\,\text{GHz}$
RHCP	RL & AR_r	IL & AR_t
LHCP	IL & AR_t	RL & AR_r

From the specified performance parameters and target values a penalty function F is introduced. Finding a suitable design implies minimizing F, which has the general form

$$F = \sum_{n=1}^{2} \sum_{m=1}^{4} c_{n,m} \int_{\Omega_n} |g_{n,m}|^{k_{n,m}} \cdot \text{H}(g_{n,m})\,\text{d}f, \qquad (3.5)$$

with

$$g_{n,m}(f) = h_{n,m}(f) - l_{n,m}, \qquad (3.6)$$

where index n is for each band, index m is for the performance parameter, $c_{n,m}$ is the weight of each function, $h_{n,m}$ are the performance functions of interest (see Table 2), $l_{n,m}$ are the thresholds under which the integrand is zero, Ω_n is the integration domain specified by the frequency bands, $k_{n,m}$ are exponent weights and H is the Heaviside (or unit step) function.

The penalty function contains several local minima which is problematic for many optimization algorithms. To avoid these undesirable minima several optimization algorithms, weight functions and thresholds were used to effectively find a well performing design. By utilizing several algorithms the strength of each algorithm was combined to reach a good design, a task which would be difficult to achieve with a single algorithm in reasonable time. Due to the number of optimization parameters and the size of the initial parameter space, a genetic algorithm was used as a starting tool. This algorithm is well suited for the problem due to its ability to deal with several local minima effectively. If the genetic algorithm did not converge to a design which had promising performance then the penalty function was tweaked based on the result and behavior of each target value (IR, RL and AR) and the algorithm was used again. However, if the design was performing well the parameter space was reduced for each relevant parameter based on how stable the solution appeared and a new algorithm was employed to further improve the design. The second algorithm used was a
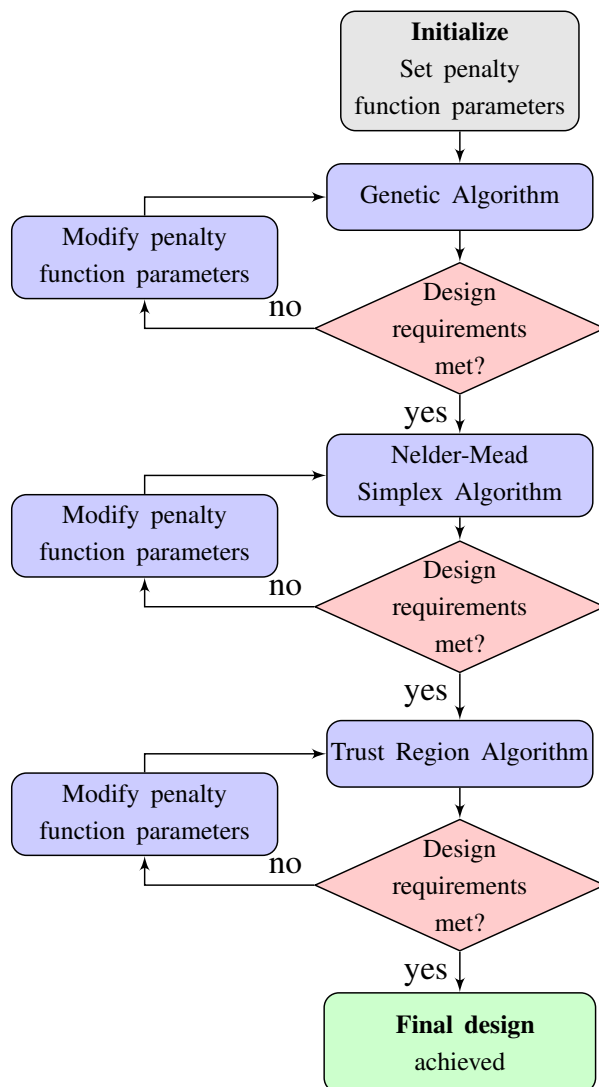
Figure 4: Flowchart for optimizing a dual band CPSS using built-in optimization algorithms in CST MWS.

Table 3: Initial Parameter Space for the genetic algorithm optimization of the 6 layer Dual band meander line CPSS.

Parameter	Range
Periodicity (mm)	$0.4 \leq P \leq 8.0$
Height (mm)	$0.0 \leq h_n \leq P$
Width (mm)	$0.1 \leq w_n \leq P/4$

Nelder-Mead simplex algorithm. This is a downhill algorithm suitable for use if it is assumed that there is one local minimum in the near surrounding of the parameter space. This is ideally the case after a successful genetic search. If the optimized results were unsatisfactory the penalty function was modified and the Nelder-Mead algorithm was rerun. Finally, a trust region algorithm was used when the design given by the Nelder-Mead algorithm was in close proximity to a minimum. This algorithm creates a linear model around the initial point and defines an initial radius in which the model is assumed to be a good approximation, a trust region. This algorithm excels when very close to a minimum, and the trust region holds well, as should be the case after a successful Nelder-Mead optimization. In summary, a genetic algorithm was used to identify the region of the optimal minima and a Nelder-Mead was used to move closer and reduce the search region for a trust region algorithm to successfully find the optimum. The described procedure can be summarized by the flowchart in Figure 4. The utilized algorithms are all available in Computer Simulation Technology Microwaves Studio (CST MWS) as built in optimization algorithms. Greater flexibility can be achieved in the optimization process if the simulation software is controlled externally by MATLAB. In this case a great number of optimization algorithms can be utilized.

A six layer CPSS design was optimized for normal incidence in CST MWS using a 32 GB RAM, Intel i7-2600 3.4 GHz CPU desktop computer, using the technique in Figure 4. The initial parameter space for the genetic algorithm was large and determined based on limitations in the manufacturing process and unwanted effects such as grating lobes. Generally, in order to avoid grating lobes for normal incidence, the periodicity had to be smaller than the wavelength of the higher band. For a frequency of 30.0 GHz this gives an upper bound on the periodicity of 10 mm. However, onset of grating lobes is spotted for smaller values of periodicity and as a consequence the maximum value was set to 7 mm. The width of the meander lines had to be larger than the smallest manufacturing size, 0.1 mm, and smaller than one fourth of the current unit cell periodicity. The meander line height can range between 0 and the current unit cell periodicity. These constraints are consequences of the geometry, see Figure 3. In total the initial parameter space for the genetic algorithm is summarized in Table 3. Based on the resulting design, the parameter space was reduced between each algorithm. This typically resulted in a reduction of the parameter space by at least an order of two.

Table 4: Material parameters of the meander line CPSS

Material	Rel. permittivity	Loss tangent	Thickness
Rohacell H31 spacers	1.043	0.002	d_1, d_2 and d_3
Arlon DiClad 880 substrates	2.17	0.003	$0.127\,\text{mm}$
Copper, wires	$\sigma = 58\,\text{MS/m}$		$18\,\mu\text{m}$
3M Scotch-Weld bonding layers	2.32	0.001	0.05 mm

A coarse simulation mesh of ten steps per wavelength was initially used in the genetic algorithm optimization in order to reduce the computation time of each iteration. Typically a few thousand iterations were carried out in this part of the procedure. The mesh settings were later gradually improved during the optimization cycles when the simplex algorithm and the trust region algorithm were employed, where roughly a few hundred iterations were carried out. A mesh convergence study was executed when a final design candidate fulfilling all requirements had been achieved. This study showed that the mesh settings used in the optimization process were satisfactory, and that almost no noticeable improvement in accuracy was achieved if a mesh finer than 16 steps per wavelength was used.

4   Simulated Results

The optimized six layer CPSS, with 60° relative rotations between subsequent layers, consists of thin Arlon DiClad 880 teflon sheets with printed copper meander lines separated by low permittivity, low loss Rohacell HF31 spacers. The components of the structure were bonded together using thin bonding layers. The electrical properties and thickness of the bonding layers were estimated using the same procedure as in [5], where a similar CPSS was designed and fabricated. The material properties and the thickness of each layer of the dual band CPSS are presented in Table 4, and a side view of the CPSS can be seen in Figure 5.

The total thickness of the simulated design is $17.22\,\text{mm}$, which corresponds to 1.08 wavelengths at the center frequency of the lower band of operation $f = 18.95\,\text{GHz}$. The meander lines of one unit cell as implemented in CST MWS can be seen in Figure 6, and the values of the meander line thickness w_i and the meandering height h_i of each layer are given in Table 5. The side length of the unit cell P and the thickness of the spacers are also presented in Table 5. Only three different meander line layers and spacer thicknesses are present in the design due to the enforced symmetry introduced in Section 3.

Simulation results are presented in Figure 7 where 20 steps per wavelength mesh setting was used, and the IL, RL and AR for transmission and reflection are
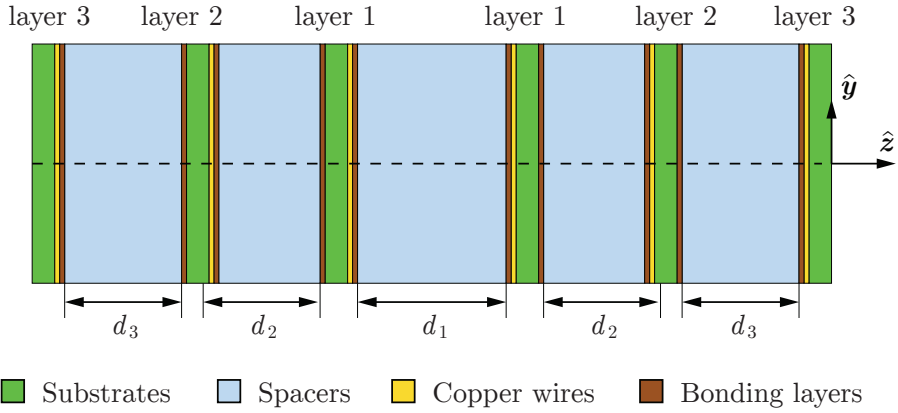
Figure 5: Side view of the dual band meander line CPSS consisting of six layers of substrates and five low permittivity spacers.
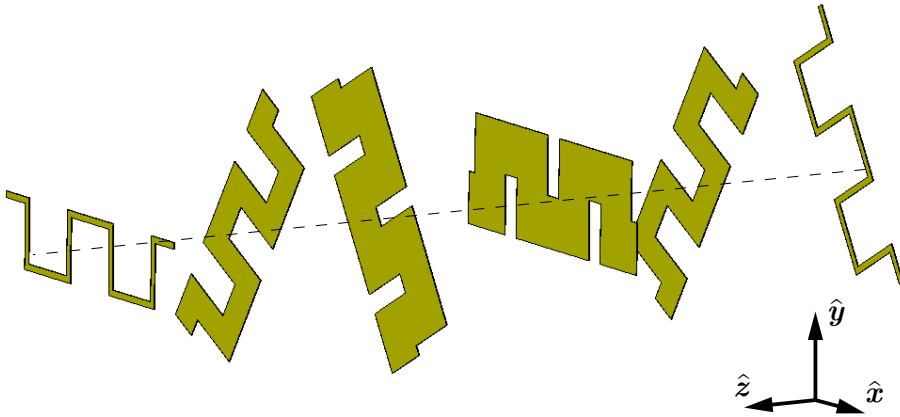
Figure 6: Meander lines of the six layers in the dual band CPSS design implemented in CST MWS. When a unit cell is defined, components extending outside of the unit cell are automatically pasted into the opposite side of the unit cell by the software.

Table 5: Geometrical parameters of the dual band meander line CPSS.

Parameter	P	d_1	d_2	d_3	h_1
Value (mm)	5.49	3.80	2.90	3.24	1.14

Parameter	h_2	h_3	w_1	w_2	w_3
Value (mm)	1.21	1.25	0.99	0.61	0.12
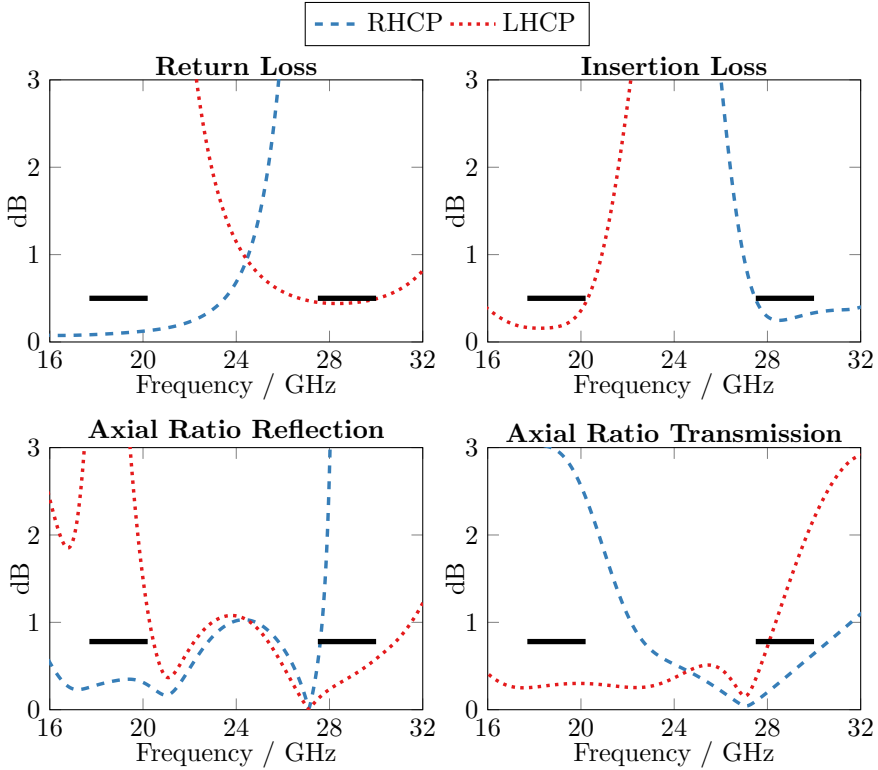
Figure 7: Simulated results of the meander line dual band CPSS, where blue curves correspond to RHCP and red curves to LHCP. The upper left plot shows the RL in both frequency bands and the lower left plot the corresponding AR. The upper right plot shows the IL in both frequency bands and the lower right plot the corresponding AR.

presented for both bands of operation. Blue curves correspond to RHCP and red curves to LHCP and it can be seen that the eight requirements specified in Table 2 are all fulfilled. When comparing the results in Figure 7 to the wideband meander line CPSS in [5] a substantial reduction in bandwidth can be observed in the dual band design. This is in part caused by the targeted dual band functionality as well as the relatively small frequency separation between the bands of operation.

Only normal incidence was considered during the optimization but in order to evaluate the performance of the design with respect to oblique angles of incidence (θ) for all possible incidence planes (ϕ), the scattering matrix for the structure was simulated for every combination of θ and ϕ, corresponding to 2376 simulations. The scattering matrix was computed for the center frequency in each frequency band i.e. 18.95 GHz for the lower frequency band and 28.75 GHz

for the higher frequency band. The results of the oblique incidence evaluation are seen in Figure 8 and Figure 9. The results are plotted as in previous work [5] where the results are projected on a unit sphere. The lower frequency band is very stable with respect to angle of incidence variations and symmetries can be identified. The RL and IL for the higher frequency band are more sensitive to angle of incidence variations. This is not surprising due to the fact that these specific target goals were not as easily fulfilled as the other goals. However, it is interesting to note that the higher frequency band has a better performance with respect to the 0.78 dB AR goal compared to the lower frequency band. The design was not optimized for oblique incidence yet it has a very good performance up to $\theta = 20°$. There are certain preferred incidence planes similar to previous observations [5].

5   Prototype Manufacturing and Error Estimates

A prototype of the optimized six layer dual band CPSS was manufactured and can be seen in Figure 10. The dimensions of the prototype are $310\,\mathrm{mm} \times 310\,\mathrm{mm}$ and the total thickness is 16.96 mm, which should be compared to the thickness of the optimized simulated design of 17.22 mm. As was mentioned in Section 4, copper meander lines were printed on thin Arlon DiClad 880 substrates. The Rohacell HF31 spacers were manufactured by Evonik Industries AG, and the thickness of each layer was controlled to an accuracy of 0.2 mm. The thickness of each spacer was measured individually, using a micrometer screw gauge, before assembling the prototype and it was concluded that the deviation between simulated and fabricated values was smaller than 0.1 mm. For the bonding layers a 3M Scotch-Weld 76 adhesive spray was used. Unfortunately, the actual thickness of the bonding layers proved difficult to estimate due to the Rohacell HF31 being porous and the adhesive penetrating the spacers in the process of assembly of the prototype. In order to investigate the impact of the bonding layer thickness on the performance of the CPSS, a parametric study was carried out where the thickness of the bonding layers was varied, while the total thickness of the CPSS was kept fixed by compensating the thickness of the spacers by the same length. The results of this study indicate that increasing the thickness of the bonding layers by a factor of two implies a negative frequency shift of about 0.7 GHz in RL and IL, as well as a detuning of the corresponding AR. Another source of error associated with the assembly of the prototype is the impact of a relative displacement in the xy-plane between subsequent layers in relation to the alignment in Figure 6. This effect was investigated by simulating the properties of the CPSS where translations in the horizontal and vertical directions were introduced using random shift variables, and where the maximum shift of each layer corresponded to a complete displacement in relation to the next layer. A total of 200 such simulations were carried out and the impact of displacements of the
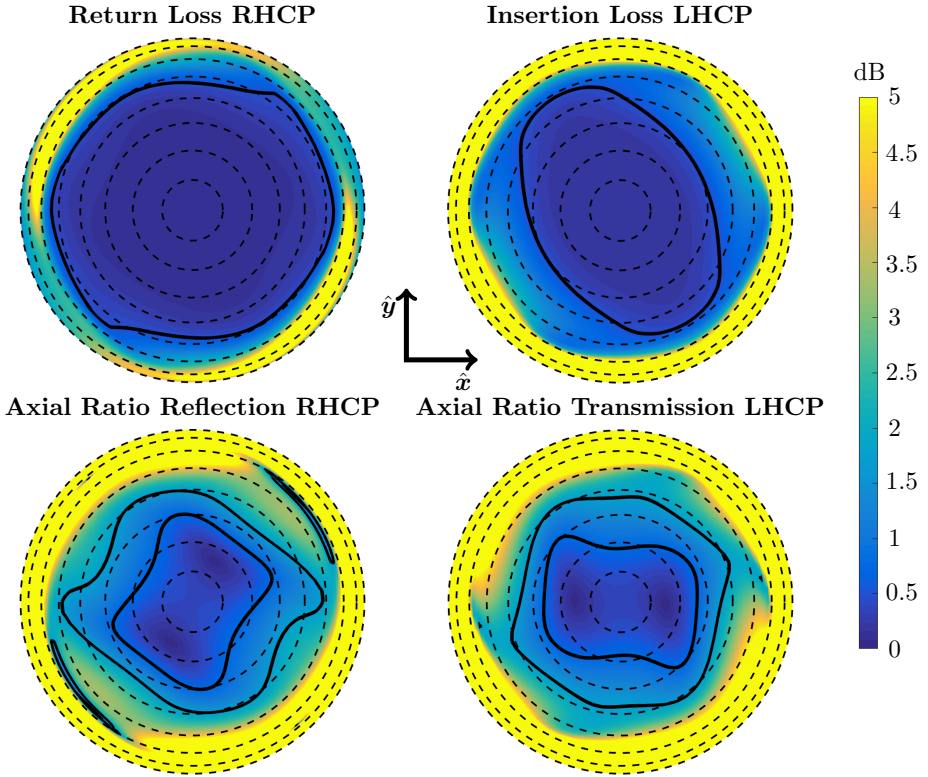
Figure 8: Simulation results for front-side illumination of the lower frequency band of the dual band CPSS for the frequency $f = 18.95\,\mathrm{GHz}$. The two left plots show the RL and AR of the reflected signal (RHCP). The two right plots show IL and RL of the transmitted signal (LHCP). All values are in dB. The dashed circles indicate an incidence angle of $\theta = \{10°, 20°, \ldots, 80°\}$. The solid lines indicate the target values of $0.5\,\mathrm{dB}$ for RL and IL, $0.78\,\mathrm{dB}$ for AR and the relaxed target of $1.74\,\mathrm{dB}$ for AR used in [5].
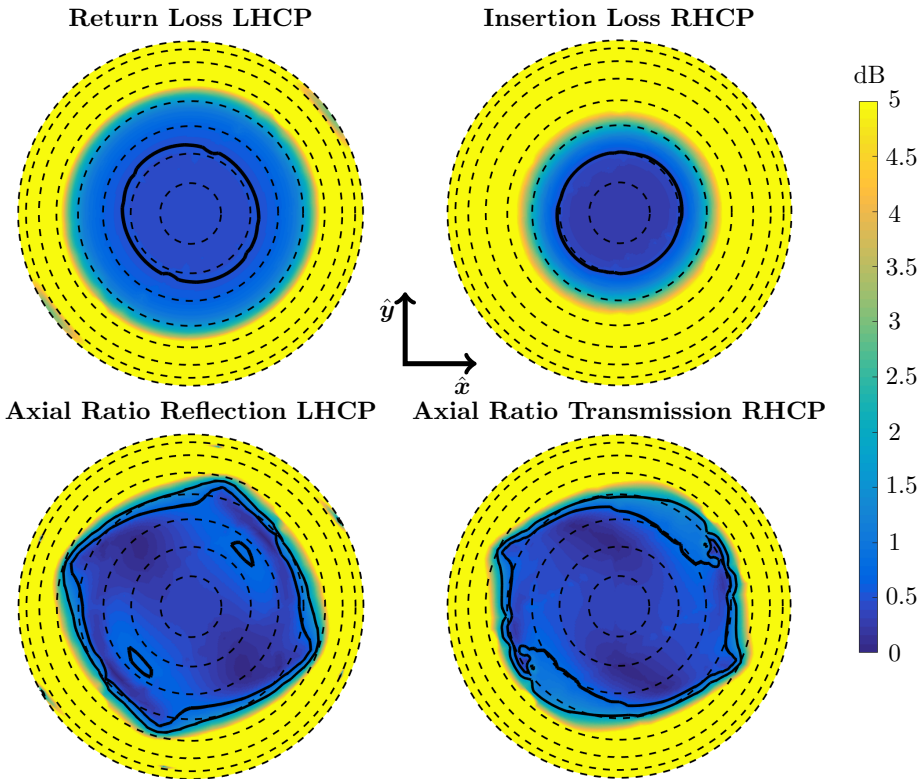
Figure 9: Simulation results for front-side illumination of the lower frequency band of the dual band CPSS for the frequency $f = 28.75\,\text{GHz}$. The two left plots show the RL and AR of the reflected signal (LHCP). The two right plots show IL and RL of the transmitted signal (RHCP). All values are in dB. The dashed circles indicate an incidence angle of $\theta = \{10°, 20°, \ldots, 80°\}$. The solid lines indicate the target values of $0.5\,\text{dB}$ for RL and IL, $0.78\,\text{dB}$ for AR and the relaxed target of $1.74\,\text{dB}$ for AR used in [5].
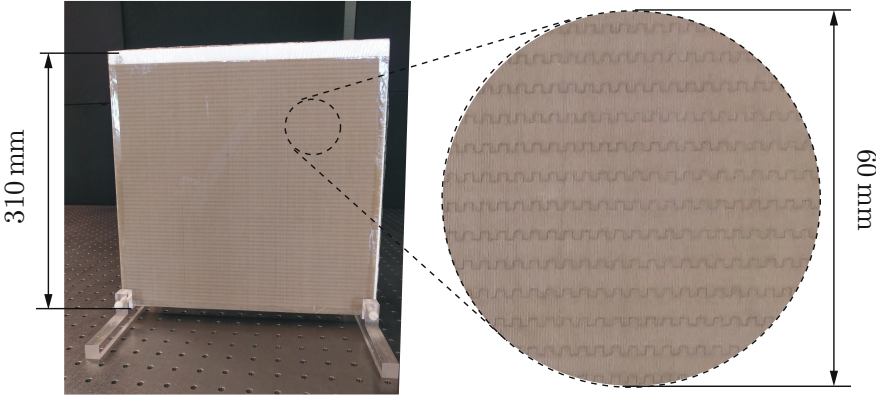
Figure 10: Manufactured dual band CPSS prototype.

layers in transverse directions is negligible in RL and IL, and on the order of 0.05 dB in AR. Similar results were presented in [22], where relative translations of subsequent layers of a multilayer CPSS in the optical regime were investigated.

6 Experimental Setup and Results

Experimental characterization of the transmission and reflection properties of the dual band CPSS prototype were carried out. The frequency range $13 - 34$ GHz was measured using two separate pairs of single-polarized, standard gain horn antennas. A frequency range greater than that of interest was measured to enable effective use of removal of unwanted multipath components using time gating and zero padding. Through this technique, described in detail in [4], the need to to carry out the measurements inside an anechoic chamber to remove unwanted multipath signals was eliminated. Two SATIMO SGH 1850 antennas were used to cover the lower frequency band, and two SATIMO SGH 2650 antennas were used for the upper frequency band. These antennas have a boresight cross-polarization discrimination better than 40 dB in their respective frequency range of interest, needed to measure low AR [4]. The experimental setup was assembled on a Newport RS2000 optical table, and the receiving and transmitting antennas were mounted on THORLABS PRMTZ8 motorized precision rotation stages. Two of such stages were used to control the yaw and the roll of each antenna, which in turn were connected to an Agilent E8364b vector network analyzer (VNA). The VNA and the rotational stages were controlled through MATLAB scripts using USB and GPIB to USB connections [9,19]. The VNA was calibrated to the ends of the cables using a calibration kit. The CPSS prototype was placed in a custom made sample holder of adjustable height made entirely of plastic and poly methyl methacrylate (PMMA). An overview of the experimental setup is presented in Figure 11.
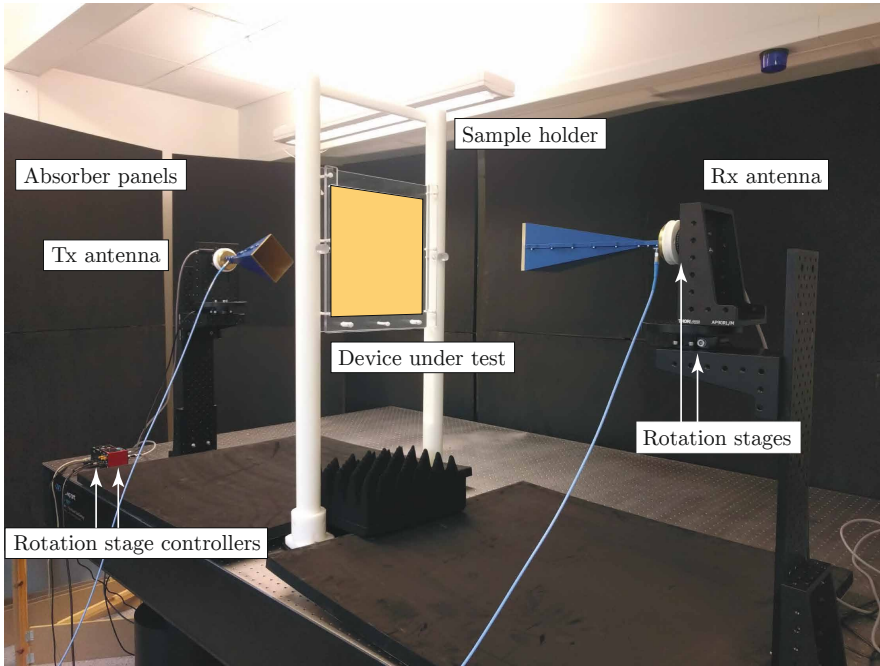
Figure 11: Experimental setup for dual/wide band characterization of a CPSS at frequencies 13–34 GHz .

The high degree of control in alignment of the setup provided by the optical table, the antenna fixtures and the rotational stages implied that the setup could easily be modified to measure at different distances between the sample and the antennas. An initial coarse alignment of all components of the setup was carried out using cross line lasers. After that, the alignments of the rotational stages were fine-tuned using feedback from the VNA. For the transmission measurements, a golden section search was utilized to maximize power throughput of the setup, given a fixed separation between the antennas, without the prototype present. In a similar way, alignment of the setup for reflection measurements used a golden section search maximizing reflection with the reference being an aluminum sheet water-glued to the prototype [4]. This method achieved an accuracy in antenna rotation and jaw alignment on the order of 0.1°.

When the setup had been properly aligned, the scattering matrix components of interest in linear polarization were acquired and processed using the post processing method described in detail in [4], involving time gating and zero padding, resulting in equivalent circular polarization scattering parameters of the device under test. When characterizing the transmission properties of the CPSS, the antennas were placed on each side of the prototype as in Figure 11. The scattering matrix components of the device under test were normalized with a corresponding reference measurement, consisting of measurements of the empty setup. In reflection, both antennas were placed on one side of the device under

test at an oblique angle of about 3°. This small incidence angle variation was simulated and it was concluded that the variations in the scattering parameters of the meander line CPSS were hardly noticeable (less than 0.02 dB), compare with Figure 8 and Figure 9. For the reference measurements in reflection, a thin aluminum foil was attached to the device under test using a small amount of water as an adhesive.

The characterized deviations between the optimized and fabricated designs due to manufacturing errors and uncertainties, discussed in Section 5, were used to generate an updated simulation model corresponding to the realized prototype. In this design, the thickness of the spacers is $d_1 = 3.78$ mm, $d_2 = 2.87$ mm, $d_3 = 3.17$ mm, and the updated bond layer thickness was set to 0.12 mm. A comparison between the updated simulation results and the experimental results are presented in Figure 12, where the colored curves correspond to measurements and the black solid and dashed curves represent simulated results. It can be seen in the experimental data that two separate pairs of antennas were used to cover the full frequency range. The experimental AR curves are only plotted in the relevant regions of interest for each component, in order to make the figures more readable. Good agreement can be observed in general between the simulated and measured results. However, it can be noticed that the RL of the higher frequency band is about 0.1–0.2 dB larger than the simulated results. This is most likely caused by the difficulty of the manufacturing process where the amount of applied adhesive is highly important. The difficulty in managing the higher RL indicates that more adhesive should have been applied. Other sources of errors are that the material parameters used in the simulations are typically defined for frequencies less than 10 GHz. Another CPSS design was manufactured using excessive amounts of adhesive (approximately 2.5 x the simulated amount). This design showed a negative frequency shift of around 1 GHz and an increase in IL, most prominent for the higher frequency band. This is expected based on the motivation above that both the Rohacell HF31 spacers and the adhesive layers most likely display increasing losses when higher frequencies are considered. A significant part these effects stem from the complicated fabrication and could be negated through a more rigorous construction method and industrial setting and or change of materials.

7   Conclusions

A dual band circular polarization selective structure for K- and K_a-band applications has been presented. The structure consists of six cascaded layers of meander lines, separated by low permittivity spacers. Simulations of the design fulfill the strict design requirements of return loss and insertion loss better than 0.5 dB, and axial ratio better than 0.78 dB over the frequency bands 17.7–20.2 GHz and 27.5–30.0 GHz, with alternating circular polarizations in the two bands. A prototype was fabricated and characterized experimentally and good agreement has been observed between simulated and measured results. This type of cascaded
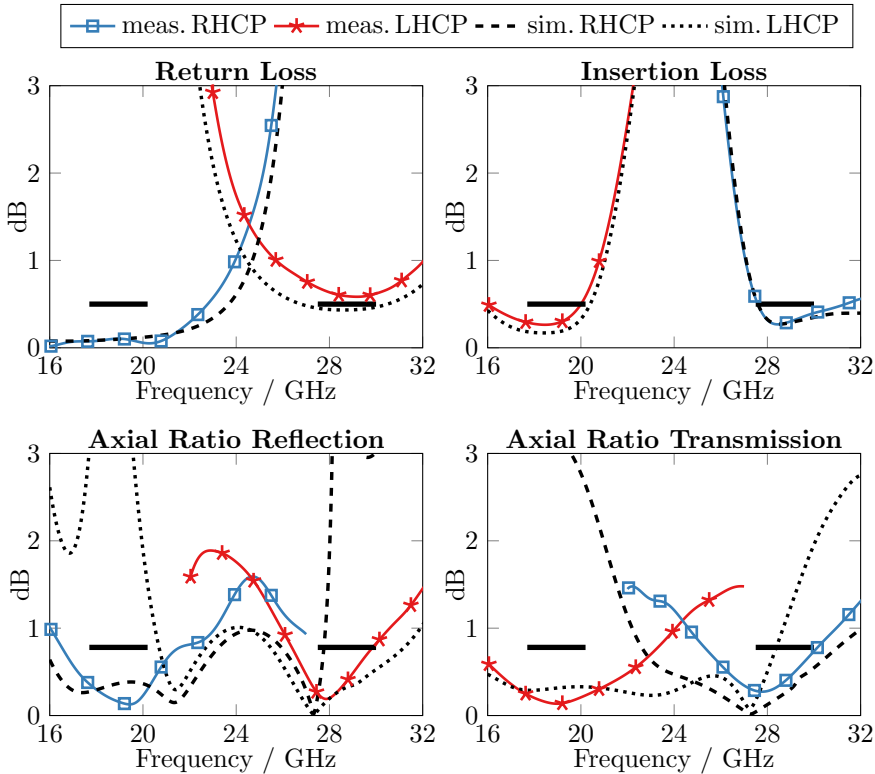
Figure 12: Experimental results of the meander line dual band CPSS. The upper left plot shows the RL in both frequency bands and the left plot the corresponding AR. The upper right plot shows the IL in both frequency bands and the lower right plot the corresponding AR. Simulation results are given by the solid and dashed black curves.

CPSS has been shown to possess great potential to achieve both wideband and multi-band filtering properties, and constitutes an interesting design concept for future ideas. Moreover the simulation for oblique incidence spurs an interest to create a single narrow band CPSS with high angle of incidence performance.

References

[1] S. M. A. M. H. Abadi and N. Behdad. A broadband, circular-polarization selective surface. *Journal of Applied Physics*, **119**(24), pp. 244901, 2016.

[2] M. Albani, P. Balling, L. Datashvili, G. Gerini, P. Ingvarson, K. Pontoppidan, M. Sabbadini, D. Sjöberg, S. Skokic, and G. Vecchi. Concepts for polarising sheets & "dual-gridded" reflectors for circular polarisation. In

ICECom Proceedings, pp. 1–4, 2010.

[3] C. Cappellin, D. Sjöberg, A. Ericsson, P. Balling, G. Gerini, N. J. G. Fonseca, and P. D. Maagt. Design and analysis of a reflector antenna system based on doubly curved circular polarization selective surfaces. In *2016 10th European Conference on Antennas and Propagation (EuCAP)*, pp. 1–5, 2016.

[4] A. Ericsson, J. Lundgren, and D. Sjöberg. Experimental characterization of circular polarization selective structures using linearly single-polarized antennas. *IEEE Trans. Antennas Propag.*, **65**(8), pp. 4239–4249, 2017.

[5] A. Ericsson and D. Sjöberg. Design and analysis of a multilayer meander line circular polarization selective structure. *IEEE Trans. Antennas Propag.*, **65**(8), pp. 4089–4101, 2017.

[6] IEEE. Ieee standard test procedures for antennas, 1979.

[7] W. A. Imbriale, S. S. Gao, and L. Boccia, editors. *Space Antenna Handbook*. Wiley, 2012.

[8] M. Joyal and J. Laurin. Design and analysis of a cascade circular-polarization-selective surface at K band. *IEEE Trans. Antennas Propag.*, **62**(6), pp. 3043–3052, 2014.

[9] Keysight Instruments and MATLAB, 2017. Available at: https://se.mathworks.com/products/instrument/supported/keysight.html, accessed 2017-09-22.

[10] G. Kristensson. *Scattering of Electromagnetic Waves by Obstacles*. SciTech Publishing, an imprint of the IET, Edison, NJ, 2016.

[11] J. Lundgren. Dual band circular polarization selective structures for space applications. Master's thesis, Lund University, Department of Electrical and Information Technology, P.O. Box 118, SE-221 00 Lund, Sweden, 2016. Rep. No. LU/LTH-EIT 2016-540.

[12] G. A. Morin. A simple circular polarization selective surface (CPSS). In *Antennas and Propagation Society International Symposium, 1990. AP-S. Merging Technologies for the 90's. Digest.*, pp. 100–103. IEEE, 1990.

[13] R. Pierrot. Reflector for circularly polarized waves, 1970. US Patent 3,500,420.

[14] S. Rao, L. Shafai, and S. K. Sharma. *Handbook of Reflector Antennas and Feed Systems Volume III: Applications of Reflectors*. Artech house, 2013.

[15] D. Sjöberg and A. Ericsson. A multi layer meander line circular polarization selective structure (MLML-CPSS). In *Proceedings of the 8th European Conference on Antennas and Propagation (EuCAP)*, pp. 464–468. IEEE, 2014.

[16] W. Tang, G. Goussetis, N. J. G. Fonseca, H. Legay, E. Sáenz, and P. de Maagt. Coupled split-ring resonator circular polarization selective surface. *IEEE Trans. Antennas Propag.*, **65**(9), pp. 4664–4675, 2017.

[17] W. Tang, S. Mercader-Pellicer, G. Goussetis, H. Legay, and N. J. G. Fonseca. Low-profile compact dual-band unit cell for polarizing surfaces operating in orthogonal polarizations. *IEEE Trans. Antennas Propag.*, **65**(3), pp. 1472–1477, 2017.

[18] I.-Y. Tarn and S.-J. Chung. A new advance in circular polarization selective surface – A three layer CPSS without vertical conductive segments. *IEEE Trans. Antennas Propag.*, **55**(2), pp. 460–467, 2007.

[19] Thorlabs PRMTZ8 motorized precision rotation stage, 2017. Available at: https://www.thorlabs.com/newgrouppage9.cfm?objectgroup_id=4134, accessed 2017-09-22.

[20] W. V. Tilston, T. Tralman, and S. M. Khanna. A polarization selective surface for circular polarization. In *Antennas and Propagation Society International Symposium, 1988. AP-S. Digest*, pp. 762–765. IEEE, 1988.

[21] J. Wang, Z. Shen, and W. Wu. Broadband and high-efficiency circular polarizer based on planar-helix chiral metamaterials. *Applied Physics Letters*, **111**(11), pp. 113503, 2017.

[22] Y. Zhao, M. Belkin, and A. Alù. Twisted optical metamaterials for planarized ultrathin broadband circular polarizers. *Nature Communications*, **3**, pp. 870, 2012.

Experimental Characterization of Circular Polarization Selective Structures using Linearly Single- Polarized Antennas

Paper III

Andreas Ericsson, Johan Lundgren and Daniel Sjöberg

Abstract

We present a technique for performing high accuracy measurements of the transmission and reflection properties in circular polarizations of a test panel. By using linearly polarized antennas and measuring at four different antenna orientations, all with a relative rotation of 45 degrees, an efficient normalization of each scattering component can be utilized. This method achieves a high signal to noise ratio in all normalized linear polarization components used to synthesize the circular polarization scattering. Furthermore, a post processing scheme is introduced to compensate for measurement uncertainties due to antenna misalignments. The novel measurement and post processing techniques are utilized to characterize a manufactured wideband circular polarization selective structure, both in transmission and reflection, and the measurement results are in excellent agreement with simulation results from a commercial software. The repeatability of the measurement results is investigated, and the results are in the expected range in comparison to estimated measurement uncertainties.

1   Introduction

A strong driving force in the development of future satellite communication systems is to increase the data transfer rate [12, 25]. This has previously been achieved using frequency and polarization reuse schemes [3, 4, 12, 25, 28]. Polarization filtering can easily be achieved in linear polarization (LP) using a strip grid, where signals polarized parallel to the grid are reflected and signals polarized orthogonal to the grid are transmitted [4]. However, in future satellite communication systems, typically designed to operate in the K, K_a-bands, it is preferable to utilize circular polarization (CP) and thus eliminating the problem of aligning receiving antennas with the polarization of the incident signals.

To filter signals of orthogonal CP is not as trivial as in the case of LP. Nevertheless, a multitude of circular polarization selective structures (CPSSs) have been presented over the last 50 years [1, 2, 5, 7, 13–15, 19–22, 26, 27, 31, 32]. The most wideband CPSS presented up to date is based on cascaded anisotropic sheets of meander lines [6, 29]. This type of structure achieves a bandwidth of approximately 45 % and shows significant improvements in stability with respect to angle of incidence variations compared to previous designs. The recent performance improvement of CPSSs over the last few years make integration of these structures in an actual satellite communication system a realistic future step. This implies an increasing importance of accurately characterizing the performance of CPSSs, both through computer simulations in commercial softwares as well as through measurements of manufactured test panels. The performance of a CPSS is commonly presented as a function of frequency for a few discrete angles of incidence, and in [5] a scheme for studying the CPSS performance at fixed frequencies as a function of all possible spherical angles of incidence was presented. In a simulation software, the complete scattering matrix in CP is

easily extracted, and from this relevant scattering quantities can be determined.

The first published measurements of the transmission properties of a CPSS were presented in [32] where the relative power transmitted in right hand circular polarization (RHCP) and left hand circular polarization (LHCP) was determined. The first comprehensive experimental quantification of the transmission, reflection, and AR properties of a CPSS was presented in [9], where a Pierrot element CPSS was characterized in the X-band. However, only the scattering properties of the CPSS with a perfect electric conductor (PEC) backing was investigated in reflection. Over the last ten years, a multitude of CPSS designs have been presented and characterized through measurements in transmission only [15, 19, 20, 30, 31]. A general remark on these measurements is that the insertion loss (IL) is often accurately characterized, but the AR is commonly deviating from expected results.

Complete experimental verifications of a CPSS in transmission and reflection in CP are, to the knowledge of the authors of this work, rarely presented. Moreover, the published experimental verifications of CPSSs are, in general, not very detailed about characterization of measurement errors or the procedures of generating the presented measurement data. In [27], a CPSS was characterized both in reflection and transmission, utilizing a state of the art measurement setup. This characterization achieves low measurement errors both in reflection and transmission, but requires expensive and advanced equipment and still shows significant deviations between measured and simulated AR. To this end, we present a simple procedure for a complete experimental characterization of a CPSS using linearly single- polarized horn antennas. A post processing scheme is introduced to reduce measurement errors due to antenna misalignments, resulting in significant improvements in the accuracy of measured AR in both reflection and transmission. By normalizing the device under test (DUT) reflection and transmission data with reference measurements, the relative transmission and reflection of the structure are determined.

The paper is organized as follows: in Section 2, the theory of characterizing a DUT by synthesizing the CP scattering from LP measurements is described. The measurement setup used in this work is presented in detail in Section 3, where separate arrangements in transmission and reflection are introduced. In Section 4, the post processing scheme used to manage and calibrate the raw measurement data and synthesize the CP scattering of a DUT is presented. A measurement methodology for achieving low reference AR in transmission and reflection is introduced, where a normalization with reference measurements is utilized. Estimates of the errors associated with this type of measurements are presented in Section 5. The lower bound in AR of the measurement setup is established through measurements of a homogeneous test panel, both in reflection and transmission. In Section 6, measurement results of a non-resonant meander line CPSS, described in detail in [6], are presented and the repeatability of the measurements is investigated. Finally, Section 7 consists of concluding remarks on the work presented.

2   Theory - Circular Polarization Measurements using Linearly Polarized Antennas

The scattering parameters of a DUT in CP can be determined experimentally in two different ways; The first is to use CP antennas, and the CP scattering parameters are then directly determined from the co- and cross-polarization transmission and reflection properties of the DUT. This method is straightforward, but to determine the scattering parameters to high accuracy requires CP antennas of high cross polarization discrimination (XPD), which can also be interpreted as low axial ratio (AR). In [27] a CPSS was characterized using CP helix antennas with $18\,\mathrm{dB}$ XPD, corresponding to AR $> 2.2\,\mathrm{dB}$, and it was concluded that the CPSS could not be accurately characterized using antennas with such low XPD. To make a CP antenna achieve levels of XPD comparable to linear single-polarized horn antennas of $40 - 45\,\mathrm{dB}$ requires careful design [10]. A number of CP antennas have been presented throughout the years with high XPD [8,18], but to achieve this over a wide bandwidth is a difficult task.

Another way of characterizing a DUT is to use LP antennas, and acquire all co- and cross polarization scattering parameters in LP. From this data, the CP scattering parameters can be determined by using simple matrix relations for converting between LP and CP bases. The scattering matrix in CP, using the IEEE standard [11, pp.61–77] and defining the z-axis as the input direction at port 1 and the output direction at port 2, can be identified as

$$
S^{\mathrm{CP}} = \begin{pmatrix} S_{11}^{\mathrm{RR}} & S_{11}^{\mathrm{RL}} & S_{12}^{\mathrm{RR}} & S_{12}^{\mathrm{RL}} \\ S_{11}^{\mathrm{LR}} & S_{11}^{\mathrm{LL}} & S_{12}^{\mathrm{LR}} & S_{12}^{\mathrm{LL}} \\ S_{21}^{\mathrm{RR}} & S_{21}^{\mathrm{RL}} & S_{22}^{\mathrm{RR}} & S_{22}^{\mathrm{RL}} \\ S_{21}^{\mathrm{LR}} & S_{21}^{\mathrm{LL}} & S_{22}^{\mathrm{LR}} & S_{22}^{\mathrm{LL}} \end{pmatrix}
$$

$$
= \frac{1}{2} \begin{pmatrix} 1 & -\mathrm{j} & 0 & 0 \\ 1 & \mathrm{j} & 0 & 0 \\ 0 & 0 & 1 & \mathrm{j} \\ 0 & 0 & 1 & -\mathrm{j} \end{pmatrix} \begin{pmatrix} S_{11}^{\mathrm{XX}} & S_{11}^{\mathrm{XY}} & S_{12}^{\mathrm{XX}} & S_{12}^{\mathrm{XY}} \\ S_{11}^{\mathrm{YX}} & S_{11}^{\mathrm{YY}} & S_{12}^{\mathrm{YX}} & S_{12}^{\mathrm{YY}} \\ S_{21}^{\mathrm{XX}} & S_{21}^{\mathrm{XY}} & S_{22}^{\mathrm{XX}} & S_{22}^{\mathrm{XY}} \\ S_{21}^{\mathrm{YX}} & S_{21}^{\mathrm{YY}} & S_{22}^{\mathrm{YX}} & S_{22}^{\mathrm{YY}} \end{pmatrix} \begin{pmatrix} 1 & 1 & 0 & 0 \\ -\mathrm{j} & \mathrm{j} & 0 & 0 \\ 0 & 0 & 1 & 1 \\ 0 & 0 & \mathrm{j} & -\mathrm{j} \end{pmatrix}, \quad (2.1)
$$

where the two ports are located on each side of the DUT. Each entry in the scattering matrix is defined as the ratio between the outgoing electric field, E_m^k at port m with polarization state k, and the incoming electric field, E_{n0}^l at port n with polarization state l, such as $S_{mn}^{kl} = E_m^k/E_{n0}^l$, when all other ports are not excited and terminated with their characteristic impedance. The indices X, Y correspond to horizontal and vertical polarization, defined by the basis vectors $\hat{\boldsymbol{x}}$ and $\hat{\boldsymbol{y}}$ in Figure 1, and R, L correspond to RHCP and LHCP, respectively.

As long as the signal from the transmitting antenna is received in two non-parallel orientations of the receiving antenna, and the relative orientations of the transmitting and receiving antennas are known, the scattering parameters in LP
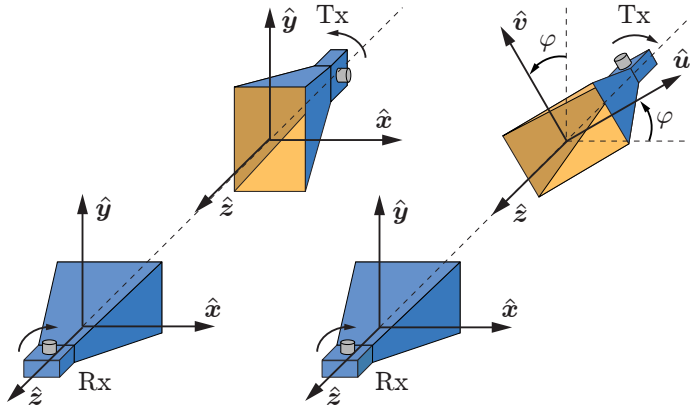
Figure 1: A principal sketch of antenna orientations in measurements of CP transmission. To the left, the main directions of the transmitting and receiving antennas are aligned, and the relative rotation between the antennas is either $0°$ or $90°$. To the right, the main directions of the transmitting and receiving antennas are not aligned, and if the antenna orientation angle $\varphi = 45°$, the relative rotation between the transmitting and receiving antenna is always $45°$.

can be extracted, and subsequently converted to CP using (2.1). If the receiving antenna is rotated around its z-axis an angle φ, as illustrated in the scenario to the right in Figure 1, the LP scattering parameters of an aligned system can be extracted through the relation

$$
S^{\mathrm{LP}} = \begin{pmatrix} S_{11}^{\mathrm{XX}} & S_{11}^{\mathrm{XY}} & S_{12}^{\mathrm{XX}} & S_{12}^{\mathrm{XY}} \\ S_{11}^{\mathrm{YX}} & S_{11}^{\mathrm{YY}} & S_{12}^{\mathrm{YX}} & S_{12}^{\mathrm{YY}} \\ S_{21}^{\mathrm{XX}} & S_{21}^{\mathrm{XY}} & S_{22}^{\mathrm{XX}} & S_{22}^{\mathrm{XY}} \\ S_{21}^{\mathrm{YX}} & S_{21}^{\mathrm{YY}} & S_{22}^{\mathrm{YX}} & S_{22}^{\mathrm{YY}} \end{pmatrix}
$$
$$
= \begin{pmatrix} S_{11}^{\mathrm{XU}} & S_{11}^{\mathrm{XV}} & S_{12}^{\mathrm{XU}} & S_{12}^{\mathrm{XV}} \\ S_{11}^{\mathrm{YU}} & S_{11}^{\mathrm{YV}} & S_{12}^{\mathrm{YU}} & S_{12}^{\mathrm{YV}} \\ S_{21}^{\mathrm{XU}} & S_{21}^{\mathrm{XV}} & S_{22}^{\mathrm{XU}} & S_{22}^{\mathrm{XV}} \\ S_{21}^{\mathrm{YU}} & S_{21}^{\mathrm{YV}} & S_{22}^{\mathrm{YU}} & S_{22}^{\mathrm{YV}} \end{pmatrix} \begin{pmatrix} \cos\varphi & \sin\varphi & 0 & 0 \\ -\sin\varphi & \cos\varphi & 0 & 0 \\ 0 & 0 & \cos\varphi & \sin\varphi \\ 0 & 0 & -\sin\varphi & \cos\varphi \end{pmatrix}, \qquad (2.2)
$$

where the indices U, V correspond to the unit vector directions $\hat{\boldsymbol{u}}, \hat{\boldsymbol{v}}$ in Figure 1. After the rotation operation (2.2), the CP scattering matrix is determined using (2.1). Note that this holds when characterizing a DUT in both reflection and transmission. The advantage of using a relative rotation of $45°$ between the principal directions the transmitting and receiving antennas is described in detail in Section 5.

3   Measurement Setup

All measurements in this work were carried out at the frequencies $9.5 - 20.5$ GHz, using two rectangular standard gain horn antennas, SATIMO SGH 1240, with a XPD in LP better than 40 dB in the full band of interest. The antennas were positioned at a height of 1.4 m using tripod antenna stands. To manually rotate the antennas in a controlled manner, custom made rotation fixtures were manufactured. Relative orientations of $0°$, $45°$ and $90°$ of the horns were achieved using alignment holes in the fixtures and alignment pins. The antennas were connected to an Agilent E8364b PNA Network Analyzer, which in turn was controlled by a laptop through a GPIB connection and a control script written in MATLAB. Further details on how to control Keysight (previously Agilent) instruments with MATLAB can be found in [16]. The DUT was placed on a table and fixated using poly(methyl methacrylate) (PMMA) holders, as can be seen in Figures 2–4. In order to suppress undesirable multipath signals, portable absorbing panels were placed around the setup. The absorbing panels are designed to operate at $20 - 100$ GHz but measurements showed them to provide a 10 dB absorption in reflection for the frequency band of interest.

Due to the fact that a two port network analyzer was used together with two single polarized antennas, the antenna placement had to be modified depending on if the transmission or reflection properties of the DUT were to be characterized. However, if a four port network analyzer had been used, either with four single polarized antennas or with two dual polarized antennas, a complete characterization could have been achieved without having to rearrange the antennas in the measurement setup.

3.1   Transmission Measurements

When characterizing the transmission properties of a DUT, the antennas were separated by distances ranging from 0.7 m to 2.0 m and the DUT was placed on a table at the center of the setup, between the two antennas, as in Figure 2. The antennas were carefully aligned using a laser, spirit-level, tape measure and several strings connecting points of interest. Moreover, by utilizing the fact that the signal strength of the co-polarized transmission of the empty setup, displayed with a few seconds delay on the network analyzer, is increased as the misalignment of the setup is decreased, small fine tuning adjustments and verifications were made to the positioning and alignment of the antennas. All four co- and cross polarization scattering matrix components S_{21}^{kl} were measured in both amplitude and phase, where $k \in (\mathrm{X}, \mathrm{Y})$ and $l \in (\mathrm{U}, \mathrm{V})$ or $l \in (\mathrm{X}, \mathrm{Y})$ depending on if $45°$ or $90°$ relative antenna orientations were used. All measurements of different test objects were accompanied by a reference transmission measurement of the empty setup (with the DUT removed).
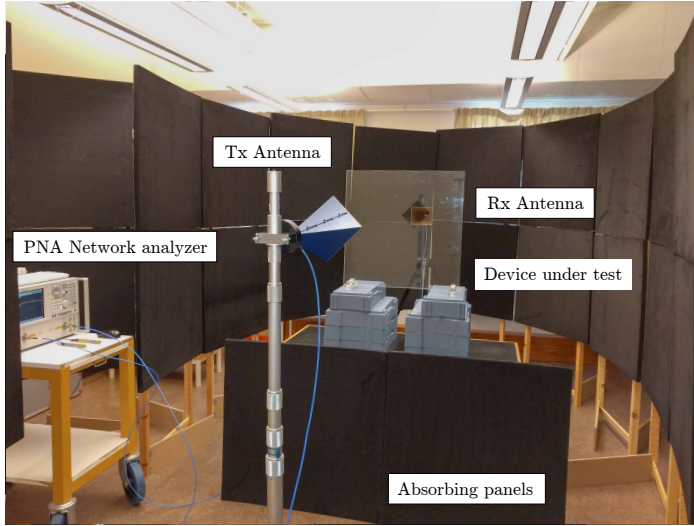
Figure 2: Measurement setup for transmission characterization of a DUT, positioned at a table centered between the transmitting and receiving antennas. The antennas are connected to a vector network analyzer and the whole setup is enclosed by portable absorbing panels.

3.2   Reflection Measurements

When characterizing the reflection properties of a DUT, both antennas were placed at the same side of the DUT at distances ranging from $0.7\,\mathrm{m}$ to $1.8\,\mathrm{m}$, and the apertures separated a distance of about $5\,\mathrm{cm}$, as in Figure 3. Thus the measurement is not of normal incidence but with angles of incidence 3–8°. As in transmission, all four co- and cross polarization scattering matrix components S_{11}^{kl} were measured in both amplitude and phase, where $k \in (\mathrm{X},\mathrm{Y})$ and $l \in (\mathrm{U},\mathrm{V})$ or $l \in (\mathrm{X},\mathrm{Y})$ depending on if 45° or 90° relative antenna orientations were used. All measurements of different test objects were accompanied by a reference measurement of a highly conducting panel of the same size as the DUT. In order to eliminate effects due to misalignment and different curvature of a separate highly conducting reference panel, the DUT was coated with a thin aluminum foil which was temporarily attached to the test object. A very thin layer of water was applied between the foil and the test panel, which for the panels used in this study exherted a strong adhesive bonding due to the surface tension of the water molecules [17] and the low weight of the aluminum foil. The small amount of water was applied evenly to the test panel using a water spray bottle, after that the aluminum foil was folded onto the test panel from one end to the other, and finally the structure was worked over with a plastic wallpaper scraper to remove any air bubbles or local collections of water. In Figure 4, a PMMA test panel used to characterize the measurement setup is presented with and without an aluminum foil attached.
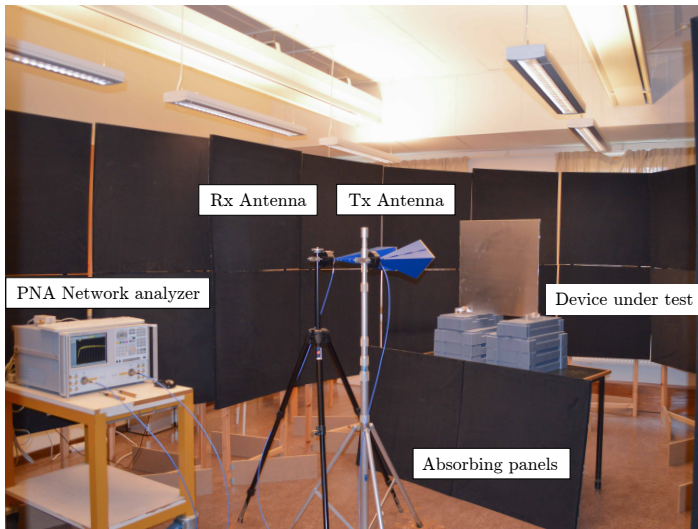
Figure 3: Measurement setup for characterization of the reflection properties of a DUT, which is positioned at a table a distance from the transmitting and receiving antennas. In order to achieve normalized reflection data of the scatterer, the test panel is coated by a conducting foil. The antennas are connected to a vector network analyzer and the whole setup is enclosed by portable absorbing panels.

4   Data Post Processing

All measurement data generated in this work were run through the post processing scheme defined in Figure 5, consisting of six steps of data processing. First, the four LP scattering parameters S_{ij}^{kl} were measured both for the DUT and for the reference scenario (empty setup measurement in transmission and conducting panel measurement in reflection), resulting in eight measurements in total for transmission characterization and another eight measurements for reflection characterization.

Next, if necessary, the data was zero padded symmetrically in the frequency domain in order to achieve an interpolation between the data points in time domain and thus improve the resolution of the time domain data [24]. After that, a tapered cosine window function (Tukey window) was applied to the data in the time domain to remove any unwanted multipath signals, such as reflections of the surroundings of the setup. In this step, the previously implemented interpolation is of significant use to make sure no crucial information is lost when applying the time domain window function.

When the scattering data of a test panel have been interpolated and gated in the time domain, they are transformed back to the frequency domain and normalized with the scattering data of the reference measurement, which have

(a)   (b)
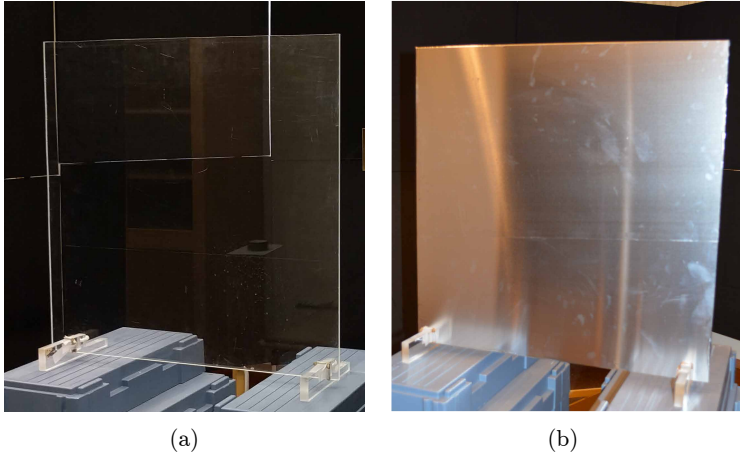
Figure 4: PMMA test panel with the measures $58\,\text{cm} \times 58\,\text{cm}$ used as a reference object to characterize the measurement setup. In (a) the PMMA panel is presented and in (b) the panel has been coated with a highly conductive aluminum foil, using a thin adhesive bonding layer of water, for reference measurements in reflection.

been processed similarly. Note that the normalization is performed before the scattering data is transformed to CP. The impact of normalizing the scattering data of a DUT with reference measurements is described in detail in Section 5. After the normalization, a previously computed rotation correction, based on the reference measurements, is applied to the data to reduce the impact of antenna misalignments in the parallel transmitting/receiving planes with respect to the propagating waves. This correction is described further in Section 5. The only remaining data processing is to convert the LP measurement data to CP. If $\varphi = 45°$ both expressions (2.1)–(2.2) are applied, and if $\varphi = 0°$ the rotation matrix in (2.2) reduce to the identity matrix and only (2.1) is applied.

After the CP scattering matrix components have been determined the main parameters of interest can be extracted. If for example a left hand circular polarization selective structure (LHCPSS) as in Figure 6 is studied, ideal CP filtering properties are achieved if the structure reflects LHCP signals and transmits RHCP signals, while maintaining the polarization state of the signals. The parameters of interest of an LHCPSS are defined in [3] as: the IL of transmitted RHCP, the return loss (RL) of reflected LHCP, and the corresponding AR in transmission and reflection, in this work denoted AR_t and AR_r. These four
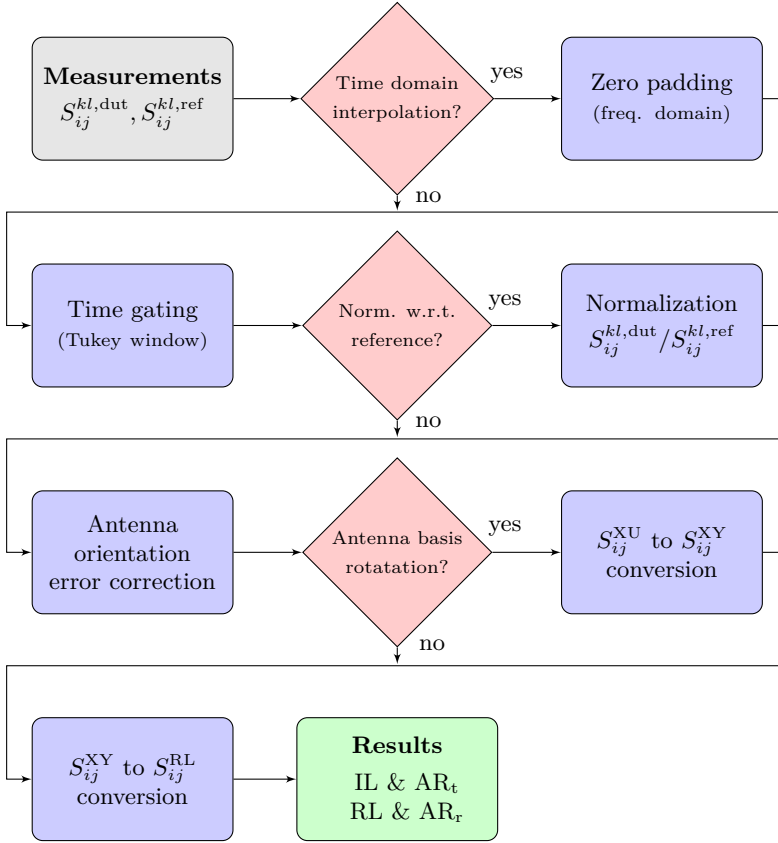
Figure 5: Post processing scheme for CP scattering measurements using LP antennas. To completely characterize the transmission and reflection of a DUT 16 measurements are required in total as input.

parameters are defined in decibels as

$$\text{IL} = -20 \log_{10}(|S_{21}^{\text{RR}}|), \tag{4.1}$$

$$\text{RL} = -20 \log_{10}(|S_{11}^{\text{LL}}|), \tag{4.2}$$

$$\text{AR}_{\text{t}} = 20 \log_{10}\left(\left|\frac{|S_{21}^{\text{LR}}| + |S_{21}^{\text{RR}}|}{|S_{21}^{\text{LR}}| - |S_{21}^{\text{RR}}|}\right|\right), \tag{4.3}$$

$$\text{AR}_{\text{r}} = 20 \log_{10}\left(\left|\frac{|S_{11}^{\text{RL}}| + |S_{11}^{\text{LL}}|}{|S_{11}^{\text{RL}}| - |S_{11}^{\text{LL}}|}\right|\right), \tag{4.4}$$

where it can be seen that IL is given by the ratio of the incident power and the transmitted power in co-polarization (RHCP), RL is defined as the ratio of the
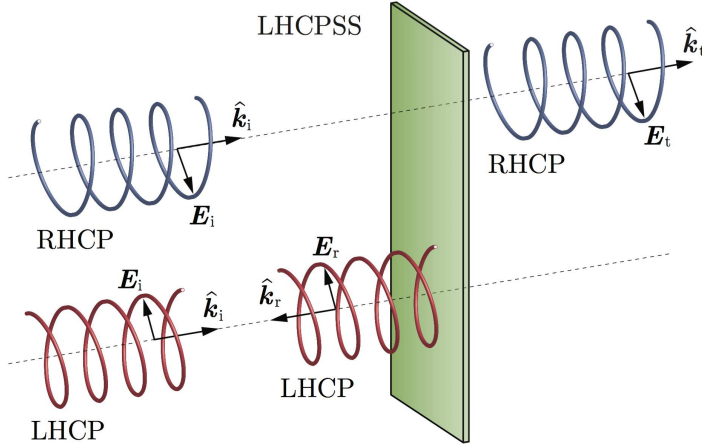
Figure 6: Operational sketch of an LHCPSS, reflecting LHCP signals in co-polarization and transmitting RHCP signals in co-polarization.

incident power and the reflected power in co-polarization (LHCP), and AR_t, AR_r are given by the quotients in (4.3)-(4.4), representing the polarization purity of the transmitted and reflected signals.

Another relevant parameter is the isolation, which is defined in decibels in [23, Ch.7]. For an LHCPSS this corresponds, in transmission and reflection, to

$$\text{Isolation}_t = -20 \log_{10}\left(|S_{21}^{\text{LL}}|\right), \tag{4.5}$$

$$\text{Isolation}_r = -20 \log_{10}\left(|S_{11}^{\text{RR}}|\right), \tag{4.6}$$

where again the subscripts t, r indicate transmission and reflection, respectively. Having defined the parameters of interest to characterize a CPSS, we now turn to the accuracy of the measurements.

5 Measurement Error Estimates and Calibration

In order to determine what accuracy that can be expected of the measurement setup, described in detail in Section 3, we describe the effects of finite XPD of the antennas, the orientation of the antennas, and antenna misalignments. The procedures are illustrated with measurements on a homogeneous and isotropic PMMA panel.

5.1   Measurement System XPD

One fundamental limiting factor of a measurement system for CP characterization is the XPD of the antennas. With perfectly aligned antennas and no cross-polarized scattering in the setup, the XPD of the synthesized CP for an empty setup is given by the individual antenna XPD in LP reduced by a factor of two (or $6\,\mathrm{dB}$), due to the presence of two antennas in the system. Given the system XPD, the AR is given by

$$\mathrm{AR} = 20\log_{10}\left(\left|\frac{10^{\mathrm{XPD}/20}+1}{10^{\mathrm{XPD}/20}-1}\right|\right). \tag{5.1}$$

The relation (5.1) is plotted in the left graph in Figure 7, where it can be noted that to determine the AR of a DUT down to levels on the order of $0.5\,\mathrm{dB}$ requires a measurement system with XPD $> 30\,\mathrm{dB}$. A measurement system with XPD $= 20\,\mathrm{dB}$ is limited to characterizing AR down to $1.8\,\mathrm{dB}$ at best, which is not accurate enough according to the requirements of a CPSS for space applications defined in [3] as

- IL and RL better than $0.5\,\mathrm{dB}$,

- AR better than $0.78\,\mathrm{dB}$ (corresponding to XPD $> 27\,\mathrm{dB}$).

The simple relation (5.1) clearly identifies the need to utilize antennas with high XPD in order to determine the AR of a test panel as accurately as possible. In this work, LP antennas with boresight XPD of 40–45 dB are used (a system XPD of 34–39 dB), which implies that the lower limit of the presented measurement system is at about AR $0.2\,\mathrm{dB}$.

5.2   Antenna Orientations and Normalization

In an ideal measurement scenario, the noise level of the setup is zero which results in an infinite signal to noise ratio (SNR). However, in a realistic measurement situation the noise level of the measurement setup is non-zero and a finite SNR of the setup can be identified. Since we make relative measurements, we need high SNR in both DUT data and data for the reference structure. If the principal directions of the transmitting and receiving antennas are aligned, as in the left part of Figure 1, the SNR:s of the reference measurements are much lower in the cross-polarized components, S_{ij}^{XY} and S_{ij}^{YX}, than in the co-polarized components, S_{ij}^{XX} and S_{ij}^{YY}, for fixed ij. But, if the principal directions of the transmitting and receiving antennas are offset by $\varphi = 45°$ as in the right part of Figure 1, the SNR:s of the reference measurements are high and equal in all four components S_{ij}^{XU}, S_{ij}^{YU}, S_{ij}^{XV}, and S_{ij}^{YV}, for fixed ij. To that end, all following measurement results in this work have been acquired using the 45° offset.

The S-parameters used when evaluating the DUT are relative to the reference measurement and ideal S-parameters, *i.e.*,

$$S_{ij}^{kl,\text{rel}} = \frac{S_{ij}^{kl,\text{dut}}}{S_{ij}^{kl,\text{ref}}/S_{ij}^{kl,\text{ideal}}}, \tag{5.2}$$

where the reference ideal LP S-parameters for 45° offset are

$$S_{21}^{\text{ideal}} = -S_{11}^{\text{ideal}} = \frac{1}{\sqrt{2}} \begin{pmatrix} 1 & -1 \\ 1 & 1 \end{pmatrix}. \tag{5.3}$$

Note that the normalization is made before the conversion from LP to CP. This guarantees that each component of $S^{\text{dut},\text{LP}}$ is divided with a component of $S^{\text{ref},\text{LP}}$ measured with a corresponding setup. If the normalization had been made after the conversion to CP, then the measurement errors of several different setups would be mixed together, reducing the accuracy further.

An alternative normalization could be proposed for the case of aligned principal directions of the antennas. We limit the discussion to the transmission case. All components $S_{21}^{kl,\text{dut}}$ could be divided by the co-polarized reference transmission, $S_{21}^{\text{XX},\text{ref}}$ or $S_{21}^{\text{YY},\text{ref}}$, which both have a high SNR. However, this would mean the cross polarized components, $S_{21}^{\text{XY},\text{dut}}$ and $S_{21}^{\text{YX},\text{dut}}$, would have to be normalized with a factor obtained in a slightly different setup, reducing the accuracy. The reflection case follows in the same way.

5.3   Antenna Misalignment Errors

One source of error associated with using LP antennas for CP measurements is antenna misalignments. In the right graph in Figure 7 the simulated AR of a system, using ideal antennas, is plotted as a function of antenna misalignments, where the solid curve corresponds to a systematic misalignment in one of the components U, V, X or Y, defined in Figure 1. In order to characterize the impact of non-systematic errors associated with antenna misalignments (*i.e.* alignment errors that vary from one measurement to another) a statistical analysis was simulated. In this case, the antennas were misaligned through a rotation with respect to the axis normal to the aperture, and the angle given on the horizontal axis in the right graph in Figure 7 represents the absolute sum of all errors of the four measured components required to extract the CP scattering of a DUT. The dashed curve in the right graph in Figure 7 corresponds to the worst case scenario of this study. As can be seen, a total misalignment of 3° has a significant impact on the accuracy of the setup. This implies that to align the antennas carefully is of high importance when characterizing a DUT in CP using LP antennas.

The errors of a measurement setup due to antenna misalignments can be quantified and to some extent corrected for in post processing. For example, if the antenna orientations corresponding to $\varphi = 45°$ in Figure 1 are utilized in a transmission scenario, the ratios $S_{21}^{\text{XU}}/S_{21}^{\text{YU}}$, $-S_{21}^{\text{XU}}/S_{21}^{\text{XV}}$, $-S_{21}^{\text{YV}}/S_{21}^{\text{XV}}$ and
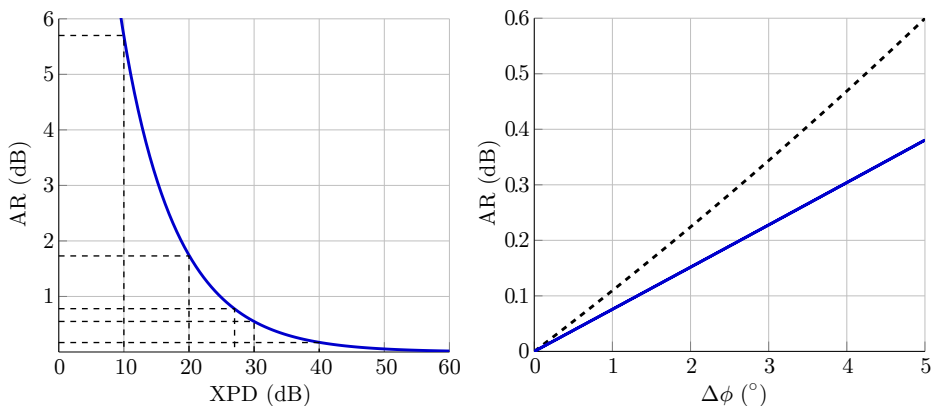
Figure 7: Simulation results of the relation between XPD and AR in a measurement system are presented to the left. The dashed lines indicate the relation at specific XPD values of interest. To the right, simulated measurement error in AR due to antenna misalignments in the plane parallel to the antenna apertures are presented. The solid curve represents a systematic error in one of the antenna orientations, and the dashed curve correspond to the worst case scenario of non-systematic errors distributed over all antenna orientations, where the angle on the horizontal axis $\Delta\phi$ here represents the absolute sum of all errors.

$S_{21}^{\mathrm{YV}}/S_{21}^{\mathrm{YU}}$ are of great interest. The same type of ratios can be evaluated in a reflection scenario. In an ideal setup, the amplitude and phase of these relations should be zero dB and $0°$ for the reference data, but in a realistic case errors due to antenna misalignment (and effects like phase changes due to cable bending in different setups) will result in non-zero values. In this work, the amplitude errors of the mentioned ratios, for time gated data, are on the order of $\pm 0.3\,\mathrm{dB}$ and the phase errors are about $\pm 3°$.

The amplitude errors can be reduced by utilizing rotation correction, mentioned in Section 4. Consider the following case depicted in Figure 8 with the measurements visualized as vectors. The ideal alignment corresponds to $45°$ angle between the basis of the receiving and transmitting antenna, indicated by the full drawn vectors and the actual alignment is shown with the dashed vectors. First the S^{YU} component is to be measured and thus the antennas are rotated for this configuration. However due to errors in alignment the assumed orientation of the vectors $\hat{\boldsymbol{y}}$ and $\hat{\boldsymbol{u}}$ does not hold, as indicated by θ_1 and θ_2 in Figure 8. The amplitude error is then given by the projection of $\hat{\boldsymbol{y}}' = R(\theta_1)\hat{\boldsymbol{y}}$ on $\hat{\boldsymbol{u}}' = R(\theta_2)\hat{\boldsymbol{u}}$, where $R(\theta_1)$ is a rotation matrix. After this measurement is completed, the antenna in the $\hat{\boldsymbol{u}}$ direction is rotated to $\hat{\boldsymbol{v}}$ in order to be able to measure S^{YV}, introducing yet another misalignment angle θ_3. For one complete
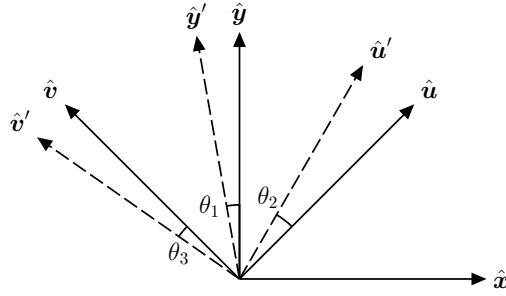
Figure 8: Error in alignment, θ introduced through the physical rotations of the antennas in the setup. The vectors $\hat{\boldsymbol{x}}$ and $\hat{\boldsymbol{y}}$ form a basis for the receiving antenna and similarly $\hat{\boldsymbol{u}}$ and $\hat{\boldsymbol{v}}$ form a basis for the transmitting antenna.

set of measurements this can be stated as,

$$S^{\mathrm{YU}} = a_1(R(\theta_1)\hat{\boldsymbol{y}})^{\mathrm{T}} R(\theta_2)\hat{\boldsymbol{u}} = a_1 \cos(\pi/4 + \phi_{12}), \tag{5.4}$$

$$S^{\mathrm{YV}} = a_2(R(\theta_1)\hat{\boldsymbol{y}})^{\mathrm{T}} R(\theta_3)\hat{\boldsymbol{v}} = a_2 \cos(\pi/4 - \phi_{13}), \tag{5.5}$$

$$S^{\mathrm{XV}} = a_3(R(\theta_4)\hat{\boldsymbol{x}})^{\mathrm{T}} R(\theta_3)\hat{\boldsymbol{v}} = a_3 \cos(3\pi/4 - \phi_{43}), \tag{5.6}$$

$$S^{\mathrm{XU}} = a_4(R(\theta_4)\hat{\boldsymbol{x}})^{\mathrm{T}} R(\theta_5)\hat{\boldsymbol{u}} = a_4 \cos(\pi/4 - \phi_{45}), \tag{5.7}$$

where R is a rotation matrix, a_i some constant and $\phi_{ij} = \theta_i - \theta_j$. In the case of the reference measurement the amplitudes should be equal, $a_i = a$, and since only differences between the angles appear in the final equations, we can set one of them to zero, for instance $\theta_1 = 0$. Since the rotations are the same for all frequencies, we find the most likely ones by minimizing the amplitude error across all frequency points. To determine these rotation errors of a measurement setup, reference measurements of the empty setup in transmission, and the reflection of a conducting plate in reflection, are utilized. This correction is then applied to the normalized scattering data of a DUT in LP. Some error due to misalignment is still expected after the correction, albeit less significant. In this work, the uncorrected data commonly resulted in θ_i on the order of $0.4°$ corresponding to an amplitude error of about $0.3\,\mathrm{dB}$. A typical correction resulted in an absolute amplitude error of $< 0.1\,\mathrm{dB}$ which is a significant improvement over the uncorrected data.

5.4 Verification Measurements

In Figure 9, the AR in transmission and reflection of a homogeneous and isotropic PMMA test panel with the measures $58\,\mathrm{cm} \times 58\,\mathrm{cm} \times 2.0\,\mathrm{cm}$ is presented. Zero padding and time gating have been applied to the data referred to as processed, and additional rotation correction and normalization with respect to a reference measurement have been applied to the data referred to as calibrated. As was stated in Section 3, the reference scenario in transmission consists of the empty
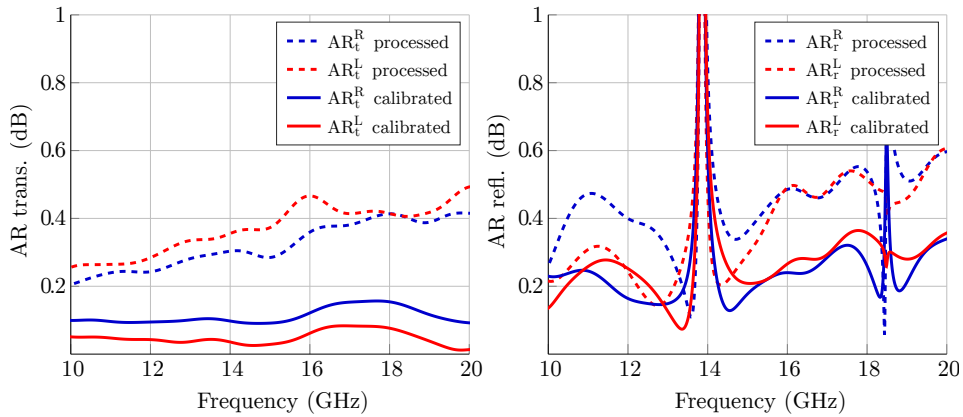
Figure 9: Measured AR of isotropic PMMA test panels, with and without calibration using $\varphi = 45°$ antenna orientations. In the left graph the transmission AR of a $58\,\text{cm} \times 58\,\text{cm} \times 2.0\,\text{cm}$ panel is presented, and in the right graph the reflection AR of the same panel is presented.

setup, and the reference in reflection corresponds to a measurement of the PMMA panel coated with an aluminum foil, as in Figure 4 (b).

A significant improvement in the AR can be noticed both in the transmission and reflection results in Figure 9 when the rotation correction and normalization are applied to the DUT data, and an AR reference level better than $0.2\,\text{dB}$ is achieved in transmission and $0.4\,\text{dB}$ in reflection. When comparing these results to the measurement error level of 0.2–$0.3\,\text{dB}$ caused by using antennas with XPD $\approx 40\,\text{dB}$, it can be seen that in transmission the curves are below this limit and the AR curves for RHCP and LHCP diverge slightly after the normalization and rotation correction. At the same time, in reflection the curves are still above this lower limit after the normalization and error correction and the RHCP and LHCP AR curves are closer to each other after the normalization. The two spikes in the AR curve in the reflection data of Figure 9 correspond to the frequencies where the electrical thickness of the DUT is equal to $n\lambda/2$, $n = 1, 2, ..$, resulting in almost perfect transmission and thus significantly reducing the SNR of the received reflected signal. This effect clearly indicates the importance of having a high SNR for accurate AR characterization of a DUT.
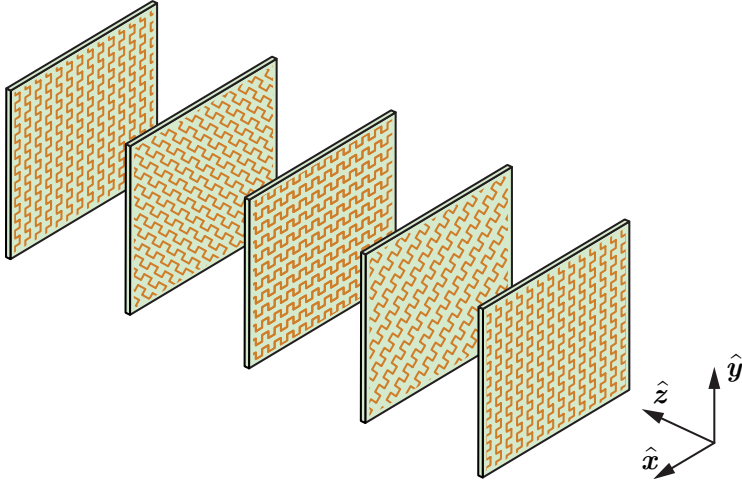
Figure 10: Concept design of the CPSS under study, consisting of meander line substrates with the pattern rotated 45 degrees with respect to the previous layer.

6   Circular Polarization Selective Structure Measurement Results

The measurement scheme described in Sections 3–4, and the calibration methods and rotation error correction described in Section 5 were utilized to characterize the transmission and reflection properties of a wideband CPSS described in detail in [6]. The CPSS is based on cascaded anisotropic layers of conducting meander line patterns, as in Figure 10, where each consecutive layer is rotated 45°. A manufactured prototype of the CPSS is presented in Figure 11. The structure consists of thin Arlon DiClad 880 substrates separated by sheets of Rohacell 31 HF low permittivity foam. The total thickness of the prototype is 13.7 mm, which corresponds to 0.69 wavelengths at the center frequency 15 GHz. Specific material properties and design parameters of the CPSS are presented in [6]. Simulated and experimental results are presented in Figures 12–14, where the transparent dotted curves correspond to raw measurement data, the dashed curves referred to as processed are measurement data after time gating and zero padding, and the dash-dotted curves referred to as calibrated are the final state of the measurement results after the rotation error correction and the normalization have been applied. The solid lines correspond to simulation data from Computer Simulation Technology Microwave Studio (CST MWS), utilizing the frequency domain solver, with 16 steps per wavelength mesh setting and local mesh refinement at specific regions of the structure.

    The transmission results in Figure 12 were acquired with a separation of 0.9 m between the antennas and the CPSS. All measured scattering data from the DUT
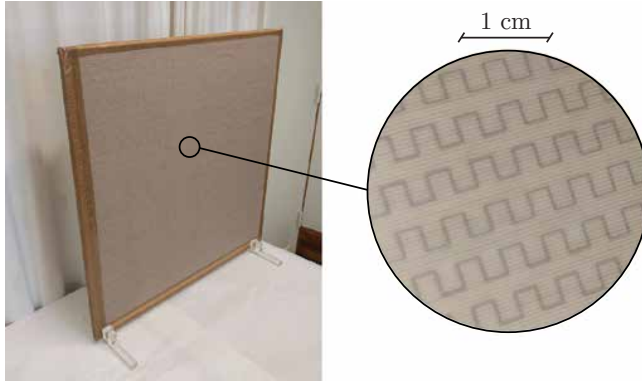
Figure 11: Manufactured CPSS prototype originally presented in [6]. To the left the $58\,\text{cm} \times 58\,\text{cm}$ panel is presented and to the right a zoomed in picture of the meander line pattern on the fist substrate is shown.
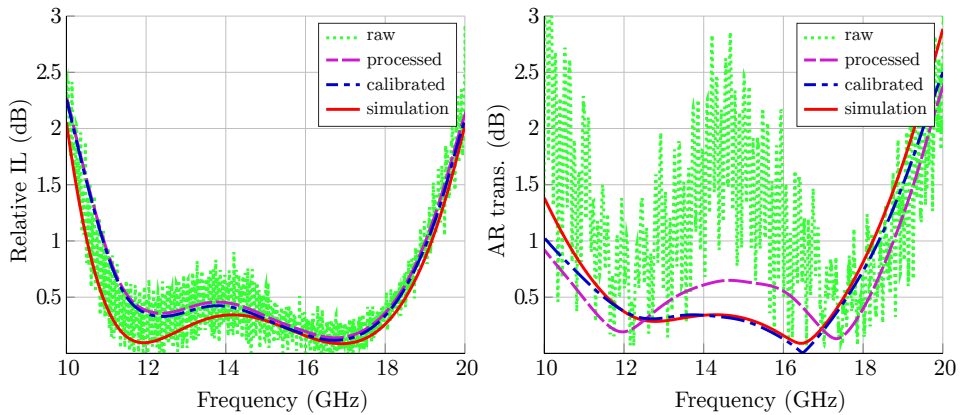
Figure 12: Transmission properties of a wideband CPSS, where the solid lines are simulation results, the dotted curves are raw measurement data, the dashed curves are processed data (after time gating and zero padding), and the dash-dotted lines correspond to data that have been calibrated and corrected for rotation errors using the scheme described in detail in Section 5. The left graph shows the relative IL for RHCP of the CPSS and the right graph shows the corresponding AR of the CPSS.
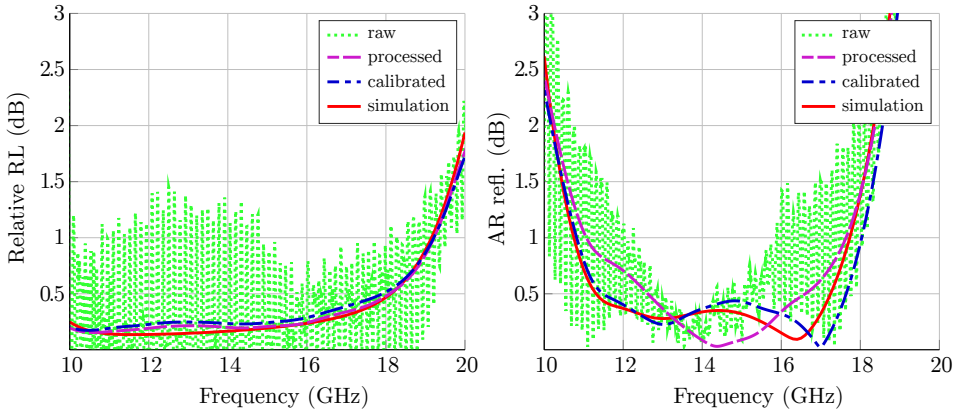
Figure 13: Reflection properties of a wideband CPSS, where the solid lines correspond to simulation results, the dotted curves to raw measurement data, the dashed curves to processed data (after time gating and zero padding), and the dash-dotted lines correspond to data that have been calibrated and corrected for rotation errors. The left graph shows the relative RL for LHCP of the CPSS and the right graph shows the corresponding AR of the CPSS.
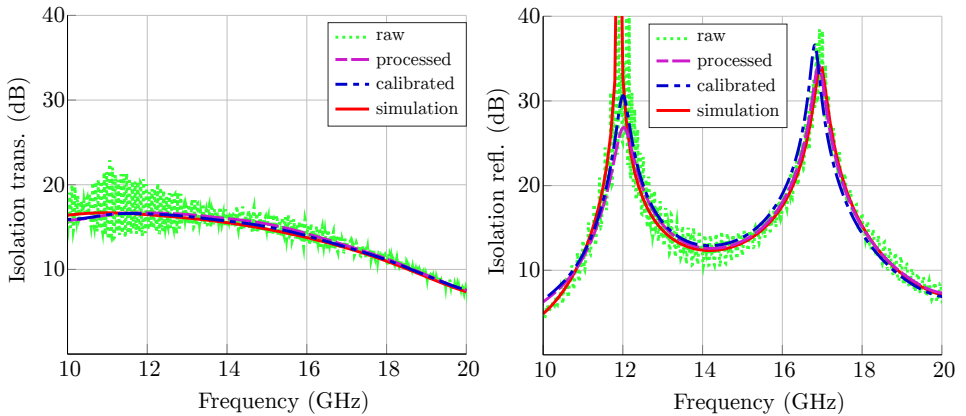
Figure 14: Isolation of the wideband CPSS, where the solid lines correspond to simulation results, the dotted curves to raw measurement data, the dashed curves to processed data (after time gating and zero padding), and the dash-dotted lines correspond to data that have been calibrated and corrected for rotation errors. The left graph shows the isolation in transmission for LHCP and the right graph shows the isolation in reflection for RHCP.

were normalized with a corresponding empty setup transmission measurement. The results in Figure 13 were achieved using a distance of 1.2 m between the antennas and the CPSS. All measured scattering data from the DUT were normalized with a corresponding reference reflection measurement, as described in Section 3. In Figure 14, the isolation of the CPSS, both in reflection and in transmission are presented.

In all graphs in Figures 12–14 a significant improvement can be noticed between the raw measurement data and the processed data. The reason for this improvement is the fact that the raw data are composed of signals from *all* possible paths from the transmitting antenna to the receiving antenna. Since the main signals of interest have a clearly defined trajectory (along the shortest path from the transmitting antenna, interacting with the DUT, to the receiving antenna) these signals can be separated from all undesired multipath signals.

The CPSS AR curves in Figures 12–13 indicate that, in the same manner as the results of the PMMA test panels in Figure 9, by applying the rotation error correction and the calibration scheme in Section 5 the accuracy of the measured AR is significantly improved. After calibration, the agreement between the measured and simulated AR is excellent both in transmission and reflection. At the same time, the calibration is not significantly affecting the IL, RL or isolation of the DUT, as can be seen in Figures 12–14. The agreement between simulated and measured IL, RL and isolation is also good.

In order to verify the repeatability of the measurement results of the wideband CPSS DUT, the complete setup was disassembled and reassembled five times in transmission and reflection respectively, using different distances between the antennas. In transmission, the distance from the DUT to the antennas was varied between 0.35–1.00 m, and in reflection the distance from the DUT to the antennas was varied between 0.7–1.8 m with angles of incidence 3–8° as a consequence of varying the distance from the antennas to the DUT.

When comparing the measured and simulated IL and AR in transmission in Figures 15–17, it can be seen that the agreement is very good and the repeatability from subsequent measurements is verified. A small deviation can be noted for lower frequencies, possibly caused by losses in the DUT unaccounted for in the simulations. The measured and simulated RL and AR in reflection also agree very well, but the spread between subsequent measurements is slightly larger than in the transmission parameters. This is mainly due to alignment issues associated with performing reflection measurements in general. Also, it should be noted that when varying the distance from the DUT to the antennas in reflection, the illumination angle is varied. In simulations of the CPSS, the mentioned angle variation implies a deviation smaller than 0.2 dB from the normal incidence results. The measured isolation between RHCP and LHCP is in good agreement with simulations both in transmission and reflection. Overall, the measurement results are in excellent agreement with the simulation data, and the spread between repeated measurements is in line with expectations.
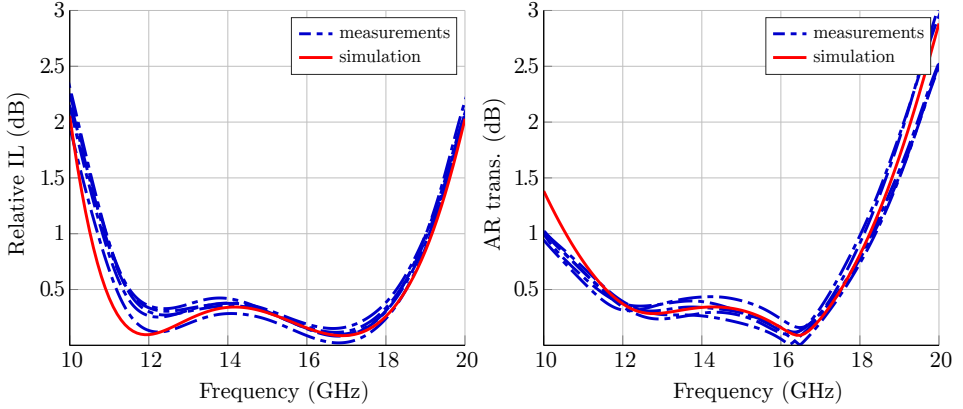
Figure 15: Multiple transmission measurements of a wideband CPSS, displaying the repeatability of the results acquired with the portable setup used in this work. The solid curves correspond to simulation data, and the dash-dotted lines correspond to measurement results acquired from five separate measurements. The left graph shows the RHCP IL and the right graph shows the corresponding AR.
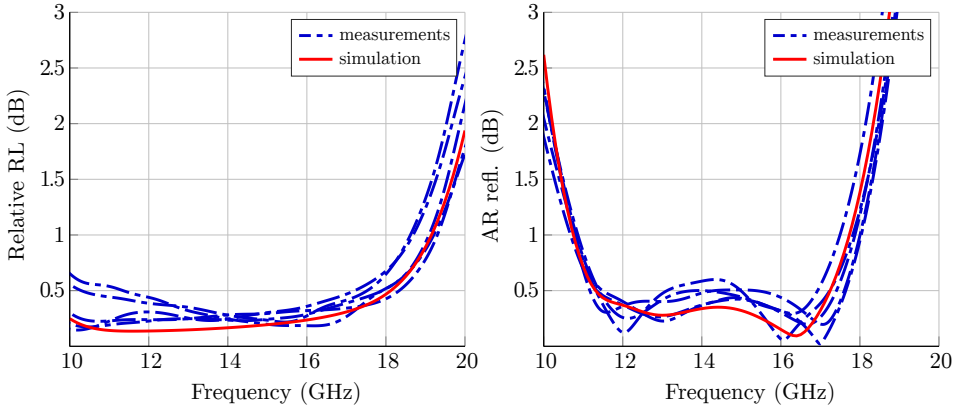
Figure 16: Multiple reflection measurements of a wideband CPSS, displaying the repeatability of the results acquired with the portable setup used in this work. The solid curves correspond to simulation data, and the dash-dotted lines correspond to measurement results acquired from five separate measurements. The left graph shows the LHCP RL and the right graph shows the corresponding AR.
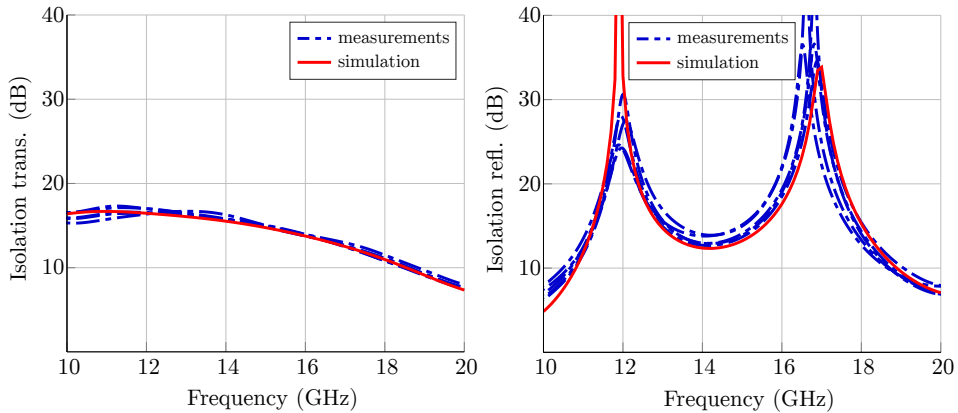
Figure 17: The isolation of a wideband CPSS from multiple transmission and reflection measurements, displaying the repeatability of the results acquired with the portable setup used in this work. The solid curves correspond to simulation data, and the dash-dotted lines correspond to measurement results acquired from five separate measurements. The left graph shows the isolation in transmission for LHCP and the right graph shows the isolation in reflection for RHCP.

7   Conclusions

A technique for measuring the CP transmission and reflection properties of a test panel has been presented. By utilizing LP antennas with a high XPD, the CP scattering of a test panel can be synthesized with high accuracy from LP measurements. A relative rotation of the transmitting and receiving antennas of 45° was introduced in order to achieve a high signal to noise ratio in all reference scattering matrix components. This arrangement introduces the possibility of calibrating the DUT data in an efficient manner, resulting in improved agreement in AR between measurements and simulated data. A post processing procedure was presented and utilized for characterizing a wideband CPSS. The agreement between measured and simulated data is excellent and the repeatability of the measurements was verified for the specific setup.

Acknowledgments

References

[1] S. M. A. M. H. Abadi and N. Behdad. A broadband, circular-polarization selective surface. *Journal of Applied Physics*, **119**(24), pp. 244901, 2016.

[2] S. M. A. M. H. Abadi and N. Behdad. Wideband linear-to-circular polarization converters based on miniaturized-element frequency selective surfaces. *IEEE Trans. Antennas Propag.*, **64**(2), pp. 525–534, 2016.

[3] M. Albani, P. Balling, L. Datashvili, G. Gerini, P. Ingvarson, K. Pontoppidan, M. Sabbadini, D. Sjöberg, S. Skokic, and G. Vecchi. Concepts for polarising sheets & "dual-gridded" reflectors for circular polarisation. In *ICECom Proceedings*, pp. 1–4, 2010.

[4] M. Baunge, H. Ekström, P. Ingvarson, and M. Petersson. A new concept for dual gridded reflectors. In *Proceedings of the fourth European Conference on Antennas and Propagation (EuCAP)*, pp. 1–5. IEEE, 2010.

[5] A. Ericsson and D. Sjöberg. A performance study of circular polarization selective structures. In *Proceedings of the 9th European Conference on Antennas and Propagation (EuCAP)*. IEEE, 2015.

[6] A. Ericsson and D. Sjöberg. Design and analysis of a multilayer meander line circular polarization selective structure. *IEEE Trans. Antennas Propag.*, **65**(8), pp. 4089–4101, 2017.

[7] A. Ericsson and D. Sjöberg. A resonant circular polarization selective structure of closely spaced wire helices. *Radio Science*, **50**(8), pp. 804–812, 2015. 2014RS005641.

[8] M. J. Franco. A high-performance dual-mode feed horn for parabolic reflectors with a stepped-septum polarizer in a circular waveguide [antenna designer's notebook]. *IEEE Antennas and Propagation Magazine*, **53**(3), pp. 142–146, 2011.

[9] V. Fusco and B. Nair. Circular polarisation selective surface characterisation and advanced applications. *IEE Proceedings Microwaves Antennas and Propagation*, **153**(3), pp. 247–252, 2006.

[10] S. S. Gao, Q. Luo, and F. Zhu. *Circularly Polarized Antennas*. John Wiley & Sons, 2013.

[11] IEEE standard test procedures for antennas, 2008. IEEE Std 149-1979 (R2008).

[12] W. A. Imbriale, S. S. Gao, and L. Boccia, editors. *Space Antenna Handbook*. Wiley, 2012.

[13] M. Joyal and J. Laurin. A cascaded circular-polarization-selective surface at K band. In *Antennas and Propagation (APSURSI), 2011 IEEE International Symposium on*, pp. 2657–2660. IEEE, 2011.

[14] M. Joyal and J. Laurin. Analysis and design of thin circular polarizers based on meander lines. *IEEE Trans. Antennas Propag.*, **60**(6), pp. 3007–3011, 2012.

[15] M. Joyal and J. Laurin. Design and analysis of a cascade circular-polarization-selective surface at K band. *IEEE Trans. Antennas Propag.*, **62**(6), pp. 3043–3052, 2014.

[16] Keysight Instruments and MATLAB, 2017. Available at: https://se.mathworks.com/products/instrument/supported/keysight.html, accessed 2017-09-22.

[17] A. Kinloch. *Adhesion and Adhesives: Science and Technology.* Springer Science & Business Media, 2012.

[18] C. A. Leal-Sevillano, J. A. Ruiz-Cruz, J. R. Montejo-Garai, and J. M. Rebollar. Wide-band compact antenna feed for multi-beam satellite communications. In *Antennas and Propagation (EuCAP), 2015 9th European Conference on*, pp. 1–4. IEEE, 2015.

[19] I. Lopez and J. Laurin. A circular polarization selective surface implemented on a flexible substrate. *IEEE Trans. Antennas Propag.*, **62**(7), pp. 3847–3852, 2014.

[20] I. Lopez and J.-J. Laurin. Alternative topologies of circular polarization selective surfaces based on modifications of the Pierrot cell. *IEEE Trans. Antennas Propag.*, **63**(4), pp. 1465–1472, 2015.

[21] G. A. Morin. A simple circular polarization selective surface (CPSS). In *Antennas and Propagation Society International Symposium, 1990. AP-S. Merging Technologies for the 90's. Digest.*, pp. 100–103. IEEE, 1990.

[22] R. Pierrot. Reflector for circularly polarized waves, 1970. US Patent 3,500,420.

[23] D. M. Pozar. *Microwave Engineering.* John Wiley & Sons, New York, NY, third edition, 2005.

[24] K. R. Rao, D. N. Kim, and J. J. Hwang. *Fast Fourier Transform-Algorithms and Applications.* Springer Science & Business Media, 2011.

[25] S. Rao, L. Shafai, and S. K. Sharma. *Handbook of Reflector Antennas and Feed Systems Volume III: Applications of Reflectors.* Artech house, 2013.

[26] J. E. Roy and L. Shafai. Reciprocal circular-polarization-selective surface. *Antennas and Propagation Magazine, IEEE*, **38**(6), pp. 18–33, 1996.

[27] J. Sanz-Fernandez, E. Saenz, and P. de Maagt. A circular polarization selective surface for space applications. *IEEE Trans. Antennas Propag.*, **63**(6), pp. 2460–2470, 2015.

[28] J. Sanz-Fernandez, E. Saenz, P. de Maagt, and C. Mangenot. Circular polarization selective surface for dual-optics CP offset reflector antennas in Ku-band. In *Proceedings of the 6th European Conference on Antennas and Propagation (EuCAP)*, pp. 2683–2687. IEEE, 2012.

[29] D. Sjöberg and A. Ericsson. A multi layer meander line circular polarization selective structure (MLML-CPSS). In *Proceedings of the 8th European Conference on Antennas and Propagation (EuCAP)*, pp. 464–468. IEEE, 2014.

[30] W. Tang, G. Goussetis, N. J. Fonseca, H. Legay, E. Saenz, and P. de Maagt. Study of coupled split-ring resonator arrays for circular polarization selective surface. In *Antennas and Propagation & USNC/URSI National Radio Science Meeting, 2015 IEEE International Symposium on*, pp. 362–363. IEEE, 2015.

[31] I.-Y. Tarn and S.-J. Chung. A new advance in circular polarization selective surface – A three layer CPSS without vertical conductive segments. *IEEE Trans. Antennas Propag.*, **55**(2), pp. 460–467, 2007.

[32] W. V. Tilston, T. Tralman, and S. M. Khanna. A polarization selective surface for circular polarization. In *Antennas and Propagation Society International Symposium, 1988. AP-S. Digest*, pp. 762–765. IEEE, 1988.

Reflection-Based Source Inversion for Sparse Imaging of Low-Loss Composite Panels

Jakob Helander, Johan Lundgren, Daniel Sjöberg, Christer Larsson, Torleif Martin and Mats Gustafsson

Paper IV

Abstract

This article presents a bistatic reflection-based imaging technique for electromagnetic testing of conductor-backed composite panels, which is based on an inverse formulation of the numerical problem at hand, and technically extends a previously demonstrated transmission-based system. The technique exploits the a priori assumption of pixel-based sparsity and retrieves the final image using data from only a single measurement, thereby removing the necessity of a reference measurement to be conducted. To demonstrate the capability of the technique, retrieved images are presented for a synthetic proof-of-concept device under test and an industrially manufactured composite panel. The presented technique can be considered as the initial model in the development of more complex bistatic imaging systems and has been developed for the purpose of extending the opportunities to conduct reflection-based electromagnetic nondestructive testing on aircraft structural components.

1   Introduction

Composite structures manufactured with low-permittivity and low-loss materials, such as honeycomb or foam, are extensively utilized in radomes and aircraft structural components [1]. A fundamental step in the production chain of these structures is to validate the electromagnetic (EM) characteristics of each individually manufactured component, since this saves both money and time in product evaluation and troubleshooting. EM nondestructive testing (NDT) techniques may be utilized for this purpose, where the aim is to reconstruct an image of any unknown sources of radiation that might exist within the device under test (DUT). As such, NDT is the science and practice of evaluating various properties of a DUT without compromising its utility and usefulness [28, 34]. For these applications, millimeter wave (mm-wave) (30–300 GHz) imaging has emerged as a favorable EM testing technique in recent years [2, 12]– much due to the high resolution achievable from the inherently short wavelengths. In addition, mm-wave NDT has also been proved well suited for detecting defects related to low conductivity and inhomogeneity [21, 22].

The imaging problem itself is effectively addressed either using a synthetic aperture radar (SAR) framework [6, 24, 32] or by formulating it as an inverse source or scattering problem [8, 17, 19]. Although the measurement arrangement for the two methods is often similar—utilizing a mechanical or electrical scan of a receiving (Rx) probe or an array of probes to collect the data across a predefined measurement surface [12, 16, 31]–the methods differ in the underlying image retrieval principle. Accordingly, the data processing routines and measurement settings (e.g., center frequency, frequency bandwidth, modulation, and geometrical setup) of the system might differ substantially depending on the method. Elaborate and complete imaging systems that enable high-resolution real-time imaging using SAR algorithms and wideband microwave cameras have been demonstrated (see [11, 24]). The range resolution in classical SAR is inversely proportional to

bandwidth, while the technique described in this article—utilizing an inverse source formulation—enables a single-frequency imaging with subwavelength resolution [18]. Image reconstruction at discrete frequencies can be useful for objects with strong frequency dependence, e.g., frequency-selective surfaces. Moreover, inverse formulations enable the permittivity profile and conductivity profile of the DUT to be imaged, thus providing an excellent foundation for EM diagnostic tools [19].

Here, the focus is on investigating and advancing inversion approaches to the EM problem of conducting NDT of aircraft structural components of low-loss and low-permittivity materials. Modern frameworks utilizing source inversion techniques have been presented in [4,9,27]. However, for structural components consisting of at least a single sheet of RF-impenetrable material, a transmission-based EM testing technique (see [18,27]) may not always be a suitable bistatic measurement approach. Rather, the underlying conducting layer of the DUT can be extended by a mount on top of a ground plane, creating a reflection-based experimental setup. To avoid physical obstruction between the transmitting (Tx) antenna and the Rx probe, the electrical scan of the Rx probe should be performed in a measurement plane that captures the specular reflection in the conducting ground plane from the static Tx antenna, i.e., favoring forward rather than backscattering. This also suppresses sidelobe interference and other coupling effects between Tx and Rx due to the vicinity of the conducting ground plane but implies the necessity of a diligent approach to the mutual treatment of the geometrical setup and numerical inversion formulation.

The inverse problem of reconstructing the unknown sources is ideal for the utilization of various optimization techniques. Specifically, regularization techniques utilizing the L_1- and/or L_2-norm have been the target of extensive and promising research over the course of more than a decade [5,25,33]. L_1-minimization techniques such as compressive sensing (CS)—suitable for solving underdetermined linear systems where the solution vector is known beforehand to contain only a few nonzero entries with respect to a defined basis [25]–introduce the possible advantage of reducing the size of the measurement data set by evading a dense and uniform spatial sampling. Instead, as demonstrated in an NDT setting in [32], a sparse measurement may be performed to recover the solution vector, enabling a significantly reduced measurement time. However, regardless of the size of the used data set, L_1-minimization techniques facilitate enhanced image contrast and resolution—compared to L_2-minimization techniques—for imaging problems where the sought for solution is known a priori to be sparse [18]. These beneficial characteristics of CS have prompted a rapid development of innovative approaches to microwave imaging and inverse scattering problems [14,26].

This work technically extends a bistatic imaging system based on source separation, previously demonstrated in a transmission-based scenario [18], and shows its utility in the considerably more complex reflection-based measurement setting for conductor-backed composite DUTs—assumed to only contain few and physically small conducting or dielectric defects. This pixel-based sparsity—-a reasonable a priori assumption in the considered EM NDT scenario—is exploited

using a L_1-minimization routine for image retrieval. The L_1-minimization routine is compared to a least square approach to demonstrate its advantages in terms of resolution and image contrast. One of the key properties of the presented technique is the complete redundancy of a reference measurement, thereby making it feasible to retrieve the DUT image with only a single measurement. Measurements have been conducted in the 60 GHz band for high resolution and for an effortless mount of the experimental setup in a limited space such as a typical university laboratory. The imaging results are presented for a proof-of-concept DUT—where synthetic measurement data have been utilized—and for an industrially manufactured composite panel with defects inserted in its core layer. The presented imaging technique demonstrates the possibility of performing reference-free bistatic imaging of conductor-backed composites based on source inversion and constitutes a progression toward more generalized reflection-based EM inverse scattering techniques that utilize the source separation principle.

The paper is organized as follows. The electric field integral representation is briefly reviewed in Section 2.1, the source separation technique is presented in Section 2.2, and remarks on the numerical modelling are discussed in Section 2.3. The minimization formulations for image retrieval are presented in Section 3. Section 4.1 introduces the experimental setup, Section 4.2 the geometrical model and Section 4.3 the device under test (DUT) that was measured. Results are provided in Section 5, followed by concluding remarks in Section 6.

2   Reflection-Based Inverse Scattering

2.1   The Electric Field Integral Representation

The source reconstruction is based on expressing the solutions to Maxwell's equations using the electric field integral representation given by [23]:

$$\boldsymbol{E}(\boldsymbol{r}) = \mathrm{j}k\eta_0 \int\limits_S \boldsymbol{J}(\boldsymbol{r}')G(\boldsymbol{r},\boldsymbol{r}') + \frac{1}{k^2}\nabla G(\boldsymbol{r},\boldsymbol{r}')\nabla' \cdot \boldsymbol{J}(\boldsymbol{r}')\,\mathrm{d}\mathrm{S}', \qquad (2.1)$$

where $\boldsymbol{E}(\boldsymbol{r})$ is the vector-valued electric field in the observation point $\boldsymbol{r}$, $\boldsymbol{J}(\boldsymbol{r}')$ is the vector-valued electric current density in the source point $\boldsymbol{r}'$, S is the source surface of integration, and k, η_0 and $G(\boldsymbol{r},\boldsymbol{r}')$ are the wavenumber, intrinsic impedance and Green's function, respectively, in free space. To numerically address the source reconstruction, (2.1) is expressed in matrix form (the vector notation is henceforth understood from its context) as:

$$\boldsymbol{E} = \mathbf{N}\boldsymbol{J}, \qquad (2.2)$$

where the column vector $\boldsymbol{E}$ contains the electric field in all spatial sampling points, and the column vector $\boldsymbol{J}$ contains the discretized currents on the reconstruction surface. To solve (2.2) for $\boldsymbol{J}$ given $\boldsymbol{E}$ constitutes the general inverse

source problem which is commonly known to be ill-posed [17]. All reconstruction surfaces in this work are discretized into rectangular mesh cells with rooftop functions acting as local basis functions. For a single performed measurement, information can only be retrieved regarding a single component of the desired field. The source currents can still be divided into its co- and cross-polarized part and, assuming Ex has been extracted from the measured data, (2.2) may be expanded as

$$\boldsymbol{E}_x = \mathbf{N} \begin{bmatrix} \boldsymbol{J}_x \\ \boldsymbol{J}_y \end{bmatrix} = \begin{bmatrix} \mathbf{N}_{xx} & \mathbf{N}_{xy} \end{bmatrix} \begin{bmatrix} \boldsymbol{J}_x \\ \boldsymbol{J}_y \end{bmatrix} . \tag{2.3}$$

The extracted field component is preferably selected with respect to the alignment of the Rx probe antenna to obtain a high signal power. For a single measurement, it is, therefore advisable to orient the probe in accordance with the orientation of the Tx antenna, illuminating the DUT with either transverse electric (TE)- or transverse magnetic (TM) polarization as depicted in Figure 1. If two measurements using two different alignments of the probe have been conducted, both polarizations can be retrieved, and (2.3) can be expanded accordingly. Lastly, if it is desired to perform the imaging using the magnetic field instead, the magnetic field integral representation may be used to obtain a similar matrix form as the one in (2.3).

2.2   Source Separation Technique

A schematic of the target measurement scenario is depicted in Figure 2. As seen, three rectangular reconstruction surfaces are defined; the DUT, the source, and the image source surface. All surfaces are defined parallel to the xy-plane to simplify the numerical implementation and realize a fast and efficient reconstruction algorithm. It should be noted that there are no restrictions on the alignment of the different reconstruction surfaces. The DUT is placed on top of a conducting ground plane, and a second illuminating source (and its corresponding image source surface) is introduced using image theory. It is evident that the matrix operator $\mathbf{N}$ has to be computed for a number of different source-field relationships, *e.g.*, between the DUT- and the measurement surface. These operators will be labeled accordingly as they are introduced.

The source separation technique aims at decomposing the measured field $\boldsymbol{E}_{\mathrm{meas}}$ into the different parts contributing to the registered field in the measurement surface; the smooth, incident field $\boldsymbol{E}_{\mathrm{inc}}$ originating from the illuminating source and its image, and the scattered field $\boldsymbol{E}_{\mathrm{sc}}$ – scattered by the defects within the DUT under the given incident field from the primary Tx source:

$$\boldsymbol{E}_{\mathrm{meas}} = \boldsymbol{E}_{\mathrm{inc}} + \boldsymbol{E}_{\mathrm{sc}} . \tag{2.4}$$

From the measurement scenario, some valuable conclusions can be drawn concerning the registered measured field and its origins that support the use of a source separation technique. First, the magnitude of the incident field should be
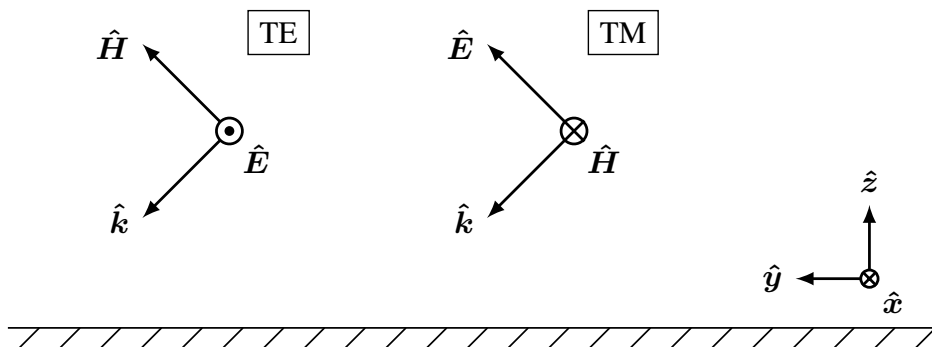
Figure 1: The transverse electric (TE)- and transverse magnetic (TM) polarizations as defined with respect to the orientation of the ground plane.
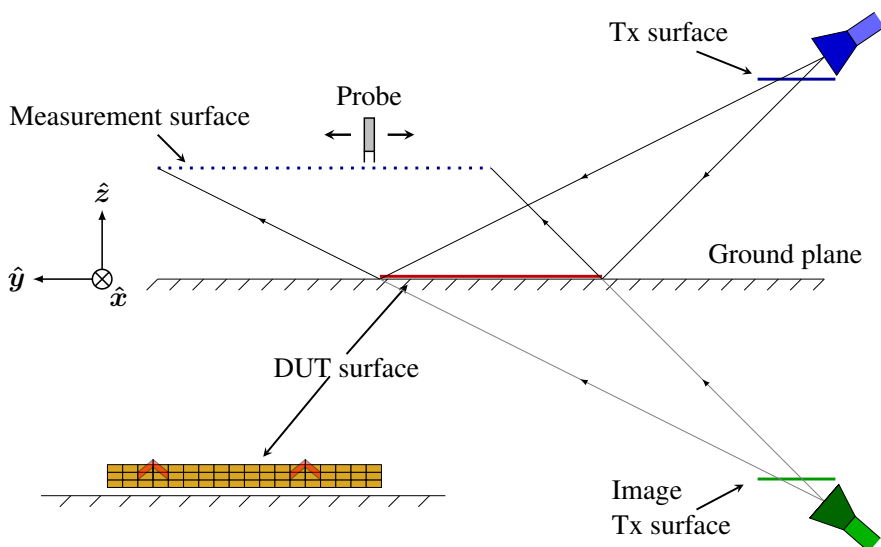
Figure 2: Schematic of the reflection-based measurement scenario. A source illuminates the device under test (DUT) - situated just above the ground plane - at an oblique angle, and the field is sampled using a probe in an xy-grid constituting the measurement surface. The three reconstruction surfaces (the DUT-, the source-, and the image source surface) are all situated in the xy-plane and discretized into rectangular mesh cells with rooftop basis functions.

considerably greater than the magnitude of the scattered field, since any potential defects are passive scatterers that have small physical dimensions. Secondly, the wavenumber spectrum of the probe will span very oblique incident angles due to its position relative to the three different excitation surfaces. The situation is depicted in Figure 3.

The source separation can thus be achieved through the use of a truncated
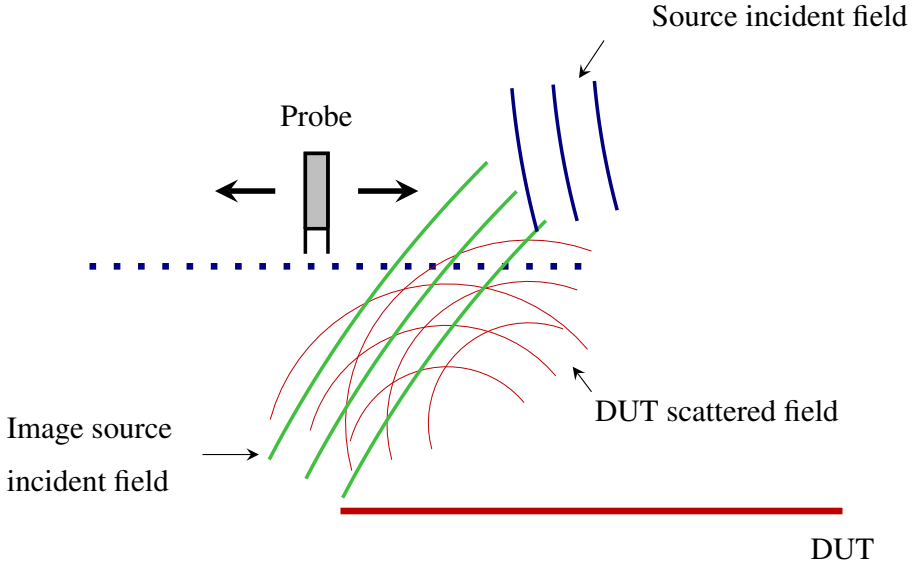
Figure 3: Principle of the source separation from the probe's field of view. The source incident field impinges at an angle far from the probe boresight, whereas the image source incident field and the scattered field impinge with an angle closer to the probe boresight. The scattered field is also considerably weaker than the incident fields, and originates from sources located more closely to the probe. This contributes to a clear distinction of the wavenumber spectrum of the fields.

singular value decomposition (SVD) regularization method [17, 18]. Let $\mathbf{N}_>$ and $\mathbf{N}_<$ be the operators from the source surface above ($z > 0$) and below ($z < 0$) the ground plane to the measurement surface, respectively, and $\boldsymbol{J}_>$ be the tangential electric current existing on the source surface above ground. By the image theory argument, the corresponding current $\boldsymbol{J}_<$ on the image source surface should then be selected as $\boldsymbol{J}_< = -\boldsymbol{J}_>$. However, what the probe antenna registers in a particular point of the finite grid constituting the measurement surface is in fact a complex-valued voltage accounting for the full probe interaction with the electromagnetic fields in its immediate surrounding, rather than the actual complex-valued field in that particular point. The influence of the receive (Rx) probe on the measured field value is usually corrected for through standard probe correction techniques [20, 31]. These, however, require a densely discretized grid in terms of wavelengths to fully model the receiving characteristics of the probe when incident fields are known to impinge on the probe from a wide spectrum of angles. Further, as seen in Figure 2 the angle between the probe boresight and the source incident field will be notably more oblique compared to the angle for the image source incident field, implying that the probe will be far less sensitive

to the former than to the latter. Hence, a clear distinction between $\boldsymbol{J}_>$ and $\boldsymbol{J}_<$ can be made if no probe correction technique is employed. To extract these independent source currents, the joint source operator

$$\mathbf{N}_{\mathrm{Tx}} = \begin{bmatrix} \mathbf{N}_> & \mathbf{N}_< \end{bmatrix} , \tag{2.5}$$

is defined and decomposed into its singular vectors and singular values by means of the SVD:

$$\mathbf{N}_{\mathrm{Tx}} = \mathbf{U}\boldsymbol{\Sigma}\mathbf{V}^{\mathrm{H}} . \tag{2.6}$$

Here, $\mathbf{U}$ and $\mathbf{V}$ are the left- and right-singular vectors, and $\boldsymbol{\Sigma}$ is a diagonal matrix containing the singular values. The Hermitian transpose is denoted $\cdot^{\mathrm{H}}$. By constructing the pseudoinverse of $\mathbf{N}_{\mathrm{Tx}}$, the currents in the two source surfaces can now be found from $\boldsymbol{E}_{\mathrm{meas}}$:

$$\boldsymbol{J}_{\mathrm{Tx}} = \begin{bmatrix} \boldsymbol{J}_> \\ \boldsymbol{J}_< \end{bmatrix} = \mathbf{V}\widetilde{\boldsymbol{\Sigma}}\mathbf{U}^{\mathrm{H}}\boldsymbol{E}_{\mathrm{meas}} . \tag{2.7}$$

Here, $\widetilde{\boldsymbol{\Sigma}}$ contains the reciprocal of all singular values whose normalized value is above a prescribed threshold τ_{SVD}. This threshold determines what fraction of $\boldsymbol{E}_{\mathrm{meas}}$ that will be bound to the currents on the two source surfaces, and thus plays a significant role in how well the incident field $\boldsymbol{E}_{\mathrm{inc}}$ and the scattered field $\boldsymbol{E}_{\mathrm{sc}}$ are modeled. This is discussed further in Section 2.3 together with a number of other factors to consider for the numerical modeling. It should also be noted that it is trivial to enforce current symmetry ($\boldsymbol{J}_< = -\boldsymbol{J}_>$) if desired. This approach was however discarded in the case of not also employing a proper probe correction technique.

With $\boldsymbol{J}_{\mathrm{Tx}}$ known, the incident field $\boldsymbol{E}_{\mathrm{inc}}$ may be extracted using

$$\boldsymbol{E}_{\mathrm{inc}} = \mathbf{N}_{\mathrm{Tx}}\boldsymbol{J}_{\mathrm{Tx}} = \mathbf{N}_{\mathrm{Tx}}\mathbf{V}\widetilde{\boldsymbol{\Sigma}}\mathbf{U}^{\mathrm{H}}\boldsymbol{E}_{\mathrm{meas}} , \tag{2.8}$$

and subsequently, the scattered field $\boldsymbol{E}_{\mathrm{sc}}$ may be retrieved using (2.4), i.e., through

$$\boldsymbol{E}_{\mathrm{sc}} = \left(1 - \mathbf{N}_{\mathrm{Tx}}\mathbf{V}\widetilde{\boldsymbol{\Sigma}}\mathbf{U}^{\mathrm{H}} \right) \boldsymbol{E}_{\mathrm{meas}} . \tag{2.9}$$

One of the key properties of this technique is that it is reference-free since it only require a single measurement to acquire the different field contributions, and finally to retrieve an image representing the DUT. An illustration of the source separation principle is depicted in Figure 4 for a synthetic example simulated in FEKO [3] using the same setup and settings as disclosed in 4.1 and 4.2

2.3   Remarks on the Numerical Modeling

There are a number of settings that need to be selected carefully when performing the source separation. The width of the source- and image source surface should enclose the projected footprint of the transmit (Tx) antenna aperture such that
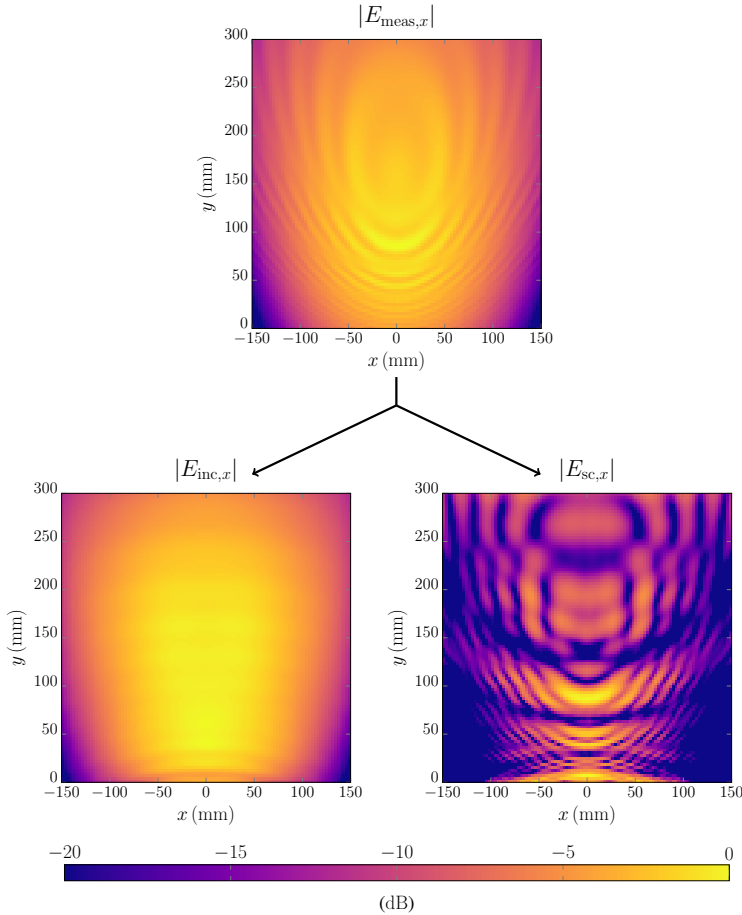
Figure 4: Illustration of the source separation technique using a synthetic TE-case simulated in FEKO. An electric field $E_{\text{meas},x}$ (top) sampled in the measurement surface is decomposed into an incident field $E_{\text{inc},x}$ (below left) originating from the illuminating source, and a scattered field $E_{\text{sc},x}$ (below right) originating from scatterers within the DUT. The figures are independently normalized, and there is $\approx 15\,\text{dB}$ difference between the maximum power of the measured- and the scattered field.

the full illumination of the DUT can be represented by currents on the discretized surface. The discretization may be selected in accordance to standard method of moments (MoM) with a spacing of $\approx \lambda/10$. However, the discretization can be selected more sparse, implying that fewer radiating modes can be modeled by the discretized source surface. This will in turn impact the fraction of $\boldsymbol{E}_{\text{meas}}$ that can be bound to sources existing on the source surfaces.

A conventional approach to selecting the threshold τ_{SVD} for the SVD regular-
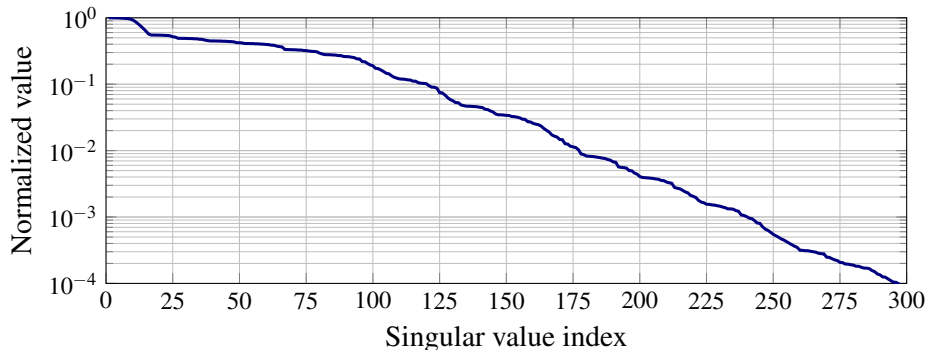
Figure 5: An example of the first 300 normalized singular values when regularizing the matrix operator $\mathbf{N}_{\mathrm{Tx}}$ using the SVD method.

ization in (2.7) is to analyze the *L*-curve [17], which, in essence, gives insight into the trade-off between the regularized solution and its fit to the given data. Since the intended use of the SVD in this work is to separate the different contributions to $\boldsymbol{E}_{\mathrm{meas}}$, it is not as straightforward to select τ_{SVD} based on the residual norm. As shown in Figure 5, there exists no distinct drop-off of the normalized singular values. Instead, using the *L*-curve as a starting point, a range of values—$\tau_{\mathrm{SVD}} \in \left[10^{-4},\, 0.5\right]$—were singled out for which the relative difference of the image quality was marginal. For the presented results, $\tau_{\mathrm{SVD}} = 10^{-3}$.

The above remarks are a reminder of that hands-on modelling is unpreventable in the source separation technique, and that the user must mutually select the appropriate settings supported by both a priori knowledge but also iterative measures.

3   Image Retrieval

The inverse scattering problem is formulated by letting the complex scattering amplitudes, $\boldsymbol{s}$, represent the EM characteristic of the DUT. The considerably more convoluted nonlinear formulation, with the associated approximations and linear reformulations [7, 19], for obtaining the dielectric contrast of the DUT is omitted due to the limitations of the available numerical source code. However, it constitutes a natural progression of the contained work. Referring to (2.2), the unknown excited currents on the DUT reconstruction surface, $\boldsymbol{J}_{\mathrm{dut}}$, is related to $\boldsymbol{E}_{\mathrm{sc}}$ as

$$\boldsymbol{E}_{\mathrm{sc}} = \mathbf{N}_{\mathrm{dut}}\boldsymbol{J}_{\mathrm{dut}}\,, \tag{3.1}$$

where $\mathbf{N}_{\mathrm{dut}}$ is the source-field operator between the DUT- and the measurement surface. Further, $\boldsymbol{J}_{\mathrm{dut}}$ may be expressed through the scattering amplitudes $\boldsymbol{s}$ given the incident field on the DUT, $\boldsymbol{E}_{\mathrm{dut}}$:

$$\boldsymbol{J}_{\mathrm{dut}} = \boldsymbol{s} \circ \boldsymbol{E}_{\mathrm{dut}}\,. \tag{3.2}$$

Here, ∘ denotes the Hadamard (element-wise) product of the spatial vectors. The single polarization measurement scenario is assumed, thus neglecting any existing cross-polarization terms. In an identical manner to (3.1), $\boldsymbol{E}_{\mathrm{dut}}$ is obtained from the source currents $\boldsymbol{J}_{\mathrm{Tx}}$ and the appropriately defined operator $\mathbf{N}$. An estimate of the scattering amplitudes $\hat{\boldsymbol{s}}_{\mathrm{pc}}$ can then be retrieved by combining (3.1) and (3.2) and applying phase conjugation:

$$\hat{\boldsymbol{s}}_{\mathrm{pc}} = \left(\mathbf{N}_{\mathrm{dut}}^{\mathrm{H}} \boldsymbol{E}_{\mathrm{sc}}\right) \oslash \boldsymbol{E}_{\mathrm{dut}} . \tag{3.3}$$

Here, $\oslash$ denotes the Hadamard (element-wise) division. The DUT is not illuminated uniformly due to the radiation characteristics of the Tx antenna, and to suppress this bias on the excited scattering amplitudes they may simply be weighted with the amplitude of $\boldsymbol{E}_{\mathrm{dut}}$ in each spatial point.

3.1 L_2- & L_1-Minimization

Instead of performing single phase conjugation for image retrieval, iterative optimization procedures can be used to improve image quality. A reasonable assumption in an NDT setting is that the DUT does not contain any spatially large anomalies; rather, any potential defects are few and small in physical size. Thus, this pixel-based, spatial sparsity can be exploited to formulate the linear inverse problem of finding the scattering amplitudes as: 1) a least square problem of sparse equations (an L_2-minimization formulation), and 2) a CS problem (an L_1-minimization formulation).

The L_2-minimization formulation reads:

$$\hat{\boldsymbol{s}}_{\ell_2} = \arg\min_{\boldsymbol{s}} \ \|\mathbf{N}_{\mathrm{dut}} \left(\boldsymbol{s} \circ \boldsymbol{E}_{\mathrm{dut}}\right) - \boldsymbol{E}_{\mathrm{sc}}\|_2^2 + \theta^2 \|\boldsymbol{s}\|_2^2 , \tag{3.4}$$

where $||\cdot||_p$ denotes the L_p-norm, and θ is a user-defined regularization parameter that controls the importance of $\|\boldsymbol{s}\|_2$ to the solution. The routine is run using the LSMR-software library [10], and is based on the conjugate gradient method.

The L_1-minimization formulation reads:

$$\begin{aligned} \hat{\boldsymbol{s}}_{\ell_1} = \arg\min_{\boldsymbol{s}} \quad & \|\boldsymbol{s}\|_1 \\ \text{subject to} \quad & \|\mathbf{N}_{\mathrm{dut}} \left(\boldsymbol{s} \circ \boldsymbol{E}_{\mathrm{dut}}\right) - \boldsymbol{E}_{\mathrm{sc}}\|_2 \le \kappa\sigma , \end{aligned} \tag{3.5}$$

where the user-defined scaling factor $\kappa \le 1$ and σ is taken as the L_2-norm of the residual for the phase conjugation solution, *i.e.*,

$$\sigma = \|\mathbf{N}_{\mathrm{dut}} \left(\hat{\boldsymbol{s}}_{\mathrm{pc}} \circ \boldsymbol{E}_{\mathrm{dut}}\right) - \boldsymbol{E}_{\mathrm{sc}}\|_2 . \tag{3.6}$$

In essence, this forces the optimized solution to produce a smaller residual (in L_2) compared to the solution of a single phase conjugation. The routine is run using the SPGL1 Matlab solver based on the basis pursuit denoise L_1-minimization problem [30]. Even though (3.5) minimizes the L_1-norm of $\boldsymbol{s}$, this essentially has
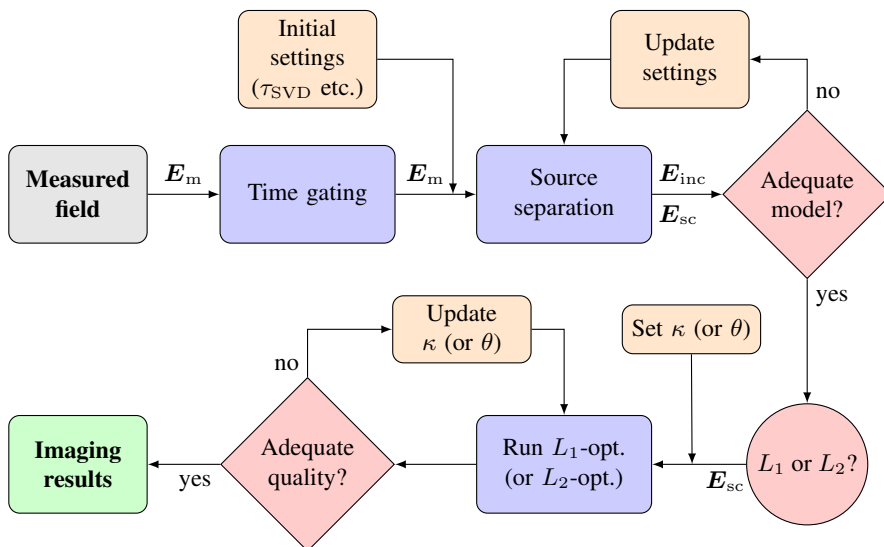
Figure 6: Flowchart of the complete imaging system incorporating the source separation technique and the two optimization routines. The "Initial settings" and "Update settings" blocks include, besides selecting the threshold τ_{SVD}, selecting the discretization and size of the source- and image source surfaces.

the effect of suppressing the number of non-zero entries in the solution vector, *i.e.*, it searches for a pixel-based sparse solution [25]. In contrast, the L_2-minimization will only try to minimize the residual L_2-norm with no respect to any potential sparsity of the solution vector.

A flowchart of the complete imaging system is shown in Figure 6. The measured field, $\boldsymbol{E}_{\mathrm{meas}}$, is first subject to time domain gating to mitigate the problem of multipath propagation. Subsequently, the source separation (Section 2.2) is conducted to extract $\boldsymbol{E}_{\mathrm{inc}}$ and $\boldsymbol{E}_{\mathrm{sc}}$ using the initial imaging settings for the numerical modeling—these include the SVD threshold, τ_{SVD}, and the size, location, and discretization of the reconstruction surfaces, as discussed in Section 2.3. The settings may then be iteratively adjusted—prior to selecting the optimization routine—by cross-referring to a synthetic incident field and, thus, corroborate the split between $\boldsymbol{E}_{\mathrm{inc}}$ and $\boldsymbol{E}_{\mathrm{sc}}$. Similarly, the parameters θ and κ for the optimization procedures may be updated if the final image, e.g., contains apparent artifacts or fails to find a reference defect.

3.2 Parallel Reconstruction Surfaces

As seen in Figure 2, the measurement- and the reconstruction surfaces are all parallel to the xy-plane at various distances from the ground plane. Intuitively, an initial setup would involve a measurement surface whose normal is aligned with the specular reflection from the center point of the ground plane, and two source

surfaces situated as to exactly discretize the aperture of the Tx antenna and its image. However, because the electrical size of the considered imaging scenario is very large (we consider a DUT on the order of $\approx 50\lambda \times 50\lambda$ here, with λ being the operational wavelength), keeping the surfaces parallel is paramount for performing the numerical inverse scattering time-efficiently and with less stringent memory requirements. By keeping the surfaces parallel and enforcing identical discretization, $\mathbf{N}_{\mathrm{dut}}$ will be a block Toeplitz matrix which in turn can be embedded into a circulant matrix. As a circulant matrix is diagonalized by a discrete Fourier transform, any operations involving $\mathbf{N}_{\mathrm{dut}}$ can be performed matrix-free using classical FFT algorithms [13,15]. Thus, instead of requiring $\mathcal{O}(N^3)$ operations and a memory order of $\mathcal{O}(N^2)$ this is reduced to $\mathcal{O}(N \log N)$ operations and a memory order of $\mathcal{O}(2N)$, making it feasible to run the reconstruction algorithm for large N on a standard laptop computer. Furthermore, the pixel resolution will not be limited by the discretization used in the measurement grid; the DUT surface can be subsampled by introducing several shifted grids of the surface that all utilize identical discretizations as in the measurement grid [18].

4   Measurements

4.1   Experimental Setup

All measurements were conducted in the microwave laboratory at Lund University, Sweden, with the experimental setup, shown in Figure 7, mounted on a Newport RS 2000 optical table. A Flann 25240-20 standard gain horn was used as the Tx antenna, and a 60 GHz RFSPIN WR15 open-ended waveguide was used as the Rx probe. The measurement surface was realized by scanning the probe using two THORLABS LTS300/M positioners. A Rhode & Schwarz ZVA 67 GHz VNA was used to retrieve the data, and both the VNA and the positioners were controlled using a GPIB connection to a laptop and in-house written Matlab scripts. All measurements were conducted for 101 linearly spaced discrete frequency points across the frequency band 59–61 GHz with an IF bandwidth of 1 kHz. The 2 GHz bandwidth enables the use of time gating of the measured data to filter out potential multipath signals. All images were retrieved at a single frequency, namely 60 GHz.

The positioners were limited to cover a $300\,\mathrm{mm} \times 300\,\mathrm{mm}$ area, and the signal was sampled over a 101×101 uniform rectangular grid, which resulted in a 3 mm sample increment in the x- and y-direction. This corresponds to a $3\lambda/5$ increment at 60 GHz (wavelength $\lambda \approx 5\,\mathrm{mm}$). With these settings, a single measurement took $\approx 4\,\mathrm{h}$ to conduct. Notably, the Nyquist criterion was slightly violated. However, the degree of aliasing can be pre-evaluated using synthetic data, and ultimately it is up to the user to determine the trade-off between measurement time, resolution and aliasing.

A final remark is that the physical ground plane was finite, whereas the imaging technique assumes an infinite ground plane. The millimeter wave (mm-wave)
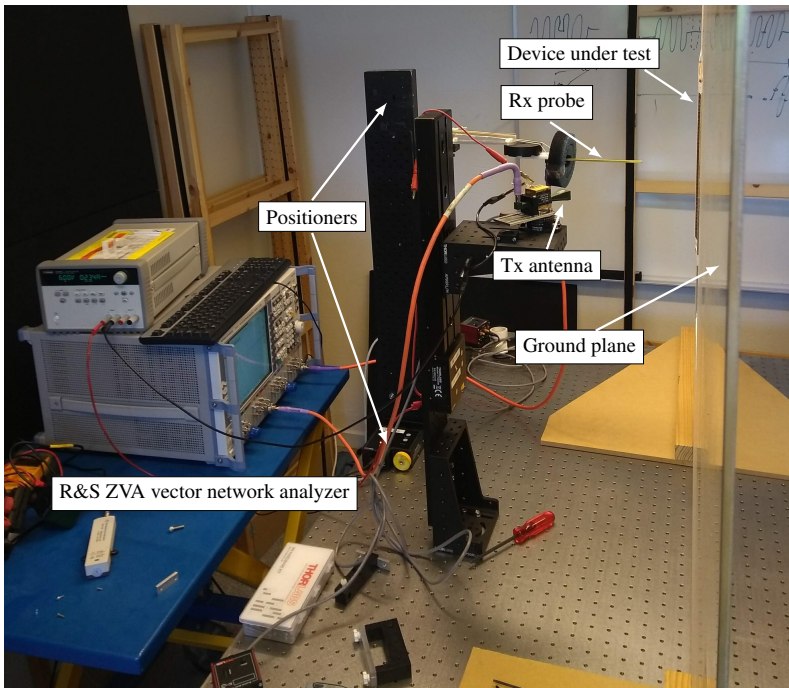
Figure 7: Experimental setup of the measurement system. The DUT is mounted above a metallic ground plane (here vertically aligned), and the spatially fixed Tx antenna illuminates the DUT from an oblique angle. The positioners scan the Rx probe to sample the signal across a vertically aligned, rectangular, measurement aperture.

frequencies are, from a practical perspective, therefore highly suitable since the physical size of the ground plane need not to be exceptionally large to realize an electrically large ground plane.

4.2   Geometrical Settings

The geometrical model, depicted in Figure 2, depends on several degrees of freedom: the absolute position of the transmitter and the angle between its boresight axis and the ground plane, the distance between the ground and measurement surface, the width of the measurement surface, and the width of the DUT. These should all be carefully chosen in order to: 1) position the DUT in the far field or the radiative near field region of the Tx antenna, 2) concentrate the radiating electromagnetic fields within the footprint of the DUT, 3) capture sufficient power of the signal - reflected in the ground plane beneath the DUT - in the measurement surface, and 4) not position the measurement surface such that the probe aperture obstructs the illumination of the DUT. Therefore, it is crucial to

consider the half power beamwidth as well as the dimensions of the aperture of the Tx antenna and the operational wavelength when designing the setup. The geometrical model can be determined once these factors have been considered. In this work, the DUT reconstruction surface was centered at the origin. The finite measurement aperture was centered in the point $\boldsymbol{r}_{\mathrm{m}} = (150\hat{\boldsymbol{y}} + 100\hat{\boldsymbol{z}})\,\mathrm{mm}$ with the ranges $x \in [-150, 150]\,\mathrm{mm}$ and $y \in [0, 300]\,\mathrm{mm}$ in x and y, respectively. Finally, the Tx antenna was situated in the point $\boldsymbol{r}_{\mathrm{Tx}} = (-300\hat{\boldsymbol{y}} + 200\hat{\boldsymbol{z}})\,\mathrm{mm}$ with its boresight axis directed towards the origin, which resulted in a 34° angle between the boresight axis and the ground plane.

4.3   Device Under Test (DUT)

The measured DUT was a $300\,\mathrm{mm} \times 300\,\mathrm{mm} \times 3\,\mathrm{mm}$ industrially manufactured composite panel provided by Saab Aeronautics. The panel consisted of a $2\,\mathrm{mm}$ thick low permittivity over-expanded Nomex honeycomb core, sandwiched between two $0.5\,\mathrm{mm}$ sheets of TenCate EX-1515, a cyanate ester quartz fabric pre-preg [29]. The panel was assembled using TenCate EX-1516, an adhesive developed for bonding solid, honeycomb or foam core structures used in aircraft and space applications [29], and covered with a fluoropolymer film. The defects, inserted into the Nomex honeycomb core, were selected in order to investigate the detection limits of the imaging technique for metallic and dielectric objects with different shapes and sizes. The DUT is shown in Figure 8. Eight groups of defects can be seen in the figure; three in the top, two in the center, and three in the lower row. The two center groups each consists of three sub-wavelength defects spaced $\approx 1\,\mathrm{mm}$ apart. The lower row contains conducting defects, whereas the other rows contain accumulations of the same adhesive used for assembling the panel. Due to the limited coverage area of the positioners, the geometrical model was constructed such that the measurement surface captured the specular reflections of a $200\,\mathrm{mm} \times 200\,\mathrm{mm}$ area of the DUT surface. The experimental setup with the mounted composite panel is shown in Figure 9.

5   Results

5.1   Proof of Concept

To provide a proof of concept, the complete imaging system was evaluated using synthetic measurement data input obtained from simulations of a test case geometry. The simulations were run in FEKO [3] at $60\,\mathrm{GHz}$ using the geometrical settings presented in Section 4.2. The simulated far-field pattern of the standard gain horn used in the measurement was used as a source, and the field was sampled over a grid identical to the measurement grid. As shown in Figure 10, the test case DUT was selected as two conducting wires of length $l = 2.5\,\mathrm{mm}$—one $\hat{\boldsymbol{x}}$-oriented and one $\hat{\boldsymbol{y}}$-oriented—each situated a distance $d = 25\,\mathrm{mm}$ from the
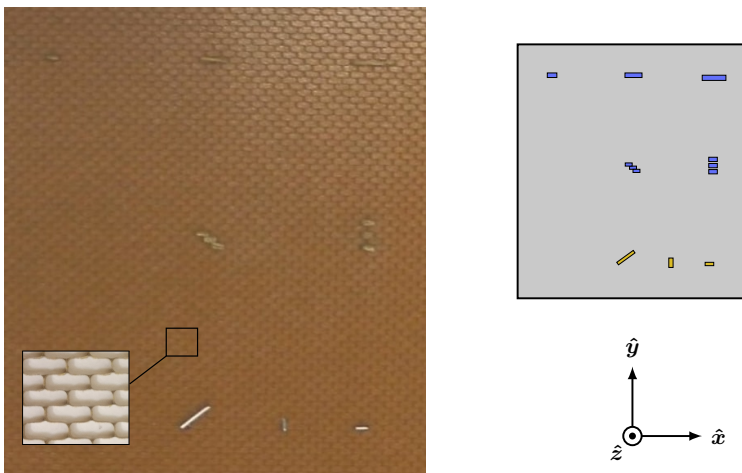
Figure 8: Left: Image of the measured DUT, a composite panel with inserted conducting- and dielectric defects and the top layer pre-preg removed (for visuality). The zoomed-in image shows the honeycomb structure, and the size of the defects are in the order of a few millimeters (sub-wavelength) to a couple of centimeters. Right: Schematic of the composite panel (top) with dielectric defects marked in blue and conducting defects marked in yellow, and the orientation with respect to the setup (bottom).

origin along the $\hat{\boldsymbol{x}}$-axis and 0.25 mm above ground. This DUT geometry thus provides a clear distinction in the final image between the two cases of TE- and TM-illumination. The area of the DUT reconstruction surface was chosen as $200 \, \text{mm} \times 200 \, \text{mm}$.

The performance of the two optimization routines based on L_2- and L_1-minimization was first validated by investigating how the solution- and relative error depend on the value of the regularization parameters κ and θ. The relative error is defined as:

$$\eta = \frac{\|\mathbf{N}_{\text{dut}} \left(\hat{\boldsymbol{s}} \circ \boldsymbol{E}_{\text{dut}} \right) - \boldsymbol{E}_{\text{sc}}\|_2}{\|\boldsymbol{E}_{\text{sc}}\|_2} \,, \tag{5.1}$$

with $\hat{\boldsymbol{s}} \in \{\hat{\boldsymbol{s}}_{\ell_1}, \hat{\boldsymbol{s}}_{\ell_2}\}$ for the two respective optimization routines. The results are shown in Figures 11(a) and 11(b) for the L_2- and L_1-minimization, respectively. The solution norm $\|\hat{\boldsymbol{s}}_{\ell_2}\|_2$ is penalized for large θ as expected, which consequently leads to η increasing up to the saturation value 1 as the left term in the numerator of (5.1) vanishes. The L_1-norm of the solution $\hat{\boldsymbol{s}}_{\ell_1}$ is monotonically decreasing for increasing κ, which is to be expected since a larger κ puts a less stringent requirement on the solution's fit to the given data in a least square sense. The L_0-norm, which represents the number of non-zero entries in the solution vector, decreases as well, clearly illustrating how the L_1-minimization searches for a sparse solution. Lastly, the relative error η, shown in the interjected image in Figure 11(b), increases linearly with κ as expected.
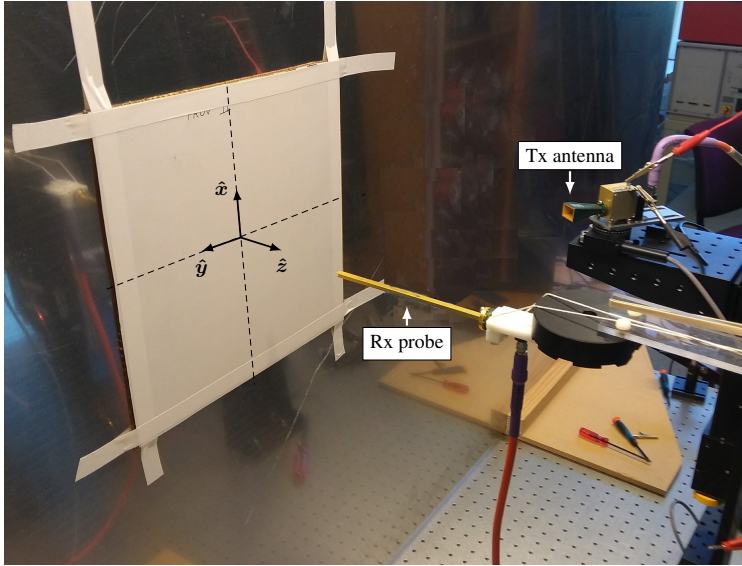
Figure 9: Measurement of the composite panel using the experimental setup. The orientation in reference to the schematic setup (seen in Figure 2) is depicted in the center of the DUT.
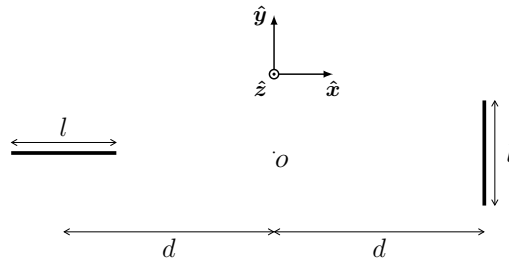
Figure 10: The test case DUT consisting of two conducting wires of length $l = 2.5\,\text{mm}$ situated a distance $d = 25\,\text{mm}$ from the origin.

The final retrieved images of the scattering amplitudes are shown in Figures 12(a) and 12(b) for TE- and TM-illumination of the test case DUT, respectively. As seen, only the wire that is co-polarized with the illumination is reconstructed. The difference between the L_2- and L_1-minimization images - shown in the left and the right column, respectively - is also evident; the L_1-minimized solutions have only a small number of non-zero valued pixels at the physical location of the excited defect, whereas the L_2-minimized solutions do not perfectly reconstruct the physical size of the defects but rather finds a smeared out image with a clear maximum at the location of the defect; this spread in the L_2-reconstructed images is related to the resolution limits of the system's point
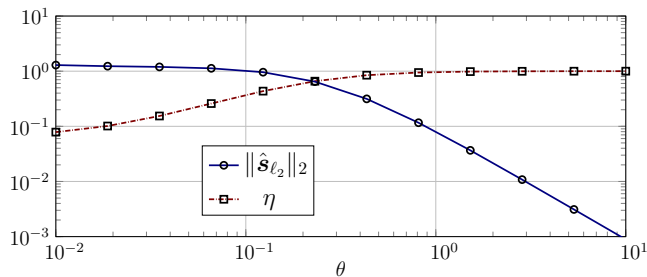
(a) Solution- and relative error η as a function of the
regularization parameter θ in eq. (3.4).
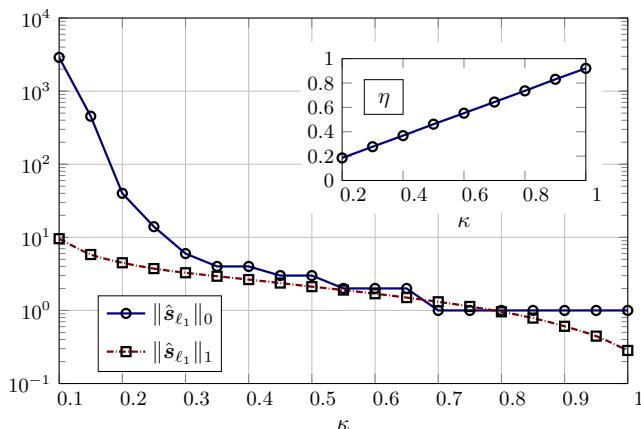
(b) Solution- and relative error η as a function of the scaling
parameter κ in eq. (3.5).

Figure 11:   Performance of the L_2- and L_1-minimization routines as a function of the corresponding regularization parameters when the synthetic test case DUT, shown in Figure 10, is illuminated by a TE-polarized source. (a): L_2-minimization. (b): L_1-minimization.

spread function [8].

5.2   Industrial Composite Panel

Due to limited time, a single TE-polarized measurement of the composite panel was carried out. The area of the DUT reconstruction surface was first chosen as $200\,\text{mm} \times 200\,\text{mm}$, which is smaller than $300\,\text{mm} \times 300\,\text{mm}$; the total area of the panel. The final retrieved images of the scattering amplitudes using L_2- and L_1-minimization are shown in Figures 13 and 14, respectively. The L_2-image shows seven of the eight defects clearly resolved, whereas the right bottom corner one
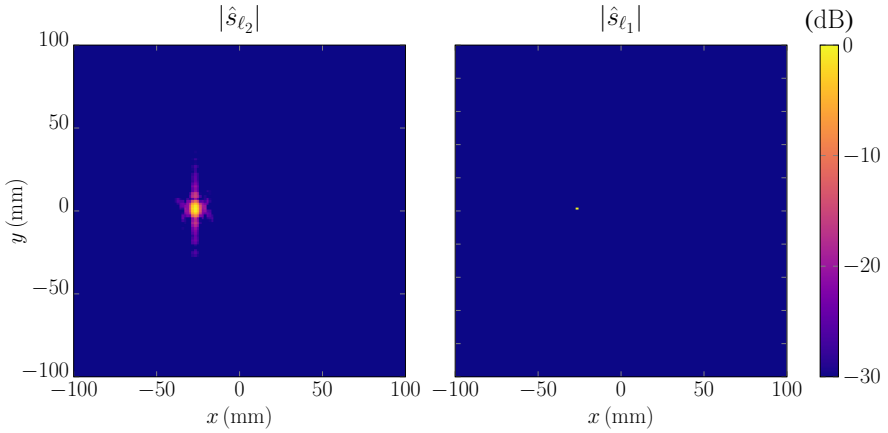
(a) TE-polarized illumination.
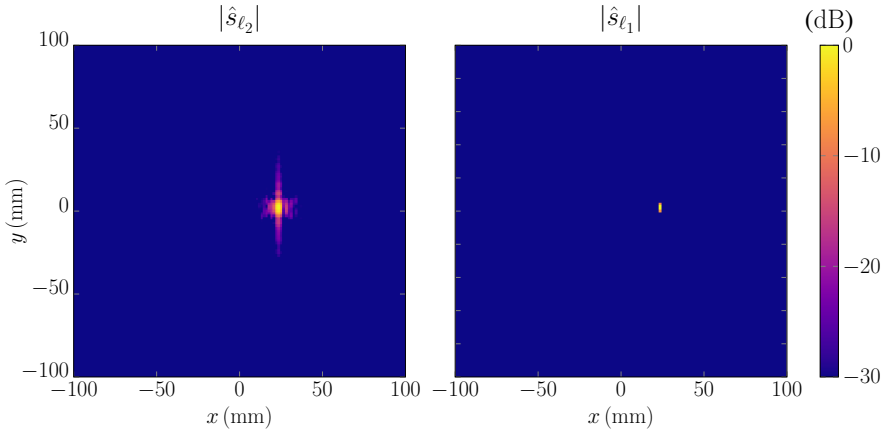
(b) TM-polarized illumination.

Figure 12: Normalized absolute value of the retrieved scattering amplitudes for the test case DUT. (a): TE-polarized illumination. (b): TM-polarized illumination. The right and the left column show the final image using L_2-minimization (with $\theta = 0.1$) and L_1-minimization (with $\kappa = 1$), respectively.

is indistinguishable from the surrounding noise. All eight defects are resolved in the L_1-image. As expected, the retrieved image using L_2-minimization contains artificial, low power scattering amplitudes constituting a spurious background. The dynamic range of the image can of course be made smaller to suppress the background, but is here kept at $30\,\mathrm{dB}$ for consistency.

In contrast, the retrieved image using L_1-minimization contains only non-zero scattering amplitudes at the physical location of the defects. Notably, the imaging technique is capable of clearly resolving the defects in the two groups of
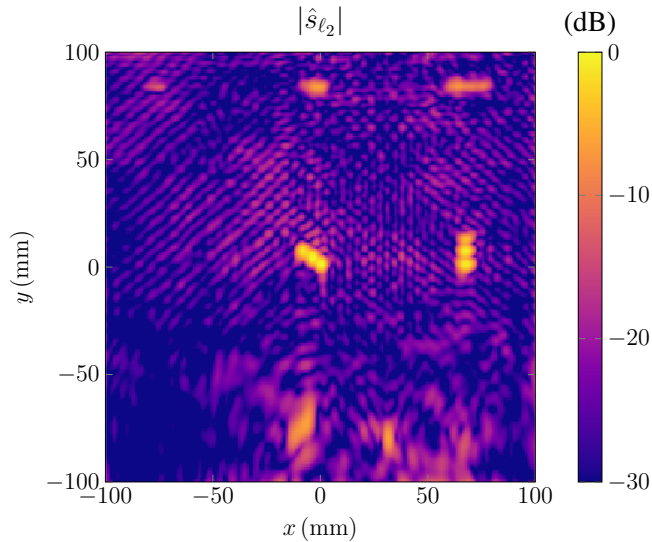
Figure 13: Normalized absolute value of the retrieved scattering amplitudes for the measured panel DUT. The image is obtained using L_2-minimization with $\theta = 0.1$.

sub-wavelength spaced dielectric defects (center and center left) independently. Note that the corner-situated defects could be made more visible by increasing the dynamic range.

A source of uncertainty that impacts the image quality should be mentioned here; since the panel DUT has a non-zero thickness and the imaging theory creates an image of the panel below ground in the numerical model of the measurement geometry, there exists a span of reasonable distances from ground for which the DUT reconstruction surface could be defined. This affects the image focus, since the DUT is in fact three-dimensional and thus no existing defects act as purely planar scatterers. The images shown here have been obtained for a DUT reconstruction surface situated a distance 2.5 mm above ground, *i.e.*, in the plane just at the interface between the honeycomb core and the overlying sheet of TenCate EX-1515.

5.3 Removal of Undesirable Scatterers

The technique of separating sources that contribute to a measured electric field can be further extended to remove undesirable scatterers from the final image. This can be deemed useful if there exists an ambiguity in how to select the size and location of the DUT reconstruction surface. By extending the area of the reconstruction surface to 350 mm × 350 mm, thereby including the full 300 mm × 300 mm panel in the image, it is evident that the edges of the finite sized
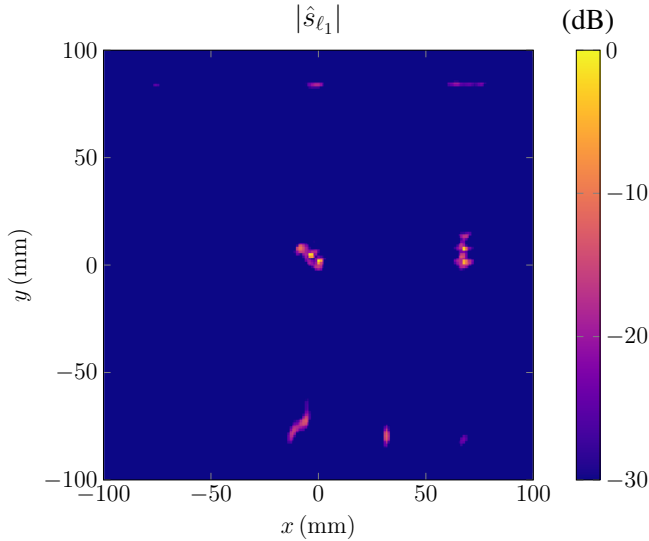
Figure 14: Normalized absolute value of the retrieved scattering amplitudes for the measured panel DUT. The image is obtained using L_1-minimization with $\kappa = 0.97$.

panel contribute significantly to the scattered field captured in the measurement surface in terms of diffraction. This is seen in the left image in Figure 15. Here it is noticeable that the top $\hat{\boldsymbol{x}}$-oriented edge causes the most substantial diffraction, caused by the TE-polarized illumination and the fact that this edge is more closely located to the measurement surface.

The undesirable scatterers can be filtered out without directly cropping the final image or selecting a smaller reconstruction surface. An exterior region Ω_{ext} can be defined, containing all spatial indices outside the reconstruction region of interest. The contribution from all scatterers within this region can then be subtracted from $\boldsymbol{E}_{\text{sc}}$:

$$\widetilde{\boldsymbol{E}}_{\text{sc}} = \boldsymbol{E}_{\text{sc}} - \mathbf{N}_{\text{dut}} \left(\hat{\boldsymbol{s}}_{\text{ext}} \circ \boldsymbol{E}_{\text{dut}} \right) ,$$

$$\text{where} \quad \hat{\boldsymbol{s}}_{\text{ext}} = \left\{ \hat{\boldsymbol{s}}_{\ell_2} \mid [\hat{\boldsymbol{s}}_{\ell_2}]_i = 0 \ \forall \ i \notin \Omega_{\text{ext}} \right\} . \tag{5.2}$$

Here, the exterior scatterers $\hat{\boldsymbol{s}}_{\text{ext}}$ are obtained from the solution to the L_2-minimization formulation in (3.4). The remaining scattered field $\widetilde{\boldsymbol{E}}_{\text{sc}}$ may now be used as a right-hand side input to the optimization routines in (3.4) and (3.5) to obtain a second set of filtered images. Figure 15 illustrates the principle, with the right image obtained using the L_2-minimization routine and $\theta = 0.1$. Clearly, all scatterers in the exterior region are suppressed. The principle is also visualized in Figures 16 and 17 for the L_1-minimization routine and $\kappa = 0.85$, where the former is obtained directly with no filtering and the latter is obtained with the same remaining scattered field $\widetilde{\boldsymbol{E}}_{\text{sc}}$ used for retrieving the right image
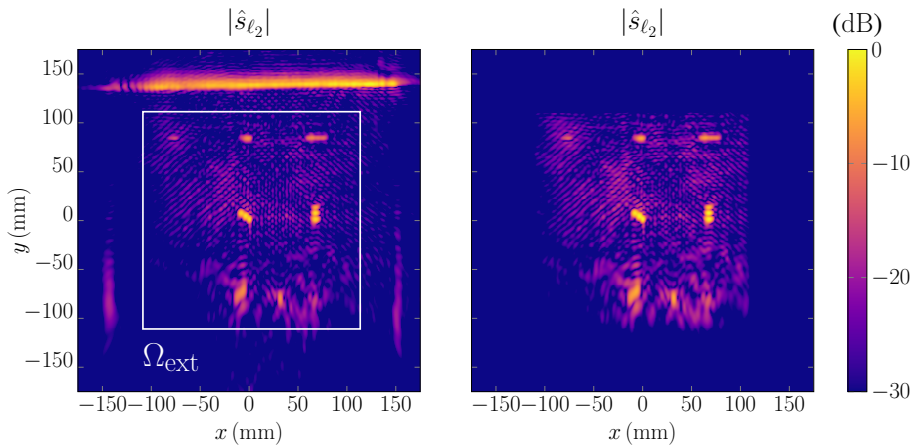
Figure 15: Normalized absolute value of the retrieved scattering amplitudes for the measured panel DUT with a reconstruction surface of $350\,\text{mm} \times 350\,\text{mm}$. The images are obtained using L_2-minimization with $\theta = 0.1$. The left and right image is obtained before and after filtering, respectively.
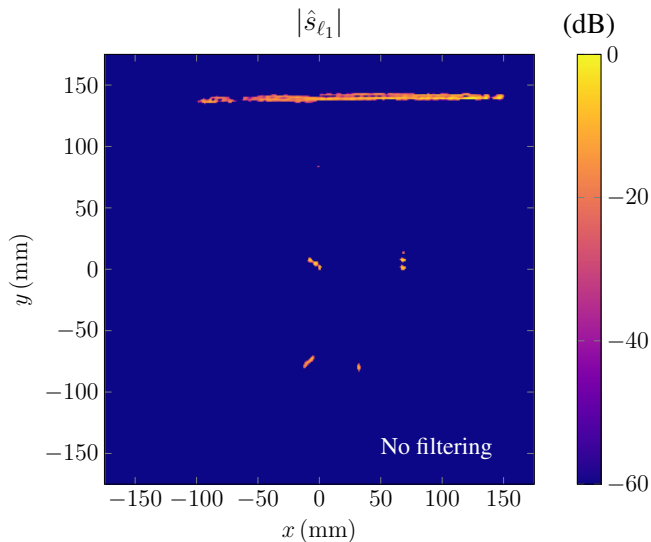
Figure 16: Normalized absolute value of the retrieved scattering amplitudes for the measured panel DUT with no filtering. The image is obtained using L_1-minimization with $\kappa = 0.85$, the area of the reconstruction surface is $350\,\text{mm} \times 350\,\text{mm}$, and the dynamic range is $60\,\text{dB}$.

in Figure 15. With the relatively strong contribution from the edge diffraction filtered out, it is noticeable how the weaker scatterers become visible. Notably,
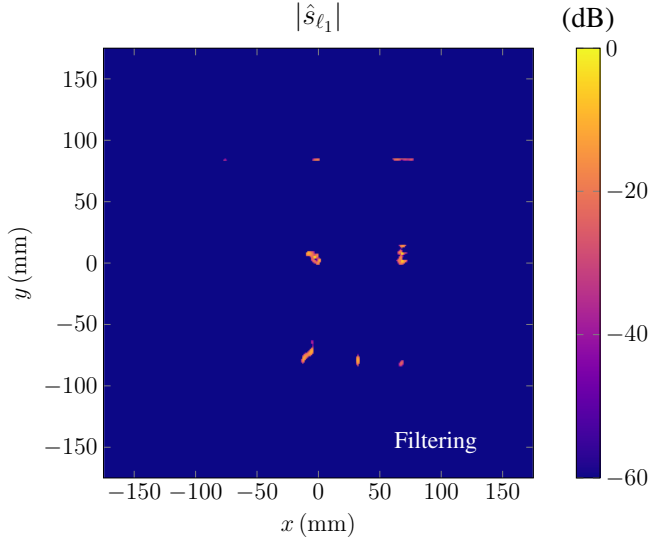
Figure 17: Normalized absolute value of the retrieved scattering amplitudes for the measured panel DUT after filtering. The image is obtained using L_1-minimization with $\kappa = 0.85$, the area of the reconstruction surface is $350\,\text{mm} \times 350\,\text{mm}$, and the dynamic range is $60\,\text{dB}$.

the filtered image is not of substantially better quality than the image using the smaller reconstruction surface shown in Figure 14. An explanation for this lies in that the edge contribution is treated as noise if not included in the reconstruction image. This noise can in turn be suppressed by choosing a larger value of the threshold scaling factor κ for the final image.

6 Conclusions

This article has presented an imaging technique based on numerical source separation – previously demonstrated in a transmission-based setting – and shown its utility in the much more intricate and complex measurement setting that is reflection-based forward scattering. The imaging technique has been demonstrated under the reasonable NDT assumption that any existing defects are few and small in physical size—equivalent to a pixel-based sparsity. Under this sparsity assumption, the numerical source separation algorithms enable a reference-free technique, i.e., only a single measurement is required to reconstruct the defects in the DUT. High resolution is achievable as defects with physical sizes on a subwavelength scale closely located can be resolved independently. The principle of separating the sources has also been demonstrated as a filtering technique for undesirable scatterers. The presented imaging technique is a fundamental stepping stone in the process of developing more generalized reflection-based EM

NDT techniques utilizing inverse scattering and the source separation principle.

Noticeably, L_1-minimization has been used jointly with a uniform measurement grid as a means to realize the high resolution and contrast – the utilization of a reduced and sparse data set (possibly incorporating multifrequency data across the full measurement bandwidth) should be considered to reduce the overall measurement time. The extension to an inverse scattering formulation (limited here by the available numerical source code) of the reconstruction problem would also enable the retrieval of a single frequency image of the complex spatial permittivity function of the DUT. Ongoing work includes modifying the imaging system to treat single curved composite structures.

References

[1] M. A. Abou-Khousa, A. Ryley, S. Kharkovsky, R. Zoughi, D. Daniels, N. Kreitinger, G. Steffes, D. O. Thompson, and D. E. Chimenti. Comparison of X-ray, millimeter wave, shearography and through-transmission ultrasonic methods for inspection of honeycomb composites. In *AIP Conference Proceedings*, volume 894, pp. 999–1006. AIP, 2007.

[2] S. S. Ahmed, A. Schiessl, F. Gumbmann, M. Tiebout, S. Methfessel, and L.-P. Schmidt. Advanced microwave imaging. *IEEE Microw. Mag.*, **13**(6), pp. 26–43, 2012.

[3] S. A. Altair Development S.A. (Pty) Ltd Stellenbosch. FEKO, Field Computations Involving Bodies of Arbitrary Shape, Suite 7.0. https://www.feko.info/, 2014. Accessed November, 2014.

[4] J. L. A. Araque Quijano, L. Scialacqua, J. Zackrisson, L. J. Foged, M. Sabbadini, and G. Vecchi. Suppression of undesired radiated fields based on equivalent currents reconstruction from measured data. *Antennas and Wireless Propagation Letters, IEEE*, **10**, pp. 314–317, 2011.

[5] S. P. Boyd and L. Vandenberghe. *Convex Optimization*. Cambridge Univ. Pr., 2004.

[6] J. T. Case, M. T. Ghasr, and R. Zoughi. Optimum two-dimensional uniform spatial sampling for microwave SAR-based NDE imaging systems. *IEEE Trans. on Instrum. Meas.*, **60**(12), pp. 3806–3815, 2011.

[7] A. J. Devaney. Inversion formula for inverse scattering within the born approximation. *Opt. Lett.*, **7**(3), pp. 111–112, 1982.

[8] A. J. Devaney. *Mathematical foundations of imaging, tomography and wavefield inversion.* Cambridge University Press, 2012.

[9] T. F. Eibert and C. H. Schmidt. Multilevel fast multipole accelerated inverse equivalent current method employing Rao-Wilton-Glisson discretization of

electric and magnetic surface currents. *IEEE Trans. Antennas Propag.*, **57**(4), pp. 1178–1185, 2009.

[10] D. C.-L. Fong and M. Saunders. LSMR: An iterative algorithm for sparse least-squares problems. *SIAM Journal on Scientific Computing*, **33**(5), pp. 2950–2971, 2011.

[11] M. T. Ghasr, M. J. Horst, M. R. Dvorsky, and R. Zoughi. Wideband microwave camera for real-time 3-D imaging. *jou-ieee-transap*, **65**(1), pp. 258–268, 2017.

[12] M. T. Ghasr, S. Kharkovsky, R. Bohnert, B. Hirst, and R. Zoughi. 30 GHz linear high-resolution and rapid millimeter wave imaging system for NDE. *IEEE Trans. Antennas Propag.*, **61**(9), pp. 4733–4740, 2013.

[13] G. H. Golub and C. F. van Loan. *Matrix Computations*. The Johns Hopkins University Press, Baltimore, MD, 1983.

[14] L. Guo and A. M. Abbosh. Microwave imaging of nonsparse domains using born iterative method with wavelet transform and block sparse bayesian learning. *jou-ieee-transap*, **63**(11), pp. 4877–4888, 2015.

[15] M. Gustafsson, M. Sebesta, B. Bengtsson, S.-G. Pettersson, P. Egelberg, and T. Lenart. High resolution digital transmission microscopy—a Fourier holography approach. *Optics and Lasers in Engineering*, **41**(3), pp. 553–563, 2004.

[16] J. E. Hansen, editor. *Spherical Near-Field Antenna Measurements*. Number 26 in IEE electromagnetic waves series. Peter Peregrinus Ltd., Stevenage, UK, 1988.

[17] P. C. Hansen. *Discrete Inverse Problems: Insight and Algorithms*, volume 7. Society for Industrial & Applied Mathematics, 2010.

[18] J. Helander, A. Ericsson, M. Gustafsson, T. Martin, D. Sjöberg, and C. Larsson. Compressive sensing techniques for mm-wave nondestructive testing of composite panels. *IEEE Trans. Antennas Propag.*, **65**(10), pp. 5523–5531, 2017.

[19] N. Joachimowicz, C. Pichot, and J. Hugonin. Inverse scattering: an iterative numerical method for electromagnetic imaging. *jou-ieee-transap*, **39**(12), pp. 1742–1753, 1991.

[20] D. Kerns. Correction of near-field antenna measurements made with an arbitrary but known measuring antenna. *Electron. Lett.*, **6**(11), pp. 346–347, 1970.

[21] S. Kharkovsky, J. T. Case, M. A. Abou-Khousa, R. Zoughi, and F. L. Hepburn. Millimeter-wave detection of localized anomalies in the space shuttle external fuel tank insulating foam. *IEEE Trans. Instrum. Meas.*, **55**(4), pp. 1250–1257, 2006.

[22] S. Kharkovsky and R. Zoughi. Microwave and millimeter wave nondestructive testing and evaluation - overview and recent advances. *IEEE Instrum. Meas. Mag.*, **10**(2), pp. 26–38, 2007.

[23] G. Kristensson. *Scattering of Electromagnetic Waves by Obstacles.* SciTech Publishing, an imprint of the IET, Edison, NJ, 2016.

[24] J. Laviada, M. T. Ghasr, M. López-Portugués, F. Las-Heras, and R. Zoughi. Real-time multiview sar imaging using a portable microwave camera with arbitrary movement. *jou-ieee-transap*, **66**(12), pp. 7305–7314, 2018.

[25] A. Massa, P. Rocca, and G. Oliveri. Compressive sensing in electromagnetics – a review. *IEEE Antennas Propag. Mag.*, **57**(1), pp. 224–238, 2015.

[26] G. Oliveri, M. Salucci, N. Anselmi, and A. Massa. Compressive sensing as applied to inverse problems for imaging: Theory, applications, current trends, and open challenges. *IEEE Antennas Propag. Mag.*, **59**(5), pp. 34–46, 2017.

[27] K. Persson and M. Gustafsson. Reconstruction of equivalent currents using a near-field data transformation – with radome applications. *Prog. Electromagn. Res.*, **54**, pp. 179–198, 2005.

[28] P. J. Shull. *Nondestructive Evaluation: Theory, Techniques, and Applications.* New York: Marcel Dekker, 2002.

[29] Tencate film adhesives. Available at: http://www.tencate.com, accessed 2017-05-20.

[30] E. van den Berg and M. P. Friedlander. SPGL1: A solver for large-scale sparse reconstruction, 2007. Available at: http://www.cs.ubc.ca/labs/scl/spgl1, accessed 2017-06-10.

[31] A. D. Yaghjian. An overview of near-field antenna measurements. *IEEE Trans. Antennas Propag.*, **34**(1), pp. 30–45, January 1986.

[32] X. Yang, Y. R. Zheng, M. T. Ghasr, and K. M. Donnell. Microwave imaging from sparse measurements for near-field synthetic aperture radar. *IEEE Trans on Instrum. Meas.*, **66**(10), pp. 2680–2692, 2017.

[33] M. Zibulevsky and M. Elad. L1-L2 optimization in signal and image processing. *IEEE Signal Processing Magazine*, **27**(3), pp. 76–88, 2010.

[34] R. Zoughi. *Microwave Non-Destructive Testing and Evaluation Principles*, volume 4. Springer Science & Business Media, 2000.

A Near-Field Measurement and Calibration Technique: Radio-Frequency Electromagnetic Field Exposure Assessment of Millimeter-Wave 5G Devices

Johan Lundgren, Jakob Helander, Mats Gustafsson, Daniel Sjöberg, Bo Xu, and Davide Colombi

Paper V

Abstract

Accurate and efficient measurement techniques are needed for exposure assessment of 5G portable devices—which are expected to utilize frequencies beyond 6 GHz—with respect to the radio frequency electromagnetic field exposure limits. Above 6 GHz, these limits are expressed in terms of the incident power density, thus requiring that the electromagnetic fields need to be evaluated with high precision in close vicinity to the device under test (DUT), i.e., in the near-field region of the radiating antenna. This work presents a cutting-edge near-field measurement technique suited for these needs. The technique—based on source reconstruction on a predefined surface representing the radiating aperture of the antenna—requires two sets of measurements; one of the DUT, and one of a small aperture. This second measurement functions as a calibration of both the measurement probe impact on the received signal, and the experimental setup in terms of the relative distance between the probe and the DUT. Results are presented for a 28 GHz and a 60 GHz antenna array; both developed for 5G applications. The computed power density is compared with simulations at evaluation planes residing as close as one fifth of a wavelength ($\lambda/5$) away from the DUT.

1 Introduction

Mobile communication systems play a large role in today's interconnected world and the amount of mobile data traffic is constantly increasing. Between the fall of 2016 and 2017, the total data traffic in mobile networks increased by 65 % [14]. The next generation of wireless access systems (5G) plays an integral role for handling the future demands on traffic capacity; and to support the increasing data rates, a plausible solution has emerged that involves exploiting the larger bandwidths (which directly translates to a capacity increase) available at frequencies above 6 GHz. Moreover, 5G systems are expected to operate within several bands comprising frequencies below 6 GHz—where the conventional bands in use today lie—up to over 100 GHz [8]. Full system trials of 5G are ongoing and commercial networks are being rolled out. Much focus is given to the frequencies between 6 and 60 GHz and a substantial amount of research is devoted to the development of mobile devices operating in this frequency range.

Several different techniques for compliance measurements exist [1]. Depending on the frequency of interest combined with the proximity of the Device Under Test (DUT), different regions of the electromagnetic field (EMF) dominate [25]. For frequencies below 6 GHz, the EMF compliance is assessed using specific absorption rate (SAR) and for frequencies above 6 GHz power density is utilized [15]—with limits for localized exposure generally taken as an average over a predefined area, *e.g.*, $4\,\mathrm{cm}^2$ [9]. An overview of radio frequency (RF) EMF compliance assessment procedures and measurement techniques applicable above 6 GHz for incident power density is provided in IEC TR 63170 [16].

One well-established measurement technique is based on amplitude measure-

ment of the electric field components [22]. The method makes use of a miniaturized diode-loaded probe (see *e.g.*, Schmid and Partner Engineering AG [24]) to scan the field at sub-wavelength distances ($< \lambda$) from the device. An estimate of the phase, which cannot be directly measured by means of such probes, is obtained by using a plane-to-plane reconstruction algorithm. This requires the amplitude of the field to be scanned on two parallel planes at different distances from the source. The power density is then reconstructed by estimating the phase based on the measured amplitude of the electric field only. In addition, the field polarization ellipse is determined by rotating the probe at different angles. Although the robustness of such algorithms has been carefully validated numerically and experimentally [22], phase retrieval represents a source of uncertainty which cannot be left out and that might vary depending on the distance from the closest scan plane to the DUT. Since retrieving the phase also requires the same scan of the electric field to be repeated on two parallel planes—in addition to rotating the probe at different angles for each measurement point—the measurement time might become exceedingly long. Other conventional measurement techniques that retrieve both amplitude and phase with non-ideal probes are problematic since even with probe calibration, the precise point in space that the measurement corresponds to is not well-defined. This leads to an error in positioning and consequently phase, thereby making it a difficult task to evaluate the power density at very close ranges to the DUT.

This work presents a measurement technique—based on amplitude and phase retrieval—for obtaining the power density at a given surface situated some arbitrary distance away from a DUT, using a reference measurement of a small aperture. Throughout this work, the term power density indicates the time-averaged, incident power density in a single spatial point at a single frequency. The technique is adapted here on antennas operating at the millimeter wave (mm-wave) frequencies 28 GHz and 60 GHz, and is based on two sets of measurements; one of the DUT, and one of a small aperture necessary to calibrate the complete measurement setup. The calibration measurement needs only to be conducted once and may be utilized for multiple DUTs, presuming the setup is not subject to substantial drifting over the complete measurement time frame. Fig. 1 shows the measurement procedure and setup; the calibration aperture is shown in Fig. 1a, and an example DUT is shown in Figs. 1c and 1d. With the measurement data retrieved and the calibration performed, numerical integral equation solvers are used to reconstruct equivalent currents on a predefined surface representing the DUT, and subsequently to compute the power density at any plane of interest. Three different DUTs were measured and compared with simulations.

The innovative calibration approach using the small aperture measurement has the substantial benefit of not only correcting for the receiving probe's impact on the measured signal, but also of handling the spatial alignment of the DUT relative to the scan plane. This second feature is essential when conducting RF EMF exposure tests at said frequencies, since the power density must be reconstructed in planes residing in the near-field region of the DUT. In accordance with the field's radial dependence in this region, a distance offset of *e.g.,* 1 mm
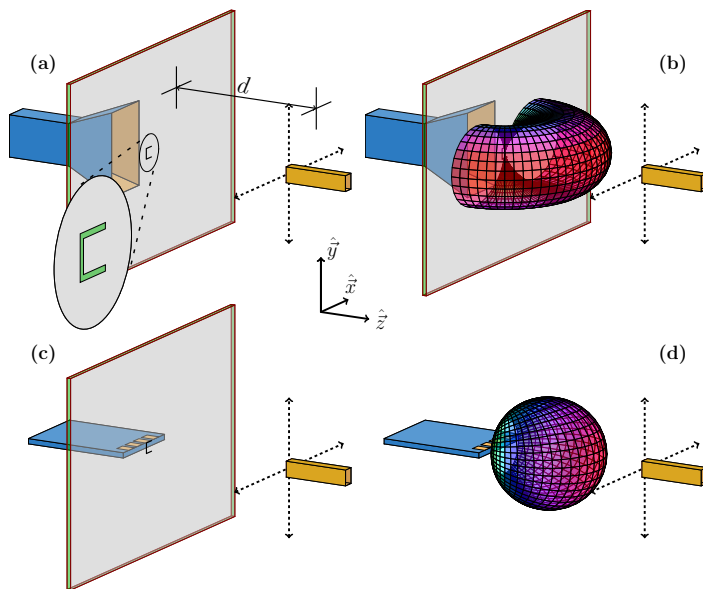
Figure 1: Schematic of the measurement procedure. **a**: A receiving probe is situated in the center of a planar measurement surface, a distance d away from a small aperture in a finite metallic plane. A transmitting antenna is positioned on the other side of the metallic plane. A high gain broadside antenna is preferable to ensure sufficient power flow through the aperture, although in theory nothing prohibits the usage of the DUT itself. **b**: The transmitting antenna excites the aperture which then radiates as a dipole. The reference measurement is conducted by sampling the fields in a discretized grid across the measurement surface using the receiving probe. **c**: The transmitting antenna is removed, and the DUT is aligned with respect to the previous position of the aperture. **d**: A second measurement is conducted on the DUT, and the field is sampled in the same grid as before.

(corresponding to $\lambda/5$ at $60\,\mathrm{GHz}$) would result in a substantial change in both the amplitude and phase of the reconstructed radiated electromagnetic fields. The small aperture calibration measurement suppresses this margin of error as the setup is calibrated to the specific distance.

The paper is organized as follows. The next section presents results from two measurement campaigns conducted at $28\,\mathrm{GHz}$ and $60\,\mathrm{GHz}$ of two antenna arrays developed for 5G applications, and a benchmark case of a $60\,\mathrm{GHz}$ standard gain horn antenna. Thereafter details regarding theory, measurement technique and post processing steps of the data are given. Then, a discussion of the results are presented, followed by conclusions, and, finally, information detailing the simulation settings and the measurement setup.

(a)

(b)   **(c)**
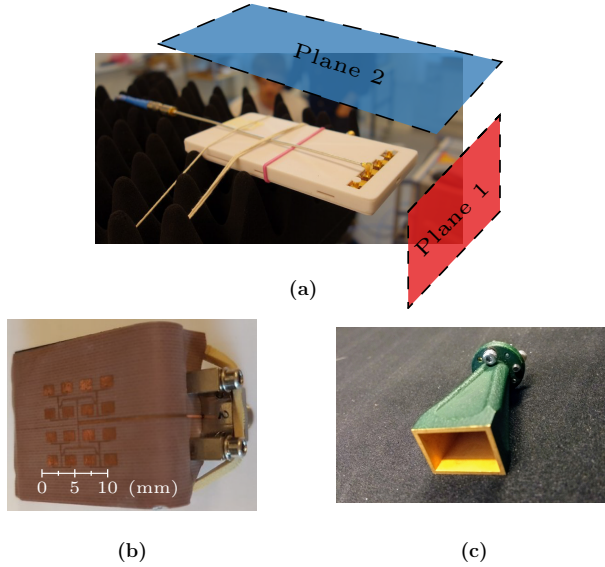
Figure 2: The DUTs used in this work. **a**: A mobile phone mockup from Sony Mobile operating at $28\,\mathrm{GHz}$. **b**: A single feed $60\,\mathrm{GHz}$ linearly polarized patch array. **c**: A Flann $25240 - 20$ standard gain horn operating at $60\,\mathrm{GHz}$.

2   Results

Three different DUTs, shown in Figs. 2a–c, had their power density reconstructed from measurements of the near field using a single polarized, linearly polarized, probe. The DUT in Fig. 2a is a mobile phone mockup, capable of operating in the frequency region of $25 - 29\,\mathrm{GHz}$, with four independently fed antennas. In this work we consider the operational frequency of $28\,\mathrm{GHz}$. The cross polarization is low and the radiating elements are covered by a plastic chassis. A detailed description of the antenna array design can be found in [13]. A device of similar design was used for the development of the use cases described in IEC TR 63170 [16]. Two reconstruction planes were defined for this DUT, labeled plane 1 and 2, respectively, as shown in Fig. 2a. The second DUT is a linearly polarized $60\,\mathrm{GHz}$ patch array fed with a single transmission line with $3.3\,\%$ bandwidth [4], shown in Fig. 2b. It is mounted on a custom 3D printed stand with the transmission line bent over a rounded edge to reduce any unwanted radiation from the connector. The third DUT, shown in Fig. 2c, is a Flann $25240 - 20$ linearly polarized standard gain horn antenna operating between $49.9 - 75.8\,\mathrm{GHz}$ [10]. This DUT was measured at $60\,\mathrm{GHz}$ and selected as a benchmarking case due to its well-known radiation characteristics with high radiation efficiency, ease of modeling in commercial simulation software programs, and its high directivity, from which errors related to the measurement plane being finite are suppressed.

Table 1:   The relative difference between the measurement data set, x and the simulation data set, y for maximum spatial peak power density (numbers in parenthesis) and maximum spatially averaged power density. The averaging was carried out over a circular area of $4\,\text{cm}^2$, and each data set has been individually normalized to the same relative output power. The rows correspond to different data sets and the columns to different reconstruction distances.

	Relative difference of the maximum spatially averaged/(peak) power density $:= |x-y|/y$		
	1 mm	5 mm	10 mm	20mm
60 GHz Horn(meas.)	<1 (<1) %	2 (7) %	<1 (2) %	-
60 GHz Horn(synt.)	<1 (2) %	<1 (7) %	2 (7) %	-
60 GHz Patch	1 (39) %	<1 (15) %	3 (2) %	-
28 GHz Plane 1	-	10 (8) %	11 (12) %	15 (21) %
28 GHz Plane 2	-	34 (67) %	33 (50) %	28 (23) %

2.1   Measured Results

The mockup shown in Fig. 2a was measured by scanning a probe in a plane, parallel to the closest surface of the DUT, distanced $d = 60\,\text{mm}$ away, see Fig. 1. The power density was then reconstructed in planar surfaces distanced 5 mm, 10 mm and 20 mm away from the DUT, corresponding to the distances used in a the IEC TR 63170 28 GHz case study [16]. The mockup was simulated with the multilevel fast multipole method (MLFMM) using the electromagnetic simulation (EM) tool FEKO [2]. Due to the similarity of the results for the different port excitations, the results shown in Fig. 3 are limited to the excitation of the left uttermost port. Figs. 3a and 3b depict the comparison between measured and simulated results for plane 1 and 2, respectively, with no spatial averaging and on a 40 dB dynamic range. The simulated power densities are seen in the top of the figure and the power densities from reconstructing the fields from measured data is seen in the bottom of the figure.

The 60 GHz patch array antenna, Fig. 2b, was measured by a probe in a plane at a distance of 25 mm. The power density was calculated for the distances 1 mm, 5 mm and 10 mm. The antenna was simulated using the EM simulation tool CST. Similar to Fig. 3, a comparison between measured and simulated power density is shown in Fig. 4.

As a verification of the technique presented in this paper a standard gain horn, shown in Fig. 2c, was measured at 60 GHz. The field was measured in a plane distanced 50 mm from the DUT. The normalized power density in the reconstruction planes distanced 1 mm, 5 mm, and 10 mm from the aperture of the standard gain horn is shown in Fig. 5. Results are shown for three different cases: 1) the direct full-wave simulation of the DUT in FEKO, 2) synthetic data, where simulated data was used as input (at the 50 mm distance) to the reconstruction
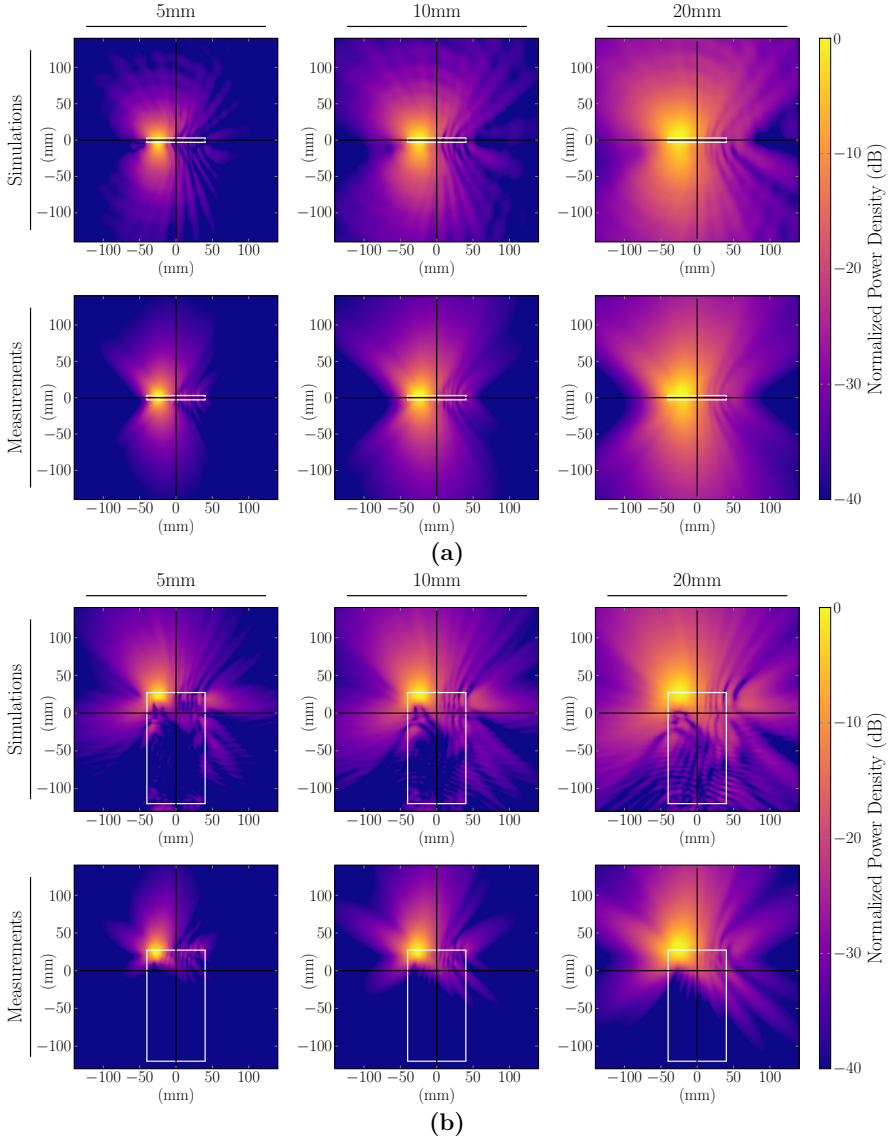
Figure 3: Normalized power density at 28 GHz in the reconstruction planes distanced 5 mm, 10 mm, and 20 mm (left to right) for the Sony Mobile phone mockup. Plane 1 is depicted in **a**, and plane 2 in **b**. The rows depict: full-wave simulations of the DUT in FEKO (top), and the results of the measurement data as input to the reconstruction technique (bottom). The white lines depict the outline of the DUT, and the black crosshair marks the mutual origin. The dynamic range of all plots is 40 dB.
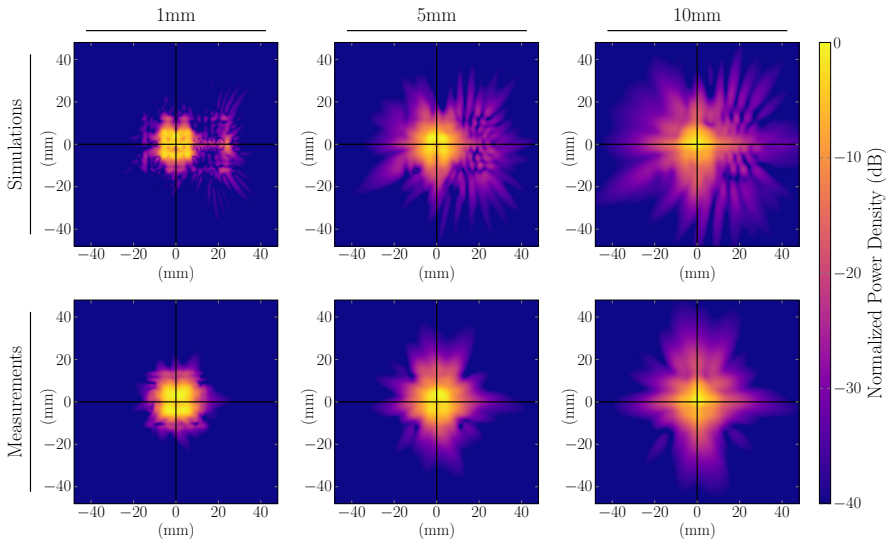
Figure 4: Normalized power density at $60\,\mathrm{GHz}$ in the reconstruction planes distanced $1\,\mathrm{mm}$, $5\,\mathrm{mm}$, and $10\,\mathrm{mm}$ (left to right) from the aperture of the patch array antenna. The rows depict: full-wave simulations of the DUT in CST (top), and the results of the measurement data as input to the reconstruction technique (bottom). The black crosshair marks the mutual origin. The dynamic range of all plots is $40\,\mathrm{dB}$.

routine, and 3) using measurement data as input to the reconstruction routine. Since the standard gain horn is a custom supplied antenna [10], it provides a benchmark case where all system losses and gains can be accounted for.

The maximum spatial peak incident power density was computed for the horn measurement, and at the plane distanced $10\,\mathrm{mm}$ away this value was $0.655\,\mathrm{W/m^2}$, $0.621\,\mathrm{W/m^2}$ and $0.656\,\mathrm{W/m^2}$ for the measurement data, synthetic data and simulation, respectively. A comparison of the maximum spatial peak power density for the three DUTs is presented as the numbers in parenthesis in Table 1. The results for all measured DUTs are compared to the respective simulations in terms of the relative difference between the simulated maximum peak power density to the maximal value reconstructed from measurements. This table presents relative values and each reconstruction plane is normalized such that each power density value in a specific plane is divided by the total power density in that specific reconstructed/simulated plane, yielding a normalized power density of 1 in each plane [20, Appendix F].

The results presented in Fig. 3-5 all show the power density, unaveraged. However, the power density averaged over a certain area is also of interest [9] and a comparison between the reconstructed fields and simulations in terms of spatially averaged power density is also seen in Table 1, numbers without parenthesis. The averaging area utilized was a circular area of $4\,\mathrm{cm^2}$ and other averaging areas are

available in [20, Appendix A].

2.2   Theory and Measurement Technique

A DUT in this work is a well functioning antenna, of arbitrary shape, radiating detectable power levels in a certain frequency interval in which the measurement is to be conducted. As disclosed in Fig. 1d, a radiating DUT is fixed at a certain position in space, and the emitted field is sampled on a surface some distance away from this DUT. It is well known that information regarding the field at other surfaces can be obtained from this measurement, and different techniques to realize this exist [3, 7, 21]. However, many of these rely on the use of well-defined measurement antennas (probes) and do not provide absolute positioning of the scanned plane in relation to the DUT, which is a necessity for accurately reconstructing the power density. This requirement on an absolute position between the DUT and the scan/measurement plane, originates from the goal to estimate the power density at sub-wavelength distances from the DUT. Any position error directly translates to large errors of the estimated power density since the electromagnetic fields have a strong radial dependence in close vicinity of the DUT.

In this work, we use a calibration method relying on a reference measurement of a small aperture in order to obtain accurate reconstruction of the radiated power density from a measured DUT. In essence, this is achieved by reconstructing the equivalent currents on a surface representing the radiating part of the DUT and thereafter calculating the corresponding radiated fields in the evaluation planes of interest using computational codes based on the Method of Moments (MoM), *i.e.*, numerical integral equation solvers. In summary, the technique is explained by the following steps:

1. Processing of raw measurement data.

2. Calibration, using measurement data of the small aperture, to remove the effects that the receiving probe has on the retrieved data, and to obtain a well-defined spatial position.

3. Reconstruction of equivalent currents on the surface of the DUT.

4. Computation of the electric and magnetic fields at a surface of interest from the reconstructed equivalent currents.

5. Calculation of the incident power density from the field in the previous step.

The rest of this section will focus on discussing these steps in more detail.

2.2.1   Measurement Data Processing

There is no inherent restriction on the shape of the measurement and reconstruction surfaces, nor of the DUT. However, the DUTs presented in this work consist
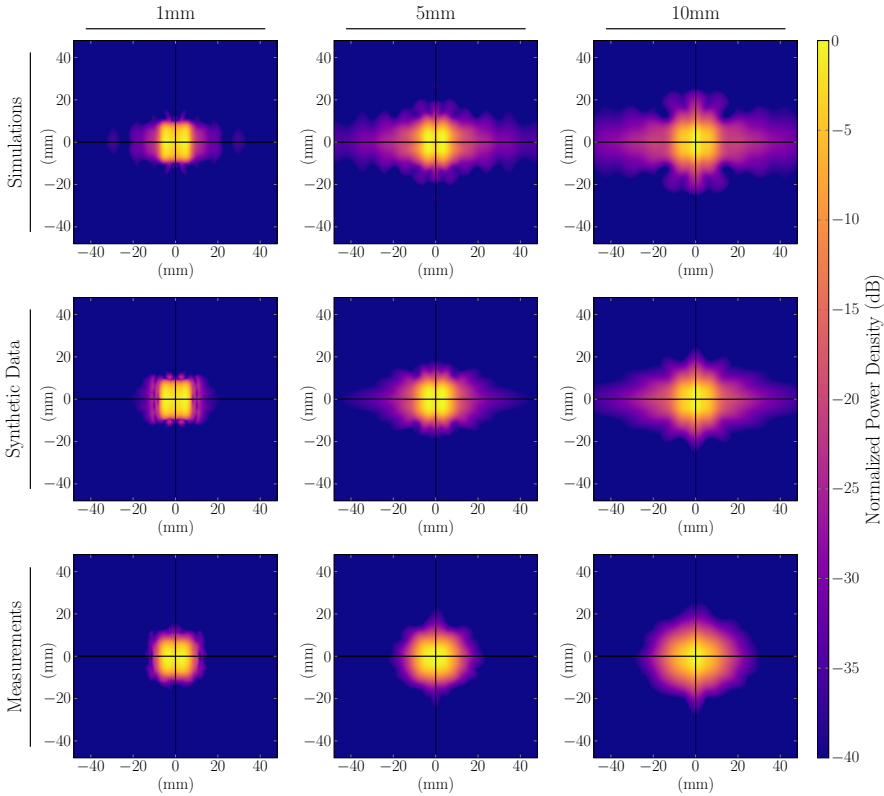
Figure 5: Normalized power density at 60 GHz in the reconstruction planes distanced 1 mm, 5 mm, and 10 mm (left to right) from the aperture of the standard gain horn. The rows depict: full-wave simulations of the DUT in FEKO (top), synthetic data where simulated data as an input to the reconstruction technique (center), and the results of the measurement data as input to the reconstruction technique (bottom). The black crosshair marks the mutual origin and the dynamic range of all plots is 40 dB.

of radiating elements confined to a plane and a standard gain horn. Furthermore, only planar surfaces parallel to that of the radiating DUT are considered throughout this work, since this constitute an appropriate setting for the purpose of EMF exposure assessment. The first measured plane is that of the aperture as disclosed in Figs. 1a and 1b. The aperture is then removed, and the DUT—aligned with respect to the previous position of the aperture—is measured in the same plane as the aperture was measured, see Figs. 1c and 1d. Samples of the transmitted signal are taken in discrete sampling points over the entire scan plane. The sampled data are extracted in order to retrieve the necessary field information in the following steps. The response is measured for several discrete frequency points in a given range $f_0 \pm \Delta f_0$. The frequency bandwidth, $2\Delta f_0$, enables the use of time gating procedures to suppress interactions with far away objects, and is specified as to realize a certain resolution of the signal in time domain [23]. Throughout this work Δf_0 was set to 2 GHz and 1 GHz for the 28 GHz and 60 GHz measurements, respectively. This provided more than adequate information to enable time gating procedures. Effects relating to choice of measurement bandwidth and frequency sampling can be further viewed in [20, Appendix D].

2.2.2 Probe Correction Using an Electrically Small Aperture

Any given physical probe has a finite size and a non-local interaction with the electromagnetic field in its immediate surrounding. The probe is connected to a Vector Network Analyzer (VNA) and the registered value in the receiving device is a complex-valued voltage signal accounting for the full probe interaction, rather than the complex-valued field in that particular discrete point of the finite aperture. This effect can be atoned for using probe correction techniques, of which there are several presented in classic literature [27]. These techniques calibrate for the interaction of the probe with the drawback of not having precise information on the position of that particular measurement point. Knowledge of the exact positioning of the system is vital, as the phase information is severely affected. Since the power density is computed from the electric and magnetic fields, a large uncertainty in the retrieved phase of the fields has a severe negative impact on the end result. In this work, a small aperture is measured as a reference measurement, see Fig. 1b, which allows for calibration of the probe and fixating the calibration to a well known physical position; that of the aperture. In turn, the position of the aperture acts as an alignment position once the DUT is inserted (Figs. 1c and 1d). This technique removes the need of delicate information regarding the probe and places that requirement on the aperture. As opposed to the probe, the aperture has a well-defined position from which the fields originate. This translates into obtaining measurements with a position put in relation to this well-defined point, removing the large uncertainty and phase error one would have obtained through traditional means of probe calibration.

Consider a small (compared to the wavelength of interest) aperture in a metal screen, see Fig. 1a. The aperture is designed preferably resonant to increase

power flow through the aperture, although it is not required. Since the aperture is electrically small, its radiation characteristics is well-defined and of the first order; corresponding to that of a magnetic dipole [26]. It has a simple geometry that is easily modeled using numerical methods such as the MoM. The fields from this aperture at the measurement surface can be evaluated numerically utilizing any standard computational EM technique. These computed fields are then compared to the measured signal to calibrate the setup. The calibration can be performed in many different ways including: determining the scattering matrix [11] of the measurement probe, using the reference measurement as the system Green function directly in the reconstruction algorithm, or as a simple point-wise division correcting the amplitude and phase of the measured signals. In this work, the latter was used and explained by considering the measured signals as an estimate of the co-polarized field value in the center of the probe.

In each discrete point, a correction term is obtained by normalizing the MoM simulation of the co-polarized component of the field from the aperture with the measurement of the aperture. These correction terms are then applied to the data of the measured DUT, and a probe corrected field with absolute positioning calibrated to the mathematical model used in the reconstruction algorithm is obtained. In this work only single polarized measurements were conducted; however, both polarizations can be incorporated by conducting a second set of measurements with a different orientation, *e.g.* a 90° rotation, of the probe [18].

The probe used for the 60 GHz measurements was an RFspin OEWG WR15, and a similar open-ended waveguide probe was used for the 28 GHz measurement.

2.2.3   Reconstruction of Equivalent Currents

The reconstruction of the sources is performed by expressing the solutions to Maxwell's equations using the electric field integral representation given by [12, 19]:

$$
\boldsymbol{E}(\boldsymbol{r}) = \mathrm{j}k\eta_0 \int_S \boldsymbol{J}(\boldsymbol{r}')G(\boldsymbol{r}-\boldsymbol{r}') + \frac{1}{k^2}\nabla G(\boldsymbol{r}-\boldsymbol{r}')\nabla'\cdot\boldsymbol{J}(\boldsymbol{r}')
$$
$$
+ \boldsymbol{M}(\boldsymbol{r}')\times\nabla G(\boldsymbol{r}-\boldsymbol{r}')\,\mathrm{d}S', \quad (2.1)
$$

where η_0 is the intrinsic impedance of free space, k is the free space wave number, G is the free space Green function, $\boldsymbol{J}$ and $\boldsymbol{M}$ are the electric and magnetic equivalent currents respectively that are positioned at $\boldsymbol{r}'$, S is the reconstruction surface and $\boldsymbol{r}$ is the position vector belonging to the measurement surface. $\boldsymbol{J}$ is needed if the problem is a half-space and $\boldsymbol{J}$ and $\boldsymbol{M}$ are needed for arbitrary geometries on the surface of the DUT. The computation of $\boldsymbol{J}$ given $\boldsymbol{E}$ is a type of problem arising in many scientific fields namely an inverse source problem [6], and it is mathematically ill-posed [11].

Numerically, the problem is addressed by defining an area representing the radiating aperture of the DUT. This area is discretized and (2.1) is reshaped into

a matrix equation, using a suitable discretization method [5] as,

$$\boldsymbol{E} = \mathbf{N}^{\mathrm{e}}\boldsymbol{J} + \mathbf{N}^{\mathrm{m}}\boldsymbol{M}, \tag{2.2}$$

where $\boldsymbol{E}$ contains the measured component of the electric field in all spatial sampling points, $\boldsymbol{J}$ contains the spatially discretized currents on the reconstruction surface and the matrix operators $\mathbf{N}^{\mathrm{e}}$ and $\mathbf{N}^{\mathrm{m}}$ describe the mapping from $\boldsymbol{J}$ and $\boldsymbol{M}$ to $\boldsymbol{E}$ for two surfaces, thus it will differ depending on the chosen plane. For the rest of this work, we consider half-space geometries and use the field equivalence principle [26] to reduce the problem to only electric currents $\boldsymbol{J}$ ($\boldsymbol{M}$ and $\mathbf{N}^{\mathrm{m}}$ in equation (2.2) are not present). As stated previously in Sec. 2.2.1, there is no requirement of planar measurement and reconstruction surfaces. However, utilization of such surfaces yields a decrease in computational time as very efficient numerical methods can be employed. The solution of (2.2) is ill-conditioned and a regularization procedure is required. A multitude of techniques exist to treat the regularization of such problems [11, 12] and we employ the truncated Singular Value Decomposition (SVD) method [11] and truncating when the singular values are lower than $0.1\sigma_{\mathrm{max}}$, where σ_{max} is the maximal singular value. This value was chosen for all presented data and further investigation of the singular values and choice of truncation is viewable in the preprint [20, Appendix C]. The input data to equation (2.2) is the probe corrected measured field from the DUT and the output data are the equivalent currents on a predefined plane, in this case, the plane where the DUT is situated.

2.2.4   Fields from Equivalent Currents

With the equivalent currents reconstructed, equation (2.2) is executed to retrieve the electric field originating from these currents in any arbitrary evaluation surface after defining the appropriate matrix operator $\mathbf{N}^{\mathrm{e}}$ that describes the electric field integral representation for the new observation points. Similarly, the magnetic field is retrieved using the corresponding matrix form of the magnetic field integral representation.

2.2.5   Power Density Computation

The power density in a spatial reconstruction point $\boldsymbol{r}$ is given by

$$S_n(\boldsymbol{r}) = \frac{1}{2}\mathrm{Re}\{\boldsymbol{E}(\boldsymbol{r}) \times \boldsymbol{H}^*(\boldsymbol{r})\} \cdot \hat{\boldsymbol{n}}, \tag{2.3}$$

where the real part is denoted $\mathrm{Re}\{\}$, $\boldsymbol{E}$ and $\boldsymbol{H}^*$ denote the electric field and the complex-conjugate of the magnetic field, respectively, $\times$ denotes the cross product, and $\hat{\boldsymbol{n}}$ denotes the unit vector normal to the evaluation surface. The power density is obtained once the full near-field measurement technique—including the previously mentioned processing steps—has been applied, and the measurement setup has been calibrated with respect to the total radiated power (presuming

all system gains and losses have been accounted for). A spatial average can subsequently be acquired through a convolution between the power density profile in the full reconstruction plane and the predefined averaging area.

3   Methods

3.1   Numerical Simulations

As the connectors are electrically large objects at 28 and 60 GHz they require enormous computational resources and were thus excluded from all simulations. The 28 GHz mockup was simulated in FEKO with the multilevel fast multipole method, and the microstrip feedlines were fed by the edge ports. The metallic sheets were treated as infinitely thin. The mesh was created through the default meshing settings.

The 60 GHz single feed linearly polarized patch array was simulated in CST using the transient solver based on the finite integration technique. An extra distance of one eighth of the free space wavelength was added between the bounding box using a perfectly matched layer boundary and the simulation model. The microstrip feedline of the array was fed by a waveguide port. The minimum number of mesh lines per free-space wavelength was set to 10.

The simulation of the standard gain horn was carried out using a simplified model with infinitely thin sheets of perfect electric conductor (PEC) in FEKO with the MoM full-wave solver.

The simulation time for these DUT model to converge were between 1 min (60 GHz Horn) to 4h (28 GHz mockup) on a 64 Gb 4.2 GHz i7-7700 machine.

3.2   Measurement Setup

All measurements were conducted with the setup mounted on a Newport RS 2000 optical table and were similar in both the measurement campaigns (28 GHz and 60 GHz), only the antennas, connectors and cables were changed. The amplitude and phase of the signal were measured using a probe connected to a Rohde & Schwarz ZVA 67 GHz. A custom-made Sony rectangular waveguide probe was utilized in the 28 GHz campaign and an RFspin OEWG WR15 probe in the 60 GHz campaign. The scan plane was realized using two THORLABS LTS300/M positioners combined with aluminum breadboards. This gives a maximum scan plane area of 30 cm × 30 cm. The points in the scan plane were sampled on an 8 mm × 8 mm (4/5 λ) grid for the 28 GHz campaign and a 2 mm × 2 mm (2/5 λ) grid for the 60 GHz campaign a view of other grid sizes and their impact can be viewed in [20, Appendix D]. The positioners and the VNA were controlled using a laptop and GPIB connection. The DUT was mounted in a similar fashion and held stationary during the measurement and the distance between the DUT and probe scan plane were realized using said positioners. The alignment

of the DUT and probe was done using the positioners and several cross laser units, achieving an accuracy of $\sim 50\,\mu$m. The cables were calibrated to their respective ends using an electrical calibration unit. The aperture was centered on a $30\,\text{cm} \times 23\,\text{cm}$ metal sheet, which was mounted on a polymethyl methacrylate (PMMA) holder.

3.3 Specifications for the 28 GHz Measurements

The DUT for the measurements at $28\,\text{GHz}$, supplied by Sony Mobile, is seen in Fig. 2a where the mockup is mounted on absorbers and with one of its ports active (port 2). The mockup was secured firmly and special care was taken when changing the active port to not change the well specified position and further impact alignment. The distance between the probe scan plane and the DUT was $6\,\text{cm}$ and the scanned plane was a $28.8\,\text{cm} \times 28.8\,\text{cm}$ plane sampled on a $8\,\text{mm} \times 8\,\text{mm}$ grid. All four antennas on the DUT were measured, and for two different planes of the antenna.

The small aperture was manufactured using a laser milling machine. The aperture was illuminated using a SATIMO SGH2650 standard gain horn antenna. The distance between the aperture and the probe scan plane was $6\,\text{cm}$. The frequency band measured for both the aperture and the DUT was 26–30 GHz with 101 linearly spaced frequency points.

3.4 Specifications for the 60 GHz Measurements

The planar patch array antenna [4] used for the $60\,\text{GHz}$ measurement was fed by a single port fixated on a custom 3D printed plastic holder, see Fig. 2c. The connector and transmission line were bent over a rounded edge of the custom made mount. This was done to reduce the impact of the connector in the measurement and to have a planar surface for the equivalent currents. The distance between the probe scan plane and the DUT was $2.5\,\text{cm}$ and the scanned plane was a $10\,\text{cm} \times 10\,\text{cm}$ plane sampled on a $2\,\text{mm} \times 2\,\text{mm}$ grid.

The measurement of the Flann $25240 - 20$ standard gain horn antenna was carried out on a $10\,\text{cm} \times 10\,\text{cm}$ plane distanced $50\,\text{mm}$ away sampled on a $2\,\text{mm} \times 2\,\text{mm}$ grid.

The $60\,\text{GHz}$ aperture was manufactured on a sheet of size, $30\,\text{cm} \times 23\,\text{cm}$. The aperture was illuminated using a Flann $25240 - 20$ standard gain horn antenna. The illuminating horn antenna had a HXI HHPAV-222 power amplifier connected to it in order to get sufficient power through the aperture. The frequency band measured for both the aperture and the DUTs was $59 - 61\,\text{GHz}$ with 101 linearly spaced frequency points.

4 Discussion

For the three different DUTs presented in this work, the measured and simulated power densities can be observed in Figs. 3-5 and alternatively viewed from the difference between them in [20, Appendix B]. The difference in the maximal spatial peak power density and the difference of the maximum spatially averaged power density is presented in Table 1. In this table $4\,\mathrm{cm}^2$ was chosen as the averaging area and more areas were investigated in [20, Appendix A].

For the 28 GHz mockup the results for plane 1 are seen in, Fig. 3a, where similarities, both in positioning and in shape, regardless of evaluation distance, can be observed. Since the radiating area of the DUT—illustrated by the white lines in the figure—is narrow and stretches only a few wavelengths horizontally ($\approx 100\,\mathrm{mm} \approx 10\,\lambda$ at 28 GHz), the source surface can be discretized and evaluated numerically with high accuracy. The difference, to the corresponding simulated value, in the maximum spatial peak power density is reasonably low, 8-21 %, and for the difference in maximum spatially averaged power density that value is 10%-15%. The difference is low for close distances and increase further away as the power density as the power density experience more spatial spread in the simulations than in the reconstructed fields, Fig. 3.

For plane 2, Fig. 3b, the position of the maximum spatial peak power density is the same for both simulations and measurements. The fields resemble each other in the two upper quadrants and some differences are spotted in the bottom two. The reason for this is that only the top half part of the chassis, indicated by the white lines, is discretized and used as a source plane. If the entire chassis were to be used, substantial computational resources would be required for storing the necessary matrices and performing the matrix operations. Consequently, the current existing on the lower part of the chassis is not captured properly, and the corresponding radiated fields are not present in the reconstructed images. The maximum spatially averaged power density values are thus heavily affected due to the normalization procedure utilized creating this apparent large difference. The difference in maximum spatial peak power density is, as such, higher than that of plane 1, 23-67 %. The same is true for the difference in maximum spatially averaged power density, 17-30%. Note however that this drawback is preventable by utilizing additional computational resources.

The results for the 60 GHz patch antenna are depicted in Fig. 4. From the simulations it is observed that the transmission line, in the left part of the graphs, is apparent in the simulations but not observed to be as prominent in the measurements. The simulation model did not have the transmission line bent around a rounded edge, as was done during the measurements, which in part might explain the results. Disregarding any effect stemming from the transmission line, the same trends are observed and the symmetries are similar, as expected based on the geometry of the object. This is further seen by the fact that the difference in the maximum spatially averaged power density is very low 1-3%. However, the difference in the maximum spatial peak power density is interestingly much

larger, 2-39 %. From studying the graphs in Fig. 4 we see that the simulated data have local high intensity regions near the patches of the array. These cannot be seen as clearly in the measured data, leading to a large difference point wise, in the peak power density, but not impacting the average power density in the region.

The results for the 60 GHz standard gain horn antenna, depicted in Fig. 5, compare well with a low difference of the maximal spatial peak power density, <1-7 % and low difference of the maximum spatially averaged power density <1-2%. By comparing the simulation to the synthetic data input and the measurement data input to the synthetic data input, the sources of inaccuracies can be isolated to the reconstruction technique and the quality of the retrieved field components, respectively. The power density along the horizontal line observed in the simulated results are not observed in the measurements and only partly in the synthetic data. This difference can be explained by having a finite measurement plane not capturing all radiated power, thus not reconstructing the side lobes fully. It is implicit that by capturing a larger fraction of the radiated power, either through measuring a more directive DUT or using a larger measurement plane (ideally an enclosing surface), the accuracy of the reconstructed fields would increase. The horn was simulated as an infinitely thin PEC and most of the deviation occur close to the device and below -20 dB in which the accuracy of the model can be questioned.

In general, for the data presented in Figs. 3-5 and in Table 1, the difference in maximum spatial peak power density between measurements and simulations is around 15 %, but varies depending on the specifics of the DUT. The difference in maximum spatially averaged power densities within $4 \, \text{cm}^2$ region is around 2 % of the corresponding simulated value for the 60 GHz measurements and around 10-30 % for the 28 GHz mockup. This comparison adds confidence to the quality of the measurement technique, primarily when used to compare averaged values rather than peak values. However, the simulated results—due to the intricately manufactured designs and difficulty to model these accurately in commercial simulation software—should not be viewed as 'true' values but rather an approximate reference. For the 60 GHz horn and patch antenna the agreement in maximum power density is best at very close distances. There is a larger deviation at distances further away due to that the fields from the measurements do not spread as much as in the simulations, see Figs. 4 and 5. The same applies to the 28 GHz results. Furthermore, for the 28 GHz mockup plane 2 exhibits a larger deviation between measured and simulated maximum power density than plane 1; this is due to the fact that, for plane 2, the surface currents existing on the lower part of the chassis are not captured by the discretized source plane area.

The technique in this work has been demonstrated utilizing several devices at different frequencies and bandwidth, measured in planes 5λ to 10λ away and sampled on different grids with promising results. The measurement distance is an important design parameter and acts as a trade off between two error sources. A short distance is needed to capture as much as possible of the radiated field and hence to minimize the errors from radiation outside the measurement plane.

On the other hand, a large distance is desired to reduce errors from multiple reflections between probe and DUT (and aperture screen) [17]. The technique should be most accurate for DUTs precisely aligned with the position of the aperture during calibration. However, in the case of the 28 GHz mockup, the presented results were that of the antenna furthest away from this origin, *i.e.* 3λ off center, yet the technique does not break down and gives promising results. A more elaborate study on the relationship between the phase center location of the DUT and the aperture position, as well as the effect of the quality of the chosen probe, is a consideration for future work.

The technique is experimentally straight forward to implement and from the indirect investigations of different parameters demonstrated in this work, it is indicated that the calibration works well for a wide array of settings and that an experimental accuracy of positioning is not mandatory as it is given through the calibration where an origin is fixated to that of the aperture position. Further work include exploring the limits of this method for a selection of parameters.

Throughout this paper, the DUTs have been linearly polarized antennas with an assumed low cross polarization. A single measurement of a DUT extracts a single field component from the registered voltage signal of the probe. Any field that is reconstructed via the technique described in this paper will thus be reliant on the information contained in a single measurement. However, two polarizations may be incorporated by conducting an additional measurement of the DUT with a modified orientation of the receiving probe and adding another polarization in the MoM code. Adding additional probes leads to a drastic improvement in measurement time as a scan currently takes between 40 min to 2 hours. Scanning with multiple probes or an array is interesting for future work as the technique should function without modification to the numerical implementation.

5   Conclusion

In this work, a measurement technique for RF EMF assessments of mm-wave 5G communication devices has been presented. The technique combines the well-known method of source reconstruction on a predefined surface representing the radiating aperture of an antenna, with an innovational calibration approach that utilizes a small aperture to calibrate both the measurement probe impact on the received signal, and the experimental setup in terms of the relative distance between the probe and the DUT. The accuracy in positioning obtained through anchoring the measurement setup to the position of the small aperture enables accurate reconstruction of the power density mere fractions of a wavelengths away from the DUT.

The measurement technique has been demonstrated on two mm-wave DUTs—specifically developed for 5G applications—operating at 28 GHz and 60 GHz respectively, and a standard gain horn as a benchmark case. The relative difference of the maximum peak power density between measurements and simulations is

around 15%, and 2% for the maximum spatial average power density.

This work provides initial findings of a new measurement technique with interesting details to investigate further in future work.

6   Acknowledgments

References

[1] L. Alon, S. Gabriel, G. Y. Cho, R. Brown, and C. M. Deniz. Prospects for millimeter-wave compliance measurement technologies [measurements corner]. *IEEE Antennas Propag. Mag.*, **59**(2), pp. 115–125, 2017.

[2] S. A. Altair Development S.A. (Pty) Ltd Stellenbosch. FEKO, Field Computations Involving Bodies of Arbitrary Shape, Suite 7.0. https://www.feko.info/, 2014. Accessed November, 2014.

[3] Y. Alvarez, F. Las-Heras, and M. R. Pino. Reconstruction of equivalent currents distribution over arbitrary three-dimensional surfaces based on integral equation algorithms. *IEEE Trans. Antennas Propag.*, **55**(12), pp. 3460–3468, 2007.

[4] A. Bondarik and D. Sjöberg. 60 GHz microstrip antenna array on PTFE substrate. In *Antennas and Propagation (EUCAP), 2012 6th European Conference on*, pp. 1016–1018. IEEE, 2012.

[5] W. C. Chew, M. S. Tong, and B. Hu. *Integral Equation Methods for Electromagnetic and Elastic Waves*, volume 12. Morgan & Claypool, 2008.

[6] A. J. Devaney. *Mathematical foundations of imaging, tomography and wavefield inversion*. Cambridge University Press, 2012.

[7] T. F. Eibert and C. H. Schmidt. Multilevel fast multipole accelerated inverse equivalent current method employing Rao-Wilton-Glisson discretization of electric and magnetic surface currents. *IEEE Trans. Antennas Propag.*, **57**(4), pp. 1178–1185, 2009.

[8] Ericsson. 5G radio access. Technical report, Ericsson white paper, Ericsson AB, Stockholm, Sweden, 2016.

[9] FCC. RF exposure: Order/NPRM issues. Technical Analysis Branch, Office of Engineering and Technology, 2018. https://transition.fcc.gov/oet/ea/presentations/files/oct18/5.1-TCB-RF-Exposure-OrderNPRM-Issues-MD.pdf, Retrieved January, 2019.

[10] Flann Microwave. *Standard Gain Horns Series 240*. Flann Microwave Ltd, 2018.

[11] P. C. Hansen. *Discrete Inverse Problems: Insight and Algorithms*, volume 7. Society for Industrial & Applied Mathematics, 2010.

[12] J. Helander, A. Ericsson, M. Gustafsson, T. Martin, D. Sjöberg, and C. Larsson. Compressive sensing techniques for mm-wave nondestructive testing of composite panels. *IEEE Trans. Antennas Propag.*, **65**(10), pp. 5523–5531, 2017.

[13] J. Helander and Z. Ying. Stripline coupled antenna with periodic slots for wireless electronic devices. U. S. Patent, no. 10,103,440, 2018.

[14] N. Heuveldop et al. Ericsson mobility report. Technical Report EAB-17 5964, Technol. Emerg. Bus., Ericsson AB, Stockholm, Sweden, 2017.

[15] ICNIRP. Guidelines for limiting exposure to time-varying electric, magnetic, and electromagnetic fields (up to 300 GHz). *Health phys*, **74**(4), pp. 494–522, 1998.

[16] IEC. IEC TR 63170 ED1: measurement procedure for the evaluation of power density related to human exposure to radio frequency fields from wireless communication devices operating between 6 GHz and 100 GHz, tech. rep., international electrotechnical commission,. Technical report, 2018.

[17] IEEE recommended practice for near-field antenna measurements. *IEEE Std 1720-2012*, pp. 1–102, 2012.

[18] D. Kerns. Correction of near-field antenna measurements made with an arbitrary but known measuring antenna. *Electron. Lett.*, **6**(11), pp. 346–347, 1970.

[19] G. Kristensson. *Scattering of Electromagnetic Waves by Obstacles*. SciTech Publishing, an imprint of the IET, Edison, NJ, 2016.

[20] J. Lundgren, J. Helander, M. Gustafsson, D. Sjöberg, B. Xu, and D. Colombi. Near-field measurement and calibration technique for rf emf exposure assessment of mm-wave 5G devices. Technical Report LUTEDX/(TEAT-7267)/1–30/(2019), Lund University, Department of Electrical and Information Technology, P.O. Box 118, S-221 00 Lund, Sweden, 2019.

[21] K. Persson and M. Gustafsson. Reconstruction of equivalent currents using a near-field data transformation – with radome applications. *Prog. Electromagn. Res.*, **54**, pp. 179–198, 2005.

[22] S. Pfeifer, E. Carrasco, P. Crespo-Valero, E. Neufeld, S. Kühn, T. Samaras, A. Christ, M. H. Capstick, and N. Kuster. Total field reconstruction in the near field using pseudo-vector E-field measurements. *IEEE Trans. Electromagn. Compat.*, **61**, pp. 476–486, 2019.

[23] S. M. Rao. *Time Domain Electromagnetics.* Academic Press, 1999.

[24] SPEAG. EUmmWVx / 5G ProbeE-Field mm-Wave Probe for General Near-Field Measurements. Schmid & Partner Engineering AG, Zurich, Switzerland, [Online] https://speag.swiss/products/dasy6/probes/new-eummwvx-vector-e-probe/, Retrieved: Jan. 2019.

[25] R. Vallauri, G. Bertin, B. Piovano, and P. Gianola. Electromagnetic field zones around an antenna for human exposure assessment: Evaluation of the human exposure to EMFs. *IEEE Antennas and Propagation Magazine*, **57**(5), pp. 53–63, 10 2015.

[26] J. G. van Bladel. *Electromagnetic Fields.* IEEE Press, Piscataway, NJ, second edition edition, 2007.

[27] A. D. Yaghjian. An overview of near-field antenna measurements. *IEEE Trans. Antennas Propag.*, **34**(1), pp. 30–45, January 1986.

IR and Metasurface based mm-Wave Camera

Johan Lundgren, Mats Gustafsson, Daniel Sjöberg, and Martin Nilsson

Paper VI

Abstract

We have developed a technique to measure low-power electromagnetic fields from mm-wave devices non-intrusively by combining a metasurface, designed to absorb power and focus the radiated power in a thermally isolated region, with an infrared camera. The metasurface consists of thermally isolated elements of low mass and highly emissive material for maximal IR conversion of the incident wave. The IR camera captures the converted energy and indirectly images the incident electromagnetic field on the metasurface. The setup combines multi-scale, multi-physical processes to conduct measurements of the incident electromagnetic fields in real time. In this work, the technique is presented and discussed. Measurements are carried out to demonstrate the technique and image the electromagnetic field of a radiating device. The results compare well with simulations and the technique can measure the low power density levels of consumer devices, as well as provide a general visualization of electromagnetic fields in a live setting.

1   Introduction

All around us, there is electromagnetic radiation, whether it is visible light, infrared, ultraviolet, or man-made signals from Wi-Fi and cellular devices. The electromagnetic spectrum is wide and humans, by nature, only detect a small fraction of it, either directly through our eyes or indirectly such as feeling warm from the infrared light near an outdoor lamp or getting tanned by the ultraviolet rays from the sun. Radiation exists even though we do not always see it and is difficult to sense.

As things radiate, and objects interact with radiation, energy will be absorbed and scattered. The absorbed electromagnetic energy gets converted to heat through the movement of electrons [14]. The heat will give rise to infrared photons. These photons can be detected at a different position, giving information on the temperature of the object. By capturing the photons with, for instance, an infrared (IR) camera, it is possible to image the electromagnetic field [3, 5, 10, 15, 16, 18, 20].

This chain of events incorporates many physical phenomena, electromagnetic and thermal, and it is important to consider them all. By doing this we construct a sensor for electromagnetic radiation over large surfaces for radiation otherwise invisible. This is a camera, of sorts, for man-made mm-Waves.

For the idea to work, energy from the electromagnetic field must be absorbed and give a detectable temperature increase, even for low power levels seen in consumer devices. The temperature increase is the signal corresponding to the squared field intensity, and should be strong. For a given absorbed energy, the temperature change can be increased by reducing the mass of the sensor and/or focusing the energy to a smaller sub-region. The strength of the signal can be maintained if these warmer regions can be thermally isolated. The heated
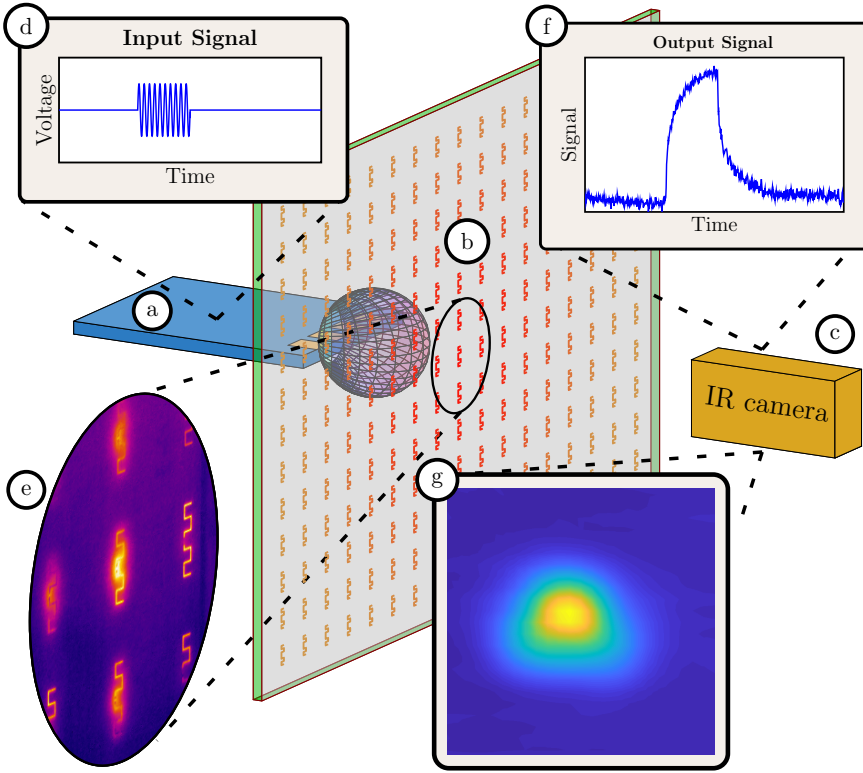
Figure 1: An illustration of a measurement using the metasurface sensor composed of an array of a radiating device (a), thermally isolated elements (b), IR camera (c), the input signal (d), IR image of the metasurface (e), temporal evolution (f), and the resulting image of the field (g).

subregions can each be viewed as measurement points of the field. For devices in the mm-wave regime these measurement points are given on a cm-scale rather than a pre-defined wavelength scale. For example, guidelines and restrictions on exposure levels average over predetermined spatial regions, typically [13] $1\,\mathrm{cm}^2$ or $4\,\mathrm{cm}^2$. Isolation hinders diffusion of thermal energy and stops blurring of the image, and is achieved by physically separating the sensor metal elements on a substrate with low thermal conductivity.

To address these challenges, and produce images of the electromagnetic field in real-time, we present a metasurface sensor. The electromagnetic response and thermal properties of the metasurface enable an observable temperature increase in localized regions for power density levels below $0.1\,\mathrm{mW/cm}^2 = 1\,\mathrm{W/m}^2$. This stands in contrast to generating a temperature increase over the entire sheet [3, 5, 20] or patches [15], which use high power density levels, $27 - 220\,\mathrm{mW/cm}^2$ for frequencies in the $2 - 20\,\mathrm{GHz}$ range [17, 18, 20, 21]. Important power density levels

are generally lower than this and determined by guidelines and restrictions. The ICNIRP [13] states that for frequencies between $6\,\mathrm{GHz}$ and $300\,\mathrm{GHz}$, a power density of $1\,\mathrm{mW/cm^2}$ is a low-end limit with a high-end limit of $40\,\mathrm{mW/cm^2}$.

Apart from the geometry, and thermal properties, of the metasurface, the impact of thermal diffusion can be suppressed in the end image by modulating the signal of the radiating device [3]. The structure and a use case is displayed in Fig. 1. A radiating device (a) is placed near the metasurface sensor (b) and in front of the infrared camera (c). The radiating device transmits a signal (d). The radiation impinges on the sensor which absorbs part of the energy and becomes warmer, seen by the infrared image (e). The camera detects the heating and generates an output signal (f) used to retrieve information of the electromagnetic field (g). We have constructed a measurement system for mm-wave radiation based on the metasurface principle outlined above. A manufactured metasurface is measured in this work, and the absorption of energy in small isolated regions shows the possibility of measuring the low power levels from consumer devices. In this letter, electromagnetic radiation refers to the fields radiated by the device, even though infrared radiation also is electromagnetic.

The rest of the paper go through the technique in more detail. The next two section cover the metasurface sensor and input/output signals. Measurement results of a small device are presented before concluding the work. Even though infrared radiation is electromagnetic radiation our mention is strictly for the fields radiated by the device.

2   Metasurface Principle

At the heart of the technique is a metasurface sensor [1, 12, 22], a two-dimensional metamaterial [6, 7]. The purpose is to convert electromagnetic radiation to detectable infrared photons [3, 5, 10, 15–21]. A high number of photons should correspond to a strong incident electromagnetic field, where we assume that the metasurface is placed outside the reactive near field of the radiating device. Being capable of measuring low power levels requires careful consideration of many physical phenomena. For this, the surface needs to have certain thermal and electromagnetic properties.

The heat should stay localized and not spread over the surface significantly, as this will lower the temperature and blur the image. Our solution is a metasurface with thermally isolated elements on a substrate with low thermal conductivity and low specific heat capacity [4], see Fig. 1. To maximize the interaction and tunability within a certain given frequency interval—that of the radiating device, Fig. 1 (a)—we constructed resonant antenna elements [15]. Each antenna element is loaded with a resistor which absorbs the energy and converts it to heat. In specific applications such as near-field measurements, reflection back to the radiating device is unwanted. In these cases the value of the load can be altered to reduce reflection, but also absorption, in effect making the metasurface invisible for the device [24]. Absorption, reflectance, and transmittance of a thin

metasurface can be tuned between the peak absorption, 50%, (25% reflectance and transmittance) and lower absorption with either high or low reflectance and transmittance by tuning the load. This is the general principle of the metasurface, of which we present one implementation, see SI.

One element corresponds to one pixel in this mm-wave imaging system. To place the elements close to each other, *i.e.* mimicking a homogeneous metasurface for the radiated field, we design miniaturized antennas. A well-designed resonant element will, in principle, interact with a surrounding region approximately of size λ^2, with λ denoting the wavelength [23]. Many choices on designs exist and in this work we explore meander line antennas, as seen in Fig. 1, a traditional design for small resonant antennas [9].

When interacting with the field, a current passes through the element and, with a resistor in the current's path, heat will be generated through ohmic losses. From this heat, infrared photons are created and must be emitted to be detected. An important parameter of the element is thus the emissivity, which describes how effective a material is in emitting thermal radiation [11]. Metal has low emissivity (high reflectance), and will in this setting appear to have a constant temperature even though the actual temperature has changed [11]. This is demonstrated in Fig. 1 (e), in which the meander lines are visible, although they have the same temperature as the surrounding sheet. The resistors used in this work were prefabricated off-the-shelf-components soldered into place by hand. They were placed in the center of the meander lines where the current is the largest. The main part of the resistor consists of a ceramic material and chromium, which has high emissivity. This yields more infrared photons to detect, and thus a higher signal-to-noise ratio in the infrared camera.

3   Metasurface Response

If a device radiates a single frequency continuously, the metasurface will heat up and eventually reach thermal equilibrium depending on the strength of the electromagnetic field. However, obtaining thermal equilibrium in each spatial measurement point and translating it to a power density is complicated and time-consuming [20]. Another way to measure is lock-in thermography [3] or modulate the transmit signal in other ways [15]. Examples include sinusoidal modulation and on/off modulation. Modulation has the benefit of reducing the impact of thermal convection and conduction at a signal-to-noise ratio cost [2]. With a low enough duty cycle of the input signal to allow for cooling back towards the initial state, then the temperature increase, and consequently photon generation, for one period of on/off modulation will approximately follow

$$T(t) \propto \begin{cases} 1 - \mathrm{e}^{-t/\tau_{\mathrm{r}}} & 0 < t \le t_0 \\ \mathrm{e}^{-(t-t_0)/\tau_{\mathrm{f}}}\big(1 - \mathrm{e}^{-t_0/\tau_{\mathrm{r}}}\big) & t > t_0 \end{cases} \tag{3.1}$$
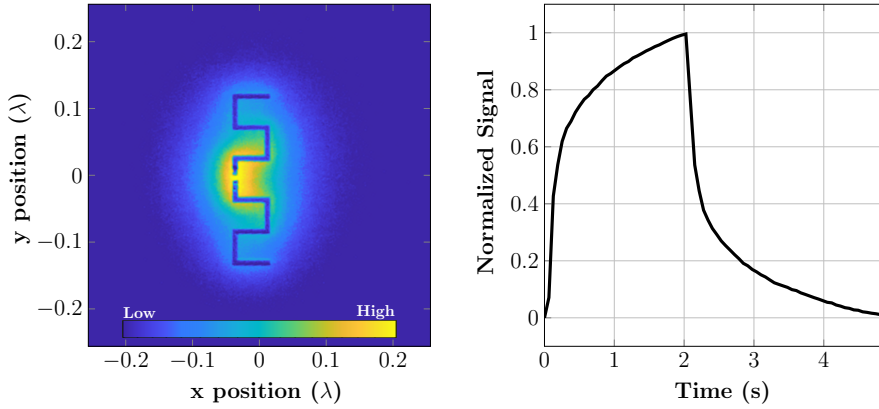
Figure 2: Measured temperature distribution over the element at peak temperature (left) and normalized temperature increase in the resistive element over time (right).

Here, $\tau_{\mathrm{r,f}}$ are the characteristic times of the system and the signal is on from $t = 0$ to $t = t_0$. The resulting output signal of a measurement with a transmitting signal, on for two seconds and off for three seconds, is displayed in the right graph of Fig. 2. The curve is well described by the approximate solution to the heat equation described by (3.1).

The spatial distribution of the temperature from a measurement over one element is seen in Fig. 2 and is directly proportional to the absolute square of the incident electric field in the element's principal direction. The temperature increase is confined to the center of the meander line where the resistor is placed. A typical measurement and the regions of interest is displayed in Fig. 3. The main region of interest, acquisition region, is the area surrounding the resistor, here labeled region *A*. At a first pass, we can investigate the maximal temporal peak temperature of the element compared to the lowest temporal value of the same region. Evident from Fig. 3, the temperature does not spread symmetrically, and the acquisition region is chosen to include most of the thermal energy. A measurement of the mean value of the temperature of region *A* is seen in the top left (the signal-to-noise ratio is higher in the image than in the graphs to show the spread of thermal energy across the metasurface). The measurement was conducted over three periods, not easily identifiable in this data. This can partly be explained by a change in temperature, due to the camera, ventilation, and other factors. By defining a reference region, region *B* in Fig. 3, this impact is reduced. In this work, we used a region along the symmetry axis of the element. Provided that an outside factor is affecting both region A and B, it can be compensated for by taking the difference between the signals. The further away the regions are, the less the desired signal in A is leaking into B. Therefore region B is placed close to the edge of the periodic cell in order to increase the signal strength. The mean temperature in region *B* is shown in the bottom left graph.
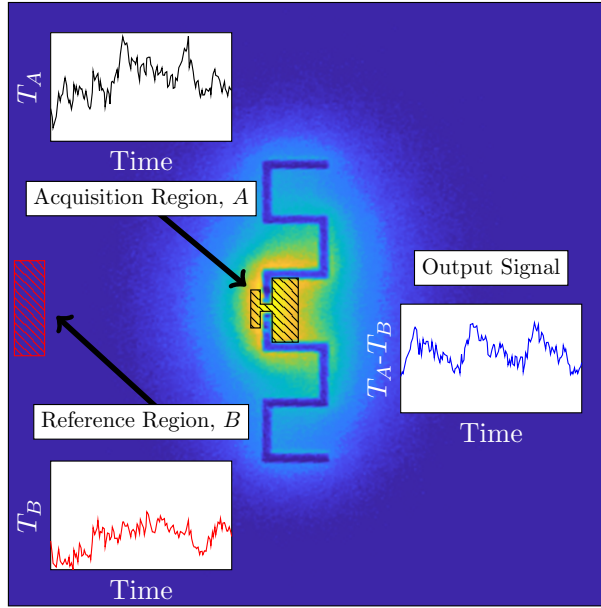
Figure 3: Regions of interest in the signal retrieval shown at peak temperature and the signals in acquisition region A, reference region B, and output signal.

The output signal, right graph in Fig. 3, obtained by subtracting the temperature of the reference region from the acquisition region, show three clear periods.

The scaling of the received signal strength for varying incident power density levels is seen in Fig. 4. The acquisition region was similar to Fig. 3. The blue lines in Fig. 4 use reference subtracted peak temperature of the acquisition regions. The red lines use the reference subtracted mean temperature of the acquisition region and are less sensitive to noise. The dashed lines show a measurement of two periods and the solid lines include around 30 periods for power densities lower than $0.1\,\mathrm{mW/cm^2}$ and around 15 periods for power densities higher than $0.1\,\mathrm{mW/cm^2}$. In an ideal setting the measured temperature, T_{obs}, is directly proportional to the incident power density, P, that is, $T_{\mathrm{obs}} = \alpha P$, where α is a constant. However, noise impacts the system and the equation is better estimated by $T_{\mathrm{obs}} = \alpha P + n$, where n is the noise level. At around 0.05-0.1 mW/cm^2 the red and blue curves changes shape due to the impact of noise in the experimental setup. With more periods, noise affects the system less, and lower power levels can be measured.

From the physics we expect the approximate response (3.1) to hold. The measured data can be estimated to be on this form, using input parameters as amplitude, characteristic rise, and fall time into simple minimization techniques. With the reference subtracted mean temperature of the acquisition region, and fitting this to an expression on the form of (3.1), we obtain the black solid curve of Fig. 4. There is a linear trend throughout the measurement range and the
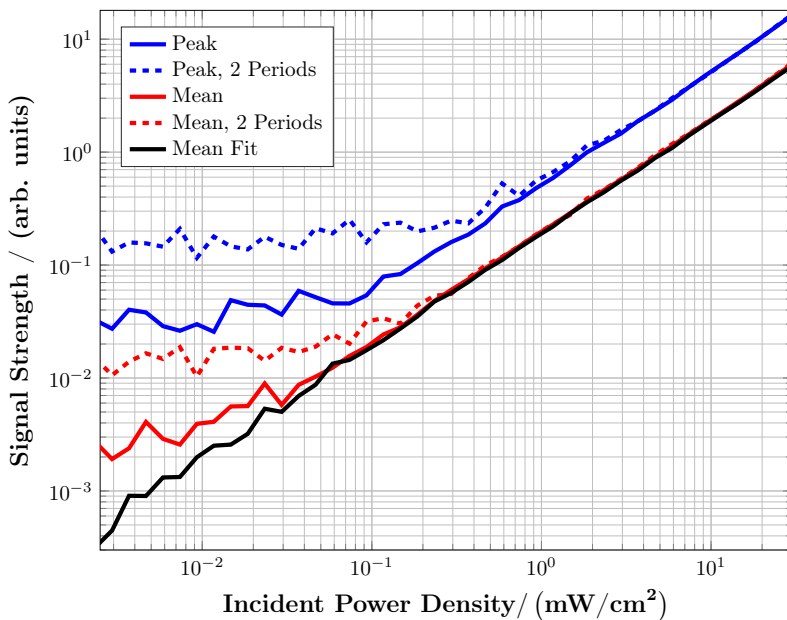
Figure 4: Signal strength in the output data for varying incident power densities for on/off modulation using the peak (blue), and the mean (red) temperature, for two periods (dashed) and around 30 periods for low power densities and around 15 periods for high power densities (solid). In the black line, the output data has been fitted to the form of (3.1).

results show that the constructed metasurface can measure power levels below $0.1\,\mathrm{mW/cm^2}$. Consequently, lower power levels can be observed with this process and form the basis of the on/off measurements in this letter. For any non-pulsed measurements, the reference subtracted mean temperature of the acquisition region was used. Thermal noise, in the non-cooled camera, can be seen to impact the system at low power density levels.

Another aspect of the measuring technique is converting from the measured temperature to a power density level. There are several approaches to calibration. In this work, we used an open-ended waveguide and a calibrated signal generator to extract a value of the incident field from the amplitude of the signal. In Fig. 4 the peak temperature for different values of input power is plotted using a periodic input signal. Fig. 4 converts the measured signal to power density and could serve as calibration.
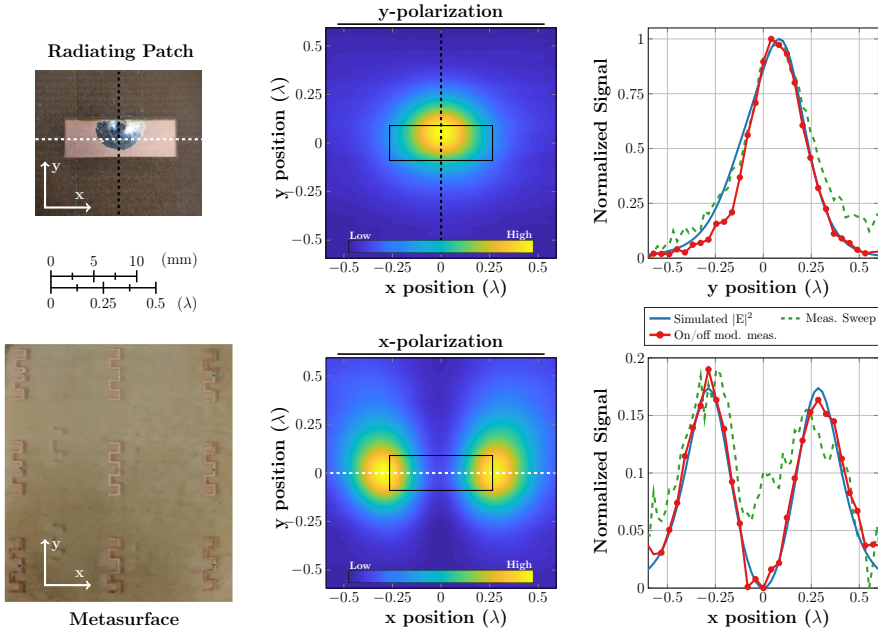
Figure 5: The metasurface and radiating patch, dimensions $12.9 \times 4.5 \, \text{mm}^2$, to scale (left column). Field distribution obtained from a continuous scan in a plane $5 \, \text{mm}$ away from the radiating device in both x (cross) and y (co) polarization with the outline of the patch in solid black (center column). The output signal along the dashed lines for on/off modulation, continuous sweep, and simulation (right column).

4 Measurement of a Device

A metasurface consisting of a 3×3 array was constructed for $10 - 13 \, \text{GHz}$ and used to measure the field distribution close to a small radiating device (a patch antenna). The metasurface and device are shown in the leftmost column of Fig. 5. The meander line is $0.2 \, \text{mm}$ wide and can be confined in a rectangle of dimensions $6.52 \times 1.38 \, \text{mm}^2$, see SI. In the image one can see meander like shapes in between the array elements. These are burn marks, a byproduct of the manufacturing, and are not made of metal. The measurements were conducted at $12.25 \, \text{GHz}$ to enable the early prototype to be constructed partially by hand. The radiating device was chosen to have a significant cross-polarization component, and we measured close to the radiating device to capture interesting patterns and investigate a region where measurements are non-trivial.

The radiating device was measured in a plane parallel to the patch $5 \, \text{mm}$ $(\lambda/5)$ away in two ways. In one setting the metasurface was swept continuously over the device and the device radiated a time-harmonic signal. In the center column of Fig. 5 the resulting images are seen for both the co-polarized (y) and

cross-polarized (x) components. The co-polarized measurement used an input power of 6 mW and the cross-polarized used 60 mW. The purpose of these two images is to show the radiated field pattern. In a patch antenna, one expects the fields to be strong near the edges of the patch. This is most obvious in the cross-polarization where two peaks are visible, and situated on each respective edge of the patch, Fig. 5 bottom center. Similarly, we expect the field in co-polarization to be strong at the feed position and the edge close to it. The feed is placed near the top edge which is where the field is strongest, top row, center, Fig. 5.

To examine the results further, we plot cuts along the x and y directions over the center of the device, see dashed green curves in the rightmost column of Fig. 5. For the measurements generating the rightmost column, a constant input power of 0.6 mW was used, translating roughly to a power density of 0.05-0.5 mW/cm^2 for the cross-polarization and co-polarization measurements. Therefore, the signal is noticeably noisier than in the center column. A second measurement is added in this figure and consisted of 12 periods on/off modulation (on two seconds, off three seconds) per measurement position and fitting the data to an exponential estimate (3.1) as described previously, see solid red curves with markers. Simulations of the patch using the software FEKO are shown in solid blue. The element on the metasurface was of comparable dimensions to the radiating device, yet we observe curves similar to the simulations. In particular for the on/off modulated signal where the technique could capture the sub-wavelength detail of a zero value of the field in the center of the patch in cross polarization, $x = 0$ bottom right Fig. 5.

5 Discussion and Conclusion

Using heat to image electromagnetic fields, as done in this letter, using a metasurface for mm-waves, is an interesting concept which combines several physical phenomena. There are many parameters to consider in construction, design, and measurement technique. The design and material might differ for different frequencies, but our focus is on presenting the technique. Although many parameters are at play, the metasurface can be tailored to specific measurement needs such as element positioning, orientation, and reflection back onto the radiating device. The metasurface is flexible and enables real-time measurements of devices without complex measurement environments such as anechoic chambers.

In this work, a technique to measure electromagnetic fields from a mm-wave device through a metasurface and an IR camera is presented. An impinging wave interacts with the surface that dissipates energy through ohmic losses, detected by an IR camera. The concept of the metasurface and a concrete design is presented. A metasurface was manufactured and used to measure a device radiating at 12.25 GHz in a plane $\lambda/5$ away. The results compare well with simulations of the field and the device could detect very low power levels, less than 0.1 mW/cm^2, compared to previous measurements in the range of 27-220 mW/cm^2 for frequencies in the 2-20 GHz range [17, 18, 20, 21].

   This mm-Wave technique is enabled by the rapid, and ongoing, development
of thermal cameras in combination with higher frequency electromagnetic waves
in everyday scenarios. The metasurface-IR camera is well suited for mm-Wave
devices, with elements having low mass and small physical size, to enable de-
tectable signals on a cm-resolution. The technique is relatively inexpensive and
flexible—manufacture a metasurface, place it, and image with an IR camera.
The technique shows promise for fast evaluation of radiated fields from everyday
devices.

Supplementary Material

See the supplementary information for details on the mechanisms of heat transfer,
metasurface elements, substrate and materials, setup and measurements and IR
cameras.

Acknowledgements

Supplementary Information

In this supplementary information (SI) more details regarding the technique are
described. First, we discuss the physical processes involved and how they affect
the metasurface. We follow this by discussing the design of the structure and
trade-offs. Lastly, additional details regarding the measurements are presented
along with additional results from multiple IR cameras.

A   Mechanisms of Heat Transfer

The mechanisms of heat transfer in the metasurface can be discussed in the
simplified context of a two-dimensional thin sheet with thickness d [11],

$$\frac{\partial u}{\partial t} = \frac{P(t)}{c_{\mathrm{p}}\rho}f(\boldsymbol{r}) + \frac{k}{c_{\mathrm{p}}\rho}\nabla^2 u + \frac{2h}{c_{\mathrm{p}}\rho d}(T_0 - u) + \frac{2\varepsilon\sigma}{c_{\mathrm{p}}\rho d}(T_0^4 - u^4), \qquad \text{(S1)}$$

where $u(\boldsymbol{r}, t)$ is the temperature in the sheet at position $\boldsymbol{r} = (x, y)$ and time t.
Heat is supplied by the DUT with total radiated power $P(t)$, where the time

dependence is due to power modulation of the DUT. The resulting spatial distribution of ohmic heat in the metasurface at unit output power of the DUT is denoted $f(\boldsymbol{r})$. The specific heat capacity at constant pressure is denoted c_{p}, and the density is ρ. The heat is dissipated in the form of diffusion, convection, and radiation, represented by the last three terms in (S1). The factor k is the thermal conductivity, h is the convective heat transfer coefficient, ε is the emissivity of the object, σ is Stefan-Boltzmann's constant, and T_0 is the background temperature [11]. The radiation term corresponds to the photons that we observe with the IR camera and can be linearized to $\frac{\varepsilon\sigma}{c_{\mathrm{p}}\rho d}8T_0^3(T_0 - u)$ for small temperature differences. The factor of 2 in the convective and radiative terms is due to the two sides of the sheet.

We aim for a design where the ohmic losses are concentrated to a small resistive part of the element, see Fig. 2, where it is desirable to dissipate as much as possible through radiation. Thus, we want to minimize the diffusion in the substrate (small k), and the convective losses (small h), while maximizing the IR-radiation from the resistor (large ε). Whereas k is available in many orders of magnitude, h is typically around $5\,\mathrm{W/(m^2K)}$ for a smooth planar surface surrounded by air, and higher if the surface is textured. [25] At room temperature ($T_0 \approx 293\,\mathrm{K}$), the heat transfer coefficient due to radiation is proportional to $\sigma 4T_0^3 = 5.7\,\mathrm{W/(m^2K)}$, and is maximized by using materials with high emissivity ε.

Solving (S1) for a metasurface requires discretization of a non-trivial geometry with several materials involved, feasible with numerical solvers, for instance, based on the finite element method [11]. For a successful design, where diffusion processes can be ignored, this is an ordinary differential equation in time that can be solved for a given excitation $P(t)$. A typical scenario may be where the DUT is on for some time t_0 and is then turned off. The solution is then composed of simple exponentials,

$$u(t) \propto \begin{cases} 1 - \mathrm{e}^{-t/\tau} & 0 < t \le t_0 \\ \mathrm{e}^{-(t-t_0)/\tau}\left(1 - \mathrm{e}^{-t_0/\tau}\right) & t > t_0 \end{cases} \tag{S2}$$

The characteristic time is $\tau = c_{\mathrm{p}}\rho d/(2h + \varepsilon\sigma 8T_0^3)$. When taking diffusion and more accurate three-dimensional modeling into account, no such simple expression is possible. In this case, (S1) is changed by letting $\boldsymbol{r} = (x, y, z)$ be a full three-dimensional position vector, and the convection and radiation terms in (S1) are instead included in the boundary conditions. This approach is used for the detailed simulations in Sec. C. However, (S2) can be improved by separating the characteristic time in rise and fall region to account for the different physical processes involved in the full model [8]. This modifies (S2) to yield (3.1).
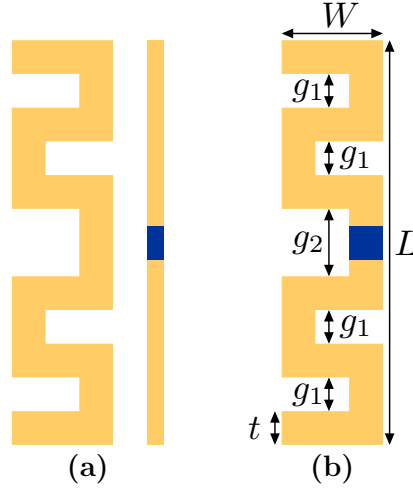
Figure S1: Example designs of meta elements: (a) capacitively coupled meander line and (b) meander line. The gold-colored material is the electrically conducting material, and the blue-colored material is the resistor.

B   Metasurface Elements

The metasurface consists of several elements, each with a region where heat can be generated, in an array fashion, see Figs. 1 and 5. Each element can be considered a measurement point in conventional probe scanning setups, which in this configuration can all be evaluated simultaneously. The temperature increase in the element is larger if the element is constructed with less material, as the absorbed energy is used to heat a region of smaller mass. The element can be designed in several ways and this section presents two designs, see Fig. S1, used in this work and suitable material properties of the different components.

The heat spreads rapidly across the gold-colored regions depicted in Fig. S1 as the material candidate of this region is metal, which inherently conducts heat well, see also Fig. 2. In order to confine the heating to a region of lesser mass, and thus possibly resulting in a higher temperature increase, a design of capacitively coupled regions in Fig. S1 (a) may be utilized, see also Sec. E.

The geometrical parameters of the designs differ depending on the frequency used, material choice, and periodicity of the elements. The chosen design depends heavily on the parameters and fabrication. As long as the skin depth is not compromised, the thickness of the element matters little for the electromagnetic properties but is very important in order to reduce mass. The materials considered in this work are primarily copper, gold, and silver as candidates for the conducting region, and for the resistive part, we have considered prefabricated resistors and alloys such as NiCr of varying compositions. Further investigations into physical and geometrical parameters are done in the following sections cover-
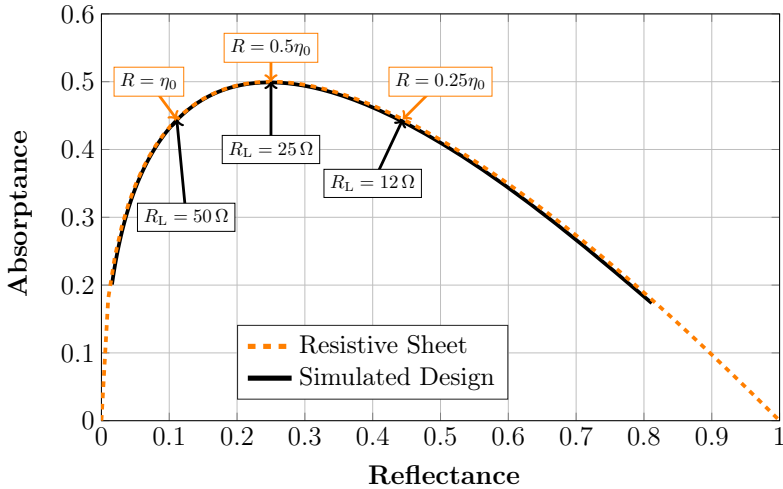
Figure S2: Relationship between reflectance and absorptance for a resistive sheet (S3), dashed, and simulated design, solid. The solid curve was generated by changing the load resistance, R_L, of a tuned design.

ing parameter studies of material parameters and optimization of the geometry.

The elements should be constructed to be resonant to the incoming electromagnetic wave, as this will increase the effective area and provide a high interaction with the electromagnetic field [23, 24] as well as tunability.

Considering the metasurface to be thin and modeling it as a resistive sheet with resistance R, we obtain the relation between reflectance and absorptance for a general resistive sheet as [24]

$$\mathcal{R} = \frac{1}{(2R/\eta_T + 1)^2} \quad \text{and } \mathcal{A} = \frac{4R/\eta_T}{(2R/\eta_T + 1)^2}, \tag{S3}$$

where η_T is the transverse wave impedance. These relations are illustrated in Fig. S2 for normal incidence with $\eta_T = \eta_0$, where η_0 is the wave impedance of free space. The transmittance $\mathcal{T}$ is obtained from power conservation, $\mathcal{R} + \mathcal{A} + \mathcal{T} = 1$. The maximal absorptance is 50 % at which the reflectance is 25 % and the transmittance is 25 %.

The software used to simulate the physics and optimize the design was COMSOL, in combination with MATLAB. A planar periodic model was constructed, including the physics, of which the simplified version was presented in Sec. A, and simulated on an i7-7700 machine. During the optimization process it is important to optimize the designs based on the end goal of detecting temperature increase with an IR camera. Increasing the average temperature in the load resistor is not enough, but rather the signal of the receiving device should be considered. Both geometrical and physical parameters were investigated during the optimization process, in which the average temperature in the acquisition region in relation to the reference region was maximized, see Fig. 3 in the main letter.

The manufactured design, used for the measurements in the letter, consisted of a meanderline as illustrated in Fig. S1 (b) of thickness $t = 0.2\,\text{mm}$, length $L = 6.52\,\text{mm}$, width $W = 1.38\,\text{mm}$, and gaps $g_1 = 0.98\,\text{mm}$ and $g_2 = 1.38\,\text{mm}$. The sheet consisted of XT-duroid 8100 and the metal part of the elements was 18 μm thick copper and the resistors were thick film resistors from Yageo. As described in Sec. B the load can be changed to adjust the reflectance and transmittance tradeoff. Using a well-optimized design and changing the load will shift the design along the resistive sheet approximation. This is seen by the solid line in Fig. S2. With a well-designed element, the load resistance may be chosen to fit the specific needs of the measurement system.

C   Substrate and Materials

The simulations presented are for an already optimized design and the impact of parameters, as presented in Fig. S3, is for this specific case. However, the general trend of parameter values and impact of different terms in the main letter remains for different designs. The thermal parameters of the resistor were also investigated. For this particular design, consisting of a very thin layer, 10 nm, of resistive material situated on a 50 μm substrate, the impact of the thermal properties of the resistor was not noticeable. For a resistor of more mass, it might differ. The important parameter of the resistor is the resistance, as seen in Fig. S2. Suitable material candidates are gold/silver etc for the meander line segment of the element and the resistive region could be NiCr, see Fig. S1.

Heat conduction in the substrate as well as convection in the air are important factors and have a large impact on an otherwise functioning design, see Sec. A. There is little to be done regarding the convection of the surrounding air. However, the substrate can be chosen freely. From the bottom graph of Fig. S3 we can see how the average temperature in the resistor is affected by changing the specific heat capacity, c_p and the thermal conductivity k of the sheet, see (S1). The parameters are normalized to that of the polytetrafluoroethylene (PTFE) sheet, labeled k_0 and c_0. From these two figures, it is seen that the sheet should have low thermal conductivity and heat capacity. Reducing the heat conduction in the sheet also reduces the impact of convection. Good candidates for substrates are PTFE based laminates such as Rogers XT-duroid 8100, $c_\text{p} \approx 1000\,\text{W/kg}$, $\rho = 1.6 \cdot 10^3\,\text{kg/m}^3$, and $k = 0.3\,\text{W/(m\,K)}$, or Rohacell 51, $c_\text{p} \approx 2400\,\text{W/kg}$, $\rho \approx 75\,\text{kg/m}^3$ and $k = 0.036\,\text{W/(m\,K)}$. PTFE can be utilized in a very thin sheet and rohacell is a porous material in sheets of thicknesses often 1 mm and larger, and as such they pose different challenges in manufacturing.

D   Setup and Measurements

The measurements were done on in-house fabricated designs of types seen in Fig. S1. They were manufactured to operate at frequencies between 10 and
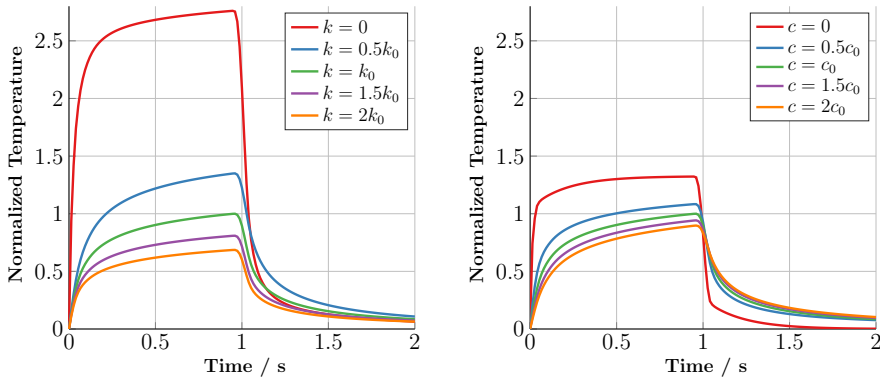
Figure S3: Temperature increase in the resistive element over time for different values of thermal conductivity (top) / specific heat capacity (bottom) in the sheet normalized to the PTFE laminate XT-duroid 8100 labeled k_0 and c_0.

13 GHz.

For the power density measurements yielding Fig. 4, a waveguide and a calibrated signal generator were used. A single element was measured and the DUT was an open-ended waveguide which the element was placed in front of. The element was illuminated by a uniform incident power density polarized in the direction of the element, provided by the waveguide. The illuminating waveguide was connected to a signal generator providing power density levels between 0–13 mW/cm^2. The output power was confirmed by a power measurement with a calibrated VNA as well as a power meter. The waveguide was used due to its simple and robust radiation pattern. The elements were placed in front of the waveguide and the signal was swept over frequency and amplitude. The data presented in Fig. 4 is for the resonance frequency.

The measurements used to generate Fig. 5 consisted of mounting a 3×3 metasurface a fixed distance from a FLIR A655sc camera. The position of the metasurface and IR camera was controlled by two positioners, enabling a scan in a 30×30 cm^2 plane. For the continuous signal measurement, *i.e.*, the 2D plots and green dashed curves in Fig. 5, the mean temperature over a region of the resistor was logged as the positioners scanned. For the on/off modulated measurements, *i.e.*, the red solid curves with markers in Fig 5, the signal was on for two seconds, off for three seconds, and 12 periods were measured for each point. The data was fitted to the estimate (3.1) and measured using the output power of 1 mW on the signal generator. Accounting for matching and cable losses etc, -1.2 dB, this yielded an input power of 0.6 mW roughly translating to a power density of 0.05-0.5 mW/cm^2 for the cross-polarization and co-polarization measurements.
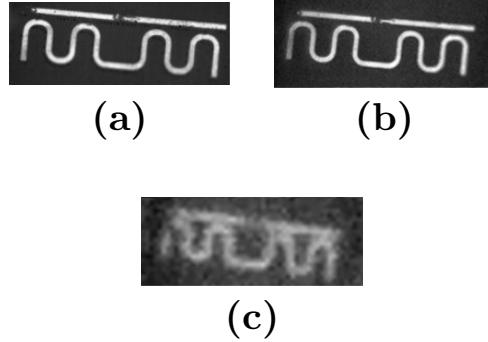
Figure S4: Images of the element as seen by the scientific grade cameras. a) A6752sc with macro lens, b) A655sc with macro lens and c) A655sc without macro lens.

E   IR Cameras

The technique was tested using three different IR cameras, in various degrees. These cameras were an entry-level budget handheld device FLIR E6, a non-cooled scientific-grade camera FLIR A655sc, and a cooled scientific-grade camera FLIR A6752sc. Macro lenses were available and utilized for the scientific grade cameras.

The lenses enabled high-resolution imaging of the single element imaged. In Fig. S4, images are shown of the element as viewed from FLIR A655sc and A6752sc where (a) is from FLIR A6752sc with a macro lens, (b) from A655sc with a macro lens, and (c) without.

The region of interest was the center of the top metal strip, in which the resistor was located. The copper is visible in these figures due to the contrast in emissivity to the background sheet. The temperature was recorded for different lengths of time, ranging from around 4 periods up to around 200 periods.

In the simulations, the temperature in the element could be directly computed, but during measurements, it has to be observed through the IR camera. This adds additional difficulty as the camera is situated a short distance away with air continuously flowing in the region between the sheet and sensor. To measure very small temperature changes a reference region, $\approx$1 cm away from the element was defined. The temperature in this region was mostly unaffected by the small temperature increase in the element but contained the temperature changes due to other unwanted effects such as drafts. The raw data was processed by comparing the acquisition region with the reference region for every measured time point. All the measured periods were then combined to create an average temperature increase in the element. The raw data and the processed corrected data are visible in Fig. S5. The reference region data is shown in green color and the mean temperature of the acquisition region in orange. The solid red line shows the time-synchronous signal average.
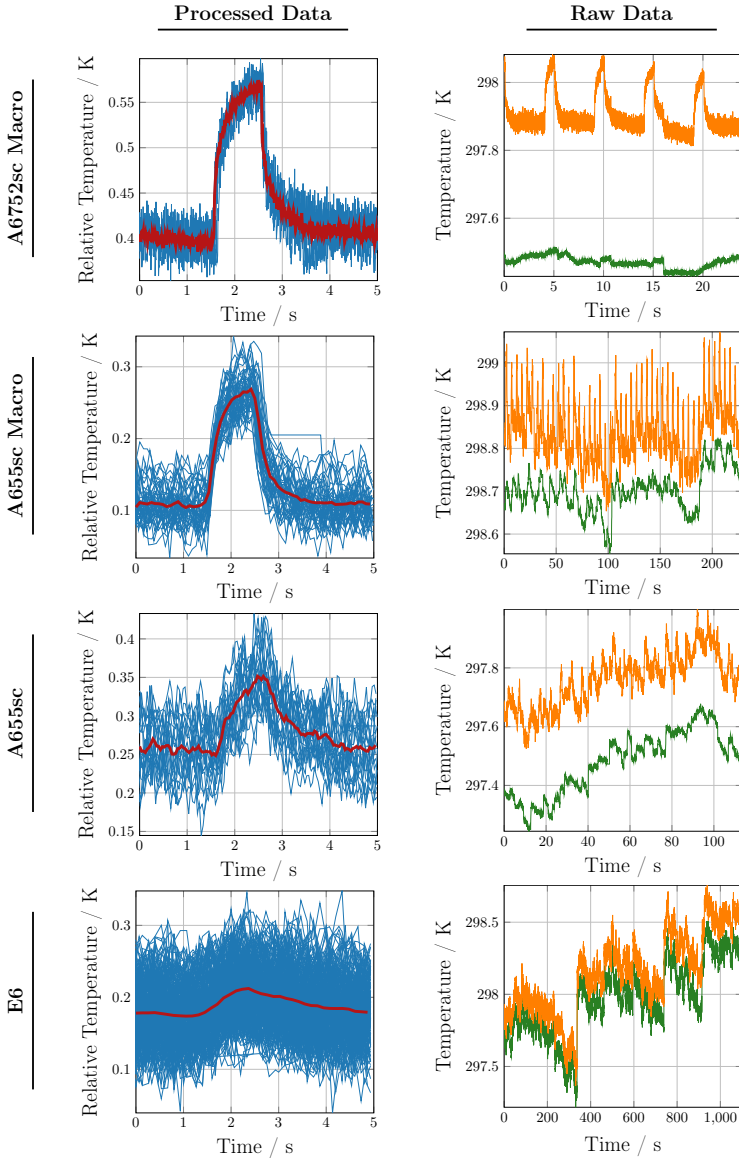
Figure S5: Measurement results of the different cameras and lenses, columns. Processed data is in the top row and raw data on the bottom. The reference data is shown in green color and the temperature of the element in orange, bottom row. The red line shows the time-synchronous signal average, and the blue line is the data gathered within one period.
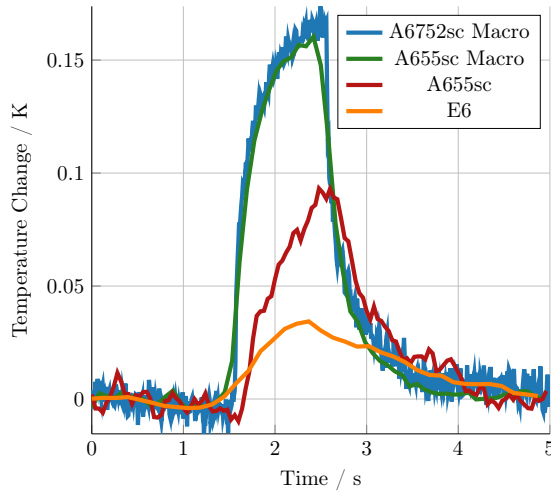
Figure S6: Time-synchronous signal average of all four measurements presented in Fig. S5.

It is immediately clear in Fig. S5 that the non-cooled cameras, column 2-4, experience internal drift in temperature, as the background temperature varies over the measurement time. This is due to the nature of the sensor. The sensors in these cameras are heated by the incoming radiation and consequently, get warmer and are subject to leaking to neighboring pixels. Periodically the camera is recalibrated by letting the pixels get in contact with a reference surface. A measurement setup using these cameras is thus required to have a reference region unless only temperature slope information during very short time intervals is to be extracted. There are also minor changes in the background temperature in the measurement utilizing the cooled camera, FLIR A6752sc. However, this is not on a significant level. Using subtraction of the reference region, the impact of these effects can be reduced and the temperature change is visible. For the non-cooled cameras, longer measurement time seems to be needed. The incident power density was the same for all measurements and an equal temperature increase is expected. The A6752sc and A655sc cameras, with a macro lens, capture a 0.17 degree temperature change in the one-second window when the signal is "on". The shape is agreeable to the curve presented in Fig. 2 in the main letter. The fine details of the heating are lost without the macro lens, and for the A655sc without a macro lens and the handheld E6 device, a temperature difference of 0.1 and 0.03 degrees was observed, respectively. The time-synchronous signal averages for all measurements are seen in Fig. S6.

The curves have been shifted to have the same baseline temperature. There is an observable change detected for all cameras, but a large difference in how easily and rapidly it can be detected. In this work, we are not interested in character-izing the temperature directly, rather the power density of the electromagnetic

field, and thus relating the performance of the graphs in Fig. S6 to a specific power density value is a calibration issue. There are also factors of camera settings and emissivity which factor into the absolute numbers of the temperature change.

References

[1] K. Achouri and C. Caloz. *Electromagnetic Metasurfaces: Theory and Applications*. Wiley-IEEE Press, 2021.

[2] D. Balageas and P. Levesque. EMIR: a photothermal tool for electromagnetic phenomena characterization. *Revue générale de Thermique*, **37**(8), pp. 725–739, 1998.

[3] D. L. Balageas, P. Levesque, and A. A. Deom. Characterization of electromagnetic fields using a lock-in infrared thermographic system. In *Thermosense XV: An International Conference on Thermal Sensing and Imaging Diagnostic Applications*, volume 1933, pp. 274–285. International Society for Optics and Photonics, 1993.

[4] R. B. Bird, W. E. Stewart, and E. N. Lightfoot. *Transport Phenomena*. John Wiley & Sons, 2006.

[5] K. Brown. Far-field antenna pattern measurement using near-field thermal imaging. *IEEE Trans. Antennas Propag.*, **66**(3), pp. 1488–1496, 2018.

[6] F. Capolino, editor. *Metamaterials Handbook*. CRC press, Boca Raton, FL, 2009.

[7] N. Engheta and R. W. Ziolkowski. *Metamaterials: physics and engineering explorations*. John Wiley & Sons, 2006.

[8] K. Fan, J. Y. Suen, X. Liu, and W. J. Padilla. All-dielectric metasurface absorbers for uncooled terahertz imaging. *Optica*, **4**(6), pp. 601–604, 2017.

[9] K. Fujimoto and H. Morishita. *Modern small antennas*. Cambridge University Press, 2013.

[10] L. G. Gregoris and K. Iizuka. Thermography in microwave holography. *Applied optics*, **14**(7), pp. 1487–1489, 1975.

[11] J. R. Howell, M. P. Menguc, and R. Siegel. *Thermal Radiation Heat Transfer*. CRC Press, 2010.

[12] H.-H. Hsiao, C. H. Chu, and D. P. Tsai. Fundamentals and applications of metasurfaces. *Small Methods*, **1**(4), pp. 1600064, 2017.

[13] International Commission on Non-Ionizing Radiation Protection (ICNIRP). Guidelines for limiting exposure to electromagnetic fields (100 kHz to 300 GHz). *Health Phys.*, **118**(5), pp. 483–524, 2020.

[14] J. D. Jackson. *Classical Electrodynamics.* John Wiley & Sons, New York, NY, third edition, 1999.

[15] S. A. Kuznetsov, A. G. Paulish, M. Navarro-Cía, and A. V. Arzhannikov. Selective pyroelectric detection of millimetre waves using ultra-thin metasurface absorbers. *Scientific reports*, **6**, pp. 21079, 2016.

[16] S. A. Kuznetsov, A. G. Paulish, A. V. Gelfand, P. A. Lazorskiy, and V. N. Fedorinin. Bolometric THz-to-IR converter for terahertz imaging. *Applied Physics Letters*, **99**(2), pp. 023501, 2011.

[17] K. Muzaffar, K. Chatterjee, L. I. Giri, S. Koul, and S. Tuli. Modelling and analysis of power distribution of electromagnetic waves on plane surfaces using lock-in IR thermography. *Journal of Nondestructive Evaluation*, **36**(3), pp. 60, 2017.

[18] K. Muzaffar, L. I. Giri, K. Chatterjee, S. Tuli, and S. Koul. Fault detection of antenna arrays using infrared thermography. *Infrared Physics & Technology*, **71**, pp. 464–468, 2015.

[19] K. Muzaffar, S. Tuli, and S. Koul. Beam width estimation of microwave antennas using lock-in infrared thermography. *Infrared Physics & Technology*, **72**, pp. 244–248, 2015.

[20] J. Norgard and R. Musselman. Direct infrared measurements of phased array near-field and far-field antenna patterns. *Quantitative InfraRed Thermography Journal*, **2**(1), pp. 113–126, 2005.

[21] D. Prost, F. Issac, and M. Romier. Imaging electric and magnetic near field of radiating structures by infrared thermography. In *2019 International Symposium on Electromagnetic Compatibility-EMC EUROPE*, pp. 311–314. IEEE, 2019.

[22] O. Quevedo-Teruel, H. Chen, A. Díaz-Rubio, G. Gok, A. Grbic, G. Minatti, E. Martini, S. Maci, G. V. Eleftheriades, M. Chen, et al. Roadmap on metasurfaces. *Journal of Optics*, **21**(7), pp. 073002, 2019.

[23] S. Silver. *Microwave Antenna Theory and Design*, volume 12 of *Radiation Laboratory Series.* McGraw-Hill, New York, NY, 1949.

[24] J. G. van Bladel. *Electromagnetic Fields.* IEEE Press, Piscataway, NJ, second edition edition, 2007.

[25] J. Welty, G. L. Rorrer, and D. G. Foster. *Fundamentals of momentum, heat, and mass transfer.* John Wiley & Sons, 2020.

Roads go ever ever on
Over rock and under tree,
By caves where never sun has shone,
By streams that never find the sea;
Over snow by winter sown,
And through the merry flowers of June,
Over grass and over stone,
And under mountains of the moon.

Roads go ever ever on
Under cloud and under star,
Yet feet that wandering have gone
Turn at last to home afar.
Eyes that fire and sword have seen
Look at last on meadows green
And trees and hills they long have known.

– J.R.R. Tolkien, *The Hobbit*